



Kent Academic Repository

Ullah, Irfan (2021) *Low power wireless technologies for AC current sensing*.
Doctor of Philosophy (PhD) thesis, University of Kent,.

Downloaded from

<https://kar.kent.ac.uk/87042/> The University of Kent's Academic Repository KAR

The version of record is available from

<https://doi.org/10.22024/UniKent/01.02.87042>

This document version

UNSPECIFIED

DOI for this version

Licence for this version

UNSPECIFIED

Additional information

Versions of research works

Versions of Record

If this version is the version of record, it is the same as the published version available on the publisher's web site. Cite as the published version.

Author Accepted Manuscripts

If this document is identified as the Author Accepted Manuscript it is the version after peer review but before type setting, copy editing or publisher branding. Cite as Surname, Initial. (Year) 'Title of article'. To be published in *Title of Journal*, Volume and issue numbers [peer-reviewed accepted version]. Available at: DOI or URL (Accessed: date).

Enquiries

If you have questions about this document contact ResearchSupport@kent.ac.uk. Please include the URL of the record in KAR. If you believe that your, or a third party's rights have been compromised through this document please see our [Take Down policy](https://www.kent.ac.uk/guides/kar-the-kent-academic-repository#policies) (available from <https://www.kent.ac.uk/guides/kar-the-kent-academic-repository#policies>).

**LOW POWER WIRELESS TECHNOLOGIES
FOR AC CURRENT SENSING**

By
Irfan Ullah

A Thesis Submitted in Fulfilment of the Requirements for the
Degree of Doctor of Philosophy in Electronic Engineering

University of
Kent

September 2020

Dedication

To My Dear Parents Salman Hussain and Bibi Farah

Acknowledgement

I would like to thank my supervisors Prof John C. Batchelor and Dr Benito Sanz-Izquierdo for their advice, guidance and consistent support throughout this study. They have been a source of constant encouragement and enthusiasm. Without their advice, trust and assistance, this work would have never been possible. I would also like to thank Prof Gareth Howells, Dr Konstantinos Sirlantzis and Dr Gang Lu for their help and guidance throughout the INCASE project.

I want to thank Mr Simon Jakes and Mr Antonio Mendoza for fabricating the tags, and Dr Robert Horne for helping in experiments. I would also like to thank members of the technical support team at the School of Engineering and Digital Arts for their help throughout my research. Special thanks to Mrs Judith Spinks and Mrs Jane Huxley from the Finance office for their help and support in purchase requisitions.

Finally, I would like to thank my family, especially Mom, Dad, and my brother Farman Ali, for their prayers and support throughout my years of study. I would not have finished this PhD without their prayers, support, and motivation.

Abstract

This thesis is concerned with the development of a novel RFID ac current sensing technique for smart power monitoring systems. The research aims to explore designing self-tuning RFID tags and antenna designs and transforming simple tags into passive ac current sensors. The sensing mechanism by which a self-tuning RFID tag is linked with a varactor tuning circuit and integrated into a current transformer is described. The proposed sensing tag structure is less complex and provides a cost-effective solution for power monitoring when many tags on individual appliances communicate wirelessly with a centrally mounted single RFID reader in the views of the tags to be read.

New optimised RFID tag antenna designs for a current transformer are introduced. Antenna miniaturisation techniques are adopted in designing tag antennas to achieve compact physical integration with the transformer housing while maintaining the tag link. These optimised tag antennas are designed in order to reduce the size of the tag system.

The proposed current sensing concept is further explored to utilise two tag antennas in a single design. The two tag antennas are coupled with different tuning circuits and integrated into a single transformer for increasing the current sensing range of the sensor. The antenna design techniques of designing two tag antennas in close proximity with each other and how the mutual coupling between the tag antennas can be reduced are also studied.

Nomenclature

List of Abbreviations

ac	alternating current
API	application programming interface
ASIC	application specific integrated circuit
CST	computer simulation technology
CT	current transformer
dc	direct current
EIRP	equivalent isotropic radiated power
EPC	electronic product code
FR4	flame retardant 4
FRAM	ferroelectric random access memory
Gen 2	generation-2
HF	higher frequency
IC	integrated chip
IoT	internet of things
LF	lower frequency

PCB	printed circuit board
PEC	perfect electric conductor
PET	polyethylene terephthalate
RF	radio frequency
RFID	radio frequency identification
RSSI	received signal strength index
SSR	solid state relay
UHF	ultra high frequency
USB	universal serial bus

List of Symbols

λ	wavelength
μ	permeability of a specific medium
Ω	ohm
ϵ	permittivity of a specific medium
A	ampere
c	speed of light in vacuum
C_J	junction capacitance
C_{eq}	equivalent capacitance
cm	centimetre
dB	decibel
dBm	decibel referred to one milliwatt
F	farad
f	frequency
G_r	tag antenna gain
GHz	gigahertz
H	henry
Hz	hertz
i_P	primary winding
kHz	kilohertz
kW	kilowatt
M	mutual inductance

m	metre
MHz	megahertz
mm	millimetre
mm^3	cubic millimetre
n	nano
N_P	number of the primary winding
N_S	number of the secondary winding
nH	nanohenry
ns	nanosecond
p	pico
P_{IC}	sensitivity of a tag chip
pF	picofarad
R	resistance
$R_{ant.}$	input resistance of a tag antenna
R_{chip}	input resistance of a tag chip
R_L	load resistor
s	second (time)
$\tan\delta$	loss tangent
V	volt
V_g	voltage source
V_R	reverse bias voltage
W	watt

$X_{ant.}$	input reactance of a tag antenna
X_{chip}	input reactance of a tag chip
X_C	capacitive reactance
Z_C	complex impedance
$Z_{ant.}$	input impedance of a tag antenna
Z_{chip}	input impedance of a tag chip
$^{\circ}\text{C}$	degree (temperature) celsius

Contents

Dedication	i
Acknowledgement	ii
Abstract	iii
1 Introduction	1
1.1 Motivation	2
1.2 Aims and Objectives	2
1.3 Scope of the Project	3
1.4 Main Contributions	3
1.5 Application	3
1.6 The State of the Art	5
1.7 Structure of the Thesis	6
1.8 List of Publications	7
2 UHF RFID Tags: A Review of Literature	11
2.1 Introduction	11
2.2 RFID System	12
2.2.1 Active RFID Tag	12
2.2.2 Passive RFID Tag	12
2.2.3 Semipassive RFID Tag	13
2.2.4 RFID Principle of Operation	14
2.2.5 Read Range	15
2.2.6 Tag Chip	15
2.3 UHF RFID Tag: Research and Development	16
2.3.1 Techniques for Conjugate Impedance Matching	16

2.3.1.1	Inductively Coupled Loop	17
2.3.1.2	T-Match	17
2.3.1.3	Nested Slotline	18
2.3.1.4	Capacitive Tip Loading	20
2.3.2	Tag Antenna Designs	21
2.3.3	RFID Sensing Mechanism	24
2.3.4	Tag Antenna Designs for AC Current Sensing	28
2.4	Conclusion	31
3	RFID AC Current Sensing Technique	37
3.1	Introduction	37
3.2	Existing AC Current Sensing Solutions	38
3.3	Self-Tuning Tag	39
3.4	System Description	41
3.4.1	Current Transformer	41
3.4.2	Tuning Circuit	43
3.4.3	RFID Tag Design	45
3.5	Simulation Results	48
3.6	Measurement Results	51
3.6.1	Capacitance to Sensor Code Relationship	51
3.6.2	Power Cable Measurement	52
3.6.3	Current to Sensor Code Relationship	53
3.6.4	Read Range	55
3.6.5	Rise and Fall Time	56
3.6.6	Sensor Comparison	57
3.7	Conclusion	59
4	Optimum RFID Tag Antenna Design	65
4.1	Introduction	65
4.2	Flow Diagram of Tag Antenna Design	66
4.3	Tag Antenna Design	66
4.3.1	Simulation Results	69

4.3.2	Parametric Design Study	72
4.3.3	Theoretical Read Range	83
4.3.3.1	Normal Tag	83
4.3.3.2	Tag Attached to Transformer	83
4.3.4	Current Transformer and Tuning Circuit	84
4.3.5	Measurement Results	85
4.3.5.1	Sensor Code and Read Range	85
4.3.5.2	Current Sensing Setup	85
4.3.5.3	Current to Sensor Code Relationship	86
4.4	Optimised Tag Antenna Design	89
4.4.1	Simulation Results	90
4.4.2	Parametric Design Study	91
4.4.3	Theoretical Read Range	93
4.4.3.1	Normal Tag	93
4.4.3.2	Tag with Tuning Circuit	95
4.4.4	Measurement Results	95
4.4.4.1	Sensor Code and Read Range	95
4.4.4.2	Current Sensing Setup	98
4.4.4.3	Current to Sensor Code Relationship	99
4.5	Further Tag Antenna Optimisation	101
4.5.1	Measurement Results	103
4.5.2	Sensor Comparison	103
4.6	Conclusion	105
5	Dual RFID Tag System	110
5.1	Introduction	110
5.2	Two Tag Antennas Design	111
5.2.1	Simulation Results	112
5.2.2	Parametric Design Study	117
5.3	Optimised Two Tag Antennas Design	123
5.3.1	Simulation Results	125

5.3.2	Parametric Design Study	125
5.3.3	Tags with Tuning Circuits	132
5.3.4	Theoretical Read Range	137
5.3.4.1	Tag with the Port 1	137
5.3.4.2	Tag with the Port 2	137
5.3.5	Current Transformer	138
5.3.6	Tuning Circuit 1	138
5.3.7	Tuning Circuit 2	138
5.3.8	Measurement Results	139
5.3.8.1	Measurement Setup	139
5.3.8.2	Sensor Code and Read Range	139
5.3.8.3	Current Sensing Setup	140
5.3.8.4	Current to Sensor Code Relationship	142
5.3.9	Sensor Comparison	144
5.4	Conclusion	145
6	Miniaturised RFID Tag Antenna Design	149
6.1	Introduction	149
6.2	Miniaturised Tag Antennas Design	150
6.2.1	Simulation Results	152
6.2.2	Parametric Design Study	156
6.2.3	Theoretical Read Range	162
6.2.3.1	Tag with the Port 1	162
6.2.3.2	Tag with the Port 2	163
6.2.4	Measurement Results	163
6.3	Conclusion	166
7	Conclusions and Future Work	169
7.1	Introduction	169
7.2	Summary and Conclusion	169
7.3	Recommendations for Future Work	172

Appendix A 24 V DC Wireless Energy Logger	173
A.1 Introduction	173
A.1.1 System Specification	174
A.2 Proposed System	174
A.2.1 DC Current Sensor	175
A.2.2 DC Voltage	175
A.2.3 Filtered Voltage Divider	176
A.2.4 5 V DC Power Adapter	176
A.3 Central Processing Unit	177
A.3.1 PCB Design	177
A.3.2 Microcontroller	178
A.3.3 USB UART Integrated Circuit	179
A.3.4 Real-Time Clock	181
A.3.5 EEPROM	182
A.3.6 3.3 V Voltage Regulator	182
A.3.7 USB Connector	183
A.3.8 Serial Peripheral Interface	184
A.3.9 Raspberry Pi	184
A.3.10 24-Bit ADC Board	185
A.4 PCB Layout	187
A.5 Software	188
A.5.1 Source Code 1	189
A.5.2 Source Code 2	191
A.6 Measurement Results	193
A.6.1 Measurement Setup	193
A.6.2 Current, Voltage and Power Measurement	193
A.7 Comparison	196
A.8 Conclusion	197
Appendix B Experimental Devices	201

List of Figures

1.1	Proposed smart metering system based on UHF RFID technology.	4
2.1	Omni-ID active RFID tag with the communication range of up to 150 m [9].	12
2.2	Temperature antenna sensor with the read range of 9 m at 868 MHz [10]. . .	13
2.3	Semipassive UHF logger tag [11].	13
2.4	A typical passive UHF RFID system.	14
2.5	Layout of an antenna structure inductively coupled with a feed loop.	17
2.6	Schematic equivalent circuit of an antenna structure inductively coupled with a feed loop.	18
2.7	T-match tag antenna consists of a planar dipole and a T-matching network. .	19
2.8	Schematic equivalent circuit of the T-match antenna.	19
2.9	A nested slotline antenna for RFID tags [8].	19
2.10	Schematic equivalent circuit of the slotline tag antenna design.	20
2.11	Tip loaded RFID tag [19].	20
2.12	A loaded meander dipole antenna design for UHF RFID tags [12].	22
2.13	Patch tag antenna for mounting on metallic surfaces.	22
2.14	Planar inverted-F antenna for RFID tags. (a) Top view; (b) Side view [24]. .	23
2.15	Small and flexible metal mountable passive UHF RFID tag.	24
2.16	Moisture antenna sensor [26].	25
2.17	Sensor code of the antenna sensor in dry and wet state.	25
2.18	Read range of the moisture antenna sensor.	25
2.19	Loop-match dipole used as fingertip tag over a 1 mm thick layer of biocom- patible silicone: (a) tag layout (dimensions are in mm); (b) exploded view of multilayers for on-skin application; (c) numerical model of the radio- frequency fingertip-augmented device [30].	26

2.20	Prototypes of the epidermal tags: (a) made of a copper wire; and (b) conductive yarn. They are (c) soft and (d) conform to body discontinuities (forearm tendons) [34].	27
2.21	Liquid pressure sensing system, implemented in a cylinder.	28
2.22	AC current impulse sensing system.	28
2.23	Dipole antenna inductively coupled to a rectangular feed loop.	29
2.24	Flexible helix antenna mounted on a power cable for ac current sensing.	30
2.25	Block diagram of the sensor for detecting the ON and OFF state of an electrical appliance.	30
2.26	Design of a meandered dipole antenna inductively coupled with a feed loop for power cables.	31
3.1	Self-tuning tag chip attached across the antenna ports, forming a self-tuning RFID tag.	39
3.2	RFID reader communication and retrieval of tag sensor codes [14].	40
3.3	Reproduced plot from [15], showing a read range of the self-tuning and standard RFID chip.	41
3.4	Schematic diagram overview of the suggested RFID ac current sensing tag from an ac electrical cable.	42
3.5	AC current to dc voltage ratio of the CT.	43
3.6	Typical schematic diagram of a CT with a load resistor (R_L) connected across its output terminals.	43
3.7	Voltage to capacitance ratio of the implemented tuning element in the tuning circuit [20].	44
3.8	The configuration of dc block capacitors and a varactor diode in the tag tuning circuit.	45
3.9	(a) RFID tag design; and (b) tuning circuit design. (All dimensions are in mm)	46
3.10	(a) Parallel circuit of the tag chip; and (b) its equivalent circuit.	47
3.11	CST simulated power reflection coefficient of the RFID tag antenna due to varying capacitor value across its terminals.	48
3.12	CST simulated input admittance of the capacitance sensing RFID tag (Real input admittance).	49

3.13	CST simulated input admittance of the capacitance sensing RFID tag (Imaginary input admittance).	49
3.14	Polar plot of CST simulated tag system realised gain: (a) yz -plane; (b) azimuth plane; and xz -plane.	50
3.15	A final tested prototype of the proposed RFID ac current sensor.	51
3.16	Measured sensor code of a self-tuning tag at 868 MHz. Black square markers: tag loaded with lumped capacitance in the range of 0.1 pF to 1 pF. Grey line square markers: tag with the tuning circuit.	52
3.17	Block diagram of the measurement setup.	53
3.18	Measured sensor code of the proposed RFID ac current sensor at 868 MHz.	54
3.19	The effect of distance variation between the tag system and the reader antenna on the sensor code of the tag system at 868 MHz.	55
3.20	Read range of the proposed RFID ac current sensor at 868 MHz.	56
3.21	Sensing set up for measuring the rise and fall time of a switching load current.	57
3.22	Rise time and fall time of the RFID ac current sensor at 868 MHz. Triangle markers represent sensor code measured by the sensor and black solid line with square markers represent load current reconstructed from sensor code. (a) Rise time (368 ms); (b) Fall time (276 ms).	58
4.1	Design process of the tag antenna design for the current transformer.	67
4.2	(a) Proposed tag antenna design; and (b) tuning circuit with dimensions in mm.	68
4.3	A current transformer design used for simulations in CST; (a) CT outside housing; and (b) CT inside components. (All dimensions are in mm)	70
4.4	3D model of the proposed tag antenna attached to the bottom of the transformer. (a) current transformer, (b) components inside current transformer, and (c) tag antenna attached to the transformer.	71
4.5	CST simulated power reflection coefficient of the RFID tag.	71
4.6	Simulated power reflection coefficient of the RFID tag when the relative permeability of the ferrite cores varies from 10 to 70.	72
4.7	Effect of the antenna parameter e in mm on the antenna port impedance while other parameters in Table 4.1 and 4.2 were fixed.	74

4.8	Power reflection coefficient of the tag when the antenna parameter e varies from 9 mm to 21 mm while other parameters in Table 4.1 and 4.2 were fixed.	74
4.9	Simulated input impedance of the antenna against frequency: (a) when the loop length l varies from 3 mm to 5 mm; (b) when the loop width varies from 4 mm to 6 mm while other parameters in Table 4.1 and 4.2 were fixed.	76
4.10	Simulated power reflection coefficient of the tag, (a) when the length l of the feed loop varies from 3 mm to 5 mm and (b) when the width of the feed loop varies from 4 mm to 6 mm while other parameters in Table 4.1 and 4.2 were fixed.	77
4.11	Simulated tag antenna designs with different tip loading structures: (a) antenna design 1 when $c = 8$ mm; (b) antenna design 2 when $f = 8$ mm; and antenna design 3 when c and $f = 8$ mm.	79
4.12	Simulated antenna port impedance of the antenna design 1, 2 and 3 presented in Figure 4.11.	79
4.13	Simulated power reflection coefficient of the antenna design 1, 2 and 3 presented in Figure 4.11.	80
4.14	CST simulated normalised surface current distribution of the tags configurations at 868 MHz: (a) normal tag with a 0.3 pF capacitor attached right across the antenna terminals (excluding the transformer); (b) tag mounted at the bottom of the transformer; and (c) tag linked with the tuning circuit and mounted at the bottom of the CT.	81
4.15	Polar plot of CST simulated tag system gain: (a) $\phi = 90^\circ$: yz -plane; (b) $\theta = 90^\circ$: azimuth plane; and (c) $\phi = 0^\circ$: xz -plane. Solid line: normal tag, dashed line: tag attached to the transformer, and asterisk: tag coupled with the tuning circuit.	82
4.16	Schematic diagram of the tuning circuit which input terminals are connected to the transformer while the output terminals are connected to the tag antenna ports.	84
4.17	Measured sensor code of the tag.	86
4.18	Measured read range of the tag.	86

4.19	A prototype of the tag antenna integrated to the transformer used for experiments to verify the simulated design.	87
4.20	Sensor code variations as the current flow changes in the power cable.	88
4.21	Measured read range of the proposed tag system.	88
4.22	(a) Optimised tag antenna design for the current transformer; and (b) a tuning circuit with dimensions in mm.	90
4.23	3D model of the tag antenna design attached at the bottom of the transformer.	91
4.24	Simulated reflection coefficient of the RFID tag design.	91
4.25	Effect of the design parameter e in mm on the tag resonance frequency while other parameters in Table 4.8 and 4.9 were fixed.	92
4.26	Simulated power reflection coefficient against frequency: (a) with different values of l in mm; and (b) w in mm while other parameters in Table 4.8 and 4.9 were fixed.	94
4.27	Normalised magnitude of the surface current distribution of the tag antenna mounted on the transformer: (a) the tag antenna with a 0.3 pF capacitor across the terminals; and (b) the tag connected with the tuning circuit.	96
4.28	Polar plot of CST simulated tag system realised gain: (a) yz -plane; (b) azimuth plane; and (c) xz -plane. Solid line: normal tag antenna with a 0.3 pF capacitor across the terminals. Dashed line: tag connected with the tuning circuit.	97
4.29	Measured sensor code and read range of the tag with a 0.3 pF capacitor across the antenna terminals.	98
4.30	Manufactured prototype of the RFID tag system.	99
4.31	Measured sensor code of the tag system at 868 MHz.	100
4.32	Measured read range of the tag system at 868 MHz.	100
4.33	The effect of distance variation between the tag system and the reader antenna on the sensor code of the tag system at 868 MHz.	101
4.34	Geometry of the tag antenna with increased realised gain.	102
4.35	Simulated reflection coefficient of the tag antenna with increased realised gain.	102
4.36	A prototype of the tag antenna with increased realised gain.	103

4.37	Measured sensor code and read range of the tag antenna with increased realised gain.	104
4.38	Comparison between the tag antenna designs for ac current sensing system: (a) optimised tag antenna; and (b) previously proposed tag antenna design. . .	104
5.1	Schematic diagram of the proposed dual RFID tag system.	111
5.2	Geometry of the proposed tag dipole antenna for dual RFID tag system. . .	112
5.3	Geometry of the proposed two RFID tag antennas design mounted at the bottom of the current transformer. (All dimensions are in mm)	113
5.4	Simulated S-parameters. All power reflection coefficients are below -10 dB. The coupling between the radiating elements are above -10 dB.	114
5.5	The normalised surface current distribution of the tag antennas configurations at 868 MHz: (a) single tag antenna attached to the transformer; (b) tag antenna with the port 1; and (c) tag antenna with the port 2.	115
5.6	Realised gain of the single tag and the two tag antennas design at 868 MHz: (a) yz -plane; (b) xy -plane; and (c) xz -plane. Black solid line: single tag antenna design. Dashed black line: tag antenna design with the port 1. Gray solid line: tag antenna design with the port 2.	116
5.7	Effect of the design parameter L in mm on the antenna port impedance while other parameters in Table 5.1 were fixed.	117
5.8	Effect of the design parameter L in mm on the reflection coefficient S_{11} of the tag while other parameters in Table 5.1 were fixed.	118
5.9	Simulated antenna port impedance with varying the antenna width W in mm while other parameters in Table 5.1 were fixed.	119
5.10	Simulated power reflection coefficient of the tag with varying the antenna width W in mm while other parameters in Table 5.1 were fixed.	120
5.11	Simulated antenna port impedance against frequency: (a) by varying the length l in mm of the feed loop; (b) by varying the width w in mm of the feed loop while other parameters in Table 5.1 were fixed.	121
5.12	Simulated power reflection coefficient of the tag: (a) at different values of the loop length l in mm; (b) at the different values of the loop width w in mm while other parameters in Table 5.1 were fixed.	122

5.13	Geometry of the proposed tag antenna for dual tag system.	124
5.14	Layout of the optimised two tag antennas design with the current transformer mounted in the centre. (All dimensions are in mm)	125
5.15	3D model of the optimised two tag antennas design with the current transformer mounted in the centre.	126
5.16	Simulated S-parameters of the two tag antennas design. All power reflection coefficients are below -10 dB. The coupling between the radiating elements is below -15 dB.	126
5.17	Simulated antenna port impedance by varying the parameter s in mm while other parameters in Table 5.6 were fixed.	127
5.18	Simulated power reflection coefficient of the tag by varying the parameter s in mm while other parameters in Table 5.6 were fixed.	128
5.19	Simulated antenna input impedance by varying the parameter p in mm while other parameters in Table 5.6 were fixed.	129
5.20	Simulated power reflection coefficient of the tag by varying the parameter p in mm while other parameters in Table 5.6 were fixed.	129
5.21	Simulated power reflection coefficient of the tag: (a) at the different values of l in mm; (b) at the different values of w in mm while other parameters in Table 5.6 were fixed.	130
5.22	Simulated power reflection coefficient of the tag: (a) at the different values of l in mm; (b) at the different values of w in mm while other parameters in Table 5.6 were fixed.	131
5.23	Proposed two RFID tag antennas coupled with the tuning circuits and integrated with the current transformer. (All dimensions are in mm)	133
5.24	3D model of the two RFID tag antennas coupled with the tuning circuits and integrated with the current transformer.	133
5.25	Simulated S-parameters of the two tag antennas linked with the tuning circuits. All power reflection coefficients are below -10 dB. The coupling between the radiating elements is below -15 dB.	134
5.26	The normalised surface current distribution of the two tag antennas design at 868 MHz: (a) tag antenna with the port 1; and (b) tag antenna with the port 2.	135

5.27	Simulated radiation pattern of the two tag antennas design at 868 MHz: (a) yz -plane; (b) xy -plane; and (c) xz -plane. Black solid lines: tag antenna design with the port 1. Dashed black lines: tag antenna design with the port 2.	136
5.28	Schematic diagram of the tuning circuit 1. The input terminals of the circuit are connected to the transformer and the output terminals are connected to the antenna ports of the tag.	139
5.29	Schematic diagram of the tuning circuit 2. The input terminals of the circuit are connected to the transformer and the output terminals are connected to the antenna ports of the tag.	140
5.30	Measured sensor code of the two tag antennas configured in the horizontal and vertical orientation.	141
5.31	Measured read range of the two tag antennas configured in the horizontal and vertical orientation.	141
5.32	Final manufactured prototype of the dual RFID tag system.	142
5.33	Measured sensor code of the dual tag system when the current in the primary winding of the transformer changes from 0 A to 13 A.	143
5.34	Measured read range of the two tag antennas across the current reading in the range from 0 A to 13 A.	143
6.1	Geometry of the proposed miniaturised tag antenna.	150
6.2	Geometry and configuration of the miniaturised two tag antennas design for the current transformer. (All dimensions are in mm)	151
6.3	3D model of the tag antennas attached to the transformer in CST Microwave Studio.	152
6.4	Simulated S-parameters of the miniaturised two tag antennas design.	153
6.5	The normalised surface current distribution of the miniaturised two tag antennas at 868 MHz: (a) tag antenna with the port 1; and (b) tag antenna with the port 2.	154
6.6	Simulated radiation pattern of the miniaturised two tag antennas at 868 MHz: (a) yz -plane; (b) xy -plane; and (c) xz -plane. Black solid lines: tag antenna with the port 1. Dashed black lines: tag antenna with the port 2.	155

6.7	Simulated antenna port impedance with different values of the parameter e in mm. The other sizes are fixed to the values in Table 6.2.	157
6.8	Power reflection coefficient of the tag with different values of the parameter e in mm. The other sizes are fixed to the values in Table 6.2.	157
6.9	Simulated tag antenna design with different values of the parameter f : (a) $f = 7.5$ mm; (b) $f = 11$ mm; (c) $f = 14.5$ mm; and (d) $f = 18$ mm.	158
6.10	Simulated antenna port impedance with different values of the parameter f in mm. The other sizes are fixed to the values in Table 6.2.	158
6.11	Simulated power reflection coefficient of the tag with different values of the parameter f in mm. The other sizes are fixed to the values in Table 6.2. . . .	159
6.12	Simulated tag antenna input impedance: (a) at the different values of l in mm; and (b) w in mm. The other sizes are fixed to the values in Table 6.2. .	160
6.13	Simulated power reflection coefficient of the tag: (a) at different values of l in mm; and (b) w in mm. The other sizes are fixed to the values in Table 6.2.	161
6.14	Final prototype of the proposed miniaturised tag antenna.	164
6.15	Measured sensor value of the miniaturised two tag antennas design.	165
6.16	Measured read range of the miniaturised two tag antennas design.	165
A.1	Block diagram of the 24 V dc smart power monitoring system.	175
A.2	Schematic diagram of the Hall effect split-core current transducer [3]. . . .	176
A.3	Filtered voltage divider for dc current sensing in the PCB schematic.	177
A.4	Filtered voltage divider for dc voltage sensing in the PCB schematic.	177
A.5	Schematic overview of the Atmel Atmega328P microcontroller [7, 10, 11]. . .	179
A.6	Schematic diagram of the FT232R USB UART Integrated Circuit [7, 12]. . . .	180
A.7	Operating circuit configuration of the DS1307 serial real time clock.	181
A.8	EEPROM microchip circuit arrangement in the PCB schematic diagram. . .	182
A.9	Schematic diagram of the 3.3 V voltage regulator circuit.	183
A.10	Schematic diagram of the mini USB connector.	183
A.11	Pin header for the Serial Peripheral Interface.	184
A.12	The pins configuration for the Raspberry Pi module in the PCB schematic diagram.	185

A.13 Pmod AD5: 4-channel, 4.8 kHz, 24-bit analog-to-digital converter. (a) Top view, and (b) bottom view.	185
A.14 Pins header for the Pmod AD5 in the PCB layout.	187
A.15 PCB layout of the 24 V dc power monitoring system.	188
A.16 A prototype of the 24 V dc power monitoring system.	188
A.17 Testing set up for the 24 V dc monitoring system.	194
A.18 Current measurements of the proposed system.	195
A.19 Voltage measurements of the proposed system	195
A.20 Power measurements of the proposed system.	196
A.21 Emoncms.org web interface for visualising energy data [26].	196
B.1 A prototype of the RFID ac current sensor (bottom view).	201
B.2 The RFID ac current sensor enclosed in an insulated box.	202
B.3 An electrical fan heater used for ac current measurements.	202
B.4 Solid state relay connected to a microcontroller used in the sensing setup for measuring the rise and fall time of the sensor.	203
B.5 The magnetic part of the current transformer is enclosed in an insulating box.	204
B.6 An optimised tag antenna for the current transformer. The antenna is bend around the transformer housing.	204
B.7 A Hall effect split-core current transducer for dc current sensing.	205
B.8 An electrical load used for dc current measurements.	205

List of Tables

2.1	Description of the LF, HF and UHF RFID system [8].	14
3.1	Comparison between the proposed tag system and commercial alternative ac current meters in terms of communication, cost, current range and power type.	59
4.1	Feed loop dimensions of the tag antenna.	66
4.2	Simulated tag antenna dimensions.	69
4.3	Material properties of the ferrite core, FR4, and PET substrate used to modelled the CT design in CST.	69
4.4	Simulated antenna port impedance ($Z_{ant.}$), gain (G_t), realised gain ($rlsd.G_t$) and radiation efficiency (η_e) of the tag at 868 MHz.	75
4.5	Simulated antenna port impedance, gain, realised gain and radiation efficiency of the proposed tag at 868 MHz by varying the design parameter l	78
4.6	Simulated antenna port impedance, gain, realised gain and radiation efficiency of the proposed tag at 868 MHz by varying the design parameter w	78
4.7	Simulated antenna port impedance, gain, realised gain and radiation efficiency of the tag antenna design 1, 2 and 3 at 868 MHz.	79
4.8	Feed loop dimensions of the tag antenna.	89
4.9	Simulated tag antenna dimensions.	90
4.10	Simulated gain (G_t), realised gain ($rlsd.G_t$) and radiation efficiency (η_e) of the proposed tag at 868 MHz by varying the design parameter e	93
4.11	Simulated gain (G_t), realised gain ($rlsd.G_t$) and radiation efficiency (η_e) of the proposed tag at 868 MHz by varying the design parameter l	93
4.12	Simulated gain (G_t), realised gain ($rlsd.G_t$) and radiation efficiency (η_e) of the proposed tag at 868 MHz by varying the design parameter w	93

4.13	Comparison between the proposed tag system and commercial alternative ac current meters in terms of communication, cost, current range and power type.	105
5.1	Simulated tag dipole antenna dimensions.	111
5.2	Simulated antenna port impedance, gain, realised gain and radiation efficiency of the proposed tag at 868 MHz by varying the design parameter L	118
5.3	Simulated antenna port impedance, gain, realised gain and radiation efficiency of the proposed tag at 868 MHz by varying the design parameter W	119
5.4	Simulated antenna impedance, gain, realised gain and radiation efficiency of the proposed tag at 868 MHz by varying the design parameter l	123
5.5	Simulated antenna impedance, gain, realised gain and radiation efficiency of the proposed tag at 868 MHz by varying the design parameter w	123
5.6	Simulated dipole antenna dimensions.	124
5.7	Simulated gain, realised gain and radiation efficiency of the tag when s varies from 3 mm to 21 mm at 868 MHz.	127
5.8	Simulated gain, realised gain and radiation efficiency of the tag when the p varies from 2 mm to 5 mm at 868 MHz while other parameters in Table 5.6 were fixed.	128
5.9	Simulated gain, realised gain and radiation efficiency of the tag when l varies from 6 mm to 8 mm at 868 MHz.	132
5.10	Simulated gain, realised gain and radiation efficiency of the tag when w varies from 1.75 mm to 3.75 mm at 868 MHz.	132
5.11	Comparison between the proposed tag system and commercial alternative ac current meters in terms of communication, cost, current range and power type.	144
6.1	Feed loop dimensions of the miniaturised tag antenna.	150
6.2	Simulated miniaturised tag antenna dimensions.	151
6.3	Simulated antenna port impedance ($Z_{ant.}$), gain (G_t , excluding input impedance mismatch losses), realised gain ($rlsd.G_t$, including input impedance mismatch losses) and radiation efficiency (η_e) of the tag when e varies from 14 mm to 2 mm at 868 MHz.	156

6.4	Simulated antenna port impedance ($Z_{ant.}$), gain (G_t), realised gain ($rlsd.G_t$), and radiation efficiency (η_e) of the tag when f varies from 4 mm to 18 mm at 868 MHz.	159
6.5	Simulated antenna port impedance ($Z_{ant.}$), gain (G_t), realised gain ($rlsd.G_t$), and radiation efficiency (η_e) of the tag when l varies from 4 mm to 6 mm at 868 MHz.	162
6.6	Simulated antenna port impedance ($Z_{ant.}$), gain (G_t), realised gain ($rlsd.G_t$), and radiation efficiency (η_e) of the tag when w varies from 3 mm to 5 mm at 868 MHz.	162
A.1	Description of the Pmod AD5 header J1 pins	186
A.2	Description of the header J2 pins of the Pmod AD5.	186
A.3	Comparison between the proposed 24 V dc wireless energy logger and the RFID tag system in terms of communication, cost, current range and power type.	197

Introduction

THIS thesis is concerned with designing self-tuning passive ultra-high frequency (UHF) radio frequency identification (RFID) tags and antenna designs and transforming simple tags into ac current sensors for smart power monitoring systems. RFID is one of the key enabling technologies of the internet of things (IoT), and its applications have been significantly increased in the recent decade. There are many applications of RFID in various areas such as asset identification and tracking, security and access control, transportation, supply chain management, toll collection, baggage handling, animal tracking, real-time location system and so on [1]. RFID uses radio waves to identify an object with certain tags (consisting of an antenna and an application-specific integrated circuit (ASIC) chip). RFID tags are termed active or passive, based on how they are powered. UHF RFID tags operate within the 866 MHz to 869 MHz band in Europe. The tag antenna can be fabricated on a low-cost dielectric substrate which makes the tags cost-effective, lightweight and to be mass-produced. The performance of the tag depends on a tag antenna design that needs to match with the input impedance of the tag chip. Furthermore, the newly released self-tuning RFID chip incorporated with the tag antenna offer interesting RFID low-cost sensing applications beyond identification and tracking. These tags have been successfully designed for real-time remote monitoring of body temperature, and moisture sensing. In this thesis, a novel application of RFID for ac current sensing in smart power monitoring systems is proposed. In this thesis, terms such as current transformer, current transducer, current sensor, transformer are used interchangeably. Section 1.1 reviews the motivation behind this research. Section 1.2 describes the aims and objectives of the research. A scope of the project will be explored in Section 1.3. The main contributions of this thesis are listed in Section 1.4. Finally, Section

1.7 will present the structure of the thesis.

1.1 Motivation

Global energy demand is set to grow by more than a quarter by 2040 with electrical contribution increasing twice as fast as the overall demand [2]. The increase in electrical demand will put pressure on generators with associated greenhouse gas emissions [3]. Energy-saving solutions including smart electricity metering can be exploited to reduce overall electricity demand, and these can be employed in houses or apartments for tracking real-time power consumption [4]. Such smart technologies would help consumers simultaneously to monitor the energy consumed by multiple individual appliances, reduce usage, and to wirelessly report readings to a data acquisition module. However, installing smart metering is expensive and gives only overall intake. Developing new passive, wireless, affordable and easy-to-install technologies could play a valuable role in multiple appliance monitoring in smart homes. UHF RFID systems potentially offer a sensing solution based on low-cost UHF RFID tags with a single reader [5–7].

1.2 Aims and Objectives

The general aim of this research is to develop ac current sensors using UHF RFID technology to enhance energy-saving solutions in smart homes. The study will explore self-tuning RFID tags and antenna designs and transforming simple tags into passive ac current sensors. The specific objective of the research is to design an RFID ac current sensor which will offer a battery-free, low-cost, and easily accessible sensing solution with a single RFID reader. This study will also aim to explore the self-tuning properties of the Axzon Magnus S2 RFID chip [8] as well as a design of a varactor tuning circuit for tuning a tag antenna impedance. Furthermore, different types of tag antennas for a current transformer will be investigated and designed. A novel two tag antennas design in close proximity integrated to a current transformer, forming a dual tag system for ac current sensing will also be studied. In addition, a miniaturised RFID tag antenna with a bending structure to reduce the size of the antenna will be studied as well.

1.3 Scope of the Project

The summary of the work which will be carried out in this study is presented here. This research will address a novel RFID technique for ac current sensing. This study will only focus on developing the sensing mechanism for small current measurement in the range of 0 A to 13 A for domestic applications. This study will only explore tag antenna designs for current transformers. The research will deal with the self-tuning Axzon Magnus S2 RFID chip. In this work, the tag system will be tuned for Electronic Product Code (EPC) Class 1 Generation 2 UHF RFID readers at 868 MHz and the study will not explore the tag system for other UHF frequency bands, such as 902–928 MHz (US) and 950–956 MHz (Japan). Furthermore, in this work, the wider metering system that the tag sensor would be connected to is not considered.

1.4 Main Contributions

The main contributions of this thesis are the following:

- A study and review of the literature on passive UHF RFID tags and antenna designs.
- The development of a novel RFID ac current sensing technique.
- A novel RFID tag antenna design for a current transformer.
- The development of a dual RFID tag system for ac current sensing.
- Design of a miniaturised RFID tag antenna for a dual RFID tag system.

1.5 Application

Smart metering systems allow consumers to constantly monitor power consumption of electrical appliances at homes, visualising energy usage and costs in real time on in-home displays, and remotely send meter readings to an energy supplier. Unlike traditional meters, smart metering systems comprise of multiple sensors to be deployed around the home, enabling continuous monitoring of power consumption of individual appliances. The majority

of smart meters available today use microcontrollers with on chip analogue-to-digital converters for computing the current and voltage measurements. These devices exhibit complex circuit design, require an external power source for its operation, and are very expensive to install in homes. Therefore, there is a need for developing very low cost and low complexity sensors for smart metering systems.

Therefore, in this thesis, I present a wireless and battery-free sensing system operating at the UHF band that can measure ac current ranging from 0 A to 13 A in a power cable. The novelty of this research work is to develop a novel RFID sensing mechanism for ac current sensing and its application in smart metering systems. Moreover, the proposed sensing system can be deployed in homes and apartments for monitoring multiple individual electrical appliances and can wirelessly stream readings to a centrally mounted RFID reader antenna at 868 MHz, as shown in Figure 1.1. Furthermore, the proposed sensing system has a simple structure, harvests its energy from an external reader device, and is less expensive than alternatives, which makes it more suitable for domestic applications where small current measurements from 0 A to 13 A are desirable. Read range is the distance at which the reader

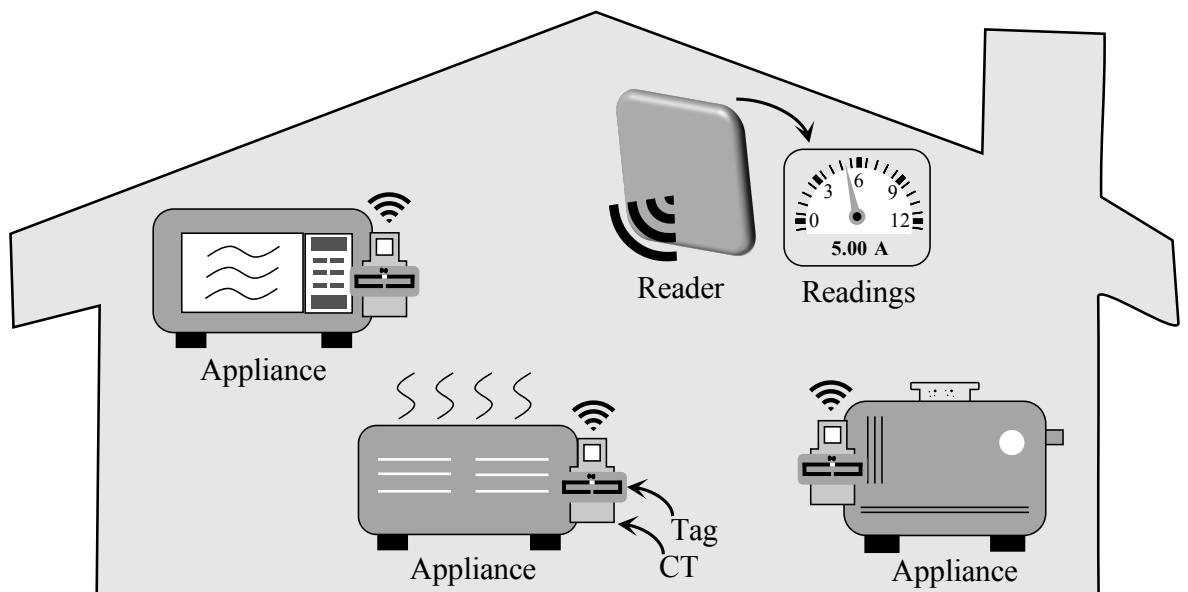


Figure 1.1: Proposed smart metering system based on UHF RFID technology.

can detect and receive back-scattering modulation from an RFID tag. Passive RFID tags are battery-free and collect power from a readout device to activate the tag chip. Therefore, the read range is one of important parameters to be considered in designing RFID tags. Typically, passive RFID tags have a read range from 0.5 m to 10 m, operating in the UHF band (860–960 MHz). Along with the tag chip sensitivity (RF power required to turn on the tag

chip), the tag antenna design plays a key role in the read range of the tag. According to the Friis free-space formula, the read range of the tag mainly depends on the tag chip sensitivity, the tag antenna gain and the impedance match between the antenna ($Z_{ant.} = R_{ant.} + jZ_{ant.}$) and tag chip ($Z_{chip} = R_{chip} + jZ_{chip}$), assuming the reader output power constant.

$$r_{max} = \frac{c}{4\pi f} \cdot \sqrt{\frac{EIRP \cdot G_r \cdot \tau}{P_{IC}}} \quad (1.1)$$

where c is the speed of light and f is operating frequency in hertz (Hz). $EIRP$ is the Equivalent Isotropic Radiated Power, depending on the local regulation (3.28 W in Europe and 4 W in the US), G_r is the tag antenna gain and τ is $1 - |S|^2$, where S is referring to the reflection coefficient. P_{IC} represents the sensitivity of the tag chip. Moreover, the read range is also specified by the tag orientation, the object the tag is mounted on, and the propagation environment.

Angle of Arrival (AoA) is determined by the position of the RFID tag antenna relative to the reader direction. Alignment of orientation and polarisation of a reader and tag antenna strongly affect the readability of the tags, though propagation effects such as reflection can alter the polarisation of received waves. One of the main problems in a passive RFID system is to enhance the tag identification rates when a large number of tags are present in close proximity. The mutual coupling between adjacent tags mainly causes for missed tags. Techniques to enhance the tag identification rates involve antenna diversity, using multiple antennas connected to a reader. Additionally, polarisation mismatch can be addressed through the use of circularly polarised reader antennas [9].

1.6 The State of the Art

Smart meters are next-generation electricity meters for monitoring real-time power consumption of electrical appliances in smart homes. They mainly consist of split-core current sensors, a microcontroller based monitor unit and an in-home display [10]. The current sensors can be clipped around power cables for sensing current of multiple individual appliances and the output of the sensors would be connected to the monitor unit. Generally, the monitor unit is embedded with an analogue to digital converter for computing power consumption

and an RF transmitter for transmitting data to the in-home display for visualising real-time energy consumption (kW and cost). However, there are some complications related to the implementation of the active low-end smart meters in homes, such as installation problems and cost as well as maintenance. Additionally, smart meters exhibit complex circuit design and the overall size of the system is comparatively large which make it hard to be installed in a compact location. To tackle these issues, in this study, I propose a high-end wireless and battery-free sensing system operating at the UHF band that can measure ac current ranging from 0 A to 13 A in a power cable. The proposed ac current sensing system uses a capacitance sensing UHF RFID tag which is integrated with a current transformer. The sensing system can be easily clipped around a power cable and can be read using a single RFID reader using the European RFID UHF band at 868 MHz. Due to its simple structure, the sensing tag can be directly fabricated on a low-cost dielectric substrate, which makes the tags cost-effective. The proposed sensing system is battery-free, small in size and can be easily deployed in homes and apartments. Moreover, the proposed sensing systems would be connected to the wider smart metering system. It may be necessary to develop new metering methods in order to log and display the simultaneous consumption of multiple appliances. The tags could be deployed in modified plugs or as inline cable devices. The reader would be centrally mounted with a view of the tags to be read.

1.7 Structure of the Thesis

The organisation of the thesis is given below.

Chapter 2 provides an overview of an RFID system, UHF RFID tags and antenna designs and highlights its applications. Several conjugate input impedance matching techniques are also discussed. RFID sensing mechanism for moisture monitoring is also explained. It also provides RFID tags and antenna designs for power cables. The previous work related to the implementation of RFID technology for sensing ac current in a power cable of households appliances is presented.

Chapter 3 presents a novel RFID ac current sensing technique. The chapter describes a schematic diagram of the proposed tag system, including the design of a capacitance sensing

RFID tag, a tuning circuit with a varactor diode and a current transformer. A theoretical explanation and simulation results of the tag antenna and the tuning circuit are also provided. In the final section, an experimental setup for testing the tag system and measured results are provided.

Chapter 4 describes the new optimum tag antenna designs for current transformers. Three new tag antennas are designed and simulated using computer simulation technology microwave studio. The first part of the chapter presents the new tag antenna for the current transformer with detail simulated and measured results. The second part of the chapter illustrates the optimum tag antenna with the improved current sensing range as well as being small in size as compared to the tag design presented in Chapter 3.

In Chapter 5, a novel dual tag system for ac current measurement is proposed. The chapter discusses two tag antennas that are designed in close proximity and integrated into a single transformer in compact form integration to reduce the overall size of the tag device. Mutual coupling between the two tag antennas and how the coupling can be minimised is explained. How the two tag chips can be used in a single design for increasing current sensing range of the sensor is also reported.

Chapter 6 details a miniaturised tag antenna design for a dual RFID tag system. The meander line technique for the tag antenna size reduction is proposed. The chapter also details antenna parametric analysis to analyse the affect of the design parameters on the tag performance. Simulation results of the tag antenna in term of antenna port impedance, reflection coefficient, gain, realised gain and radiation efficiency are provided, followed by measurement results to validate the tag performance.

Chapter 7 concludes the research described in the thesis and discusses the future work arising from this research work.

1.8 List of Publications

1. I. Ullah, R. Horne, B. Sanz-Izquierdo and J. C. Batchelor, "RFID AC Current Sensing Technique," in *IEEE Sensors Journal*, vol. 20, no. 4, pp. 2197–2204, Feb.15, 2020, doi: 10.1109/JSEN.2019.2949856.
2. I. Ullah, R. Horne, B. Sanz-Izquierdo and J. C. Batchelor, "UHF RFID Tag Design

for AC Current Sensing,” *IET’s Antennas and Propagation Conference (APC–2019)*, Birmingham, UK, Nov. 11–12, 2019, pp. 1–4, doi: 10.1049/cp.2019.0728.

3. I. Ullah, R. Horne, B. Sanz-Izquierdo and J. C. Batchelor, “Tag Design for RFID AC Current Sensing System,” *14th European Conference on Antennas and Propagation (EuCAP)*, Copenhagen, Denmark, 2020, pp. 1–5, doi: 10.23919/EuCAP48036.2020.9135550.

In Preparation

1. Dual RFID Tag System for AC Current Sensing, in *IEEE Sensors Letters*.

References

- [1] Finkenzeller, Klaus. “RFID handbook: fundamentals and applications in contactless smart cards, radio frequency identification and near-field communication”. John Wiley & Sons, 2010.
- [2] International Energy Agency (2019, Feb. 13). World energy outlook 2018: The gold standard of energy analysis [Online]. Available: <https://www.iea.org/weo2018/>
- [3] United States Environmental Protection Agency (2019, Feb. 13). Greenhouse gas emissions [Online]. Available: <https://www.epa.gov/ghgemissions/sources-greenhouse-gas-emissions>
- [4] Government UK, “Smart meters: unlocking the future,” [Online], Dec. 31, 2018. Available: <https://www.gov.uk/government/publications/smart-meters-unlocking-the-future/smart-meters-unlocking-the-future>
- [5] M. A. Ziai and J. C. Batchelor, “Smart radio-frequency identification tag for diaper moisture detection,” in *IET Healthc. Technol. Lett.*, vol. 2, no. 1, pp. 18–21, 2015.
- [6] A. A. Babar, S. Manzari, L. Sydanheimo, A. Z. Elsherbeni and L. Ukkonen, “Passive UHF RFID tag for heat sensing applications,” in *IEEE Trans. Antennas Propag.*, vol. 60, no. 9, pp. 4056–4064, Sept. 2012.
- [7] M. A. Ziai and J. C. Batchelor, “Multi-state logging freeze detection passive RFID tags,” in *IEEE Trans. Antennas Propag.*, vol. 62, no. 12, pp. 6406–6411, Sep. 2014.
- [8] Axzon sensing data insights (2019, Feb. 13). Silicon [Online]. Available: <https://axzon.com/>

-
- [9] Y. B. Ouattara, C. Hamouda, B. Poussot, J. M. Laheurte, “Compact diversity antenna for UHF RFID readers”, *Electronics Letters*, 2012, 48, (16), pp. 975–977, DOI: 10.1049/el.2012.1805 IET Digital Library, <https://digital-library.theiet.org/content/journals/10.1049/el.2012.1805>
- [10] Open energy monitoring. (2020, Feb. 23). Guide, home energy. [Online]. Available: <https://guide.openenergymonitor.org/applications/home-energy/>

UHF RFID Tags: A Review of Literature

2.1 Introduction

RADIO frequency identification (RFID) is the fast-growing multidisciplinary technology as it is inexpensive, energy-efficient, wireless and lightweight and has various applications in the ambient environment, as described in Chapter 1. The UHF RFID system has gained much interest in recent decades due to its long identification range, typically several metres (~ 10 m). Several research studies have been conducted to design passive UHF RFID tags and transform into RFID sensors for enabling low-cost monitoring of temperature [1, 2], moisture [3], liquid [4], vapour [5, 6], and so on. Antenna design is the most critical part of designing passive UHF RFID tags. The form factors (design and size) of antenna sensors can be different from design to another and can be optimised for a particular application. In this chapter, various types of antenna sensors and their applications will be discussed. This chapter will also detail various conjugate impedance matching techniques that can be used for designing antenna sensors. Furthermore, this chapter will review the use of RFID technology in the context of ac current sensing of electrical appliances in smart homes. The rest of the chapter is organised as follows. Section 2.2 will describe the RFID system, types of RFID tags and the principle of operation of a typical passive RFID system. Section 2.3 will detail the research and development of passive UHF RFID tags, focuses on tag antenna designs and RFID sensing mechanisms. Section 2.3.4 will present the tag antenna designs for power cables and ac current sensing. Finally, Section 2.4 will conclude the chapter.

2.2 RFID System

An RFID system consists of two key components: (i) an interrogator or reader; and (ii) a transponder or tag. RFID uses radio waves to identify an object with certain tags. The interrogator is the data capture devices, which consists of an RF electronic module (transmitter and receiver) and an electronic control module, and a linear or circular polarised antenna. The transponder performs a basic function of storing and transmitting data to the reader. The transponder consists of an antenna, application-specific integrated circuit (ASIC) chip and sometimes a battery. There are three types of RFID tags: (i) passive RFID tag (battery-free); (ii) active RFID tag (battery-supported); and (iii) semi-active RFID tag.

2.2.1 Active RFID Tag

Active RFID tags are battery-operated tags and will continuously emit a signal. Active tags have the longest reaching distance of up to ~ 150 m and are the most expensive due to the battery and active transmitter cost. The size of the active tags is much larger than passive tags due to the onboard battery and other electronic components.



Figure 2.1: Omni-ID active RFID tag with the communication range of up to 150 m [9].

2.2.2 Passive RFID Tag

Passive RFID tags are battery-free. These tags harvest energy from incoming electromagnetic waves from an RFID reader. The read range of passive tags are far less (typically < 10 m) as compared to active tags (~ 150 m), but they are less expensive and require no main-

tenance cost. For example, Figure 2.2 depicts the Smartrac sensor Dogbone for temperature sensing. The sensor is only consisting of an antenna and a self-tuning Axzon Magnus S3 chip.

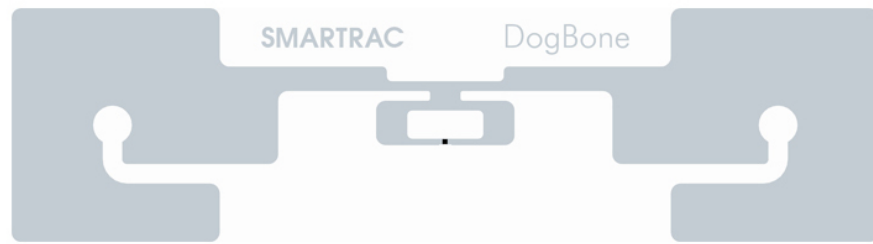


Figure 2.2: Temperature antenna sensor with the read range of 9 m at 868 MHz [10].

2.2.3 Semipassive RFID Tag

Semipassive (battery-assisted) tags include an on-tag power supply. The on-tag power supply is only used to power up the tag chip (so the chip will always have sufficient energy to turn on). These tags are less expensive than active tags due to the lack of active transmitter onboard.



Figure 2.3: Semipassive UHF logger tag [11].

Moreover, the RFID system is classified into three groups based on the operating frequency: (i) lower frequency (LF); (ii) higher frequency (HF); and (iii) ultra-high frequency (UHF), as summarised in Table 2.1. The LF RFID band covers from 125 kHz to 134 kHz, the HF RFID operates at 13.56 MHz, and the UHF RFID system transmission frequencies range is 865–956 MHz. Furthermore, the transmission frequencies of the UHF system vary in each country, depending on the country regulations. In Europe, the UHF frequencies range 865–868 MHz (868 MHz) is standardised for RFID systems, in the USA, the frequency range is

902–928 MHz (915 MHz), and in Japan, the frequency range is 950–956 MHz [7]. Another important parameter of the RFID system is the read range. The LF and HF RFID systems are close-coupling systems, and they are coupled using both electric and magnetic fields and having a lower read range. The LF and HF RFID system is mainly used in electronic door locking systems or contactless smart card systems with payment functions. On the other hand, the UHF RFID systems have long identification range above 1 m and operate using electromagnetic waves (electromagnetic backscatter coupling). The UHF RFID system is mainly used in identification and tracking, smart cards logistic, and item management.

Table 2.1: Description of the LF, HF and UHF RFID system [8].

	LF	HF	UHF
Operating frequency	125–134 kHz	13.56 MHz	865–956 MHz
Read range	0.5 m	0.7 m	0.5–10 m
Data transfer rate	1 kbit/s	25 kbit/s	30 kbit/s

2.2.4 RFID Principle of Operation

Figure 2.4 illustrates the operating principle of the passive UHF RFID system, which consists of an RFID reader with an antenna and a passive RFID tag, as mentioned above. The reader antenna carries a signal to and from the tag antenna. The antenna of the RFID reader continuously transmits electromagnetic waves toward the RFID tag. When these waves are falling on the tag antenna, it forms current which energises the tag chip. When the tag chip received enough power to turn on, it propagates information back to the RFID reader on its reflected RF signal [7].

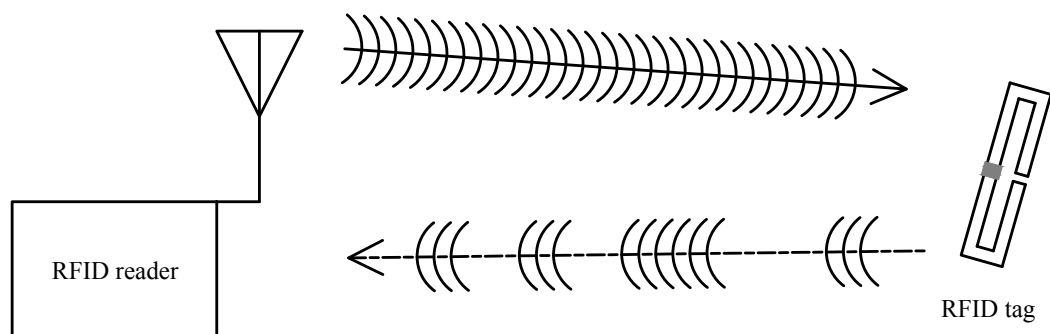


Figure 2.4: A typical passive UHF RFID system.

2.2.5 Read Range

The read range is the maximum distance at which the RFID reader can receive a signal from the tag antenna. The read range is the most important characteristic of the RFID tag and determined by the sensitivity of the tag chip as the sensitivity of the reader is typically high when compared to the tag. Moreover, the read range is also specified by the tag orientation, the object the tag is mounted on, and the propagation environment [12]. The read range can be calculated by using the well-known Friis free-space formula:

$$r_{max} = \frac{c}{4\pi f} \cdot \sqrt{\frac{EIRP \cdot G_r \cdot \tau}{P_{IC}}} \quad (2.1)$$

where c is the speed of light and f is operating frequency in hertz (Hz). $EIRP$ is the Equivalent Isotropic Radiated Power, depending on the local regulation (3.28 W in Europe and 4 W in the US), G_r is the tag antenna gain and τ is $1 - |S|^2$, where S is referring to the reflection coefficient. P_{IC} represents the sensitivity of the tag chip.

2.2.6 Tag Chip

An RFID transponder consists of an antenna and an ASIC chip with internal read and write memory. A typical RFID tag chip has a complex input impedance (2.2), which have conjugately matched with the input impedance of the tag antenna (2.3) for improving the power transfer to the chip. The input impedance of the tag antenna has to be inductive as the tag chip impedance is capacitive. The UHF RFID tag chips can be grouped into two broad categories: (i) standard RFID tag chip [13]; and (ii) self-tuning RFID tag chip [14]. The self-tuning tag chip will automatically adjust its input impedance to improve matching with antenna impedance to extract maximum energy from an incident RF wave. As a result, the tag performance remains more consistent and offers better readability with different environmental conditions. Additionally, the self-tuning chip covers all Worldwide RFID frequency bands (860–960 MHz). Alternatively, a tag chip having fixed input impedance cannot compensate its internal impedance with the antenna impedance. Therefore, the tag performance will significantly degrade due to the mismatch between the tag antenna and the chip. Furthermore, the tag sensitivity (P_{tag}) is determined by the tag chip sensitivity (P_{chip}) and the tag

antenna parameters (2.4). The P_{tag} is the minimum power requires to turn on the tag [15].

$$Z_{chip} = R_{chip} + jX_{chip} \quad (2.2)$$

where Z_{chip} represents the input impedance of the tag chip, R_{chip} and X_{chip} represent the tag chip input resistance and reactance, respectively.

$$Z_{ant.} = R_{ant.} + jX_{ant.} \quad (2.3)$$

where $Z_{ant.}$ represents the input impedance of the tag antenna, $R_{ant.}$ and $X_{ant.}$ represent the tag antenna input resistance and reactance, respectively.

$$P_{chip} = P_{tag}G\tau \quad (2.4)$$

where G is the gain of the tag antenna, and τ is the power transmission coefficient, which is given by:

$$\tau = 1 + |\Gamma|^2 = \frac{4R_{chip}R_{ant.}}{|Z_{chip} + Z_{ant.}|^2} \leq 1 \quad (2.5)$$

where Γ is the reflection coefficient between the antenna and the tag chip input impedances:

$$\Gamma = \frac{Z_{chip} - Z_{ant.}^*}{Z_{chip} + Z_{ant.}} \quad (2.6)$$

2.3 UHF RFID Tag: Research and Development

2.3.1 Techniques for Conjugate Impedance Matching

Several impedance matching techniques for designing RFID tags are proposed in the literature. The impedance matching between the tag antenna and the tag chip (2.7) is critical for transferring maximum power between them. The most commonly used impedance matching techniques in designing RFID tags are inductively coupled feed loop matching, T-match,

nested slotline matching, and capacitive tip loading.

$$Z_{chip} = Z_{ant}^* \quad (2.7)$$

2.3.1.1 Inductively Coupled Loop

In [16], an inductively coupled feed matching technique is demonstrated for designing RFID tag antennas. In inductive feeding structure, an antenna structure is not physically connected to a feed loop but positioned near to the loop about a few mm away from each other, and they are inductively coupled. Figure 2.5 and Figure 2.6 show the radiating element inductively coupled with the feed loop and its equivalent circuit, respectively. The coupling M is defined by two factors. One is the distance d between the radiating body and the feed loop. Generally the further apart the radiating body from the feed loop causes to reduce the magnitude of the coupling. The second is the shape of the loop. The tag antenna terminals impedance is:

$$Z_{in} = Z_{loop} + \frac{(2\pi fM)^2}{Z_{ant}} \quad (2.8)$$

where Z_{ant} is the impedance of the main antenna, $Z_{loop} = j2\pi fL_{loop}$ is the feed loop impedance where L_{loop} is the self-inductance of the feed loop, and M is the mutual inductance between the antenna and the feed loop.

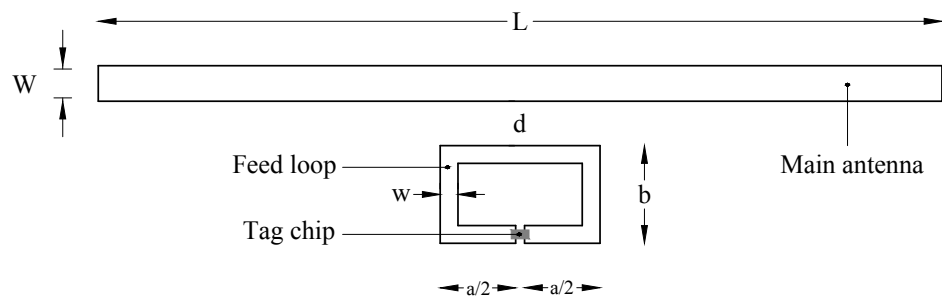


Figure 2.5: Layout of an antenna structure inductively coupled with a feed loop.

2.3.1.2 T-Match

Figure 2.7 illustrates a T-match tag antenna and Figure 2.8 shows its equivalent circuit [17]. The T-match tag antenna consists of a dipole connected to a rectangular feed loop, the T-matching network. This technique is particularly used to overcome the problem of very

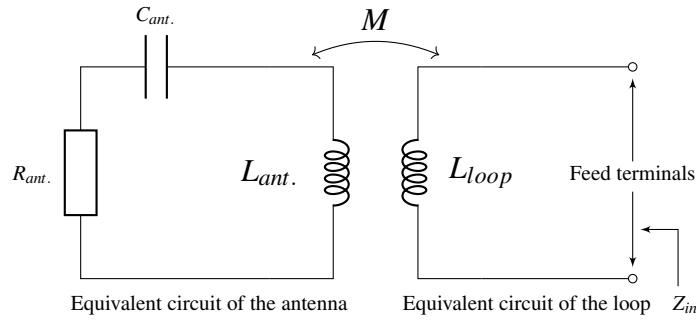


Figure 2.6: Schematic equivalent circuit of an antenna structure inductively coupled with a feed loop.

high input reactance in designing RFID tags. The input impedance of the tag antenna terminals will determine by adjusting a , b and width w of the trace. The tag antenna terminals impedance is:

$$Z_{in} = \frac{2Z_t (1 + \alpha)^2 Z_{ant.}}{2Z_t + (1 + \alpha)^2 Z_{ant.}} \quad (2.9)$$

where Z_t is the input impedance of the feed loop and equal to (2.10), $Z_{ant.}$ is the input impedance of the dipole without the T-matching network, α is the current division factor between the two conductors and equal to (2.12).

$$Z_t = jZ_0 \tan\left(\frac{ka}{2}\right) \quad (2.10)$$

where Z_0 is the impedance of the conductor with the length of d and equal to:

$$Z_0 = 276 \log_{10} \left(\frac{b}{\sqrt{r_e r_e'}} \right) \quad (2.11)$$

$$\alpha = \frac{\ln\left(\frac{b}{r_e'}\right)}{\ln\left(\frac{b}{r_e}\right)} \quad (2.12)$$

where $r_e = 0.25w$ is the radii of the dipole, and $r_e' = 8.25w'$ is the radii of the T-matching network.

2.3.1.3 Nested Slotline

A nested slotline is another method used for impedance matching in designing RFID tag antenna [8, 17]. Figure 2.9 illustrates the nested slotline tag antenna design for on-body

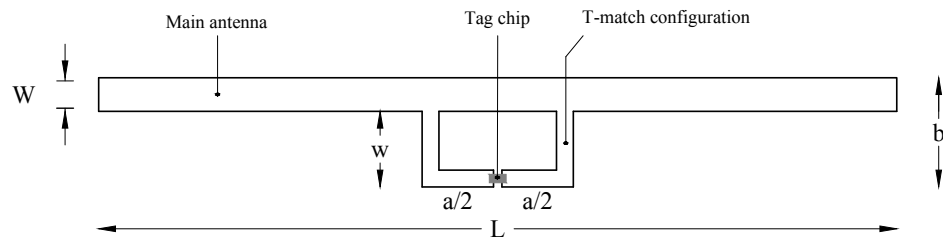


Figure 2.7: T-match tag antenna consists of a planar dipole and a T-matching network.

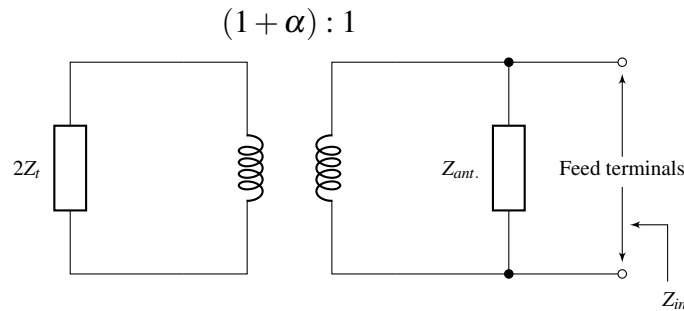


Figure 2.8: Schematic equivalent circuit of the T-match antenna.

applications. A nested slotline is introduced in a patch to achieve inductive reactance to overcome the capacitive reactance of the tag chip. The input impedance of the antenna can be determined by the length l and width w of the slot. For example, the resonance frequency of the tag antenna and inductive reactance can be controlled by the length l of the nest slotline. However, the gain of the tag mainly depends on the size of the patch. Furthermore, the nested slot patch antenna matching technique can also be used when the tag needed to be mounted on the high permittivity surfaces. Figure 2.10 shows the schematic diagram of the equivalent circuit of the slotline, where the voltage source V_g and the capacitive impedance Z_g represent the tag chip.

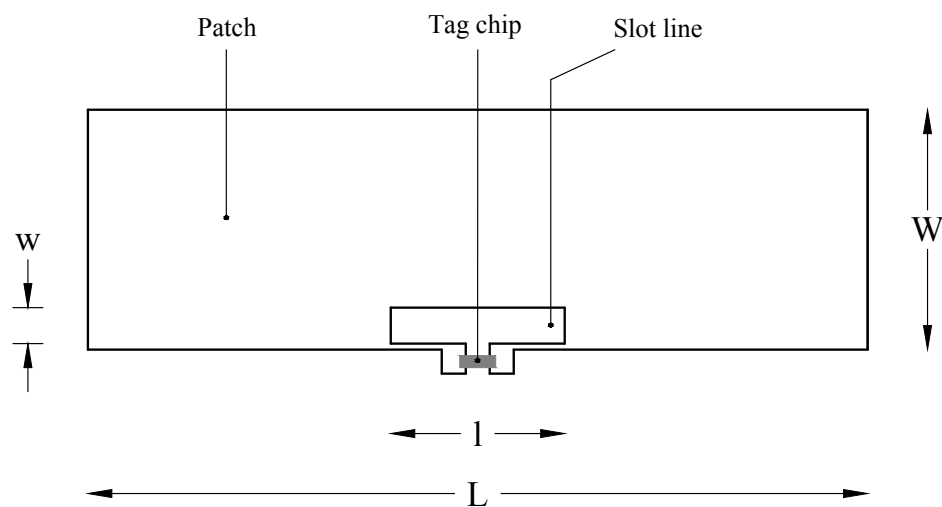


Figure 2.9: A nested slotline antenna for RFID tags [8].

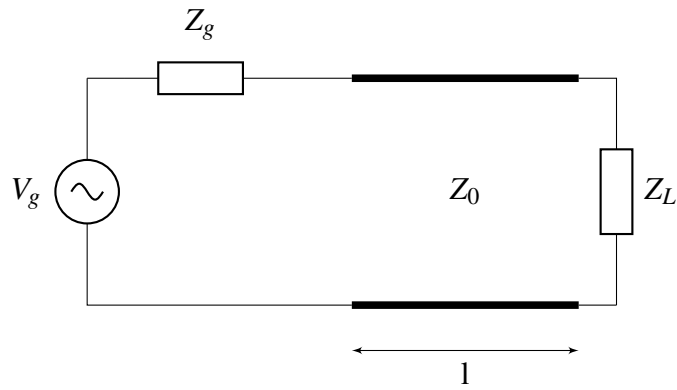


Figure 2.10: Schematic equivalent circuit of the slotline tag antenna design.

The input impedance $Z_{ant.}$ for the antenna slotline transformer is:

$$Z_{ant.} = Z_0 \left\{ \frac{(Z_L \cos(\beta l) + jZ_0 \sin(\beta l))}{(Z_0 \cos(\beta l) + jZ_L \sin(\beta l))} \right\} \quad (2.13)$$

where Z_0 is the characteristic impedance, Z_L is the load impedance, and β is the propagation constant .

2.3.1.4 Capacitive Tip Loading

With the reference to Figure 2.11, the design of the tip load RFID tag antenna is similar to the structure of a meander dipole apart from the capacitive tip loading structures, added at the end of the meander dipole. The tip loading structures help to reduce the size of the tag antenna. These shapes allow the antenna structure to store more electrical charges at the same antenna length and thus reduce the size of the antenna. This technique can be used to design a shorter tag antenna with a suitable impedance match.

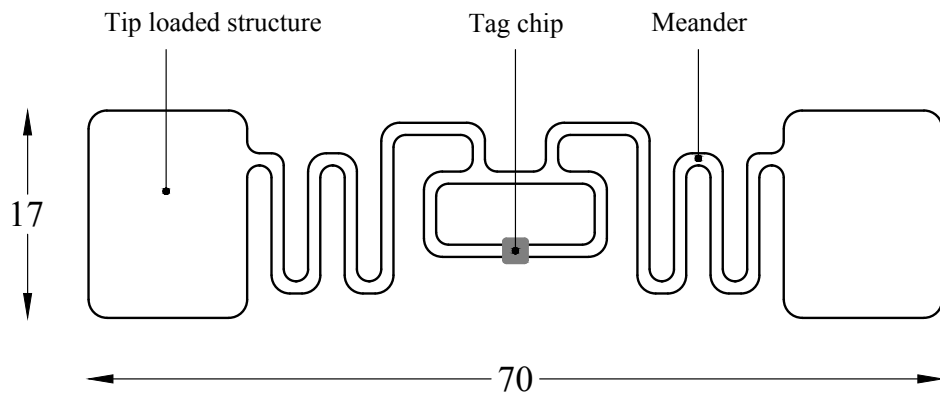


Figure 2.11: Tip loaded RFID tag [19].

2.3.2 Tag Antenna Designs

There are different types of antenna designs for passive RFID tags, and their applications are proposed in the literature. These antennas types are dipole (folded dipole or meandered dipole), patch, and planar inverted-F antenna (PIFA). The design and size of tag antennas are varied, depending on the application to be used for. For example, dipole structures are most commonly used since they can be printed on low-cost and flexible substrates and are suitable for mounting on planar surfaces. However, the performance of dipole antennas significantly changes when mounted on an object with high conductivity or permittivity such as metallic surfaces. For such applications, a patch antenna and PIFA are considered to be effective candidates.

The main challenge of designing passive UHF RFID tags is the antenna design. The performance of the passive RFID tags mainly depends on the input impedance matching between the tag antenna and the chip. Therefore, the antenna input impedance needs to be perfectly matched with the tag chip impedance to improve the power transfer from the tag antenna to the tag chip. In addition, the tag antenna needs to be small in size while maintaining the read range of the tag. The size of the tag antenna contributes to reducing the overall size of the tag. Furthermore, there are two advantages of the small tag antenna design: (i) low fabrication cost; and (ii) can be easily tagged on small objects. There are several techniques that have been implemented and proposed by the researchers to reduce the size of tag antennas. The meandering techniques with the capacitive tip loading structures are the most common techniques used for miniaturising tag antennas.

Figure 2.12 depicts a loaded meander dipole antenna design for UHF RFID tags, proposed in [12] for box tracking in warehouses. The meandering structure is adopted to reduce the size of the dipole as well as to achieve omnidirectional performance. In addition, the resonance frequency of the tag antenna will be optimised by changing the length of the dipole. The tag has a good read range of about 5.5 m at 920 MHz. Similarly, a zigzag dipole antenna is another prominent solution for reducing the dipole size [20]. However, for some applications, mismatching problem may occur as the input impedance of tag chip is capacitive. To overcome this problem, the T-match or U-match network can be coupled with the main antenna structure, as discussed earlier.

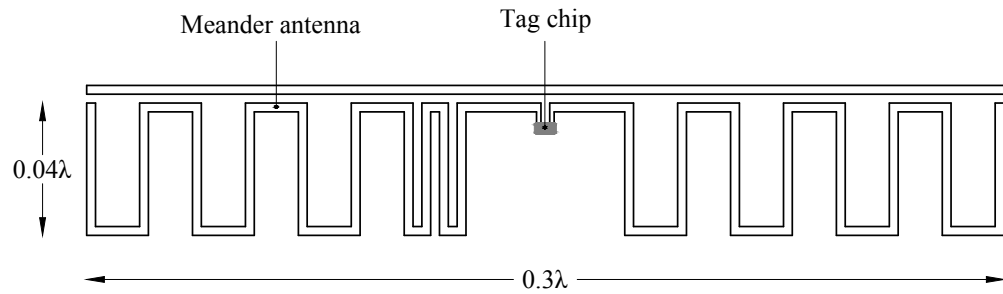


Figure 2.12: A loaded meander dipole antenna design for UHF RFID tags [12].

The patch-type antenna structures and planar inverted-F antennas (PIFA) are widely used for designing RFID tags for metallic object applications. The patch antenna consists of a metal patch with a finite ground plane form an RFID tag. In [21, 22], a small RFID tag antenna design consists of two rectangular patches which are connected to the ground plane through vias without connected to the inter-conductive layer, as illustrated in Figure 2.13. The resonance frequency of the tag antenna is 925 MHz. Despite the small size, the tag has a good read range of 1.5 m when mounted on a metallic object. However, the tag design is complex in structure due to the multiple rectangular patches and hence increases the fabrication cost.

Alternatively, a planar UHF RFID tag antenna with an open stub feed for metallic objects is presented in [23]. The authors investigate the design of a planar tag antenna without using via holes and shorting pins, which can reduce the fabrication cost of the tag. The antenna geometry is optimised to operate at 920 MHz. The input impedance of the tag antenna terminals can be tuned by changing the length of the open stub of the radiation patch. The dimensions of the radiation patch is $74.5 \times 20 \times 3 \text{ mm}^3$ excluding the feed line with length of 46 mm. The proposed tag has a good read range of about 6.8 m at 915 MHz. But, the size

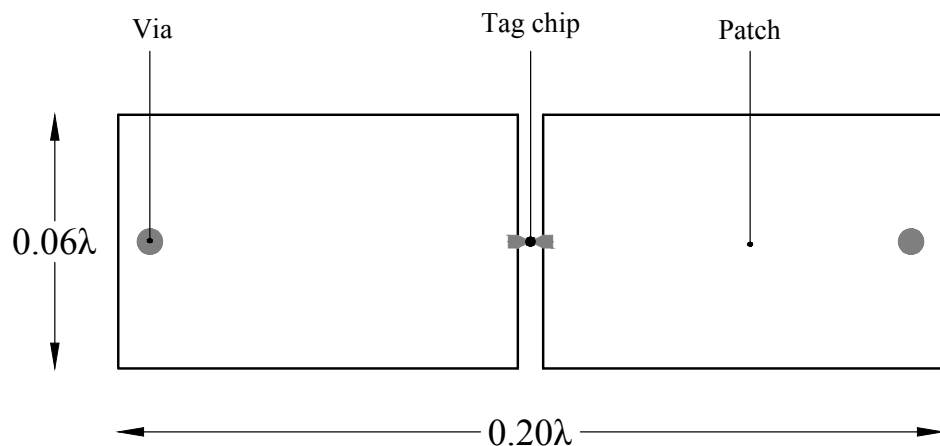


Figure 2.13: Patch tag antenna for mounting on metallic surfaces.

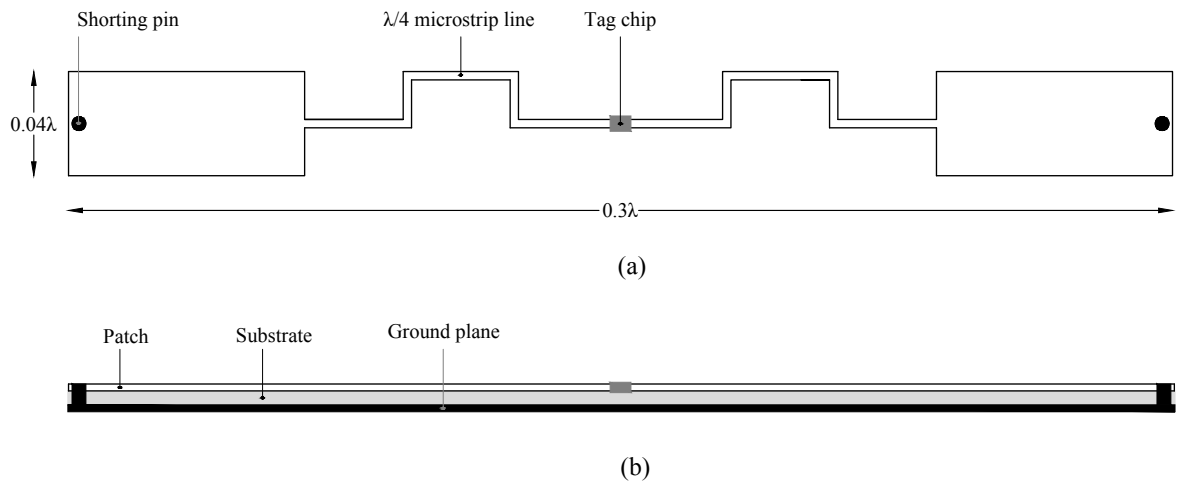


Figure 2.14: Planar inverted-F antenna for RFID tags. (a) Top view; (b) Side view [24].

of the antenna is comparatively large for tagging of small items.

A planar inverted-F antenna (PIFA) for RFID tags operating in the UHF band of 915 MHz is proposed in [24], shown in Figure 2.14. There are two shorting pins at the edges of the tag antenna which are connected to the ground plane to reduce the size of the tag antenna. Two shorting pins are employed at edge of the antenna, and two quarter-wavelength microstrip lines are used to achieve complex impedance matching between the antenna and the chip. The PIFA has dimensions of $100 \times 15 \times 0.8 \text{ mm}^3$. The read range of the proposed tag in free space is 2.5 m at the UHF frequency band (902–928 MHz). The antenna design is still comparatively large in size and has a complex structure geometry.

Furthermore, a flexible UHF RFID tag for mounting on metallic objects is investigated in [25], as shown in Figure 2.15. The T-matched method is used for matching the impedance of the antenna and the tag chip. The tag is fabricated on a high-dielectric polymer-ceramic composite substrate with a thickness of 1.5 mm to reduce the effect of interference from the metallic surface. The flexible substrate allows the tag to be mounted on a non-flatted metallic surface. The maximum measured read range of the tag mounted on a flat metallic surface sheet and on a cylindrical metallic object is 2.4 m and 2.8 m at 880 MHz, respectively.

A temporary on skin mountable passive UHF RFID tag sensor is presented [8] for various identification applications in ambient environments. The tag requires no printable surface as the tag consists of a single conducting layer which can be directly printed on the skin as a transfer tattoo. The resonance frequency of the tag is 915 MHz. The read range of the tag on a forearm, stomach and a chest is 80 cm, 120 cm, and 110 cm respectively.

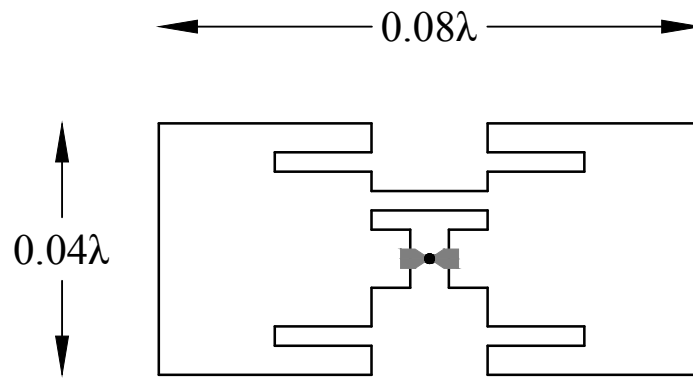


Figure 2.15: Small and flexible metal mountable passive UHF RFID tag.

2.3.3 RFID Sensing Mechanism

Most of the RFID sensing mechanisms are based on the tuning of the tag antenna and the chip impedance. When the input impedance of the tag antenna and the chip is mismatched, resulting in an increase in the transmitted power. The transmitted power is the maximum power that is required to turn on the tag. As the transmitted power increases, more power will require to activate the tag and hence lower the read range. The RFID reader can detect these two parameters: (i) the transmitted power; and (ii) the read range and hence the tag response.

Furthermore, recently introduced self-tuning RFID chips offer exciting possibilities for low-cost sensing [14]. The self-tuning tag chip does not have a fixed input impedance as compared to the standard tag chip. When the tag antenna is detuned, the chip auto-tunes its internal impedance to match with the tag antenna input impedance and stores the detuning results in the form of 5-bit sensor code. For example, Figure 2.16 shows the antenna sensor for moisture sensing [26]. The sensor consists of a dipole antenna embedded with the self-tuning Axzon Magnus S2 chip and coupled with interdigital electrodes (a digital or fingerlike periodic pattern). The sensing mechanism of the sensor is based on the detuning of the tag antenna via the interdigital electrodes, which is used to build up the capacitance. The capacitance of the electrodes changes when it exposes to moisture and thus detunes the tag antenna. The antenna impedance is compensated by the tag chip and return the degree of detuning results in the form of 5-bit sensor value, as shown in Figure 2.17. The chip auto-tunes its internal impedance and finds the best possible match with the tag antenna, and therefore, the tag performance remains stable, such as the tag read range, as shown in Figure 2.18. In this thesis, this RFID sensing mechanism will be further explored for ac current sensing.

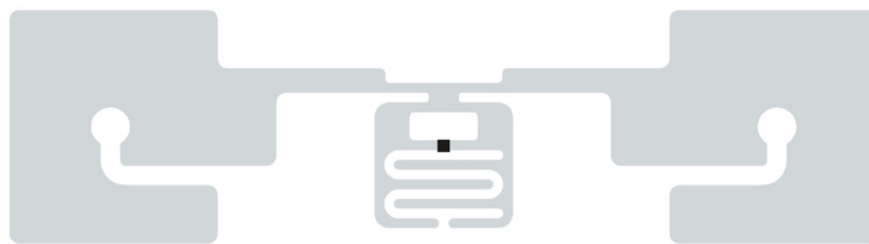


Figure 2.16: Moisture antenna sensor [26].

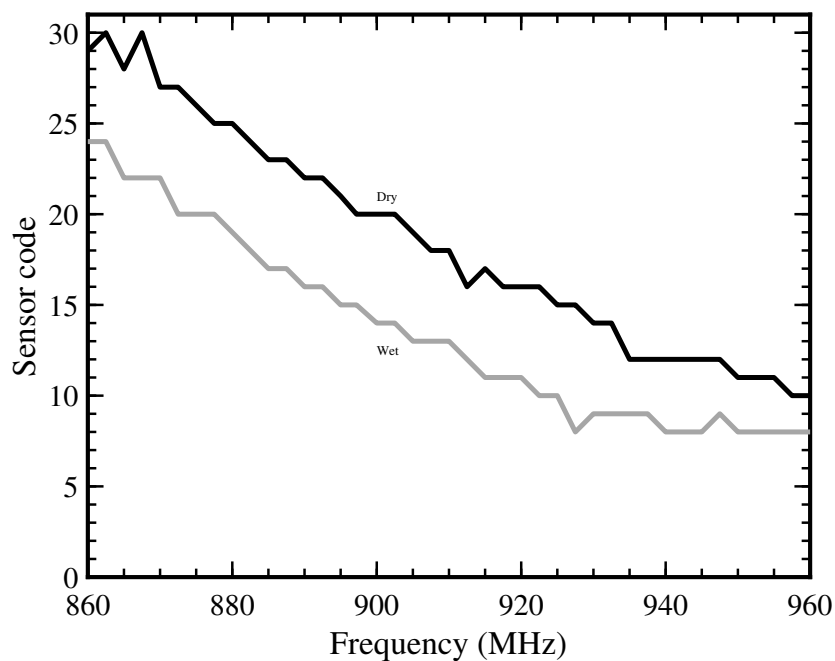


Figure 2.17: Sensor code of the antenna sensor in dry and wet state.

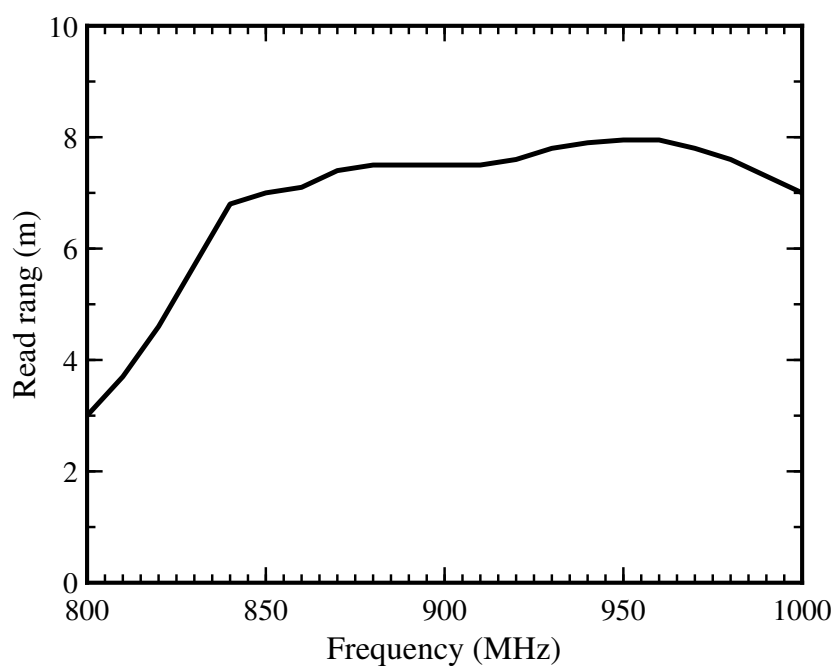


Figure 2.18: Read range of the moisture antenna sensor.

Furthermore, the self-tuning RFID tags have been explored for other sensing purposes. For example, in [28], a commercial moisture sensing self-tuning UHF RFID tag is transformed into a dielectric sensor for aqueous electrolytes. The electrodes of an auto-tuning RFID tag is covered with the polydimethylsiloxane-based thin-film and the effects of PDMS film thickness were characterised as a function of RFID tag code value. Furthermore, the addition of the film also enables the sensor to sense dielectric constant of various concentration aqueous salt solutions, such as NaCl, KCl, LiCl and RbCl.

Similarly, fingertip self-tuning RFID antennas based on multi-state microchips for the discrimination of dielectric objects is proposed in [29, 30], as shown in Figure 2.19. This concept is proposed to develop a radio-frequency fingertip-augmented device (FAD) [31, 32], which can be used as a dielectric probe on a finger to discriminate different types of materials and their discontinuities. The self-tuning fingertip antenna returns the sensor code at 868 MHz which is directly correlated with the permittivity of the materials.

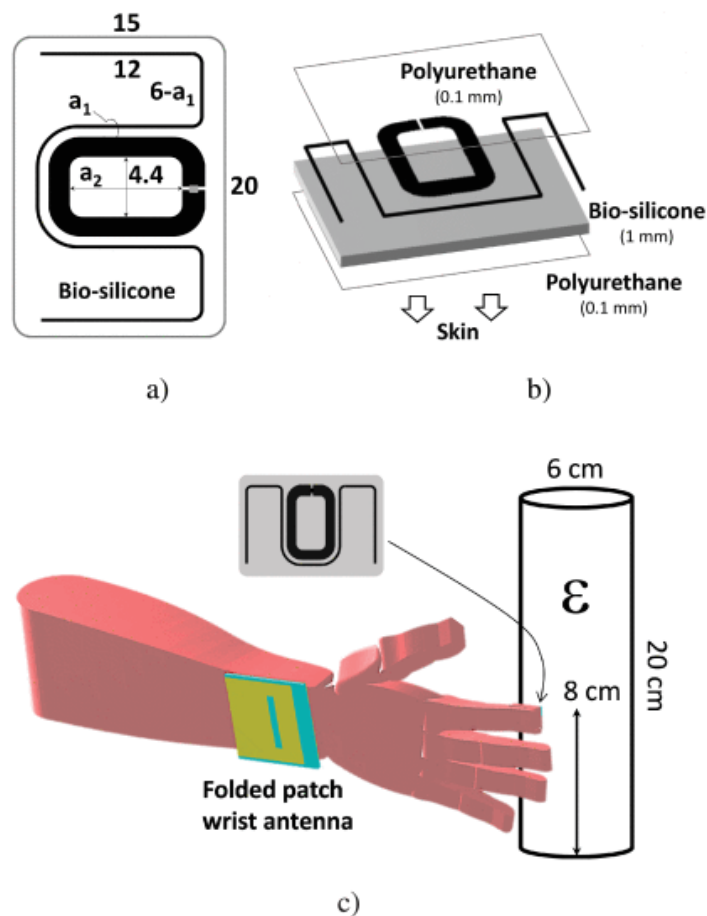


Figure 2.19: Loop-match dipole used as fingertip tag over a 1 mm thick layer of biocompatible silicone: (a) tag layout (dimensions are in mm); (b) exploded view of multilayers for on-skin application; (c) numerical model of the radio-frequency fingertip-augmented device [30].

Moreover, an epidermal sensor (Figure 2.20) based on the self-tuning UHF RFID tag for monitoring the skin temperature is demonstrated in [33, 34]. The sensor is fabricated by deploying the conductive wire on an ultra-thin biocompatible film of polyurethane with the thickness of 22 μm , allowing the tag to be attached onto the skin like a thin and flexible plaster. The sensor covers the whole worldwide RFID band (860–960 MHz) and has a good read range of more than 1 m.

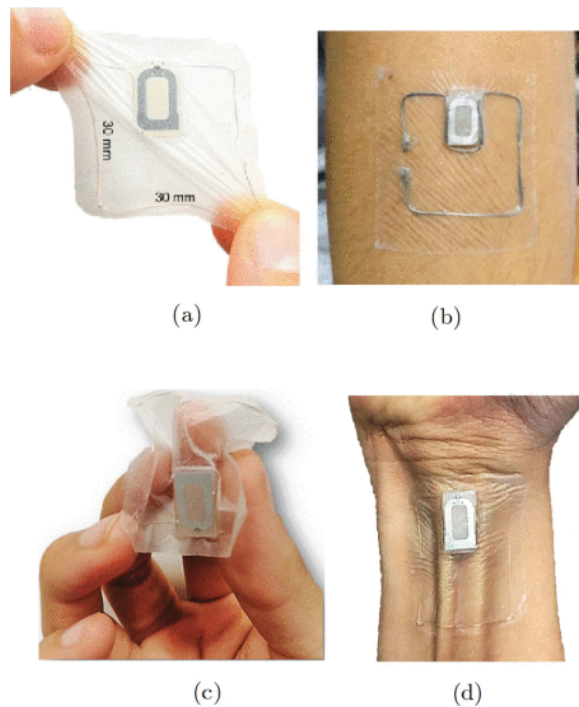


Figure 2.20: Prototypes of the epidermal tags: (a) made of a copper wire; and (b) conductive yarn. They are (c) soft and (d) conform to body discontinuities (forearm tendons) [34].

Similarly, a novel bio-integrated wireless RFID sensor based on the new generation self-tuning Axzon Magnus S3 chip with on-chip temperature sensor is proposed in [35, 36]. The sensor performs the on-skin temperature measurements with an average accuracy of $\pm 0.25\text{ }^{\circ}\text{C}$. In addition, the sensor response is more robust with no need to control neither the interrogator-sensor distance nor the radiated power.

Alternatively, a liquid pressure sensing system using self-tuning RFID tags is proposed in [37], as shown in Figure 2.21. Two self tuning tags, a fixed tag attached to a plate and a sliding tag attached to a piston, are located at the distance d . The reactance of the tags varies as a function of d . The variation in the input impedance of the tags is detected by an external RFID reader and hence, the sensor response.

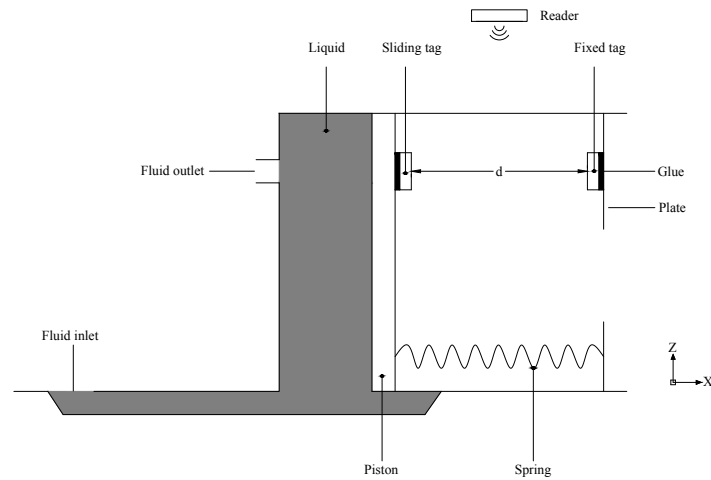


Figure 2.21: Liquid pressure sensing system, implemented in a cylinder.

2.3.4 Tag Antenna Designs for AC Current Sensing

There have been several RFID sensing solutions for ac current sensing are proposed in the literature [38–40]. They used an impulse sensing board connected to an RFID sensing tag, as shown in Figure 2.22. The impulse sensing board consists of an impulse detector, an ultra-low power microcontroller and a battery. The impulse detector is used to detect a signal and connected to the tag chip, which allows updating the status bit in the chip memory at each impulse detection using I2C protocol. There are two antennas proposed for the impulse sensing board: (i) an inductively coupled dipole antenna; and (ii) a helix antenna.

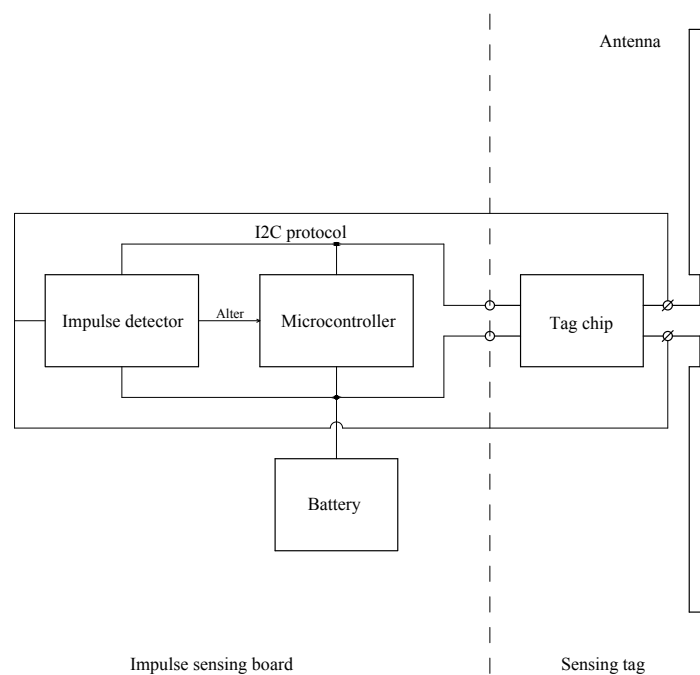


Figure 2.22: AC current impulse sensing system.

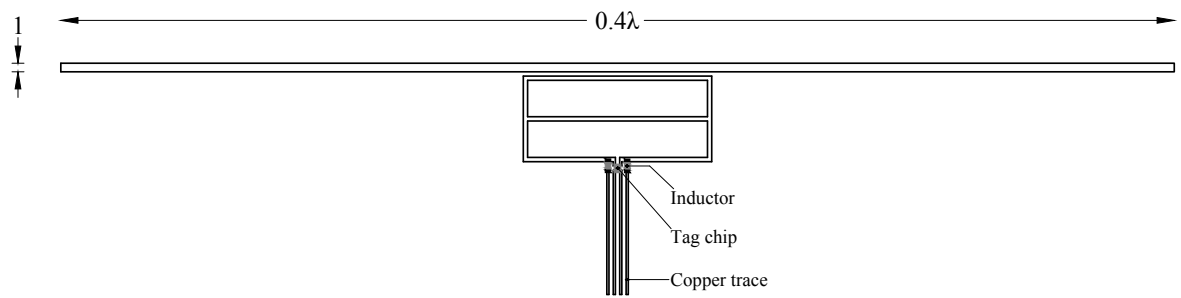


Figure 2.23: Dipole antenna inductively coupled to a rectangular feed loop.

In [38], a flexible RFID impulse sensing tag which consists of a dipole antenna inductively coupled with a feed loop for detecting the impulse in a power cable is proposed, as shown in Figure 2.23. The tag antenna is designed on a flexible substrate, which can be easily wrapped around a power cable of an electrical appliance. The proposed tag has a read range of approximately 5 m to 6 m at 915 MHz. The proposed impulse sensing tag has the ability to detect the ON and OFF status of electrical appliances and is ill-suited for real time ac current sensing in smart power monitoring systems. However, the other drawback of the proposed tag sensing solution is the impulse acquisition block, to which the tag antenna is connected, as described above. This proposed sensing system needs an external power supply and leads to high maintenance costs and the tag device is comparatively large in size. In addition, the radiation pattern of the dipole antennas significantly changes when the tag antenna is wrapped around the power cable due to close proximity with the electrical wires embedded inside the power cable.

In addition, a flexible helix tag antenna for ac current sensing is proposed in [39], as depicted in Figure 2.24. The tag has a good read range of 7 m to 8 m in the US band of 915 MHz. It is observed that the helix antenna has a high gain of -0.7 dB with a total radiation efficiency of 61% when compared to a straight dipole presented in [38]. Moreover, the proposed flexible helix antenna design can be easily mounted on a power cable. Furthermore, the proposed helix antenna can be integrated into the impulse sensing board for detecting ON/OFF current impulse.

The authors further optimised the impulse sensing design by replacing the impulse detector with a magnetometer, as depicted in Figure 2.25. In such a solution, the time-varying magnetic field, generated by the ac current passing in a power cable to an electrical appliance, is sensed by the magnetometer coupled to the RFID tag which is utilised for determining the ON/OFF state of the electrical device [40].

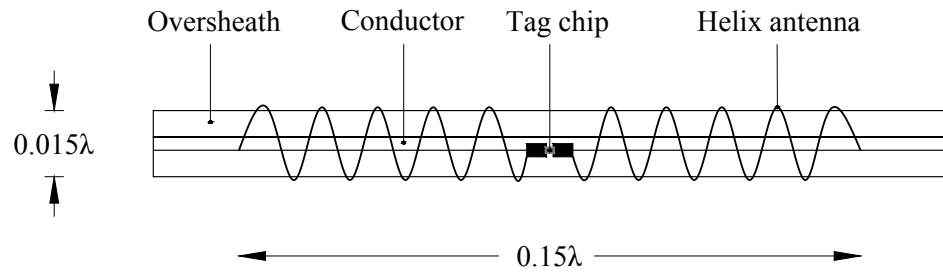


Figure 2.24: Flexible helix antenna mounted on a power cable for ac current sensing.

The operation and behaviour of the UHF RFID tag mounted on a power cable are

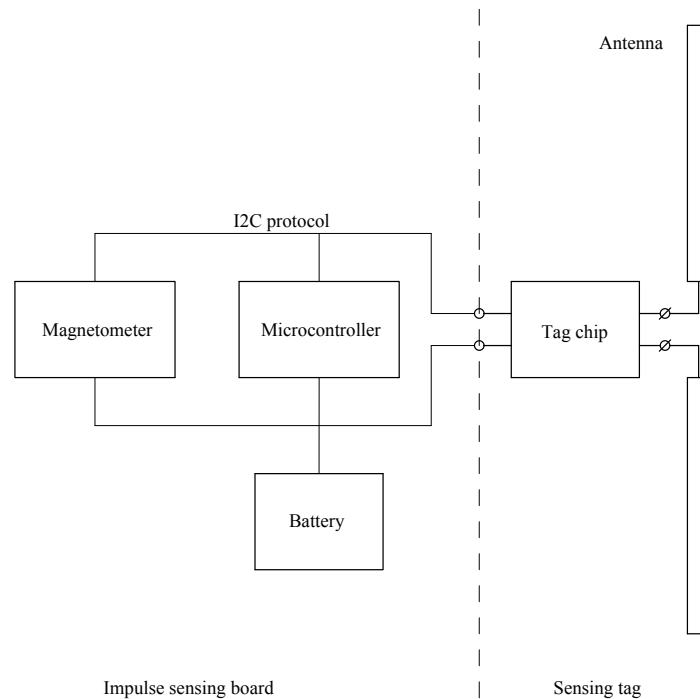


Figure 2.25: Block diagram of the sensor for detecting the ON and OFF state of an electrical appliance.

demonstrated in [41]. With the reference to the tag antenna design shown in Figure 2.26, a microstrip dipole is coupled with a feed loop to realise the RFID tag. The distance effect between the main antenna and feed loop on the mutual coupling and antenna matching is analysed. It is observed that the gap of 1.5 mm between the rectangular feed loop and antenna give high transmission coefficient at 868 MHz and 915 MHz. The tag has a read range of 5 m, which is more than double as compared to commercial RFID tags with a read range of 2 m at 915 MHz. It is suggested that using a thick insulator layer between the tag and the electrical wires can enhance the performance of the tag. Furthermore, the study can be extended to other geometries of power cables inclusive of a third ground wire to ensure the versatility of the tag concept for commercial developments.

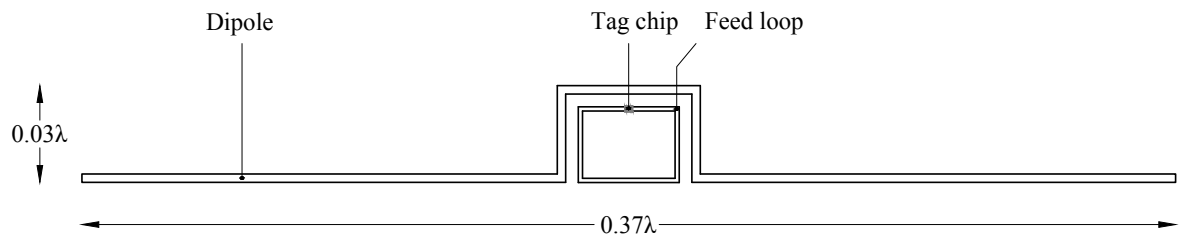


Figure 2.26: Design of a meandered dipole antenna inductively coupled with a feed loop for power cables.

2.4 Conclusion

In this chapter, a review of literature on designing passive UHF RFID tags and antenna designs for various sensing applications has been discussed. The chapter briefly overviews different types of RFID systems and tags. The RFID systems are classified into three groups LF, HF and UHF based on the frequency band they are operated. RFID tags are classified as active or passive, based on how they are powered. The principle of operation of a typical passive UHF RFID system is illustrated. Different types of tag antenna designs for various sensing applications in the ambient environment are discussed. Several conjugate impedance matching techniques including inductively coupled loop, T-matching network, nested slot-line, meandering and capacitive loading are also discussed, and later in this study, these techniques will be implemented in designing passive UHF RFID tags for ac current sensing. Various types of passive RFID tags and antenna designs including dipole antenna inductively coupled with a feed loop and a helix antenna mounted around a power cable for ac current sensing in a power cable has been demonstrated.

References

- [1] K. Zannas, H. El Matbouly, Y. Duroc and S. Tedjini, "Self-Tuning RFID Tag: A New Approach for Temperature Sensing," in *IEEE Transactions on Microwave Theory and Techniques*, vol. 66, no. 12, pp. 5885–5893, Dec. 2018, doi: 10.1109/TMTT.2018.2878568.
- [2] M. A. Ziai and J. C. Batchelor, "Multi-State Logging Freeze Detection Passive RFID Tags," in *IEEE Transactions on Antennas and Propagation*, vol. 62, no. 12, pp. 6406–6411, Dec. 2014, doi: 10.1109/TAP.2014.2359474.
- [3] Axzon sensing data insights (2020, Aug. 10). RFM2100 wireless flexible moisture sensor [Online]. Available: <https://axzon.com/rfm2100-wireless-flexible-moisture-sensor/>
- [4] M. C. Caccami and G. Marrocco, "Electromagnetic Modeling of Self-Tuning RFID Sensor Antennas in Linear and Nonlinear Regimes," in *IEEE Transactions on Antennas and Propagation*, vol. 66, no. 6, pp. 2779–2787, June 2018, doi: 10.1109/TAP.2018.2820322.
- [5] Belsey, K. E., Parry, A. V. S., Rumens, C. V., Ziai, M. A., Yeates, S. G., Batchelor, J. C., and Holder, S. J.. "Switchable disposable passive RFID vapour sensors from inkjet printed electronic components integrated with PDMS as a stimulus responsive material," in *Journal of Materials Chemistry C*, vol. 5, no. 12, Mar. 2017, pp. 3167–3175, doi: 10.1039/C6TC05509E.
- [6] Rumens, C. V., Ziai, M. A., Belsey, K. E., Batchelor, J. C. and Holder, S. J. "Swelling of PDMS networks in solvent vapours; applications for passive RFID wireless sensors,"

- in *The Royal Society of Chemistry*, vol. 3, no. 39, Aug. 2015, pp.10091–10098, doi: 10.1039/C5TC01927C.
- [7] Finkenzeller, Klaus. “RFID handbook: fundamentals and applications in contactless smart cards, radio frequency identification and near-field communication”. John Wiley & sons, 2010.
- [8] M. A. Ziai and J. C. Batchelor, “Temporary On-Skin Passive UHF RFID Transfer Tag,” in *IEEE Transactions on Antennas and Propagation*, vol. 59, no. 10, pp. 3565–3571, Oct. 2011, doi: 10.1109/TAP.2011.2163789.
- [9] Omni-ID (2020, Aug. 4). The evolution of active RFID [Online]. Available: <https://www.omni-id.com/active-rfid-tags/#>
- [10] Smartrac (2020, Aug. 4). Sensor temperature dogbone [Online]. Available: <https://www.smartrac-group.com/sensor-temperature-dogbone.html>
- [11] CAENRFID (2020, Aug. 17). RT0005 easy2log low cost, semi-passive UHF logger tag [Online]. Available: <https://www.caenrfid.com/en/products/rt0005/>
- [12] K. V. S. Rao, P. V. Nikitin and S. F. Lam, “Antenna design for UHF RFID tags: a review and a practical application,” in *IEEE Transactions on Antennas and Propagation*, vol. 53, no. 12, pp. 3870–3876, Dec. 2005, doi: 10.1109/TAP.2005.859919.
- [13] Alien technology (2020, Aug. 4). Higgs RFID ICs [Online]. Available: <https://www.alientechnology.com/products/ic/>
- [14] Axzon sensing data insights (2020, Aug. 4). Silicon [Online]. Available: <https://axzon.com/silicon/>
- [15] Ahson, Syed A., and Mohammad Ilyas. “IRFID Handbook: Applications, Technology, Security, and Privacy,” CRC press, 2017.
- [16] H. -. Son and C. -. Pyo, “Design of RFID tag antennas using an inductively coupled feed,” in *Electronics Letters*, vol. 41, no. 18, pp. 994–996, 1 Sept. 2005, doi: 10.1049/el:20051536.

- [17] G. Marrocco, "The art of UHF RFID antenna design: impedance-matching and size-reduction techniques," in *IEEE Antennas and Propagation Magazine*, vol. 50, no. 1, pp. 66–79, Feb. 2008, doi: 10.1109/MAP.2008.4494504.
- [18] Xin Ai, Hai Bao and Y. H. Song, "Novel method of error current compensation for Hall-effect-based high-accuracy current transformer," in *IEEE Transactions on Power Delivery*, vol. 20, no. 1, pp. 11–14, Jan. 2005, doi: 10.1109/TPWRD.2004.837820.
- [19] Alien technology (2020, Jun. 29). ALN-9762 Short Higgs 4 [Online]. Available: <https://www.alientechnology.com/products/tags/short/>
- [20] H. Wong, K. Luk, C. H. Chan, Q. Xue, K. K. So and H. W. Lai, "Small Antennas in Wireless Communications," in *Proceedings of the IEEE*, vol. 100, no. 7, pp. 2109–2121, July 2012, doi: 10.1109/JPROC.2012.2188089.
- [21] S. Chen and K. Lin, "A Slim RFID Tag Antenna Design for Metallic Object Applications," in *IEEE Antennas and Wireless Propagation Letters*, vol. 7, pp. 729–732, 2008, doi: 10.1109/LAWP.2008.2009473.
- [22] S. Chen, "A Miniature RFID Tag Antenna Design for Metallic Objects Application," in *IEEE Antennas and Wireless Propagation Letters*, vol. 8, pp. 1043–1045, 2009, doi: 10.1109/LAWP.2009.2032252.
- [23] L. Mo and C. Qin, "Planar UHF RFID Tag Antenna With Open Stub Feed for Metallic Objects," in *IEEE Transactions on Antennas and Propagation*, vol. 58, no. 9, pp. 3037–3043, Sept. 2010, doi: 10.1109/TAP.2010.2052570.
- [24] H. Chen and Y. Tsao, "Low-Profile PIFA Array Antennas for UHF Band RFID Tags Mountable on Metallic Objects," in *IEEE Transactions on Antennas and Propagation*, vol. 58, no. 4, pp. 1087–1092, April 2010, doi: 10.1109/TAP.2010.2041158.
- [25] A. A. Babar, T. Bjorninen, V. A. Bhagavati, L. Sydanheimo, P. Kallio and L. Ukkonen, "Small and Flexible Metal Mountable Passive UHF RFID Tag on High-Dielectric Polymer-Ceramic Composite Substrate," in *IEEE Antennas and Wireless Propagation Letters*, vol. 11, pp. 1319–1322, 2012, doi: 10.1109/LAWP.2012.2227291.

- [26] Smartrac (2020, Aug. 4). Sensor bogbone [Online]. Available: <https://www.smartrac-group.com/sensor-dogbone.html>
- [27] K. H. Lin, S. L. Chen and R. Mittra, "A Capacitively Coupling Multifeed Slot Antenna for Metallic RFID Tag Design," in *IEEE Antennas and Wireless Propagation Letters*, vol. 9, pp. 447–450, 2010, doi: 10.1109/LAWP.2010.2048991.
- [28] A. J. R. Hillier, V. Makarovaite, C. W. Gourlay, S. J. Holder and J. C. Batchelor, "A Passive UHF RFID Dielectric Sensor for Aqueous Electrolytes" in *IEEE Sensors Journal*, vol. 19, no. 14, pp. 5389–5395, 15 July 15, 2019, doi: 10.1109/JSEN.2019.2909353.
- [29] G. M. Bianco and G. Marrocco, "Fingertip Self-tuning RFID Antennas for the Discrimination of Dielectric Objects," *2019 13th European Conference on Antennas and Propagation (EuCAP)*, Krakow, Poland, 2019, pp. 1–4.
- [30] G. M. Bianco, S. Amendola and G. Marrocco, "Near-Field Constrained Design for Self-Tuning UHF-RFID Antennas," in *IEEE Transactions on Antennas and Propagation*, vol. 68, no. 10, pp. 6906–6911, Oct. 2020, doi: 10.1109/TAP.2020.2995315.
- [31] G. M. Bianco, S. Amendola and G. Marrocco, "Near-field modeling of Self-tuning Antennas for the Tactile Internet," *2020 XXXIIIrd General Assembly and Scientific Symposium of the International Union of Radio Science*, Rome, Italy, 2020, pp. 1-3, doi: 10.23919/URSIGASS49373.2020.9232032.
- [32] G. M. Bianco, C. Vivarelli, S. Amendola and G. Marrocco, "Experimentation and calibration of Near-Field UHF Epidermal Communication for emerging Tactile Internet," *2020 5th International Conference on Smart and Sustainable Technologies (SpliTech)*, Split, Croatia, 2020, pp. 1-4, doi: 10.23919/SpliTech49282.2020.9243753.
- [33] F. Amato, C. Miozzi, S. Nappi and G. Marrocco, "Self-Tuning UHF Epidermal Antennas," *2019 IEEE International Conference on RFID Technology and Applications (RFID-TA)*, Pisa, Italy, 2019, pp. 380–383, doi: 10.1109/RFID-TA.2019.8892222.
- [34] C. Miozzi, F. Amato and G. Marrocco, "Performance and Durability of Thread Antennas as Stretchable Epidermal UHF RFID Tags," in *IEEE Journal of Radio Fre-*

- quency Identification*, vol. 4, no. 4, pp. 398–405, Dec. 2020, doi: 10.1109/JR-FID.2020.3001692.
- [35] F. Camera and G. Marrocco, "Electromagnetic-Based Correction of Bio-Integrated RFID Sensors for Reliable Skin Temperature Monitoring," in *IEEE Sensors Journal*, vol. 21, no. 1, pp. 421–429, 1 Jan.1, 2021, doi: 10.1109/JSEN.2020.3014404.
- [36] F. Camera, C. Miozzi, F. Amato, C. Occhiuzzi and G. Marrocco, "Experimental Assessment of Wireless Monitoring of Axilla Temperature by Means of Epidermal Battery-Less RFID Sensors," in *IEEE Sensors Letters*, vol. 4, no. 11, pp. 1–4, Nov. 2020, Art no. 6002304, doi: 10.1109/LSENS.2020.3036486.
- [37] R. Feng, Y. Chang, L. Mao and J. Li, "Liquid Pressure Sensing System With Coupling RFID and HMM Based on Distance Measurement," in *IEEE Sensors Journal*, vol. 21, no. 2, pp. 1051–1058, 15 Jan.15, 2021, doi: 10.1109/JSEN.2020.2981734.
- [38] A. Louzir, R. Kumar and J. Le Naour, "RFID based solution for the sensing of home electrical devices activity," *I2016 International Symposium on Antennas and Propagation (ISAP)*, Okinawa, 2016, pp. 1002–1003.
- [39] R. Kumar, A. Louzir and J. Le Naour, "RFID helix antenna on power cord for the sensing of home electrical devices activity," *2017 11th European Conference on Antennas and Propagation (EUCAP)*, Paris, 2017, pp. 2554–2558, doi: 10.23919/EUCAP.2017.7928549.
- [40] R. Kumar, A. Louzir and J. L. Naour, "RFID Tag Coupled with a Magnetic Sensor for Wireless Sensing of Home Electrical Devices," *2018 48th European Microwave Conference (EuMC)*, Madrid, 2018, pp. 981–984, doi: 10.23919/EuMC.2018.8541682.
- [41] J. M. Laheurte, S. Protat and A. Louzir, "Performance Analysis of UHF RFID Tags Dedicated to Power Supply Cords," in *IEEE Transactions on Antennas and Propagation*, vol. 63, no. 11, pp. 5241–5245, Nov. 2015, doi: 10.1109/TAP.2015.2478148.

RFID AC Current Sensing Technique

3.1 Introduction

IN this chapter, the mechanism by which a passive UHF RFID tag coupled with a tuning circuit is integrated with a current transformer for sensing ac current in an electrical wire for smart power monitoring of individual appliances in a smart home is described. A capacitance change in the tuning circuit results from a reverse bias voltage from the current transformer. The tuning circuit reactance is detected by a capacitance sensing RFID tag, and the value is transmitted as a 5-bit sensor code which is directly related to the ac current drawn by an electrical load. The passive tag harvests energy and offers an innovative solution for energy management in future smart homes and for industry 4.0. As well as indicating current level, the technique can also be used to detect the ON and OFF state of an electrical device and is demonstrated to work for a rapidly switching load. The sensor is tuned for Electronic Product Code (EPC) Class 1 Generation 2 UHF RFID readers at 868 MHz [1]. The remainder of the chapter is organised as follows: In Section 3.2, existing ac current sensing solutions for smart power monitoring systems are discussed. Section 3.3 describes the self-tuning RFID tag chip. In Section 3.4, a schematic diagram of the proposed RFID tag system is introduced. It covers the design and integration of a current transformer, a tuning circuit, and an RFID tag antenna. The measurement results of the tag system are reported in Section 3.6. Finally, Section 3.7 concludes the chapter.

3.2 Existing AC Current Sensing Solutions

There have been RFID based solutions proposed for the sensing of home electrical devices [2–4], but which require the integration of an impulse acquisition circuit with the RFID tag. This needs an external power supply and leads to high maintenance costs. Furthermore, they only have the ability to detect the transition between On and Off states and are ill-suited for real-time load current sensing. Alternatively, [5], [6] report ZigBee-based wireless current transformers with complex architectures including a sensing platform which do not require a mains voltage ac-dc converter but do include the complexity of a signal processing circuit, an analogue-to-digital converter and a wireless transmission module, which increases the expense. Alternatively, the Monjolo energy-harvesting energy meter does not require a mains ac-dc converter but still involves the complexity of an energy harvesting IC, a microcontroller, an IEEE 802.15.4 compatible radio and FRAM (ferroelectric random access memory) [7]. Finally, a new energy harvesting technique for capturing power from ac power lines using a miniature linear permanent magnet synchronous generator is described in [8]. However, such a device is most useful for monitoring high power consumption in emerging smart grids.

Furthermore, there are some commercial ac current sensors available serving wireless sensing devices. They have integrated CT into an energy monitoring unit with the onboard high gain antenna. Such as a NCD long-range IoT wireless ac current monitor [9] is designed to measure ac current in the range of 0 A to 100 A. The sensor is integrated with a monopole antenna operating at 868 MHz, 900 MHz and 2.4 GHz. However, the sensor is suitable for industrial uses and is cost-intensive to use in domestic applications and needs an external power source. Similarly, an Alta wireless ac current meter is designed to measure ac current up to 20 A [10], embedded with a monopole antenna working at 868 MHz and 900 MHz. The meter uses a 3–3.8 V battery which increases the maintenance cost. Alternatively, Pressac wireless current sensor [11] is a passive sensor for measuring real-time energy usage, which communicates data via the EnOcean wireless radio protocol. The sensor required a smart gateway to wirelessly transmit data via WiFi or LTE (4G) to the consumer access device.

In this chapter, the proposed tag structure is less complex than the alternatives [2–8], and provides a cost-effective solution for power monitoring when many tags on individual appli-

ances communicate wirelessly with a centrally mounted single RFID reader in the views of the tags to be read. The tag offers a solution for small current measurements in the range of 2 A to 10 A without requiring a microcontroller, and which harvests energy from the interrogator radio wave in the read range of about 4 m.

3.3 Self-Tuning Tag

A self-tuning RFID tag consists of an antenna and a multi-state chip, as shown in Figure 3.1. The self-tuning chip can vary its internal capacitance between 2 pF to 3 pF in the presence of detuning element. The overall capacitance of the chip can be calculated from (3.5).

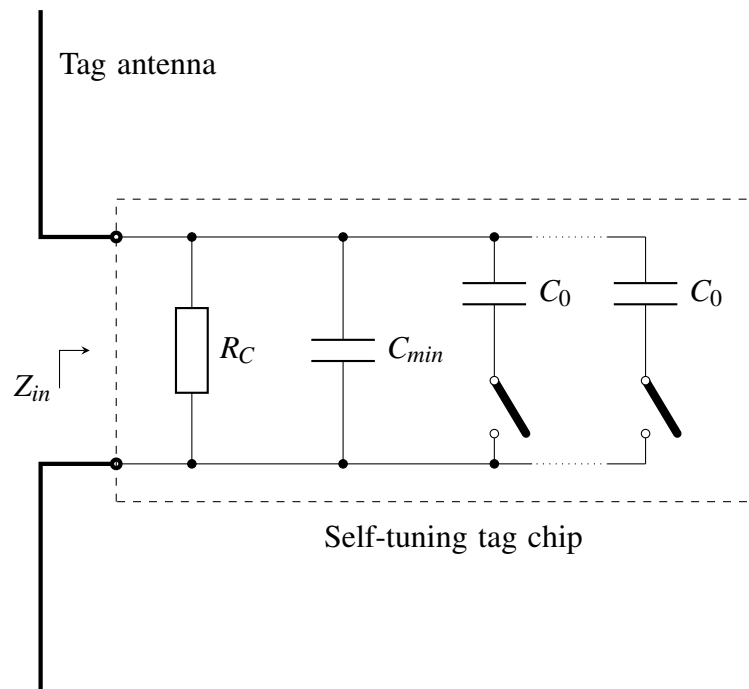


Figure 3.1: Self-tuning tag chip attached across the antenna ports, forming a self-tuning RFID tag.

$$C_T(n) = C_{min} + nC_o \quad (3.1)$$

where $C_T(n)$ is the total capacitance, C_{min} is the minimum capacitance of 2 pF of the chip, n is the sensor value in the range of 0 to 31 and C_o is a tunable step (1 pF/31) within the 1 pF tunable range.

The current sensing tag incorporates a self-tuning Axzon Magnus S2 transponder chip which provides two key features: a 5-bit sensor code and a 5-bit on-chip RSSI (Received

Signal Strength Index) code which can be transmitted to an external RFID reader [12, 13]. The sensor code indicates the impedance mismatch between the tag chip and the tag antenna, while the RSSI code relays the strength of the incoming signal from the reader. Figure 3.2 illustrates how a reader communicates with the RFID tag and retrieves its sensor codes using standard GEN2 READ commands [14]. While a tag is receiving transmitted power from the dedicated reader, it writes sensor values into its reserved memory bank. In addition, the changes in the sensor code of the microchip depend on the impedance changes of the tag antenna which means that less detuning of the tag antenna will cause less change in the sensor code, and vice versa. All EPC-compliant RFID reader should be able to read the sensor code.

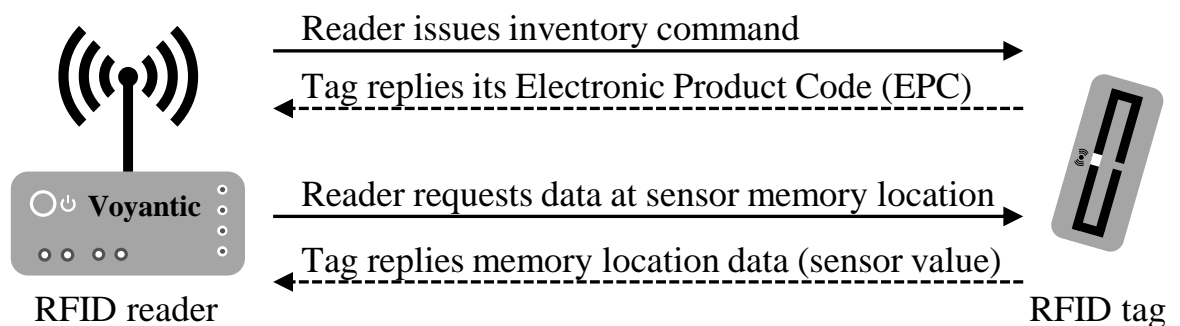


Figure 3.2: RFID reader communication and retrieval of tag sensor codes [14].

Furthermore, the tag antenna impedance may vary in the presence of detuning elements such as metal, moisture, dielectric materials near the tag, etc. The self-tuning tag chip will automatically adjust its internal input impedance to improve matching with the antenna input impedance to extract maximum energy from an incident RF wave. As a result, the tag performance remains more consistent and offers better readability with different environmental conditions. Alternatively, a tag chip having fixed input impedance cannot compensate its internal input impedance with the antenna impedance. When a mismatch happened between the tag antenna and chip impedance and thus caused to reduce the overall tag performance, i.e. read range. Therefore, the tag antenna coupled with auto-tuning tag chip provides more consistent tag performance over a wide range of frequency when compared to the tag having fixed input impedance, as shown in Figure 3.3.

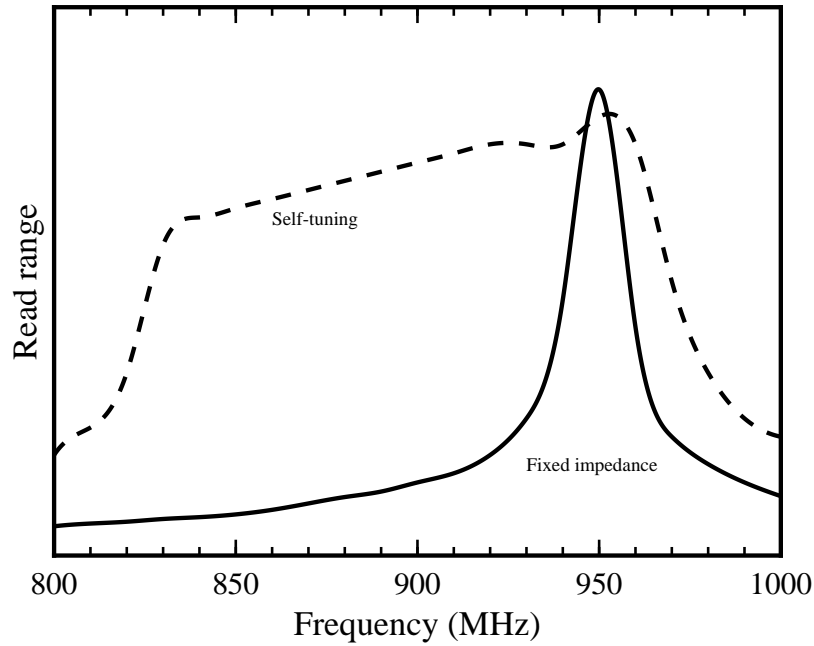


Figure 3.3: Reproduced plot from [15], showing a read range of the self-tuning and standard RFID chip.

3.4 System Description

The schematic diagram of the tag system is shown in Figure 3.4 and comprises of three elements: (i) a Current Transformer (CT); (ii) a tuning circuit; and (iii) a capacitance sensing passive UHF RFID tag. The CT is used to detect the ac current from a cable and transforms it into dc voltage which controls the reactance of a tuning circuit. This effects a reactance change at the capacitance sensing RFID chip which generates a proportionate sensor code. The changes in the tuning circuit capacitance as a function of the reverse bias voltage from the CT are proportional to the sensor code as the transformer has a linear relationship between primary current and secondary voltage, and as the mains frequency is fixed, the secondary voltage relates to the primary ac magnitude in the electrical load.

3.4.1 Current Transformer

An off-the-shelf split-core CT with a full bridge rectifier [16] was used to sense input currents of 0 A to 10 A ac and transform them to 0 V to 10 V dc voltage output, Figure 3.5, with a stated full-scale accuracy of $\pm 2\%$ at frequencies of 50/60 Hz. The CT also includes a burden resistor, a low-pass filter and a zener diode. The burden resistor across the bridge rectifier

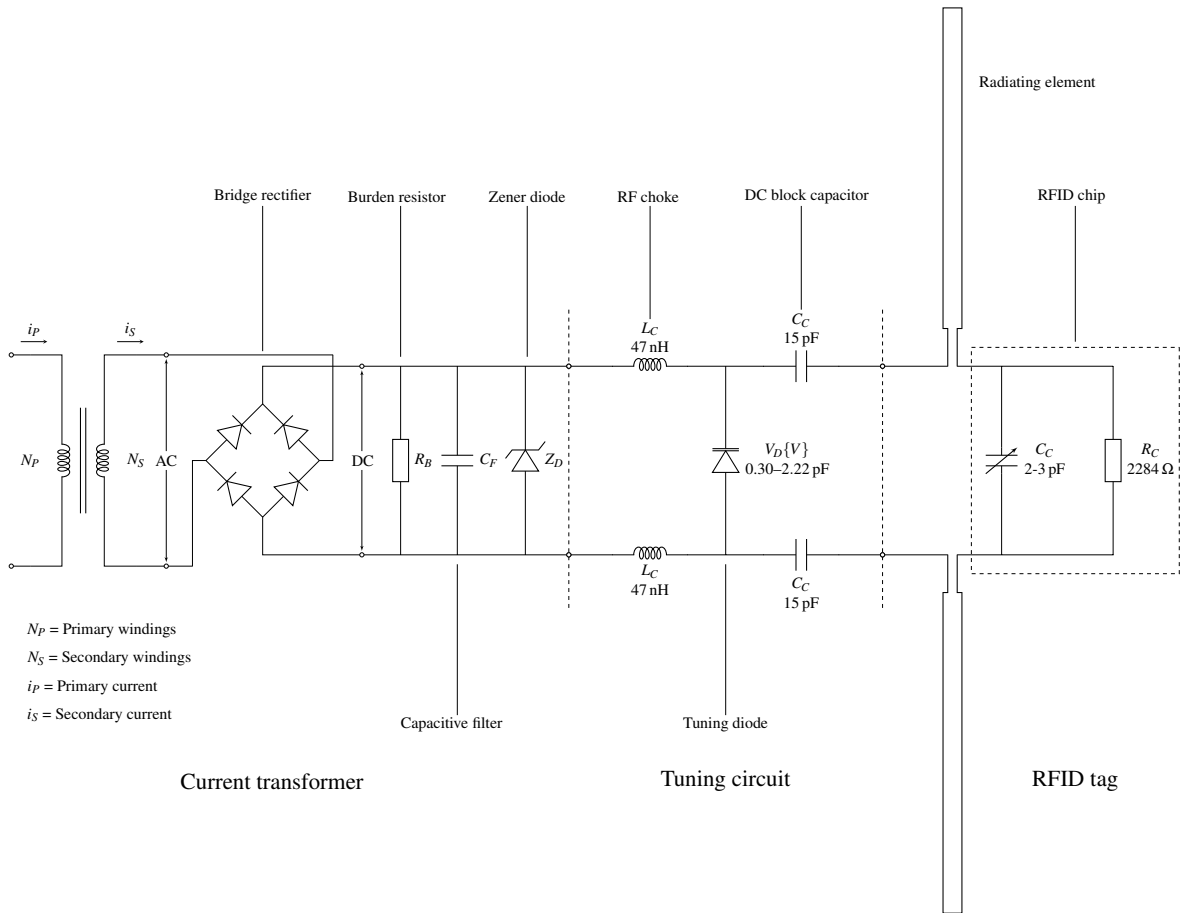


Figure 3.4: Schematic diagram overview of the suggested RFID ac current sensing tag from an ac electrical cable.

provides the output voltage for measurement purposes while the filter capacitor parallel to the output attenuates higher frequency components. The bi-directional zener diode maintains the unloaded voltage output up to a 15 V dc limit and prevents the development of high voltage spikes across the output. Two M3 screw terminals beneath a removable cover can be connected to the output leads. The relationship between the primary current and the secondary current of the current transformer is [17]:

$$N_p i_p = N_s i_s \quad (3.2)$$

where N_p is the number of the primary winding and i_p represents ac current flow in the primary winding, while N_s is the number of the secondary winding and i_s represents induced ac current in the secondary coil due to the i_p . A typical current transformer schematic circuit is illustrated in Figure 3.6. In an ideal transformer, the primary of the transformer is directly proportional to the secondary, and therefore the voltage generated across the load resistor (R_L) is equal to $R_L i_p$. The load resistor connected across the CT output terminals is known

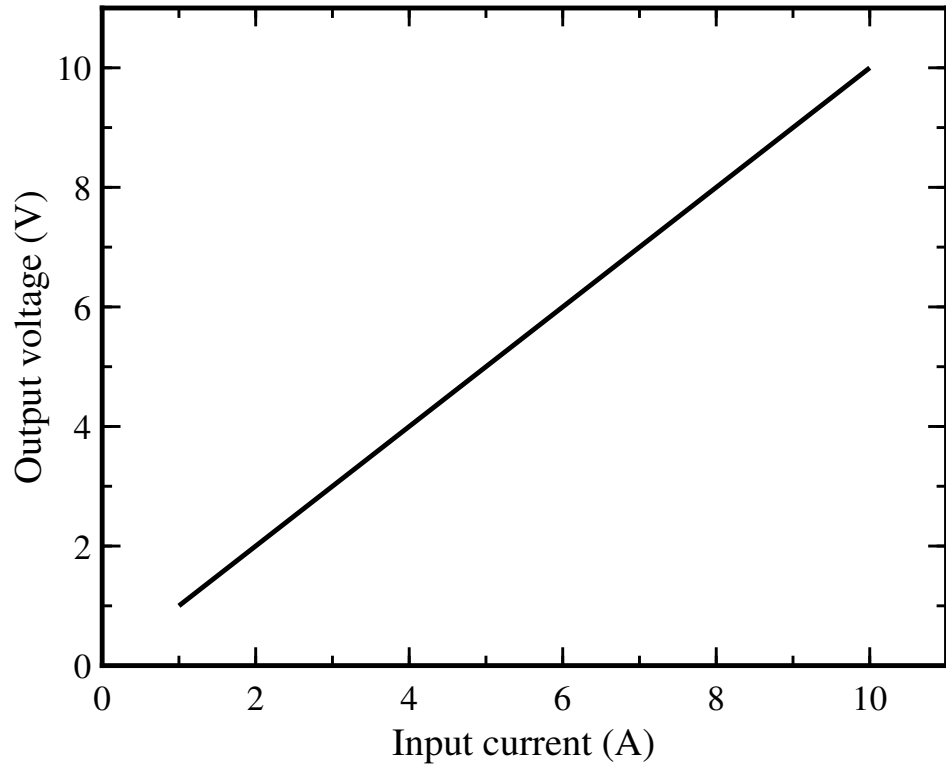


Figure 3.5: AC current to dc voltage ratio of the CT.

as the burden resistor and the value of the burden resistor determines the output voltage value of the transformer.

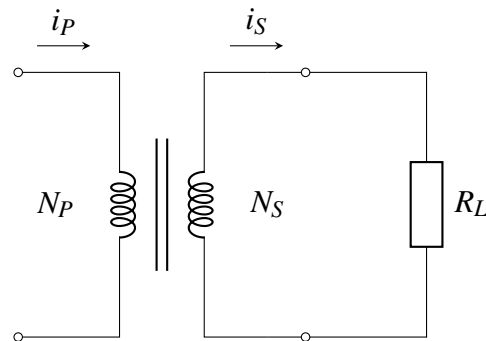


Figure 3.6: Typical schematic diagram of a CT with a load resistor (R_L) connected across its output terminals.

3.4.2 Tuning Circuit

The tuning operating circuit in Figure 3.4 is composed of two inductors of 47 nH, a tuning varactor diode and two capacitors of 15 pF. The reverse-biased varactor diode [18] capacitance V_D {V} is a function of the applied CT voltage V . The diode typically requires a reverse bias of 0 V to 20 V to produce capacitance in the range of 0 pF to 2.22 pF, though the diode capacitance starts to saturate at 10 V. In a hyperabrupt junction, the capacitance C_J of the

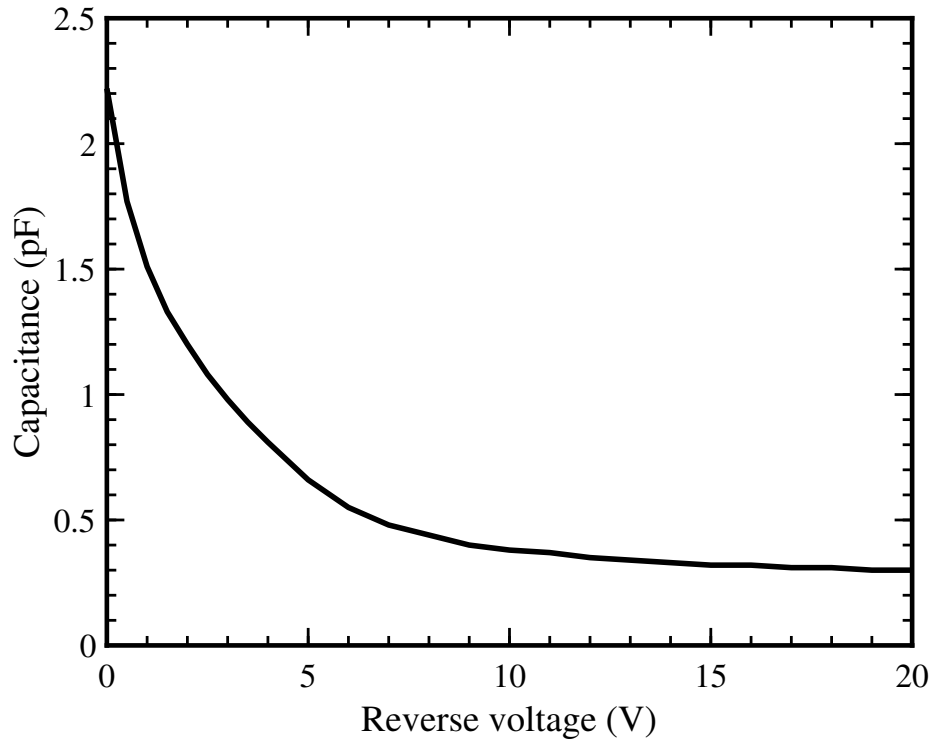


Figure 3.7: Voltage to capacitance ratio of the implemented tuning element in the tuning circuit [20].

tuning diode as a function of the reverse bias voltage is derived from [19]:

$$C_J(V_R) = \frac{C_J(V_X)}{\left(\frac{V_R + \phi}{V_X + \phi}\right)^\gamma} \quad (3.3)$$

where $C_J(V_R)$ is the junction capacitance at reverse bias voltage, V_R , $C_J(V_X)$ is the junction capacitance at V_X (V_X is an arbitrary reference voltage, typically 0 V), ϕ is the built in voltage (0.7 V for Si), γ is the slope exponent (0.5 for abrupt junction and greater than 0.5 for the hyperabrupt junction)

The inductors isolate the RF from the tag antenna from the CT secondary. The 15 pF capacitors are used to block the CT output dc voltage from the input of the tag chip, as shown in Figure 3.4 and the relationship between the capacitance and the reverse bias voltage taken from [20] is illustrated in Figure 3.7. Therefore, the equivalent capacitance (C_{eq}) of the tuning circuit is equal to the total series capacitance. The upper or lower output capacitance of the tuning circuit can be determined through different values of the lumped elements, i.e. an increased dc block capacitor value C_B will lead to an increase in the overall tuning circuit

capacitance:

$$\frac{1}{C_{eq}} = \frac{1}{C_B} + \frac{1}{C_D\{V\}} + \frac{1}{C_B} \quad (3.4)$$

The tag antenna and tuning circuit layout are shown in Figure 3.9. Two 1 mm wide, 20 mm long copper straps with a 4 mm gap are used to connect the CT to the lumped elements of the tuning circuit. The tuning circuit uses 0603 surface mount components with a pitch of 0.5 mm and was fabricated along with the RFID tag on a 0.14 mm thick flexible Mylar substrate with a copper layer of 0.04 mm thickness.

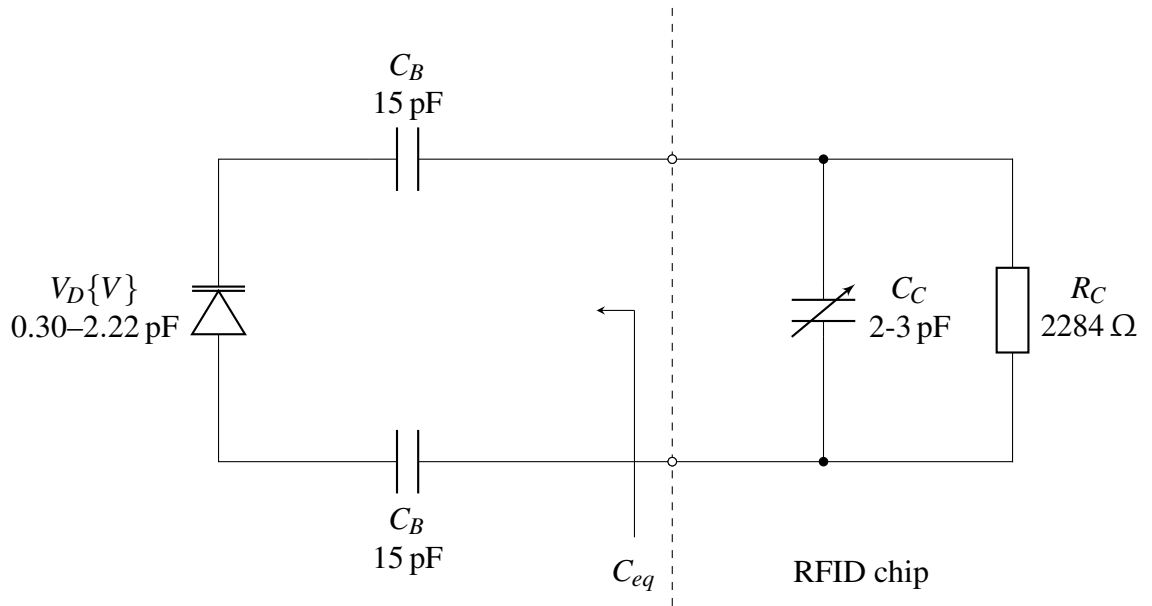


Figure 3.8: The configuration of dc block capacitors and a varactor diode in the tag tuning circuit.

3.4.3 RFID Tag Design

The RFID dipole antenna in Figure 3.9(a) operates at 868 MHz and is similar to the structure presented in [21]. The tag was simulated in the electromagnetic software Computer Simulation Technology (CST) Microwave Studio [22] and the length of the antenna feed loop was adjusted to shift its resonance frequency. The Axzon Magnus S2 chip required turn-on power is -16.1 dBm and the tuning capacitance range is 2 pF to 3 pF in parallel with 2284Ω . The chip covers all Worldwide RFID frequency bands (860–960 MHz) and can vary its capacitance between 2 pF to 3 pF in the presence of a detuning element. The total load capacitance for the antenna model is [12]:

$$C_T(n) = C_{min} + nC_o \quad (3.5)$$

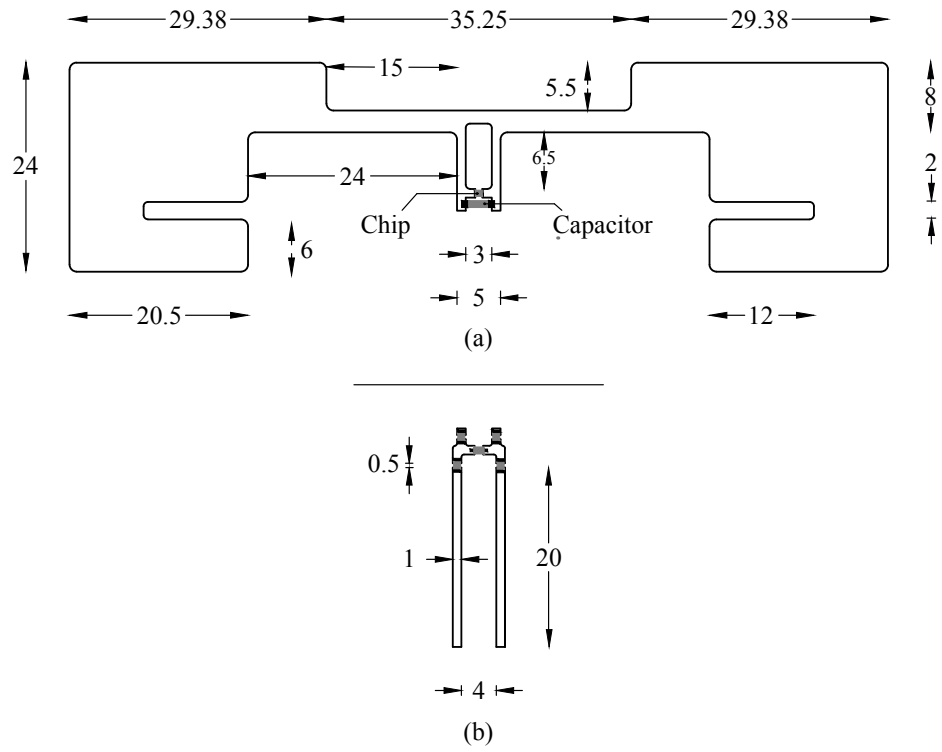


Figure 3.9: (a) RFID tag design; and (b) tuning circuit design. (All dimensions are in mm)

where $C_T(n)$ is the total capacitance, C_{min} is the minimum capacitance of 2 pF of the chip, n is the sensor value in the range of 0 to 31 and C_o is a tunable step (1 pF/31) within the 1 pF tunable range. Therefore, for simulation, the chip impedance was fixed to $Z_C = 1.63 \Omega - j 61.07 \Omega$, at 868 MHz (corresponding to 3 pF). The complex input impedance of the RC parallel equivalent circuit of the tag chip was calculated using (3.6). The tag was designed on a Mylar substrate with a dielectric constant (ϵ_r) of 2.8, loss tangent (δ) of 0.003, and with a total height of 0.18 mm including the copper thickness of 0.04 mm. The tag performance was simulated for two scenarios: (i) in the absence of detuning elements; and (ii) including the detuning elements, i.e. a total capacitance of 2.1 pF to 3 pF.

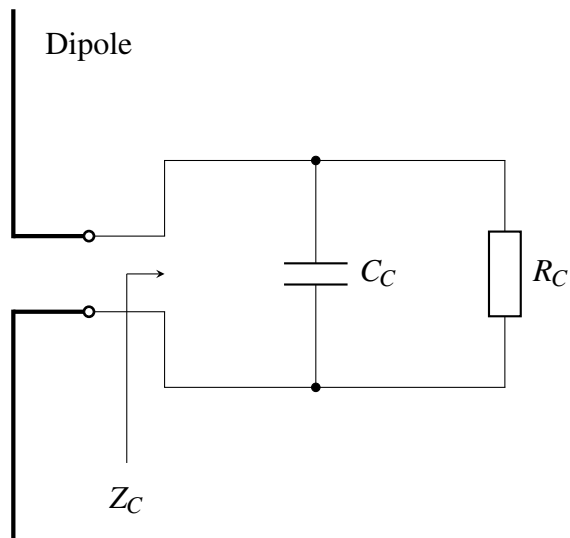
$$Z_C = \frac{R \times X_C^2}{R^2 + X_C^2} - j \cdot \frac{R^2 \times X_C}{R^2 + X_C^2} \quad (3.6)$$

where Z_C is the complex impedance of the RC parallel equivalent circuit of the chip, R is the resistance in ohms (Ω), j is the imaginary unit and X_C is the capacitive reactance:

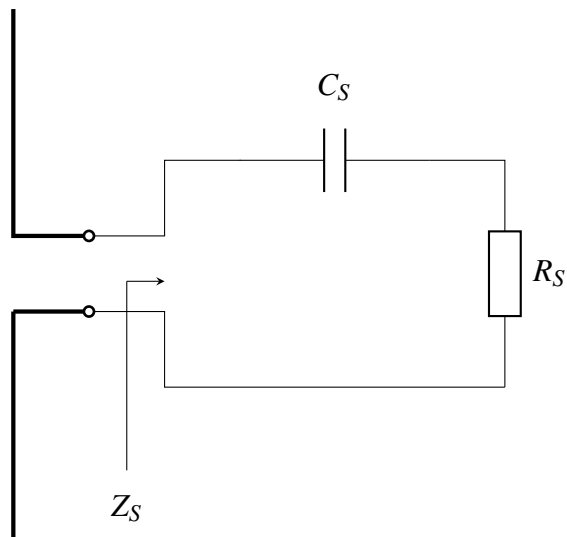
$$X_C = \frac{1}{2\pi f C} \quad (3.7)$$

where f is the frequency in hertz (Hz) and C is the capacitance in farad (F).

In addition, the RC equivalent circuit of the chip and its typical input impedance may



(a)



(b)

Figure 3.10: (a) Parallel circuit of the tag chip; and (b) its equivalent circuit.

vary depending on the manufacturing of the integrated chip (IC) design, i.e. the equivalent circuit of the tag chip can also be an RC series circuit. Figure 3.10 illustrates the comparison between the RC series and RC parallel equivalent circuit of the tag chip. The complex input impedance of the RC series circuit is [23]:

$$Z_S = R_S + \frac{1}{j2\pi f C_S} \quad (3.8)$$

3.5 Simulation Results

CST Microwave Studio was used to simulate the tag antenna design. In CST, mesh plays a critical role in simulation speed and accuracy. High accuracy can be achieved by keeping the mesh size smaller but it directly impact the total simulation time. Therefore, in order to achieve good accuracy, the wavelength spatially sampled at a rate of at least 20 mesh cells per wavelength. Figure 3.11 illustrates the simulated effect of varying applied terminal capacitance on the reflection coefficient S_{11} of the tag antenna in Figure 3.9. In the absence of the auto-tuning function, increasing the applied capacitance to 1 pF causes the antenna resonance to drop to 800 MHz. Furthermore, the simulated results in Figure 3.12 and in Figure 3.13 show the variation of antenna admittance with a change of applied capacitance. The relation between the chip and the antenna susceptance is:

$$|B_C(n) + B_A(\Psi)| \rightarrow 0 \quad (3.9)$$

where B_C is the susceptance of the tag chip, B_A is the susceptance of the tag antenna, and Ψ is an external reactance (0.1 pF to 1 pF). When the tag antenna susceptance changes as a result of the applied reactance this will be compensated by the self-tuning tag chip and returned in the form of the sensor code (n).

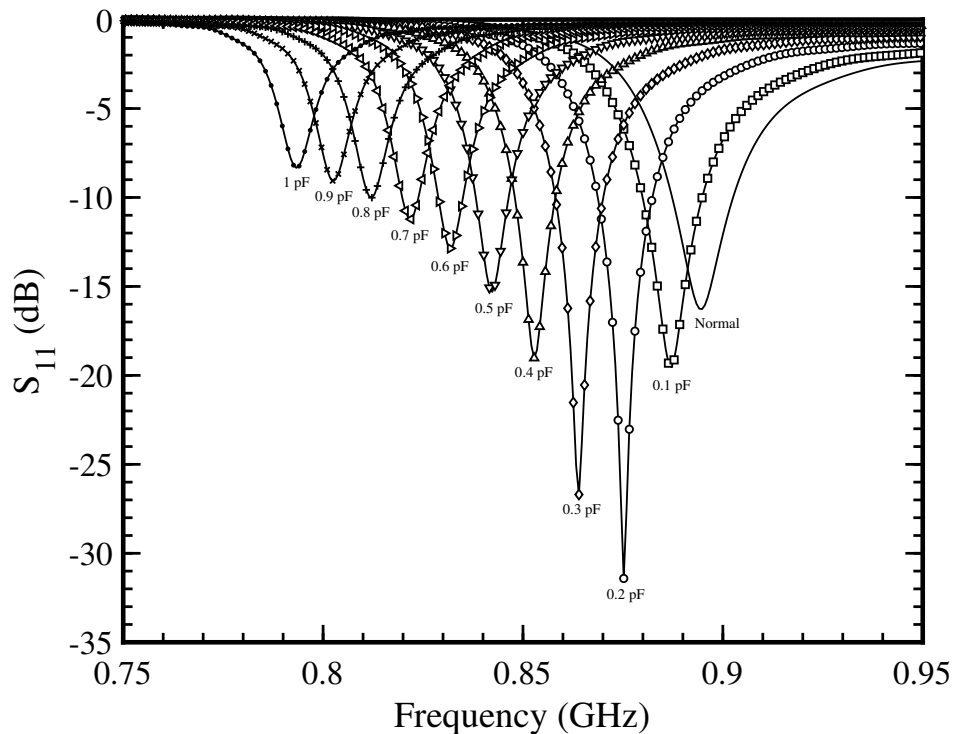


Figure 3.11: CST simulated power reflection coefficient of the RFID tag antenna due to varying capacitor value across its terminals.

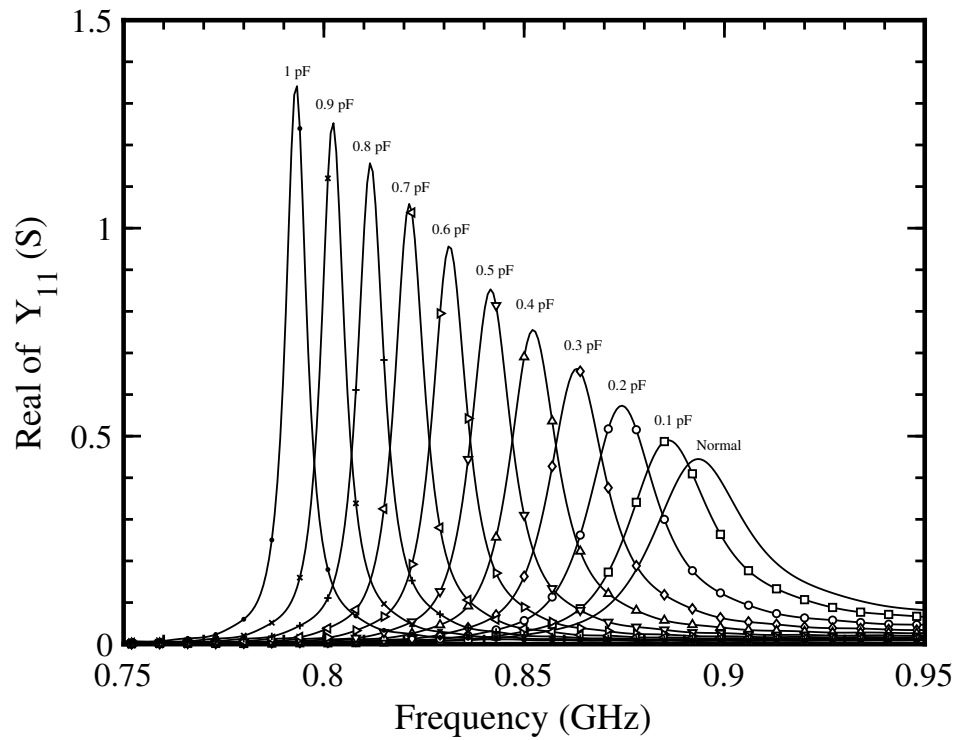


Figure 3.12: CST simulated input admittance of the capacitance sensing RFID tag (Real input admittance).

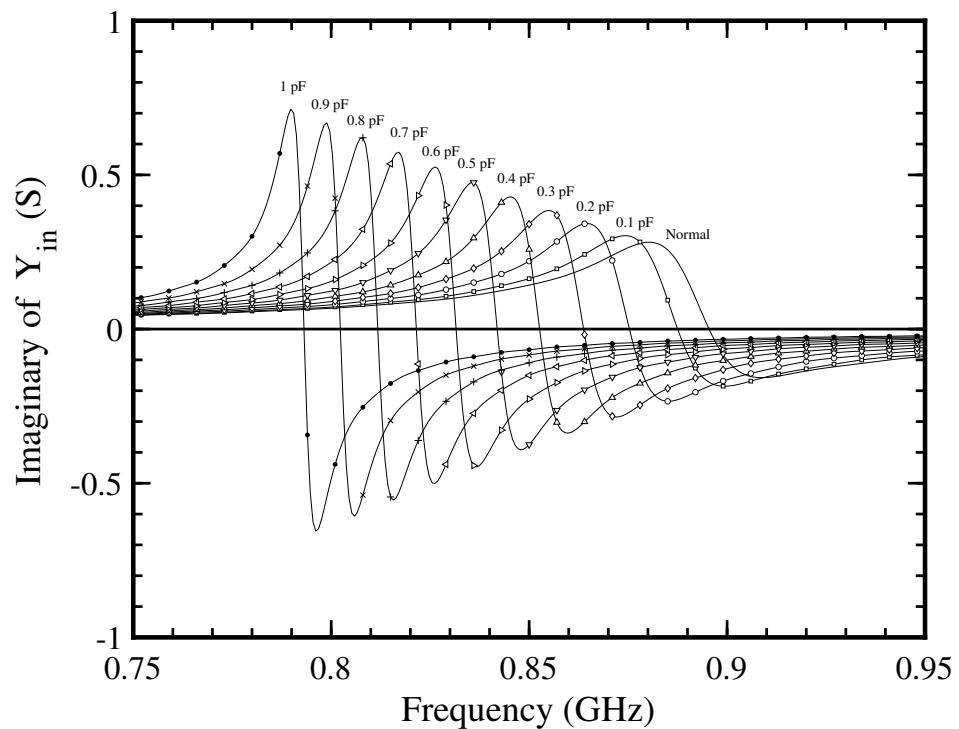
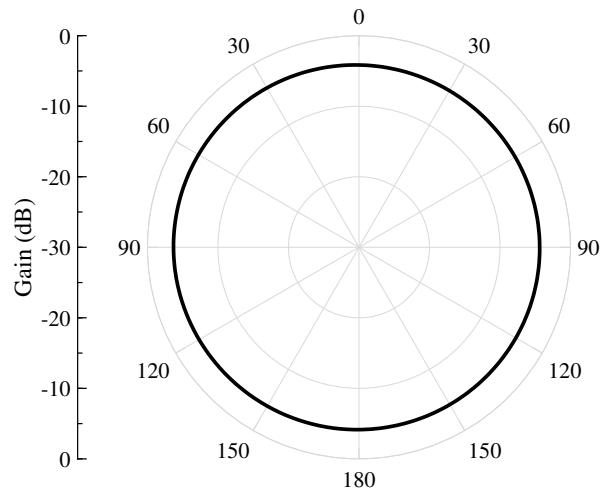


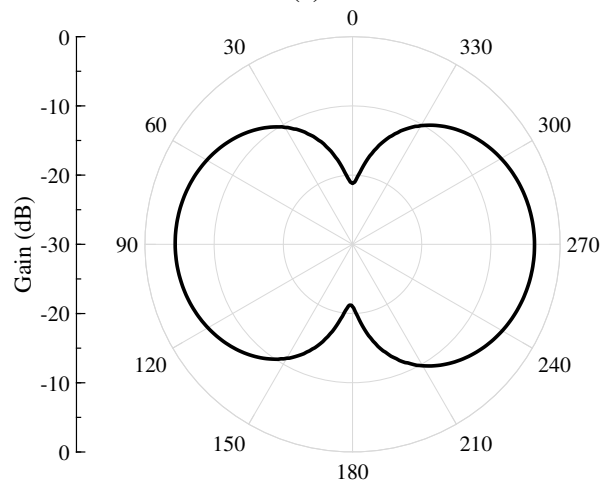
Figure 3.13: CST simulated input admittance of the capacitance sensing RFID tag (Imaginary input admittance).

Figure 3.14 displays the radiation patterns of the tag system with a realised gain of -3.95 dBi at 868 MHz. It can also be observed that the tag antenna have an omnidirectional radiation pattern in yz -plane, Figure 3.14(a). Additionally, the tag simulated radiation efficiency

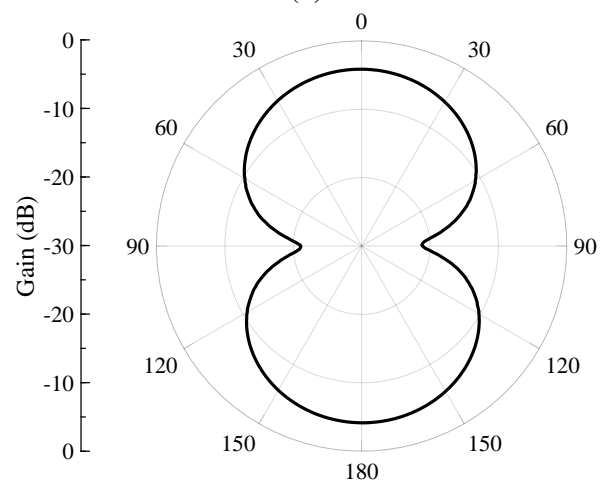
was recorded of about -0.86 dB.



(a)



(b)



(c)

Figure 3.14: Polar plot of CST simulated tag system realised gain: (a) yz -plane; (b) azimuth plane; and xz -plane.

3.6 Measurement Results

3.6.1 Capacitance to Sensor Code Relationship

To assess the performance, ten tag samples were fabricated on the Mylar substrate. Ten different capacitors in the range of 0.1 pF to 1 pF were placed across at the terminals of each tag antenna, as shown in Figure 3.9(a). The tags were interrogated by a UHF reader Tagformance Pro System, comprising of a linear polarised antenna of 6 dBi gain and placed a fixed distance of 30 cm away from the sensor [24]. The tag is capable of operation at distances greater than 30 cm, and the calibrated Tagformance system was able to assess the maximum read distance achievable in each measurement. The set up was also able to record the sensor code as well as provide tag threshold power analysis.

Firstly, the tags were measured by the Voyantic reader to obtain the sensor code values, Figure 3.16. These results demonstrate a linear relationship between the sensor value and the applied capacitance. Sensor code values of 26 and 3 were returned for zero applied reactance, and 1 pF respectively. Increasing capacitance over 1 pF falls outside the tag tuning capability and the tag frequency would deviate from 868 MHz.

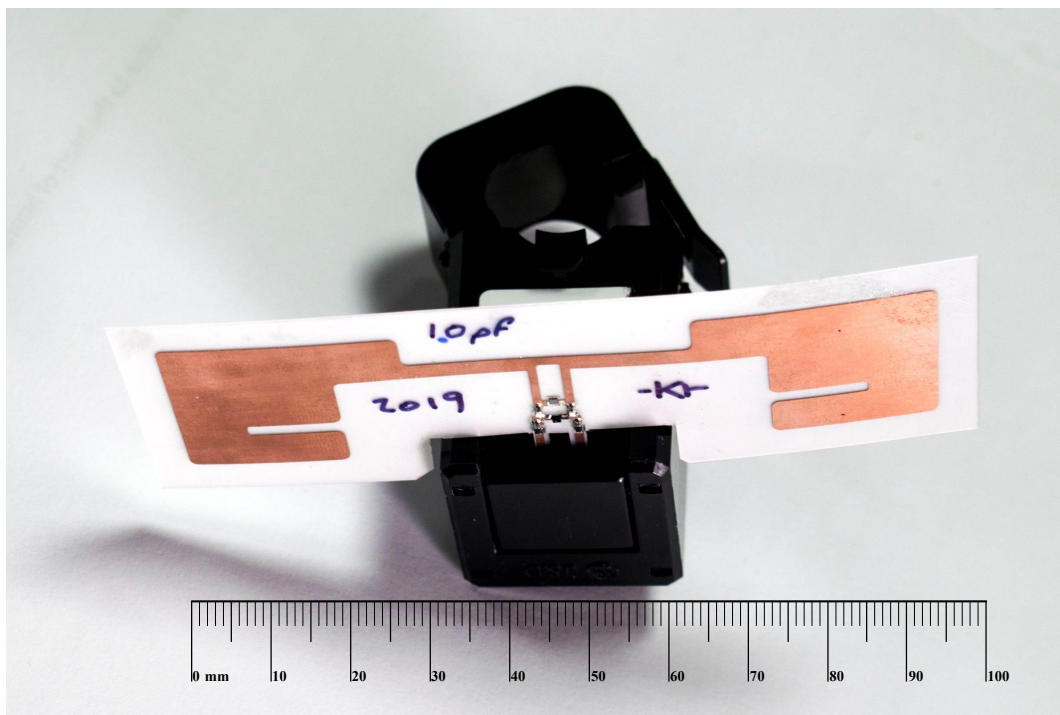


Figure 3.15: A final tested prototype of the proposed RFID ac current sensor.

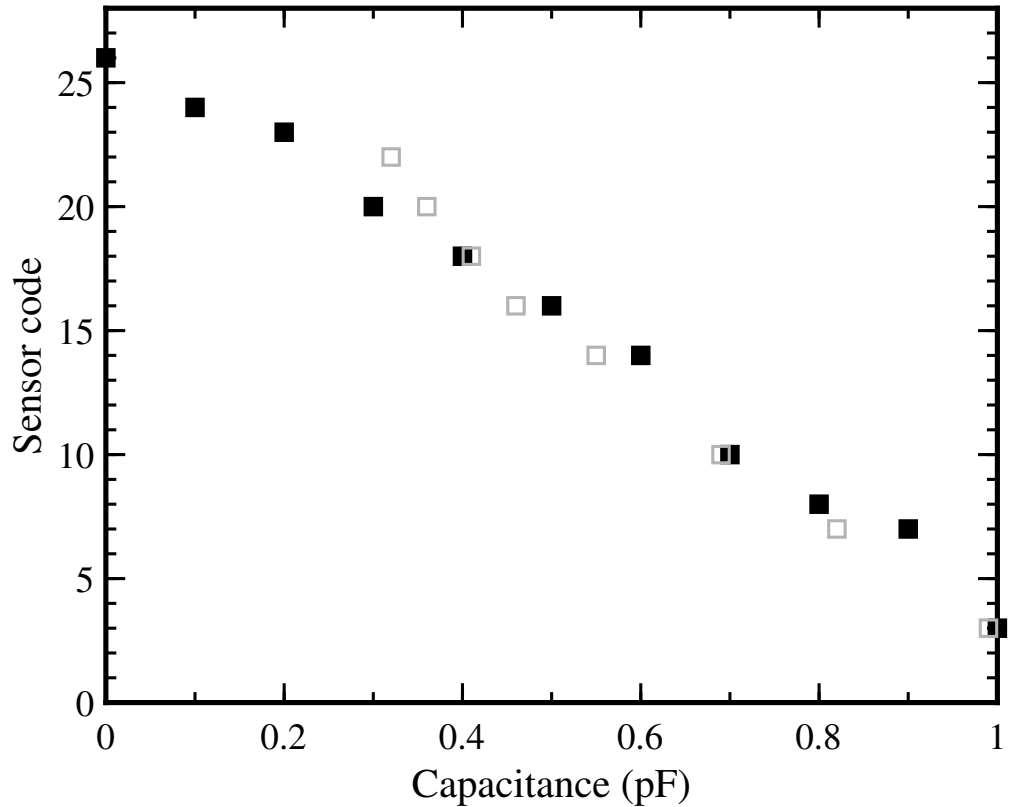


Figure 3.16: Measured sensor code of a self-tuning tag at 868 MHz. Black square markers: tag loaded with lumped capacitance in the range of 0.1 pF to 1 pF. Grey line square markers: tag with the tuning circuit.

An RFID tag was then connected to the tuning circuit, Figure 3.15. A voltage of 0 V to 10 V dc was applied to the copper straps of the tuning circuit and the sensor code was measured. The total equivalent capacitance of the varactor tuning circuit was calculated with (3.4) and is compared with the measured sensor codes in Figure 3.16. The tag response when connected to lumped capacitances is seen to agree strongly with the response to the tuning circuit reactance indicating the transducer functioned as expected. A slight difference in response of the tuning circuit to the lumped values near 0.3 pF arises from the non-linear junction capacitance of the varactor (Figure 3.7). Although this non-linearity can be compensated for, it does influence the lower limit of the sensing range. However, the overall agreement between the two measurements can be seen to be very good without the need for any complex calibration.

3.6.2 Power Cable Measurement

In the final set of experiments, the RFID tag along with the tuning circuit was linked with the CT using the copper straps and the M3 screw terminals. The magnetic circuit of the CT

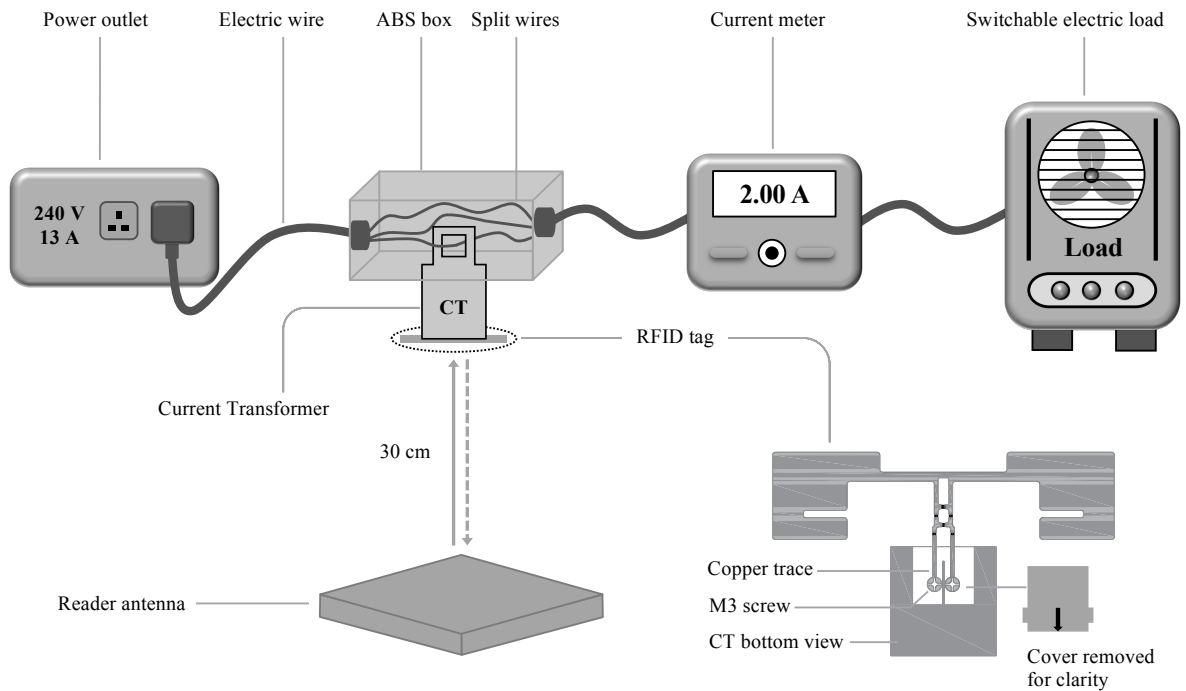


Figure 3.17: Block diagram of the measurement setup.

encircled a single split-core cable that was enclosed in an insulating box as the CT must be installed on a single live or neutral current carrying wire, Figure 3.17. The sensor response was measured with the Tagformance Pro System as described earlier. A switchable electrical heater with an adjustable load was used to test the system. The sensor tag was placed 30 cm away from the dedicated reader antenna to obtain calibrated read range results and sensor codes. A commercial Brennenstuhl PM 231 E current meter with $\pm 1\%$ accuracy [25] was used to benchmark the tag results.

3.6.3 Current to Sensor Code Relationship

Measurements were carried out for load currents ranging from 0 A to 10 A with a step of 0.1 A and each measurement were taken ten times for a single tag. Figure 3.18 illustrates the mean values of the measured sensor code and also indicates the spread for each point. The experiment was repeated with a second tag and the response was consistent. The results show that the proposed sensor can detect in the range of 2 A to 10 A with a resolution of 0.5 A. As this passive sensor operates on the principle of self-tuning variable capacitance, there is a limited tuning window to the capacitance tuning before the value starts to saturate. Therefore, where less than 2 A or more than 10 A ac current measurement is required, then the tuning circuit could be adjusted or a current transformer with a different turns ratio could

be employed.

To assess the effect of distance on the tag response, the tag system was placed at different distance intervals from the reader antenna. At 2 cm the tag response changed by approximately 3 sensor values as compared to the tag response at 30 cm distance at 868 MHz. It was observed that at 8 cm the tag response became stable i.e. same as the tag response at 30 cm distance as shown in Figure 3.19. Additionally, as the tag returns RSSI data, the reader could be programmed to compensate for non-linearity at high signal strengths.

The input impedance of the tag chip remains stable between -40°C to 85°C . According to the IEEE Std C57.13 [26], the average winding temperature of the CT must not exceed 55°C at 100% rated input current while in an average ambient temperature of 30°C . Therefore, the CT temperature is well below 85°C (considering the CT input rating of 100 A). Furthermore, the CT secondary coil is well insulated therefore the minor heat that is generated in the CT coil will not conduct to the tag chip and there is a large physical separation between the CT coil and tag chip. Hence, the input impedance will remain stable.

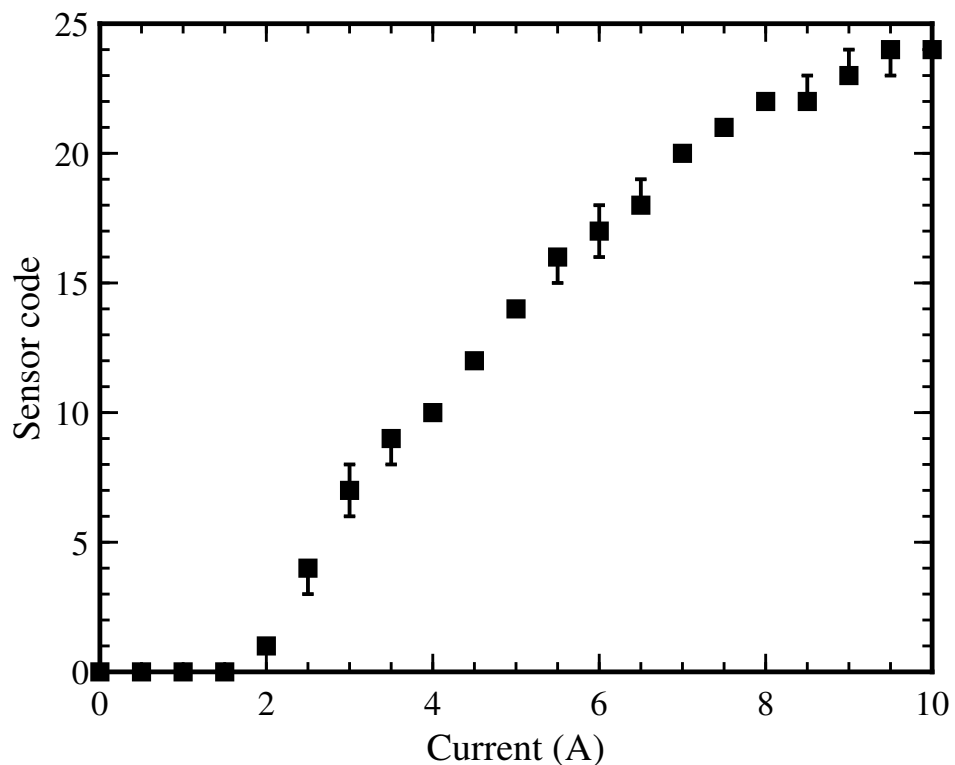


Figure 3.18: Measured sensor code of the proposed RFID ac current sensor at 868 MHz.

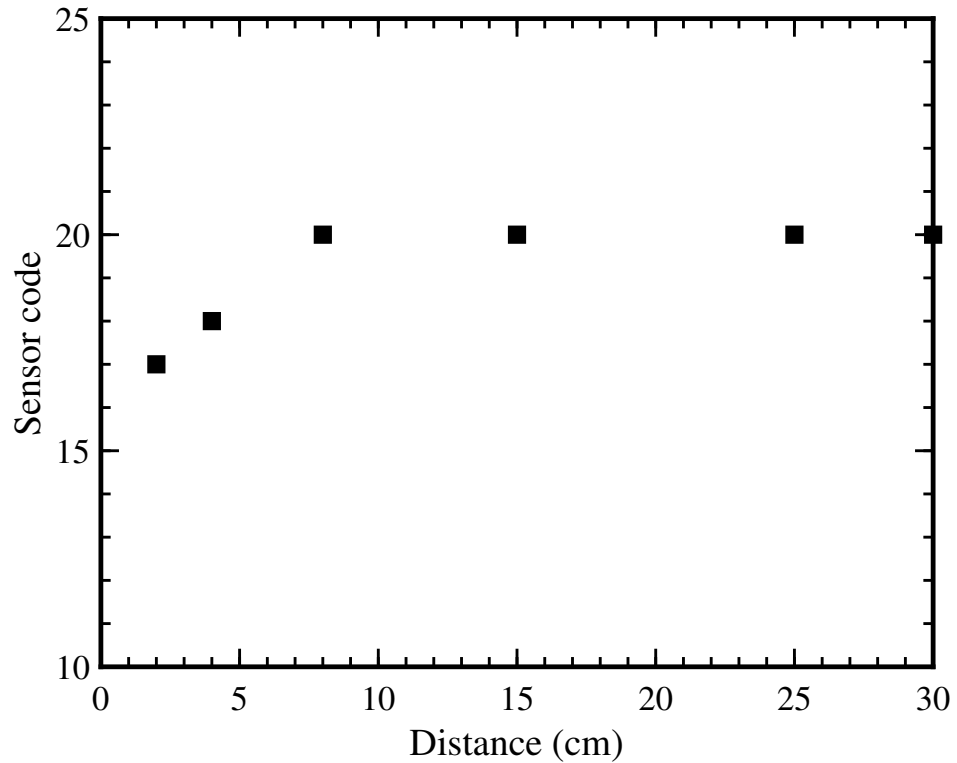


Figure 3.19: The effect of distance variation between the tag system and the reader antenna on the sensor code of the tag system at 868 MHz.

3.6.4 Read Range

Figure 3.20 shows the maximum read range of the sensor to be 3.5 m to 4 m across all readings. The lowest read range was recorded at 0 current because the tag is out of tuning range and the antenna power transfer coefficient τ decreases. The read range can be calculated by using the well-known Friis free-space formula:

$$r_{max} = \frac{c}{4\pi f} \cdot \sqrt{\frac{EIRP \cdot G_r \cdot \tau}{P_{IC}}} \quad (3.10)$$

where c is the speed of light and f is operating frequency in hertz (Hz). $EIRP$ is the Equivalent Isotropic Radiated Power, depending on the local regulation (3.28 W in Europe and 4 W in the US), G_r is the tag antenna gain and τ is $1 - |S|^2$, where S is referring to the reflection coefficient. P_{IC} represents the sensitivity of the tag chip. Simulation of the tag antenna mounted directly on the current detector unit showed the tag realized gain (including input reflection loss) to be -3.95 dBi, and the S_{11} value at 868 MHz was -1.6 dB before the tag autotunes to improve the match. For the specified chip turn on power of -16 dBm, the calculated read range was 4.6 m which agrees well with measurement. Purposely, the tag

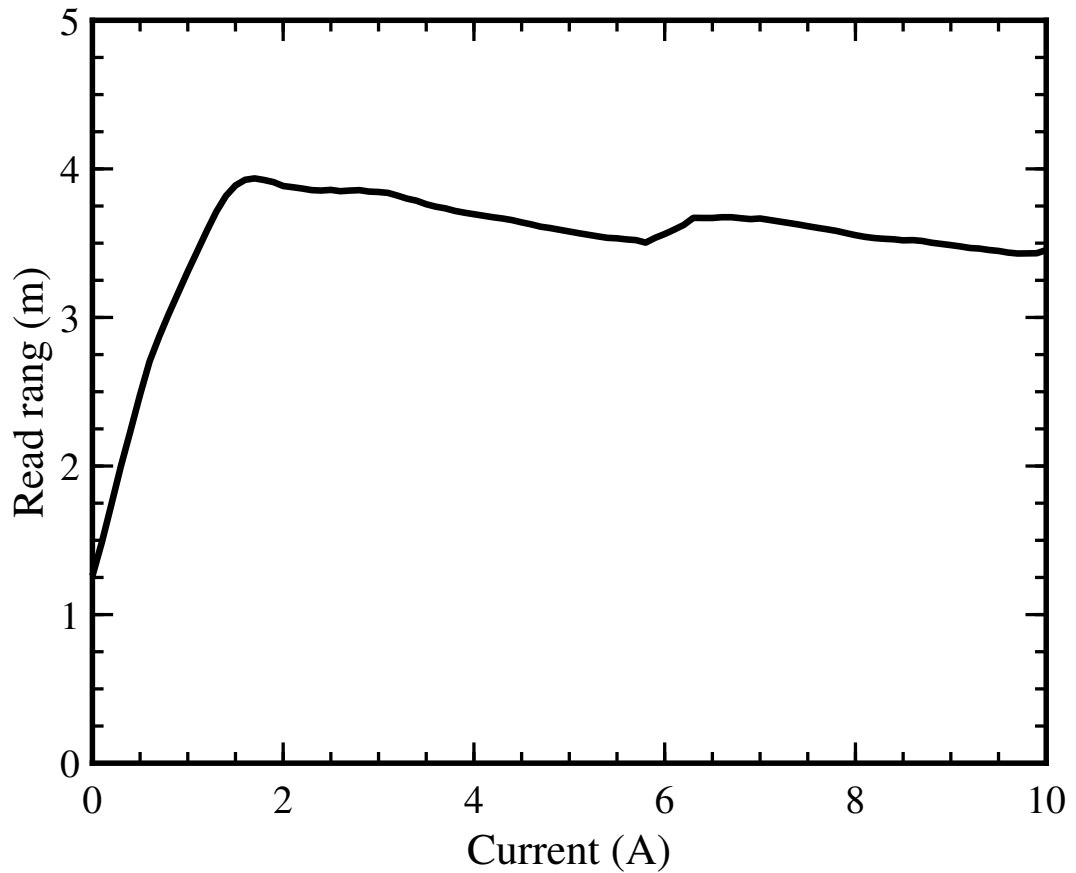


Figure 3.20: Read range of the proposed RFID ac current sensor at 868 MHz.

resonance frequency was slightly shifted from 868 MHz to effectuate maximum possible sensing range (0 to 31) of the tag at 868 MHz. The tag resonance frequency was compensated by changing the value of the inductor to 47 nH of the tuning circuit as inductance influences the tag resonance frequency. As inductance disrupts the surface current distribution of the tag resulting in a change in the tag resonance frequency.

3.6.5 Rise and Fall Time

To assess if the tag sensor sample rate was sufficient to track a switching response in the test load, the electrical load was switched at 0.5 Hz by a Solid State Relay (SSR) [27] controlled by a microcontroller and linked to the ThingMagic M6e RFID reader [28] as shown in Figure 3.21. A custom software application on the ThingMagic API synchronised the Tag Memory read function with the SSR toggle status obtained from the microcontroller serial output. This enabled the logging of the rise and fall time of the load current. The time taken by the waveform to reach 90% of the peak was defined as the rise time under loaded (ON) condition, and the fall time for the unloaded (OFF) condition was the period taken to fall

90% from the maximum. Figure 3.22 shows the switched waveform obtained from the tag with rise and fall times of 368 ms and 276 ms respectively. Occasionally, the reader will drop an initial read cycle and if this occurs, reading the subsequent data packet takes longer according to the RFID EPC GEN2 protocol. As a consequence, the sample period of the sensor varied between 30 ms and 61 ms, though this was adequate to capture the switching waveform. There is also an inherent delay between requesting and receiving samples which varies from a few to a dozen milliseconds. This is caused by factors including the SSR response time of 10 ms, the time taken by the RFID reader to detect, read and request the sensor data and also the time taken between sending and receiving commands from computer to microcontroller and vice versa via a USB serial port.

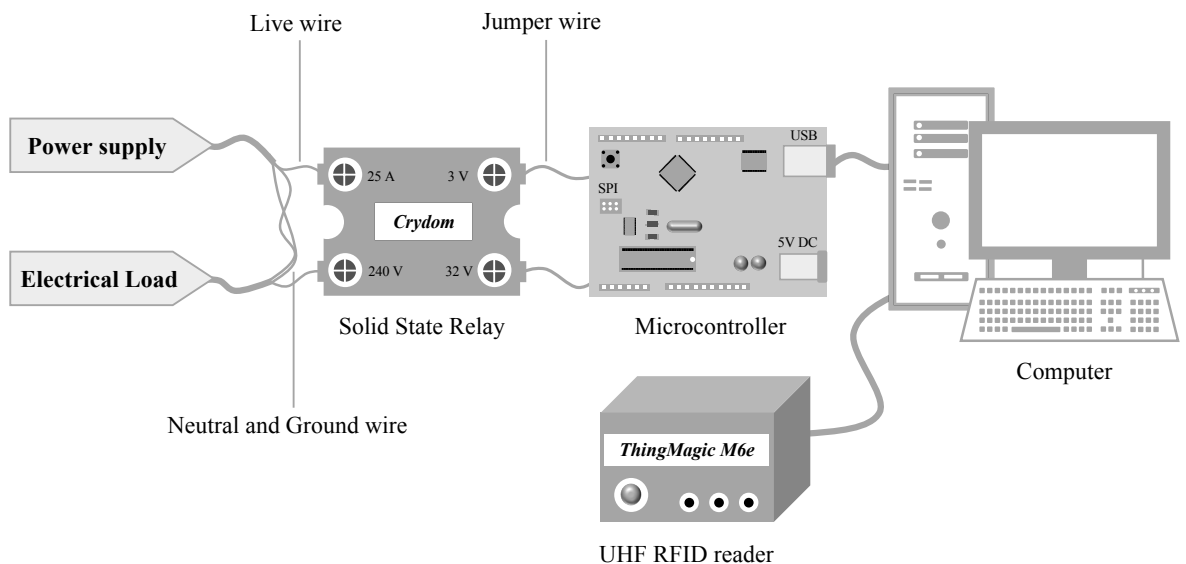
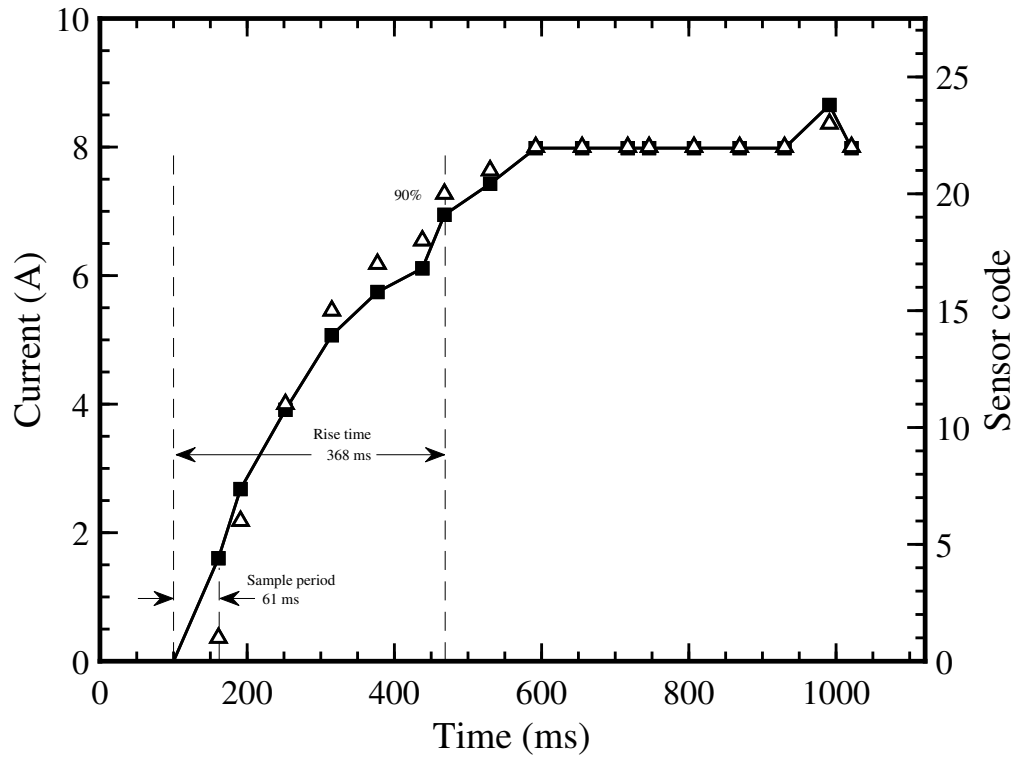


Figure 3.21: Sensing set up for measuring the rise and fall time of a switching load current.

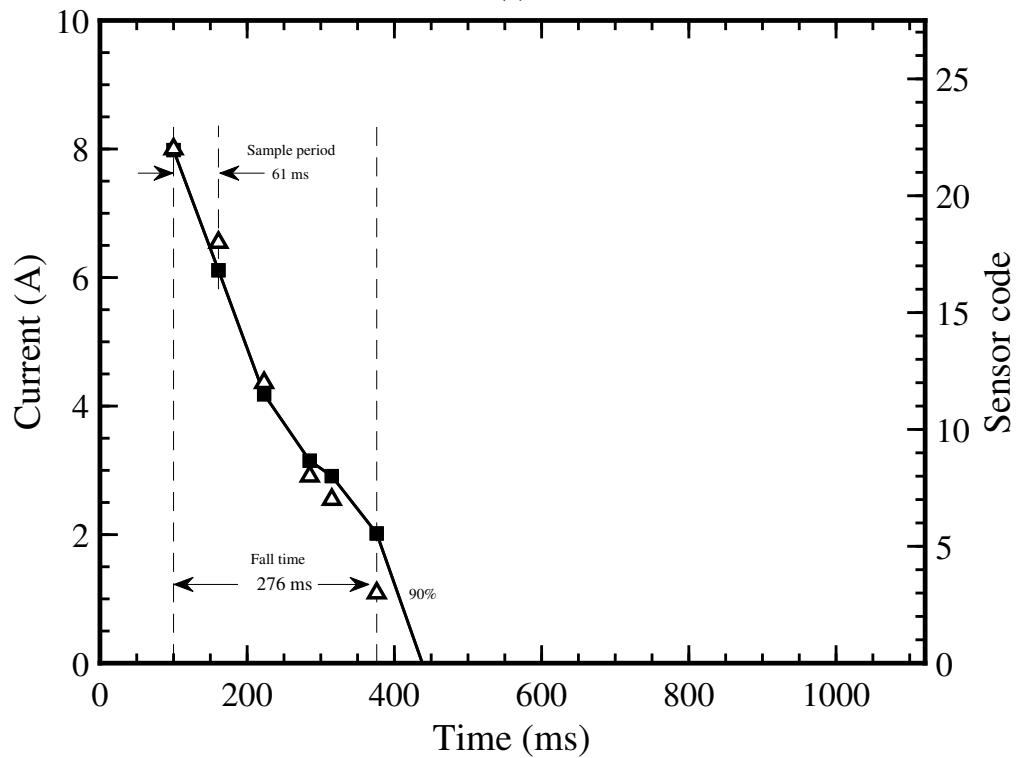
3.6.6 Sensor Comparison

Table 4.13 shows the comparison of the proposed tag system with the commercial alternative ac current meters. The total cost of the tag device is inclusive of the cost of the CT (\$45.00) and the estimated cost of the tag (\$5.00). In order to be cost-effective for a domestic setting the RFID reader should be redeveloped for domestic use and price range.

The proposed tag structure is less complex than the alternatives, and provides a cost-effective solution for power monitoring when many tags on individual appliances communicate wirelessly with a centrally mounted single RFID reader in the views of the tags to be read. The tag offers a solution for small current measurements in the range of 2 A to 10 A



(a)



(b)

Figure 3.22: Rise time and fall time of the RFID ac current sensor at 868 MHz. Triangle markers represent sensor code measured by the sensor and black solid line with square markers represent load current reconstructed from sensor code. (a) Rise time (368 ms); (b) Fall time (276 ms).

without requiring a microcontroller, and which harvests energy from the interrogator radio wave in the read range of about 4 m

Table 3.1: Comparison between the proposed tag system and commercial alternative ac current meters in terms of communication, cost, current range and power type.

Ref.	Sensors	Communication	Cost (\$)	Current Range (A)	Power Type
[9]	IoT long range wireless ac current monitor	DigiMesh protocol	179.95	0–100	Active
[10]	Alta wireless ac current meter - 20 A - AA battery powered	Monnit proprietary protocol	150.00	0–20	Active
[11]	Pressac current sensor: one channel	EnOcean wireless radio protocol	98.00	0–60	Passive
[29]	SCT-125W-100 by Mag-nelab	IEEE 802.15.4, 2.4 GHz technology	245.00	0–100	Active
[30, 31]	AC power meter	Universal serial bus	–	0–100	Active
[32]	Web based smart meter	WiFi network	–	0–100	Active
[33]	Piezoelectromagnetic wireless current monitoring system	Digi XBee radio	–	0–20	Active
[34]	Smart power meter	Wired network	–	0–20	Active
–	Proposed tag system	Radio frequency Identification	50.00	2–10	Passive

3.7 Conclusion

A new RFID current sensor using an electronic tuning technique has been developed and experimentally tested with an electrical load. The device can detect ac current in the range of 2 A to 10 A from an ac electrical cable in smart power monitoring systems. The rise and fall times of the sensing tag is 368 ms and 276 ms respectively. The suggested mechanism could be modified for detecting currents lower than 2 A or higher than 10 A depending on the requirements of an application by altering the transformer turns ratio and tuning circuit. The proposed device is passive with a read range of about 4 m and is cost-effective for multiple appliance monitoring through a single reader as opposed to more accurate, but relatively

expensive single point smart meters.

In this work, we have not considered the wider metering system that the tag sensor would be connected to. It may be necessary to develop new metering methods in order to log and display the simultaneous consumption of multiple appliances. The tags could be deployed in modified plugs or as inline cable devices. The reader would be centrally mounted with a view of the tags to be read.

Future work includes creating a new tag antenna design to be integrated with the CT housing in a compact form. The main aim will be to reduce the overall size of the tag system to make it suitable for use in a location or environment where a compact device is usually required.

The main contribution of this chapter has been,

- Design of a tuning circuit for tuning a tag antenna input impedance.
- Investigate self-tuning characteristics of the Axzon Magnus S2 tag chip.
- Optimisation of an RFID tag antenna for a current transformer.
- The development of a novel RFID ac current sensing technique.

In the next chapter, an optimum tag antennas for a current transformer is introduced.

References

- [1] I. Ullah, R. Horne, B. Sanz-Izquierdo and J. C. Batchelor, “RFID AC Current Sensing Technique,” in *IEEE Sensors Journal*, vol. 20, no. 4, pp. 2197–2204, Feb.15, 2020, doi: 10.1109/JSEN.2019.2949856.
- [2] A. Louzir, R. Kumar and J. -Y. L. Naour, “RFID based solution for the sensing of home electrical devices activity,” in *Proc. ISAP*, Okinawa, Japan, 2016, pp. 1002–1003.
- [3] R. Kumar, A. Louzir and J. -Y. L. Naour, “RFID helix antenna on power cord for the sensing of home electrical devices activity,” in *Proc. EUCAP*, Paris, France, 2017, pp. 2554–2558.
- [4] R. Kumar, A. Louzir and J. -Y. L. Naour, “RFID tag coupled with a magnetic sensor for wireless sensing of home electrical devices,” in *Proc. EuMC*, Madrid, Spain, 2018, pp. 981–984.
- [5] K. -L. Chen, Y. -R. Chen, Y. -P. Tsai, N. Chen, “A novel wireless multifunctional electronic current transformer based on ZigBee-based communication,” in *IEEE Trans. Smart Grid.*, vol. 8, no. 4, pp. 1888–1897, Mar. 2016.
- [6] CLEODE (2019, Feb. 10). ZPlug Boost [Online]. Available: <http://www.cleode.fr/en/produits.php?page=zplug>
- [7] S. DeBruin, B. Campbell, and P. Dutta, “Monjolo: an energy-harvesting energy meter architecture,” in *SenSys’13*, Roma, Italy, Nov. 2013, pp. 18:1–18:14.

- [8] T. Hosseinimehr, and A. Tabesh, "Magnetic field energy harvesting from AC lines for powering wireless sensor nodes in smart grids," in *Opt. Lett.*, vol. 63, no. 8, pp. 4947–4954, Feb. 1986.
- [9] NCD (2019, Aug. 26). IoT long range wireless ac current monitor [Online]. Available: <https://store.ncd.io/product/wireless-ac-current-monitor/>
- [10] Monnit (2019, Aug. 26). Alta wireless ac current meter - 20 A - AA battery powered [Online]. Available: <https://www.monnit.com/Product/MNS2-9-W2-CM-020/>
- [11] Pressac (2019, Aug. 26). Current sensor: one channel [Online]. Available: <https://www.pressac.com/current-monitoring-sensors/>
- [12] M. C. Caccami and G. Marrocco, "Electromagnetic modeling of self-tuning RFID sensor antennas in linear and nonlinear regimes," in *IEEE Trans. Antennas Propag.*, vol. 66, no. 6, pp. 2779–2787, Jun. 2018.
- [13] K. Zannas, H. El Matbouly, Y. Duroc and S. Tedjini, "Self-tuning RFID tag: a new approach for temperature sensing," in *IEEE Trans. Microw. Theory Techn.*, vol. 66, no. 12, pp. 5885–5893, Dec. 2018
- [14] Smartrac-group (2019, Feb. 10). AN-FAM1601: passive sensors technical guide [Online]. Available: <https://www.smartrac-group.com>
- [15] Axzon Sensing Data Insights (2020, Apr. 01). Chameleon Sensor Engine [Online]. Available: <http://rfmicron.com/technology/chameleon/>
- [16] Magnelab (2019, Feb. 10). DCT-0016-10/10Vdc split-core current sensor [Online]. Available: <http://www.magnelab.com/products/ac-splitcore-current-sensor-dct-0016-100/>
- [17] K. L. Williams, "Fundamentals of current transformers," in *Proceedings: Electrical Electronics Insulation Conference and Electrical Manufacturing & Coil Winding Conference*, Rosemont, IL, USA, 1995, pp. 23–25. doi: 10.1109/EEIC.1995.482331
- [18] Skyworks (2019, Feb. 5). SMV2019 series hyperabrupt junction tuning varactors [Online]. Available: https://www.skyworksinc.com/Product/668/SMV2019_Series

- [19] Skyworks (2020, Mar. 20). The Nuts and Bolts of Tuning Varactors [Online]. Available: <https://www.skyworksinc.com/>
- [20] Skyworks, "SMV2019 to SMV2023 series: hyperabrupt junction tuning varactors," SMV2019 to SMV2023 varactors datasheet, Aug. 2015.
- [21] Axzon (2019, Feb. 10). RFM2100 wireless flexible moisture sensor [Online]. Available: <https://axzon.com/rfm2100-wireless-flexible-moisture-sensor/>
- [22] Computer Simulation Technology (CST) Microwave Suite 2017. [Online]. Available: <https://www.cst.com>
- [23] Ahson, Syed A., and Mohammad Ilyas. "RFID Handbook: Applications, Technology, Security, and Privacy," CRC press, 2017.
- [24] Voyantic (2019, Feb. 10). Tagformance Pro [Online]. Available: <http://voyantic.com/products/tagformance-pro>
- [25] Brennenstuhl smart technology (2018, Feb. 9). Primera-line wattage and current meter PM 231 E [Online]. Available: <https://www.brennenstuhl.co.uk/en-GB/products/adapter-plugs/primera-line-wattage-and-current-meter-pm-231-e-gb>
- [26] IEEE standards association (2019, Aug. 25). IEEE C57.13–2016 - IEEE Standard Requirements for Instrument Transformers [Online]. Available: https://standards.ieee.org/standard/C57_13-2016.html
- [27] Crydom GN Series (2019, Feb. 10). Panel mount easy pick: 84134210 [Online]. Available: <http://www.crydom.com/en/products/panel-mount/easy-pick/84134210/>
- [28] JadaK tech (2019, Feb. 10). ThingMagic M6e RFID [Online]. Available: <https://www.jadaktech.com/products/rfid/embedded-uhf-rfid-readers/mercury6e-m6e/>
- [29] Magnelab (2019, Aug. 26). SCT-125w-100 by Magnelab [Online]. Available: <https://www.magnelab.com/products/wireless-ac-current-sensor-system-sct-125w/>
- [30] N. Tamkittikhun, T. Tantidham and P. Intakot, "AC power meter design based on Arduino: Multichannel single-phase approach," in *2015 International Computer Science*

- and Engineering Conference (ICSEC)*, Chiang Mai, 2015, pp. 1–5, doi: 10.1109/IC-SEC.2015.7401422.
- [31] N. Tamkittikhun, T. Tantidham and P. Intakot, “AC power meter design for home electrical appliances,” in *2015 12th International Conference on Electrical Engineering/Electronics, Computer, Telecommunications and Information Technology (ECTI-CON)*, Hua Hin, 2015, pp. 1–6, doi: 10.1109/ECTICon.2015.7207005.
- [32] S. Yildiz and M. Burunkaya, “Web Based Smart Meter for General Purpose Smart Home Systems with ESP8266,” in *2019 3rd International Symposium on Multidisciplinary Studies and Innovative Technologies (ISMSIT)*, Ankara, Turkey, 2019, pp. 1–6, doi: 10.1109/ISMSIT.2019.8932931.
- [33] Q. R. Xu, I. Paprotny, M. Seidel, R. M. White and P. K. Wright, “Stick-On Piezoelectromagnetic AC Current Monitoring of Circuit Breaker Panels,” in *IEEE Sensors Journal*, vol. 13, no. 3, pp. 1055–1064, March 2013, doi: 10.1109/JSEN.2012.2234738.
- [34] R. Morello, C. De Capua, G. Fulco and S. C. Mukhopadhyay, “A Smart Power Meter to Monitor Energy Flow in Smart Grids: The Role of Advanced Sensing and IoT in the Electric Grid of the Future,” in *IEEE Sensors Journal*, vol. 17, no. 23, pp. 7828–7837, 1 Dec.1, 2017, doi: 10.1109/JSEN.2017.2760014.

Optimum RFID Tag Antenna Design

4.1 Introduction

THIS chapter reviews a new tag antenna design for an RFID ac current sensing system. The new tag antenna design is created to bent around the current transformer housing to achieve a compact form integration with the current transformer while maintaining the tag link. To do so, the overall size of the proposed tag system is reduced by half compared to the previously proposed tag system [1]. Three prototypes of the tag antenna were tested to validate the battery-free compact tag that streams current measurement data over a read range of about 3 m to 5 m using the European RFID UHF band at 868 MHz. The tag and antenna were experimentally tested with a switchable electrical load, and the measured results show that the sensing tag can detect ac current in the range of 1 A to 13 A with a resolution of 0.5 A. The tag could be used for wirelessly sensing the load current of an individual domestic appliance and where a single reader could simultaneously monitor multiple tags, enabling smart reading of electricity consumption across multiple devices in smart homes. The remainder of the chapter is organised as follows: Section 4.2 outlines the flow diagram of the proposed tag antenna design. A novel RFID tag antenna design for the current transformer is proposed in Section 4.3. The tag antenna design is further optimised for the current transformer and reported in Section 4.4 and Section 4.5. Finally, Section 4.6 concludes the chapter.

4.2 Flow Diagram of Tag Antenna Design

Figure 4.1 illustrates the design process of the tag antenna for the current transformer. The antenna design process includes five main stages: (i) Choose the antenna type and specify the parameters, (ii) The tag antenna is designed in EM simulator. The antenna design is simulated until a good match is achieved between the antenna and the chip at 868 MHz. (iii) A transformer design is included in the simulation to evaluate the tag antenna performance. The resonance frequency of the antenna is shifted from the central frequency, and thus more simulations are performed to optimised the tag performance at 868 MHz. (iv) The antenna terminals are coupled with the tuning circuit and simulated again. (v) A final tag antenna design is etched on a substrate and experimentally investigated with the RFID interrogator. The measured results are compared with the simulated results to prove the proposed concept of the tag antenna design. For the sake of simplicity, the transformer design was not included in the simulation at stage (ii) because the simulation will run faster without including a complex structure like a transformer which takes hours to be simulated.

4.3 Tag Antenna Design

The tag antenna was designed to achieve compact physical integration with the transformer housing, as well as achieve a good read range. The antenna design has a square form factor with a central space for the transformer, as depicted in Figure 4.2 [2]. The design consists of two radiating arms bent around the transformer. The total length of the antenna is 0.137λ and with the total width of 0.141λ at 868 MHz. There is a 0.091λ long and 0.095λ wide slot occupied for the transformer. The antenna was simulated with computer simulation technology (CST) Microwave Studio [3]. The simulation included the Mylar substrate with a dielectric constant (ϵ_r) of 2.8, loss tangent ($\tan \delta$) of 0.003 and thickness of 0.18 mm including the copper thickness of 0.04 mm [4].

Table 4.1: Feed loop dimensions of the tag antenna.

Parameters (mm)	l	w	t
	4	5	6

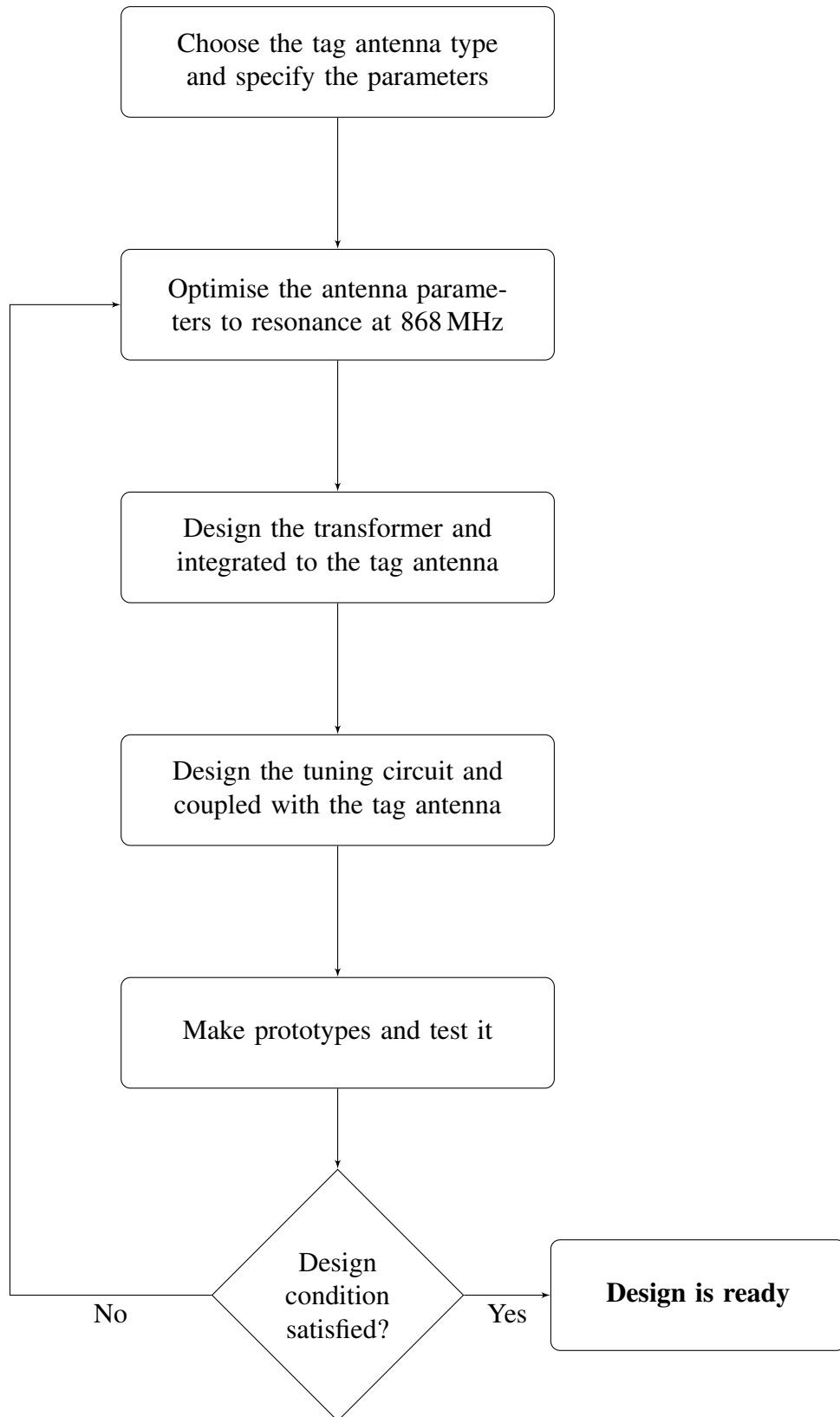


Figure 4.1: Design process of the tag antenna design for the current transformer.

The feed loop is 4 mm long and 5 mm wide, where the port is created. By changing either the length or the width of the loop, the resonance frequency of the tag antenna will change significantly. Such as, by decreasing the width of the loop will cause to shift the resonance frequency of the tag to high frequency, and vice versa. However, if the size of

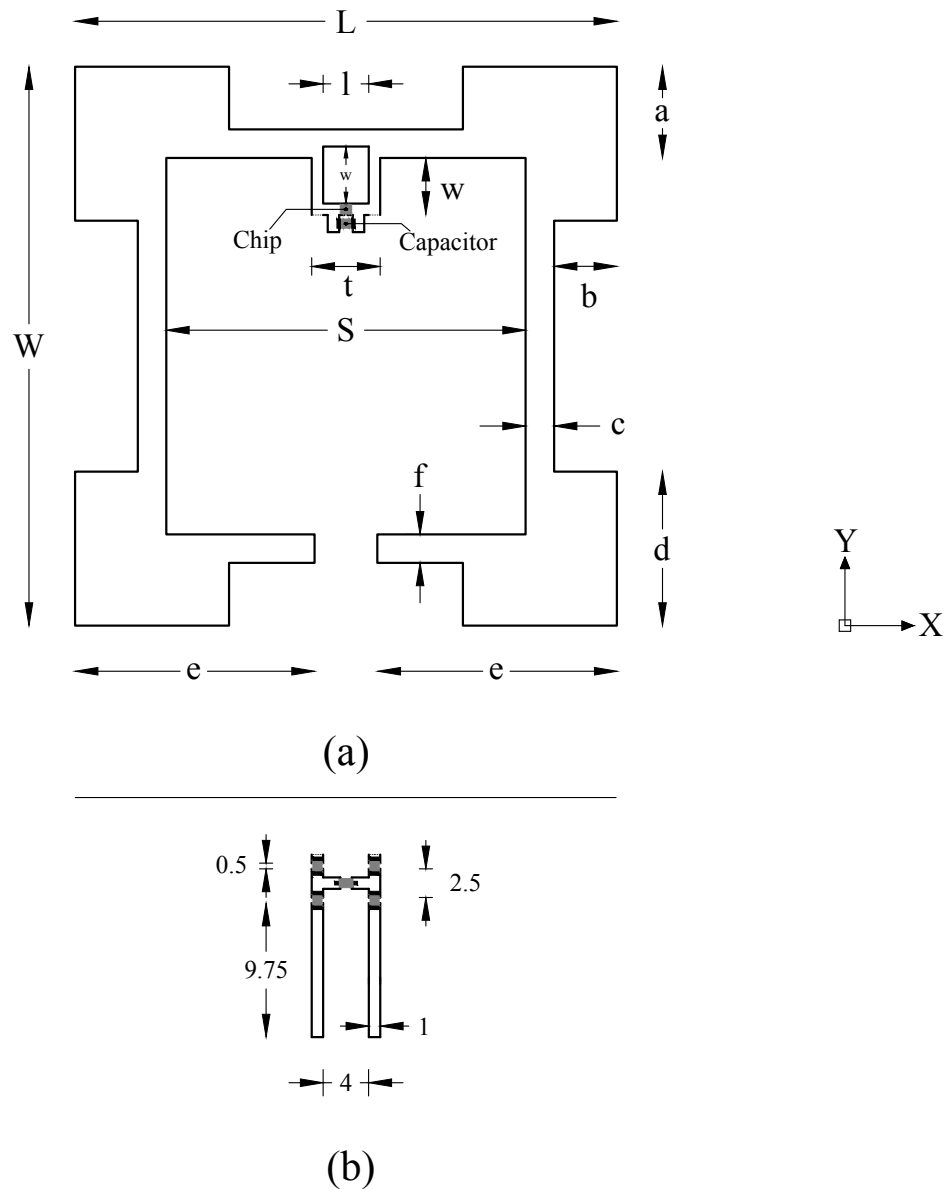


Figure 4.2: (a) Proposed tag antenna design; and (b) tuning circuit with dimensions in mm.

the feed loop is changed, then the antenna dimensions need to optimise to find the best match with chip impedance at the required frequency. The RFMicron S2 chip [5] requiring input power -16 dBm and the impedance of 2 pF to 3 pF in parallel with 2284Ω was used in simulation for designing the tag antenna. The chip covers all worldwide UHF bands (860–960 MHz). The total capacitance of 3 pF for the tag antenna design was derived from (3.5). Therefore, for simulations, the antenna impedance was matched with the microchip impedance of $1.63 \Omega - j 61.07 \Omega$, at 868 MHz. For the simplicity, a capacitor of 0.3 pF was attached right across the antenna terminals which represents the minimum capacitance of the tuning circuit. The tag antenna is formed of balanced lines wrapped around transformer housing occupies a small area of $47.5 \times 49 \text{ mm}^2$ when compare to the tag antenna design

Table 4.2: Simulated tag antenna dimensions.

Parameters (mm)	L	W	S	a	b	c	d	e	f
	47.5	49	31.5	8	5.5	2.5	13.5	21	2.5

proposed in Chapter 1 which occupies area of $94 \times 24 \text{ mm}^2$.

The CT design [7], as shown in Figure 4.3, was modelled in CST Microwave Studio. The external dimensions of the CT are $29.5 \times 31 \times 55 \text{ mm}^3$. There is a PET enclosure with a sheet thickness of 2 mm used to cover the inside components of the CT. The inside components of the CT design consist of: (i) two U shape ferrite cores; (ii) a secondary winding made of the perfect electric conductor (PEC); (iii) a printed circuit board (PCB) made of flame retardant 4 (FR4) substrate; and (iv) polyethylene terephthalate (PET) plastic used for the CT housing, as well as to support and insulate the inside components of the CT. The size of the U core is $26 \times 14 \times 16.5 \text{ mm}^3$. A PEC with the size of $19 \times 9 \times 20.5 \text{ mm}^3$ was attached to the bottom U core representing the secondary coil of the transformer. An FR4 substrate with the size of $21 \times 18.5 \times 1.6 \text{ mm}^3$ is located below the secondary coil, to which the output of the secondary winding and the M3 screw terminals are connected. All dimensions of the CT were practically measured because the datasheet of the CT lacks the dimensions of the internal parts of the CT. The material properties of the internal components of the transformer are given in Table 4.3.

Table 4.3: Material properties of the ferrite core, FR4, and PET substrate used to modelled the CT design in CST.

Material	Relative permittivity (ϵ_r)	Relative Permeability (μ_r)	Loss tangent ($\tan \delta$)
Ferrite core	1	50	0.003
FR4	4	1	0.02
PET	2.8	1	0.002

4.3.1 Simulation Results

The tag antenna was simulated in three states: (i) an independent antenna with a 0.3 pF capacitor attached across the terminals; (ii) an antenna with a 0.3 pF capacitor attached across

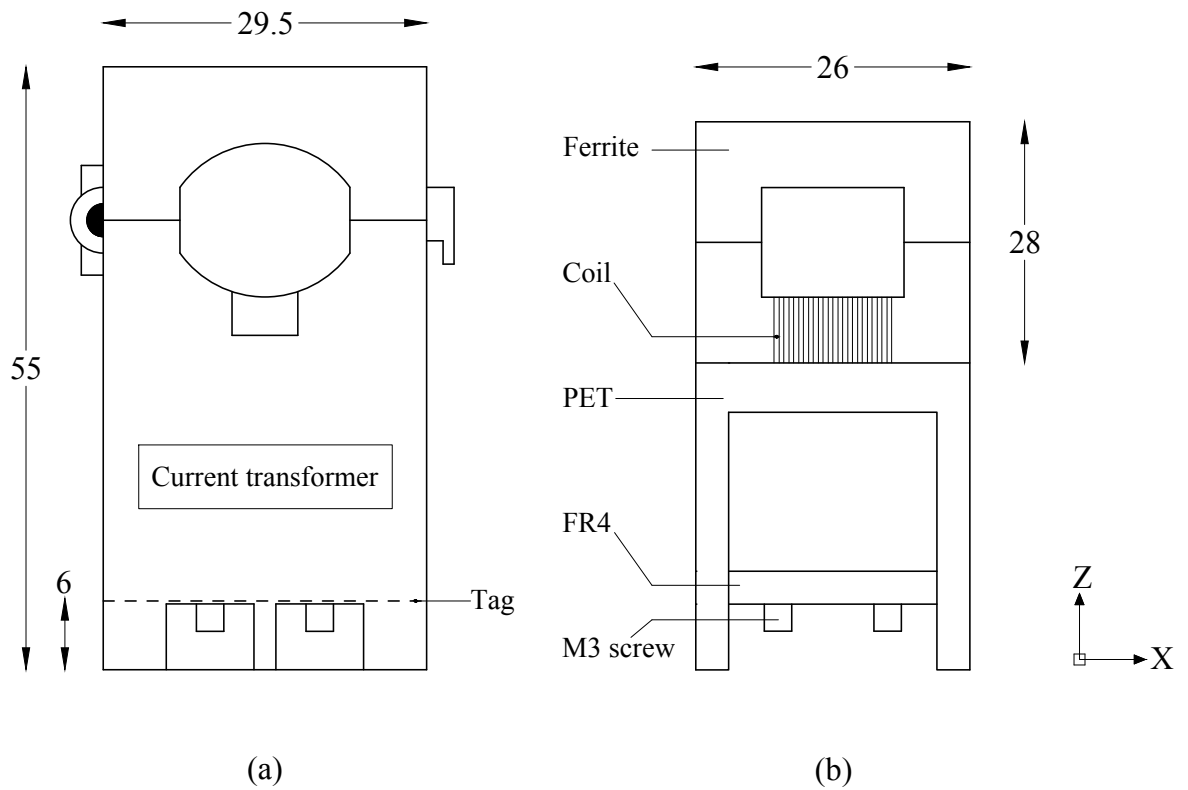


Figure 4.3: A current transformer design used for simulations in CST; (a) CT outside housing; and (b) CT inside components. (All dimensions are in mm)

the terminals and mounted at the bottom of the CT; and (iii) the antenna terminals linked with tuning circuit (set the total capacitance of the circuit to 0.3 pF) and mounted at the bottom of the CT. When the independent tag antenna, Figure 4.2(a) was simulated, a good match was achieved at the UHF RFID band with the S_{11} of -23 dB at 862 MHz, as illustrated in Figure 4.5. To assess the impact of the CT on the tag antenna performance, the current transformer was included in the antenna model in CST, Figure 4.3 and the tag antenna design Figure 4.2 was attached to the bottom of the transformer. The simulated results show that the resonance frequency of the tag shifted from 862 MHz to 838 MHz when the tag antenna was attached to the bottom of the CT. Finally, the tag in Figure 4.2(a) and the tuning circuit in Figure 4.2(b) were linked and integrated with the transformer. It is observed that the resonance frequency of the tag remains stable when the tag was coupled with the tuning circuit. The reflection coefficient S_{11} of the normal tag, the tag mounted on the CT and the tag coupled with the tuning circuit is illustrated in Figure 4.5.

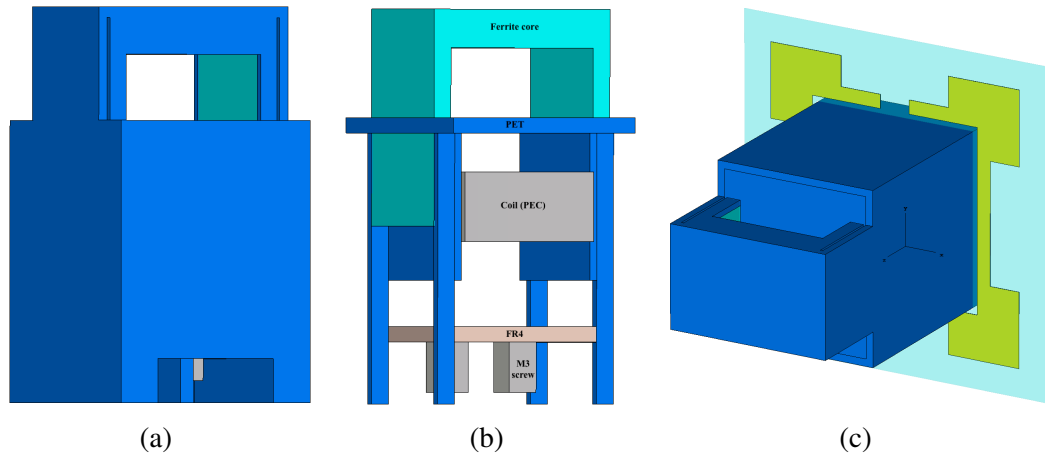


Figure 4.4: 3D model of the proposed tag antenna attached to the bottom of the transformer. (a) current transformer, (b) components inside current transformer, and (c) tag antenna attached to the transformer.

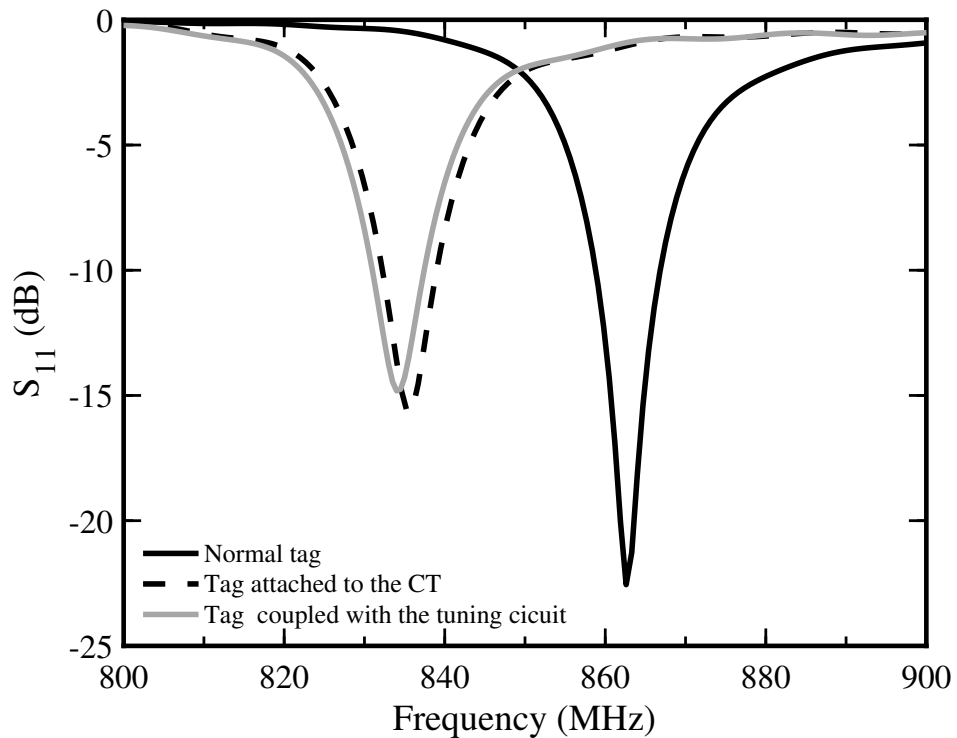


Figure 4.5: CST simulated power reflection coefficient of the RFID tag.

Furthermore, the material properties of the PET, PEC and FR4 are well known. However, the relative permeability of the ferrite core may vary depending on the materials used to make the ferrite core, such as nickel zinc ferrite and manganese zinc ferrite. The data sheet of the transformer does not include the material properties of the ferrite core. Therefore, to analyse the effect of relative permeability of the ferrite on the reflection coefficient of the tag antenna, simulations were performed to evaluate the antenna performance. Figure 4.6 illustrates the reflection coefficient of the tag when the relative permeability of the ferrite varies from 10

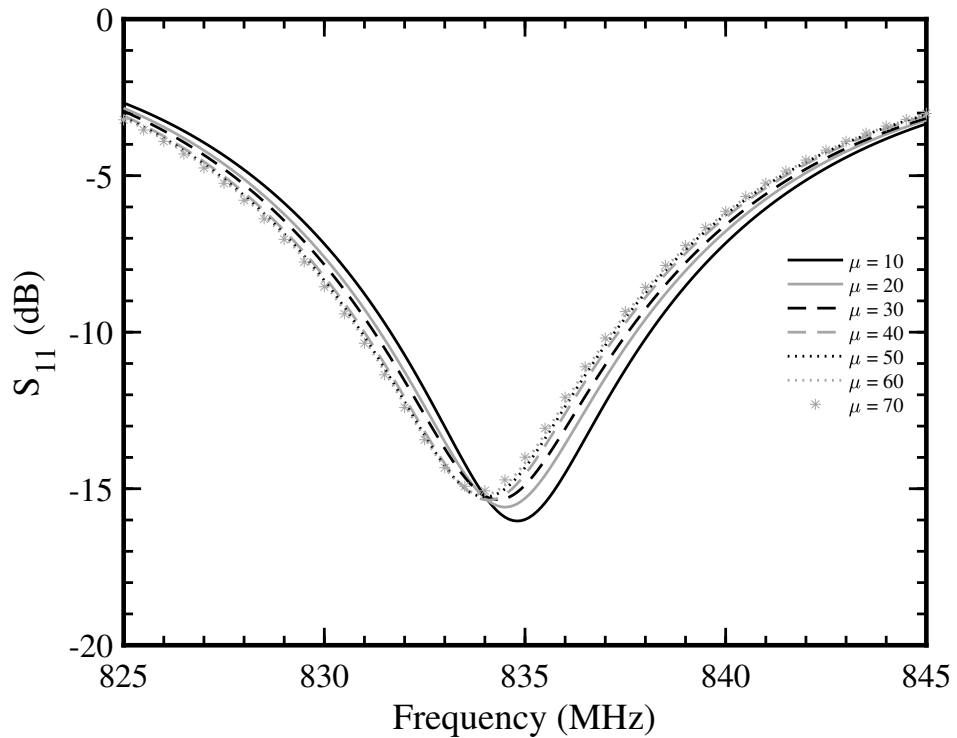


Figure 4.6: Simulated power reflection coefficient of the RFID tag when the relative permeability of the ferrite cores varies from 10 to 70.

to 70. There is a minor shift in the resonance frequency of the tag was observed because the tag antenna is located at the bottom of the CT which is far well from the ferrite core which locates at the top part of the CT. However, when the permeability reaches 50, the resonance frequency of the tag became stable.

4.3.2 Parametric Design Study

The antenna comprises of a feed loop for T-matching network and two radiating arms that extend onward from the loop for radiation. To achieve a compact form integration with the current transformer with the dimension of $29.5 \times 31 \times 55 \text{ mm}^3$, the tag antenna was designed in a square form factor with a hollow space in the centre for the transformer. Additionally, this tag antenna configuration was adopted to achieve good omnidirectional detection with acceptable read range. Furthermore, the feed loop acts as an input transformer and its dimensions are important design parameters for adjusting the antenna port impedance. The Magnus S2 tag chip has high a capacitive input reactance and therefore, a T-matching loop is introduced to achieve a conjugate impedance matching between the antenna and the tag chip.

Simulations were performed to analyse the effect of the various antenna parameters on

the tag resonance frequency, antenna port impedance, gain and radiation efficiency. The tag and antenna were simulated in three configurations and only one design parameter was changed at the time: (i) the parameter e of the antenna which determines the total length of the radiating arms; (ii) the length (l) and the width (w) of the feed loop; and (iii) the size of the tip loading structures at the corners of the antenna.

The total length of the radiating arms ($L + 2W + 2e$) is equal to 187.5 mm. The design parameter e can be used as a tuning parameter to tune the resonance frequency of the tag. Simulations were performed to analyse the effect of reducing the length of the radiating arms on the antenna port impedance and the tag resonance frequency as well as the gain and the radiation efficiency while keeping the remaining antenna parameters constant (referring to the parameter values presented in Table 4.1 and 4.2). Figure 4.7 shows the input impedance of the antenna port. It is observed that reducing the length of e cause the input resistance to reduce. Similarly, the input reactance of the antenna also increases with the parameter e . Furthermore, Figure 4.8 shows the power reflection coefficient of the tag when antenna parameter e varies from 9 mm to 21 mm. As expected, the resonance frequency of the tag is shifted to a higher frequency range when the length of the antenna decreases. When $e = 21$ mm, the input impedance of the antenna and the chip is well matched at 862 MHz and however, as the antenna length decreases, the losses increase away from this frequency. For finding the best possible impedance match at the higher frequency range, the dimensions of the feed loop need to be adjusted.

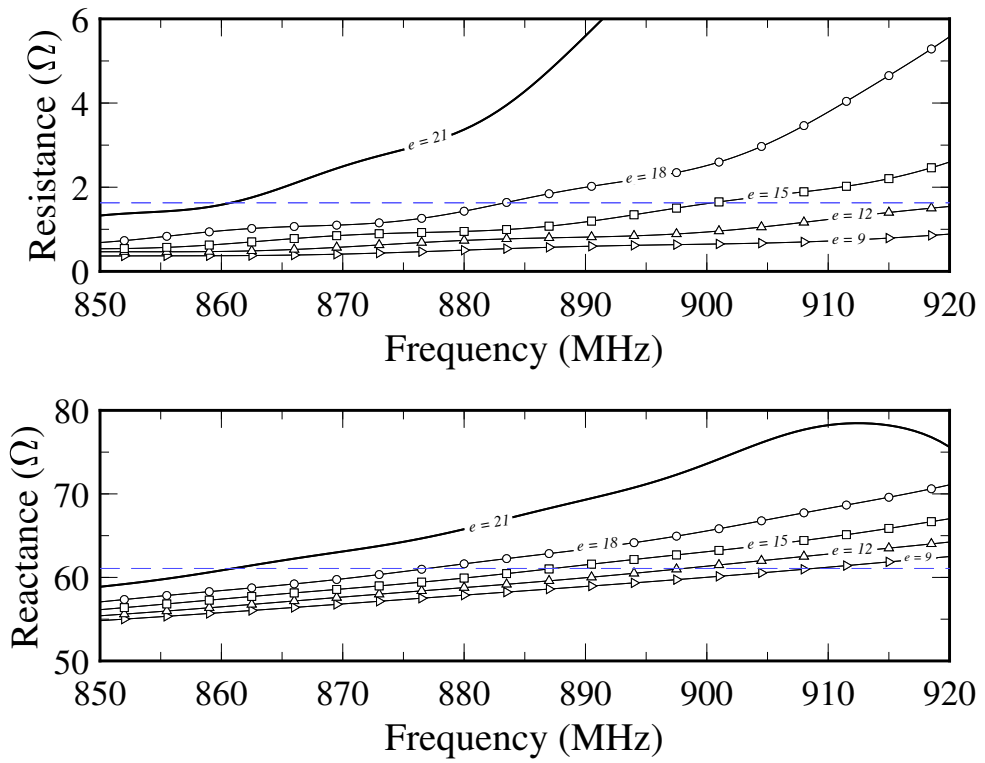


Figure 4.7: Effect of the antenna parameter e in mm on the antenna port impedance while other parameters in Table 4.1 and 4.2 were fixed.

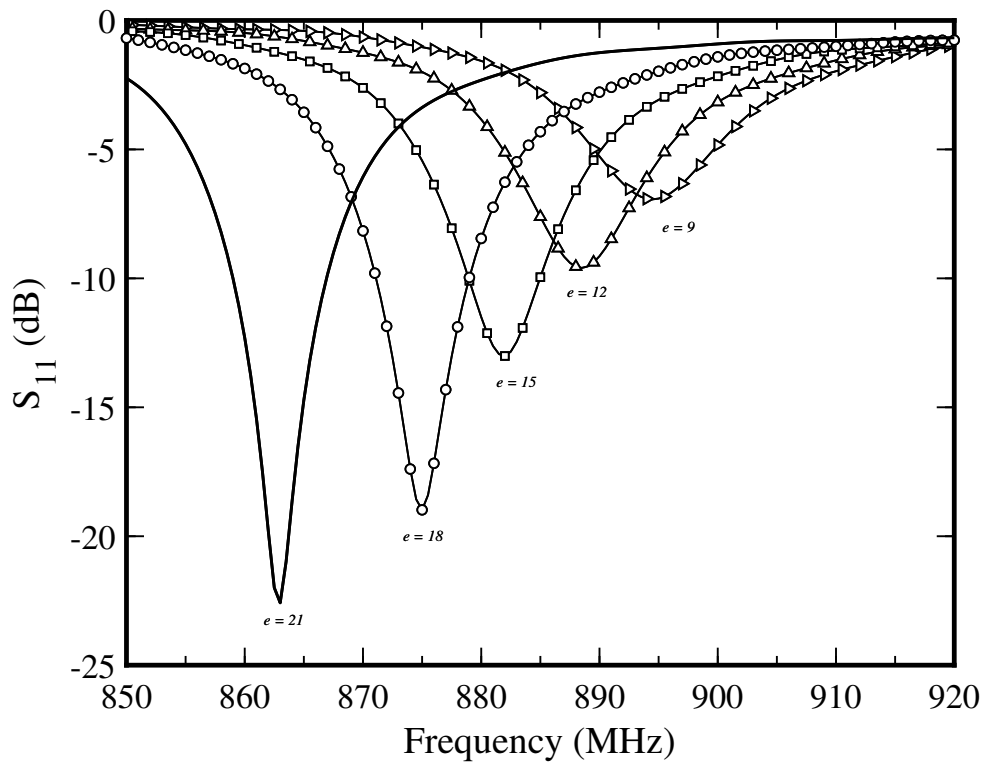


Figure 4.8: Power reflection coefficient of the tag when the antenna parameter e varies from 9 mm to 21 mm while other parameters in Table 4.1 and 4.2 were fixed.

Table 4.4 summarises the antenna port impedance ($Z_{ant.}$), gain (G_t , excluding the impedance mismatch loss), realised gain ($rlsd.G_t$, including the impedance mismatch loss) and radia-

tion efficiency (η_e) of the tag at 868 MHz. It is observed that the tag gain and the radiation efficiency are degraded as the antenna length decreases.

Table 4.4: Simulated antenna port impedance ($Z_{ant.}$), gain (G_t), realised gain ($rlsd.G_t$) and radiation efficiency (η_e) of the tag at 868 MHz.

e (mm)	9	12	15	18	21
$Z_{ant.}(\Omega)$	0.45 + j56.62	0.56 + j57.43	0.74 + j58.40	1.08 + j59.69	2.26 + j62.60
$G_t(dB)$	0.25	0.10	0.64	0.83	1.13
$rlsd.G_t(dB)$	-9.44	-6.71	-3.66	-0.51	0.42
$\eta_e(dB)$	-1.19	-1.33	-0.74	-0.59	-0.33

A good impedance matching is required for maximising the RF power transmit from the antenna to the tag chip. Since the tag chip input impedance is mostly capacitive, a feed loop is added to the design to achieve high input inductance and hence, it cancelled out the negative reactance of the tag chip. The length l and width w of the feed loop strongly affect the antenna port impedance and as a consequence the resonance frequency of the tag. The effect of the feed loop on the tag resonance frequency is investigated in two scenarios: (i) the length of the loop varies from 3 mm to 5 mm when the width w of the loop is fixed; and (ii) the width w of the loop varies from 4 mm to 6 mm when the length l remains constant.

Figure 4.9(a) and 4.9(b) depict the input impedance observed at the antenna port. The real and imaginary magnitude increases with the size of two parameters (l , w), and vice versa. Referring to Figure 4.9(b), it is observed that the imaginary magnitude of the antenna impedance is significantly effected by the width w of the feed loop. However, the resistive part of the antenna impedance is less influenced by the loop width w .

Figure 4.10(a) shows the power reflection coefficient of the tag when the parameter l of the loop varies from 3 mm to 5 mm. As l decreases, the resonance frequency of the tag is shifted to a higher frequency range. When $l = 3$ mm, the tag resonates at 900 MHz. Conversely, as e increases, the resonance frequency to the tag is moved toward a lower frequency range. For $l = 5$ mm, the tag resonates at about 820 MHz. Figure 4.10(b) shows the power reflection coefficient of the tag as the width w of the loop varies from 4 mm to 6 mm. It is observed that the wider the loop, the lower the resonance frequency, and vice versa. When $w = 6$ mm, the tag resonates at about 830 MHz. Meanwhile, the resonance frequency of the

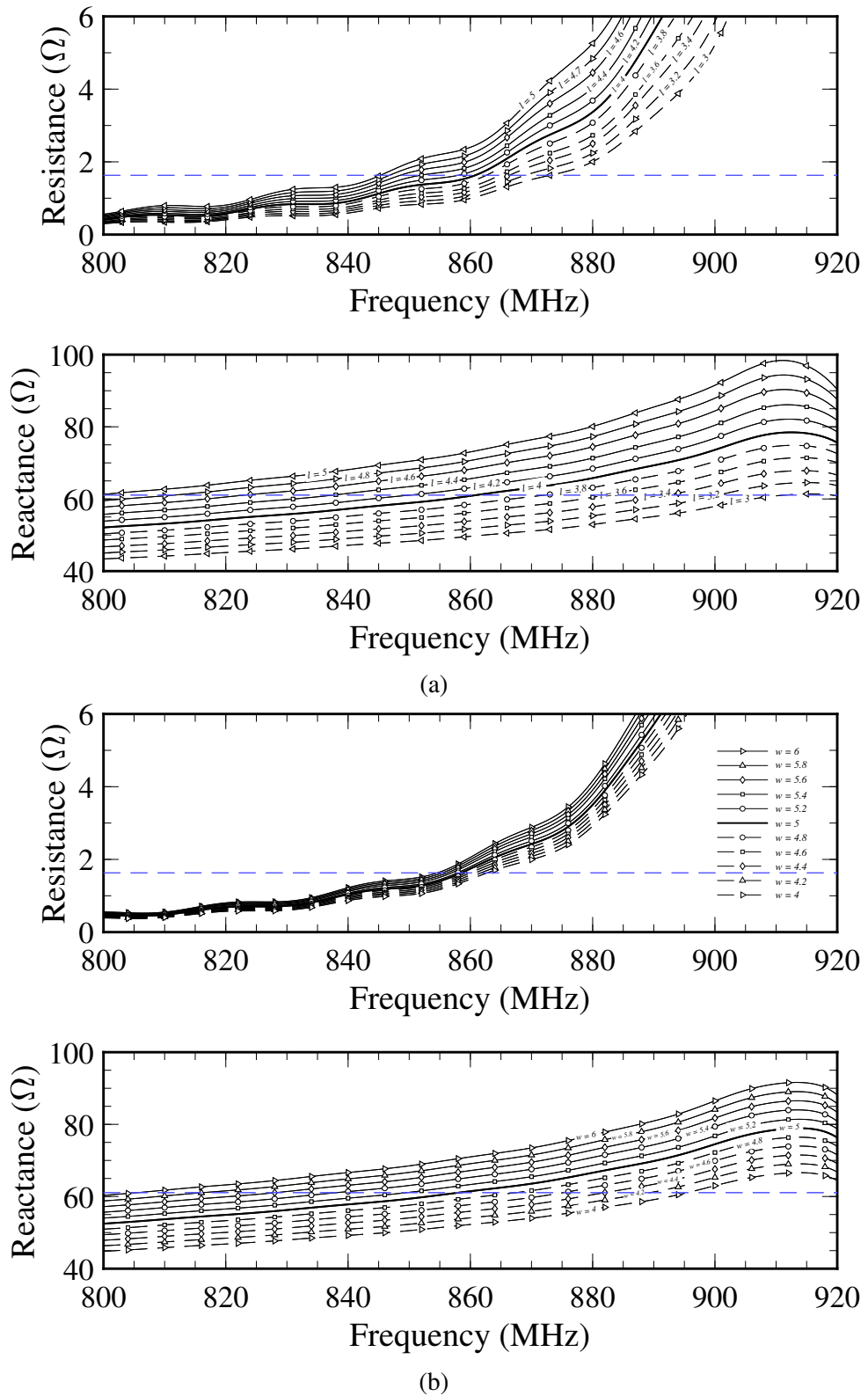
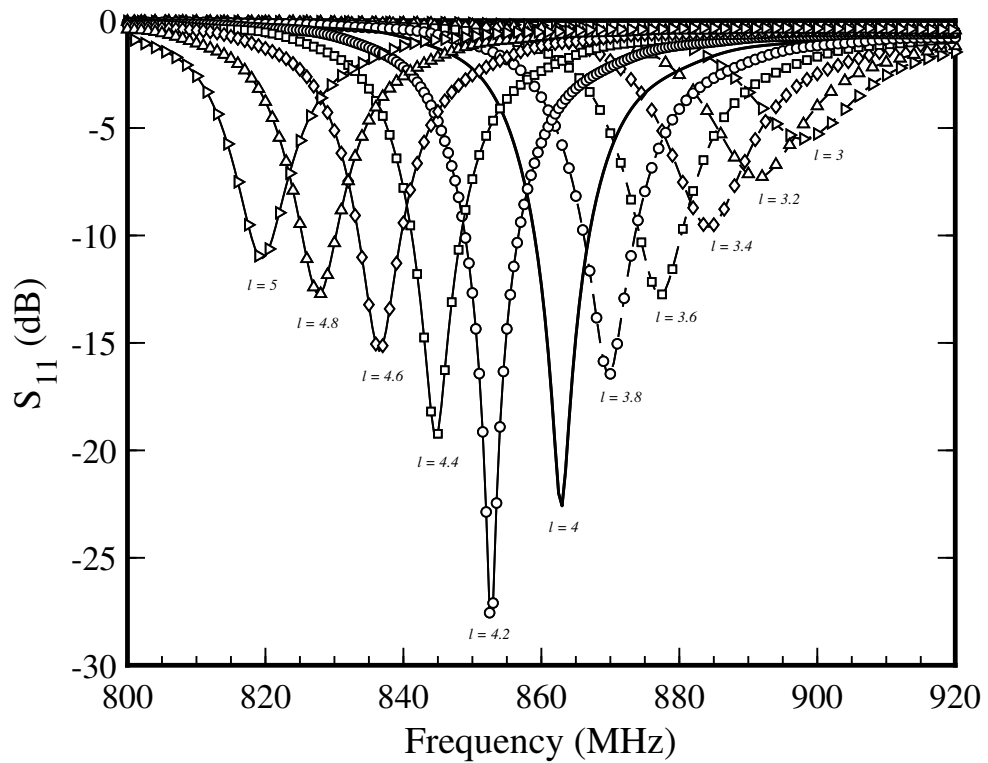


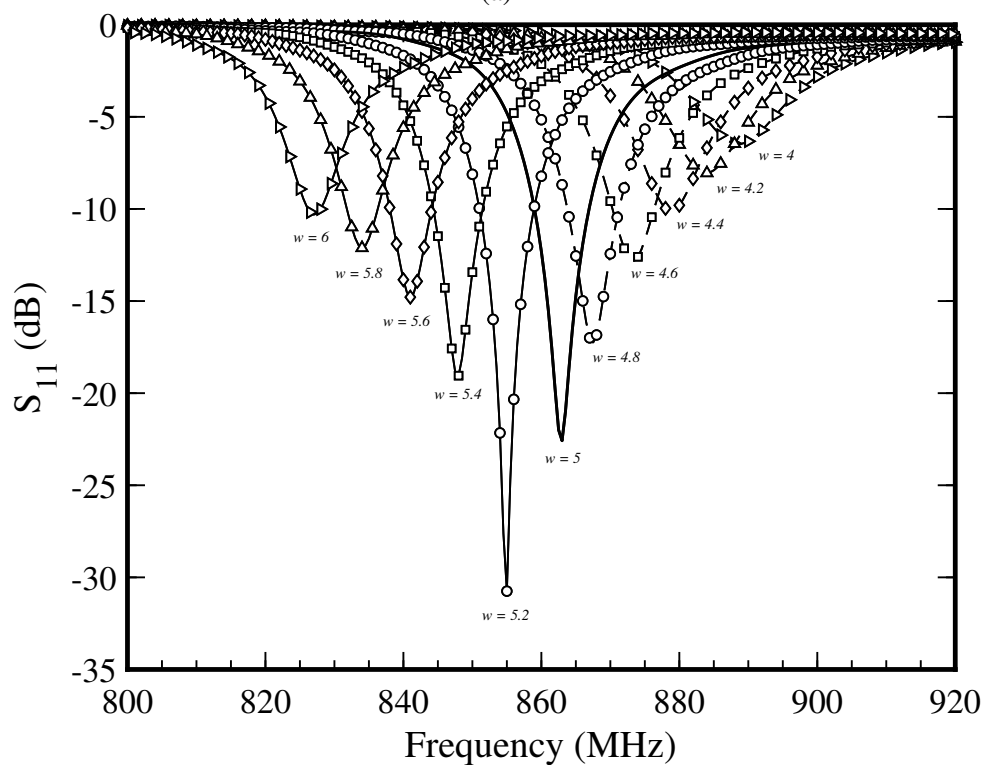
Figure 4.9: Simulated input impedance of the antenna against frequency: (a) when the loop length l varies from 3 mm to 5 mm; (b) when the loop width varies from 4 mm to 6 mm while other parameters in Table 4.1 and 4.2 were fixed.

tag is shifted to a higher frequency range as the width of the loop decreases.

To investigate how the tip loading structures at the corners of the antenna affect the tag performance, the antenna was simulated in three configurations: (i) changing the width of



(a)



(b)

Figure 4.10: Simulated power reflection coefficient of the tag, (a) when the length l of the feed loop varies from 3 mm to 5 mm and (b) when the width of the feed loop varies from 4 mm to 6 mm while other parameters in Table 4.1 and 4.2 were fixed.

the parameter c from 2.5 mm to 8 mm; (ii) changing the width of the parameter f from 2.5 mm to 8 mm; and (iii) changing the width of both parameters f and c of the radiating arms from 2.5 mm to 8 mm; as shown in Figure 4.11. Figure 4.12 shows the antenna port

Table 4.5: Simulated antenna port impedance, gain, realised gain and radiation efficiency of the proposed tag at 868 MHz by varying the design parameter l .

l (mm)	3	3.2	3.4	3.6	3.8	4	4.2	4.4	4.6	4.8	5
$Z_{ant.}(\Omega)$	1.41 +j50.81	1.57 +j53.04	1.74 +j55.33	1.89 +j57.83	2.1 +j60.24	2.26 +j62.60	2.48 +j65.11	2.69 +j67.77	2.94 +j70.61	3.16 +j73.20	3.39 +j75.77
$G_t(dB)$	1.15	0.84	0.96	1.06	0.98	1.13	0.92	1.2	0.98	1.07	1.33
$rlsd.G_t(dB)$	-9.71	-7.25	-4.44	-1.25	0.80	0.42	-2.70	-4.78	-6.61	-8.25	-9.39
$\eta_e(dB)$	-0.31	-0.57	-0.41	-0.32	-0.46	-0.33	-0.45	-0.20	-0.47	-0.35	-0.09

Table 4.6: Simulated antenna port impedance, gain, realised gain and radiation efficiency of the proposed tag at 868 MHz by varying the design parameter w .

w (mm)	4	4.2	4.4	4.6	4.8	5	5.2	5.4	5.6	5.8	6
$Z_{ant.}(\Omega)$	1.90 +j53.59	1.98 +j55.48	2.06 +j57.37	2.14 +j59.28	2.25 +j61.32	2.26 +j62.60	2.39 +j65.00	2.49 +j67.06	2.57 +j69.00	2.66 +j70.96	2.74 +j72.91
$G_t(dB)$	0.88	1.01	1.1	1.02	1.03	1.13	1.02	1.06	1.04	1.17	0.92
$rlsd.G_t(dB)$	-6.44	-4.42	-2.03	0.07	0.93	0.42	-2.04	-3.98	-5.78	-7.14	-8.48
$\eta_e(dB)$	-0.5	-0.35	-0.27	-0.39	-0.43	-0.33	-0.39	-0.32	-0.39	-0.28	-0.49

impedance while Figure 4.13 represents the power reflection coefficient of the tag designs shown in Figure 4.11. It is observed that increasing the width of c of the vertical radiating arms improve the impedance matching between the antenna and the tag chip at the UHF band. However, increasing the width of the parameter f strongly effect the resonance frequency of the tag. Table 4.7 shows the gain, realised gain and radiation efficiency of the proposed tag at 868 MHz. It is observed that the antenna design 3 has a high gain of 1.45 dB with the radiation efficiency of -0.03 dB. It can be concluded that increasing the width of the copper trances c and f of the antenna can significantly increase the antenna gain, resulting in the higher read range. However, the mismatching problem can occur as shown in Figure 4.11 and to overcome this problem, the T-match network with the main antenna structure can be optimised to achieve the desired impedance matching at the UHF band.

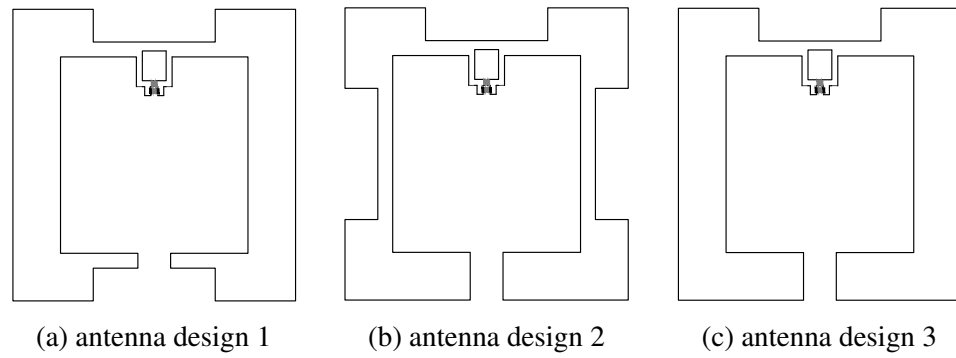


Figure 4.11: Simulated tag antenna designs with different tip loading structures: (a) antenna design 1 when $c = 8$ mm; (b) antenna design 2 when $f = 8$ mm; and antenna design 3 when c and $f = 8$ mm.

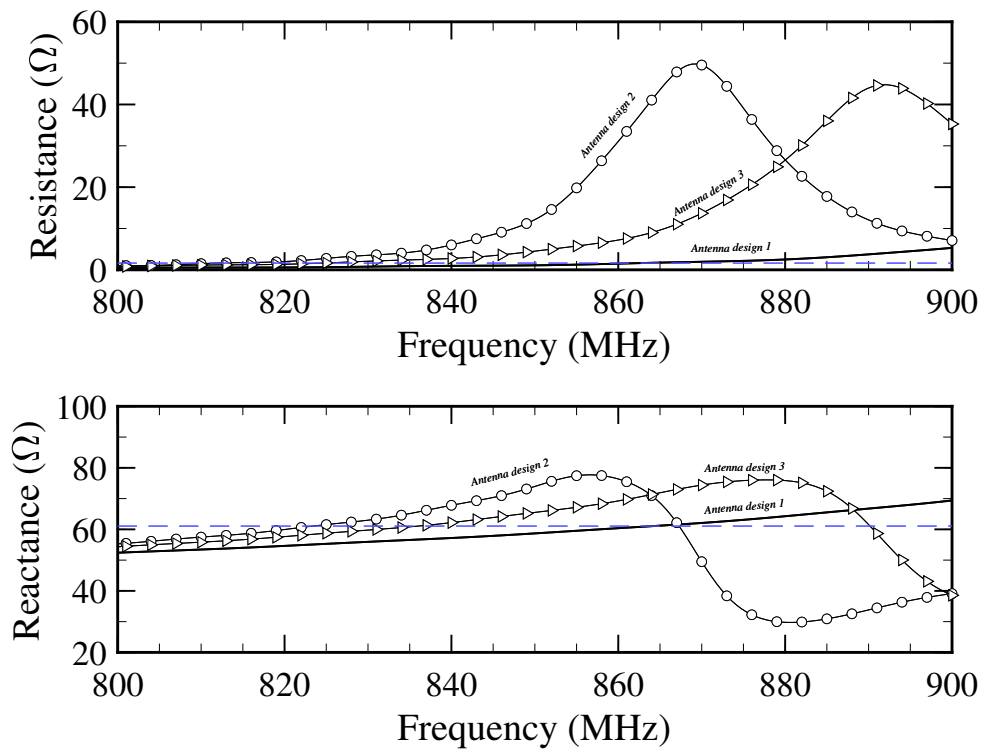


Figure 4.12: Simulated antenna port impedance of the antenna design 1, 2 and 3 presented in Figure 4.11.

Table 4.7: Simulated antenna port impedance, gain, realised gain and radiation efficiency of the tag antenna design 1, 2 and 3 at 868 MHz.

Antenna design	1	2	3
$Z_{ant.}(\Omega)$	$1.86 + j61.71$	$49.19 + j58.16$	$11.84 + j73.48$
$G_t(dB)$	1.11	1.39	1.45
$rlsd.G_t(dB)$	0.99	-7.79	-4.85
$\eta_e(dB)$	-0.42	-0.01	-0.03

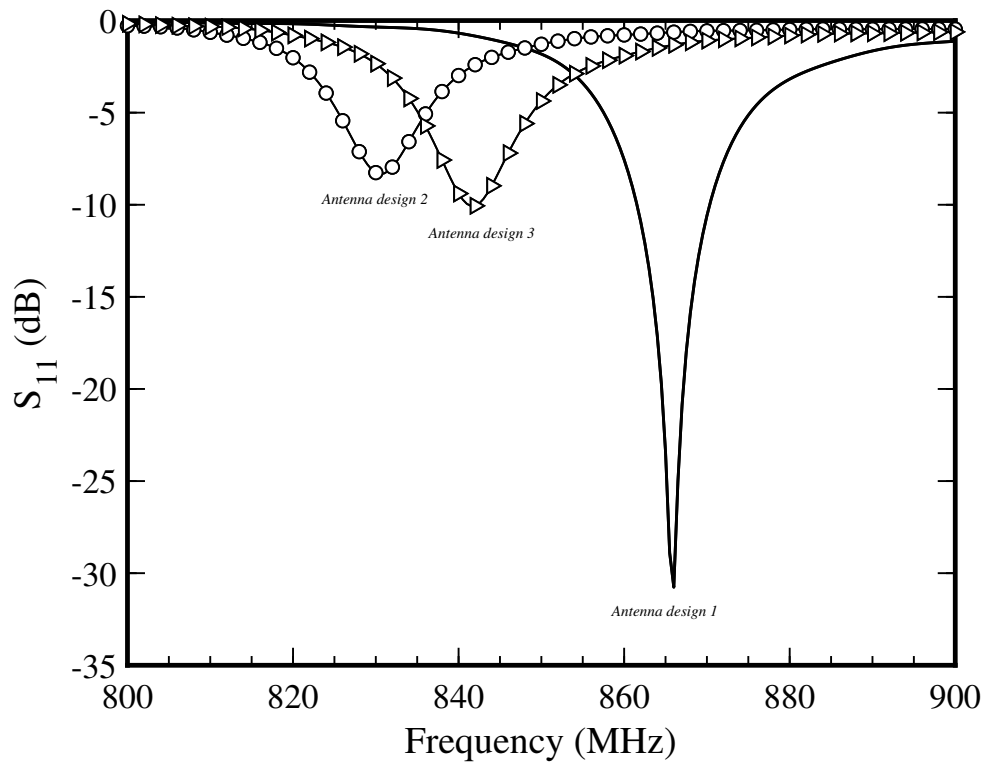
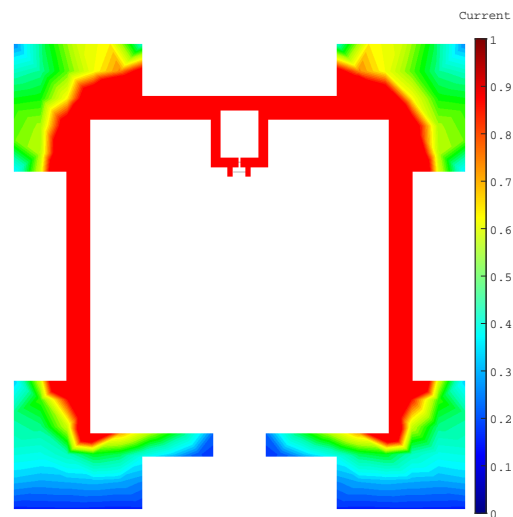


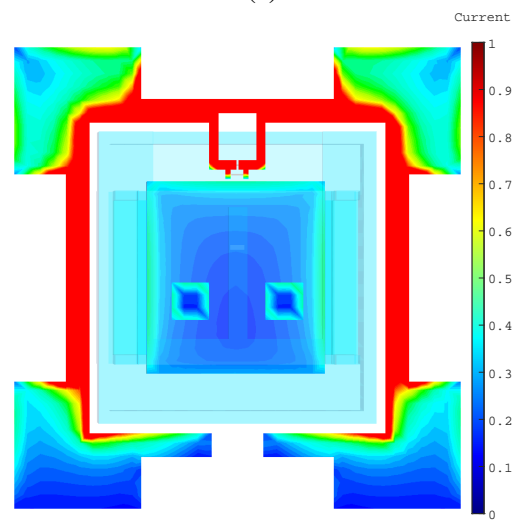
Figure 4.13: Simulated power reflection coefficient of the antenna design 1, 2 and 3 presented in Figure 4.11.

Figure 4.14 depicts the normalised magnitude of the current distribution of the tag antenna at 868 MHz. It is observed that the maximum current distribution is located in the two radiating arms that extend outward from the feed loop. The corners of the antenna contribute to less current distribution. However, the current density is increased in the vertical axes from the corner to corner, which are responsible for radiating more power. The magnitude of current distribution in Figure 4.14(b) and Figure 4.14(c) are identical because the tags are resonant at the same frequency, whereas the overall current density is higher in Figure 4.14(a).

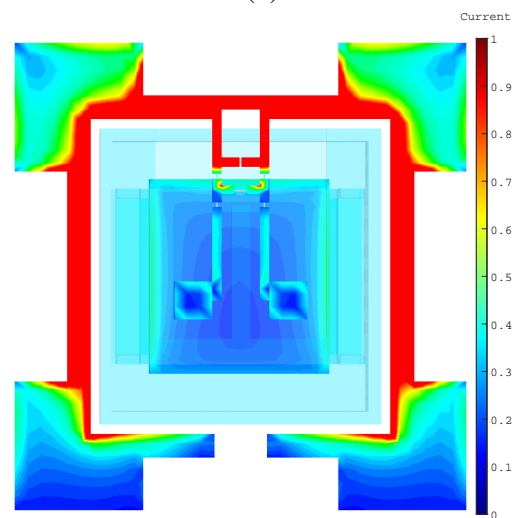
The radiation patterns of the tag simulated in three configurations are shown in Figure 4.15, indicating the tag antenna, and the tag antenna mounted on the CT, and the tag antenna couple with tuning circuit has a gain (excluding the reflection losses) of 1.1 dB, and 1.4 dB, and 1 dB, respectively, at 868 MHz. Additionally, the realised gain of the normal tag and the tag mounted on the transformer are 0.42 dB and -6.674 dB. Furthermore, the tag antenna simulated radiation efficiency was -0.324 dB, and the radiation efficiency of the tag antenna mounted at the bottom of the CT was -0.0171 dB.



(a)

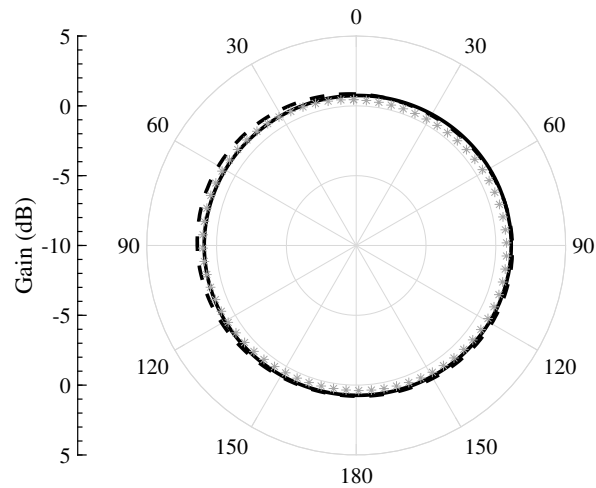


(b)

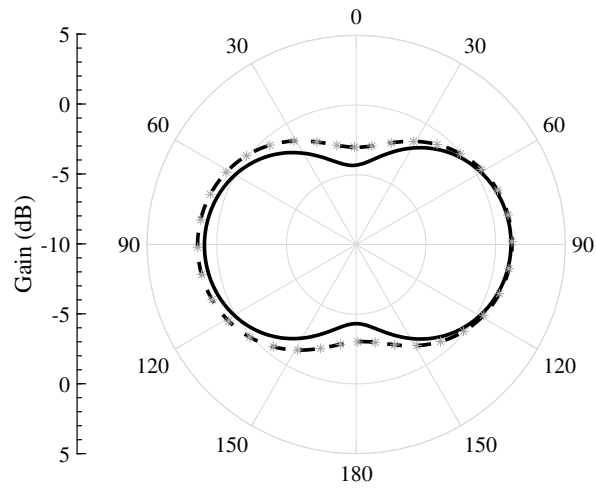


(c)

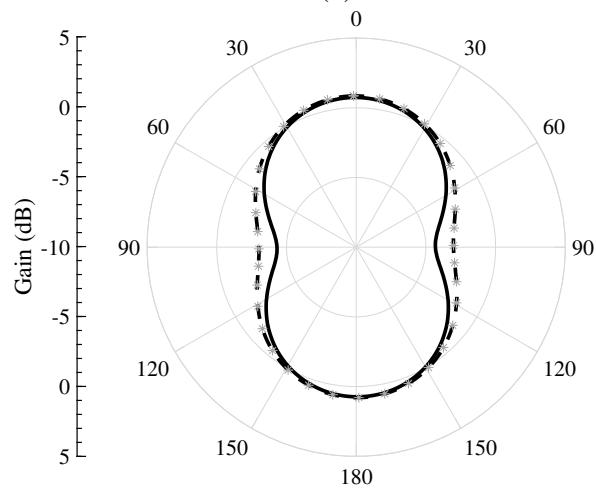
Figure 4.14: CST simulated normalised surface current distribution of the tags configurations at 868 MHz: (a) normal tag with a 0.3 pF capacitor attached right across the antenna terminals (excluding the transformer); (b) tag mounted at the bottom of the transformer; and (c) tag linked with the tuning circuit and mounted at the bottom of the CT.



(a)



(b)



(c)

Figure 4.15: Polar plot of CST simulated tag system gain: (a) $\phi = 90^\circ$: yz -plane; (b) $\theta = 90^\circ$: azimuth plane; and (c) $\phi = 0^\circ$: xz -plane. Solid line: normal tag, dashed line: tag attached to the transformer, and asterisk: tag coupled with the tuning circuit.

4.3.3 Theoretical Read Range

4.3.3.1 Normal Tag

Theoretical read range of the tag can be calculated using the Friis free-space formula:

$$r_{max} = \frac{\lambda_0}{4\pi} \cdot \sqrt{\frac{EIRP \cdot G_r \cdot \tau}{P_{IC}}} \quad (4.1)$$

where λ_0 is the wavelength, EIRP is the effective isotropic radiative power transmitted by the reader antenna, and P_{IC} is the tag chip sensitivity which is the minimum threshold power required to turn on the tag chip. The values of these parameters are following:

$$\lambda_0 = 345.62 \text{ mm } (f_0 = 868 \text{ MHz})$$

$$P_{IC} = -16.1 \text{ dBm } (= 0.0245 \text{ mW})$$

$$EIRP = 3.28 \text{ W}$$

The simulated value of the tag realised gain (G_r) and reflection coefficient (S_{11}) are:

$$G_r = 0.42 \text{ dB } (= 1.1015)$$

$$S_{11} = -7.925 \text{ dB } (= 0.01612)$$

$$\tau = 1 - |S_{11}|^2 (= 0.9740)$$

The maximum theoretical distance between tag and reader can be calculated to be:

$$r_{max} = 10.42 \text{ m.}$$

4.3.3.2 Tag Attached to Transformer

The simulated value of the tag realised gain (G_r) and reflection coefficient (S_{22}) are:

$$G_r = -6.674 \text{ dB } (= 0.2150)$$

$$S_{11} = -0.7444 \text{ dB } (= 0.8424)$$

$$\tau = 1 - |S_{11}|^2 (= 0.2903)$$

The maximum theoretical distance between tag and reader can be calculated to be:

$$r_{max} = 2.51 \text{ m.}$$

4.3.4 Current Transformer and Tuning Circuit

The split-core current transformer [7] can detect ac current in the range of 0 A to 13 A from a power cable of an electrical load and transform it into 0 V to 10 V dc proportionally was connected to the terminals of the tuning circuit of the capacitance RFID tag to evaluate the performance of the tag system. The transformer has a full-scale accuracy of $\pm 2\%$ with the operating frequency of 50/60 Hz. The CT comes with two M3 screw terminals, which were used to connect the CT with the tuning circuit, as described earlier.

The tuning circuit was designed consisting of two inductors of 400 nH, a varactor diode [8] and two 15 pF capacitors. The relationship of the reverse voltage and capacitance of the tuning diode is derived from the varactor diode datasheet [9]. The input terminals of the tuning circuit were connected to the CT, while the output terminals of the tuning circuit were linked to the tag antenna terminals. Two 10 mm long and 1 mm wide copper straps with a 4 mm gap connect to the voltage from the CT, Figure 4.2(b). Figure 4.16 illustrates the schematic diagram of the tuning circuit linked to the tag antenna. The tuning circuit used 0603 size components with a pitch of 0.5 mm between contacts, and was fabricated along with the tag antenna on a 0.18 mm thick Mylar substrate.

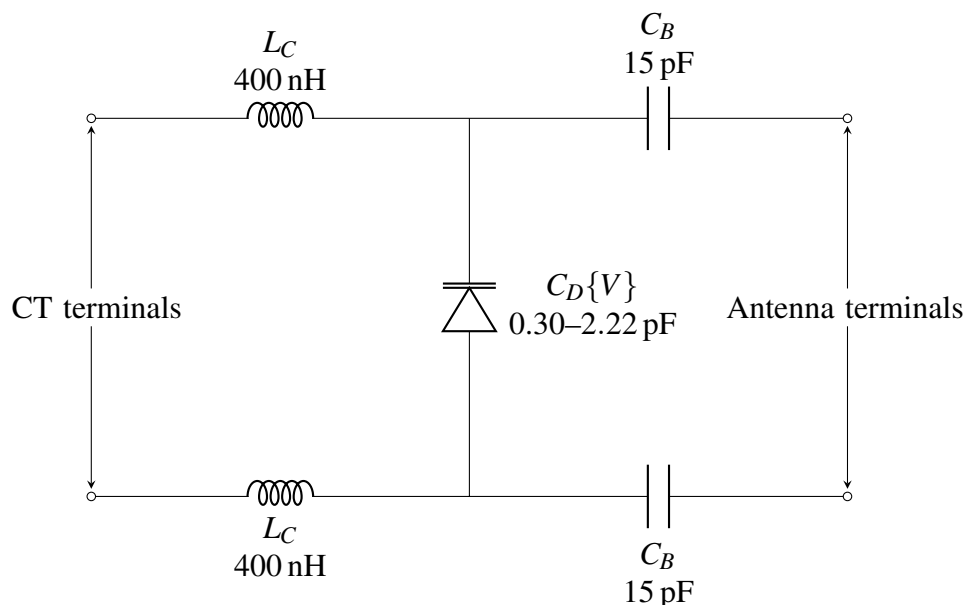


Figure 4.16: Schematic diagram of the tuning circuit which input terminals are connected to the transformer while the output terminals are connected to the tag antenna ports.

4.3.5 Measurement Results

4.3.5.1 Sensor Code and Read Range

In the first experiment, the normal tag and the tag mount on the CT with the attached of a 0.3 pF capacitor were experimentally interrogated with the UHF reader Tagformance Pro System [10], comprising of a 6 dBi gain linear polarised antenna and placed at the fixed distance of 30 cm away from the tag. Figure 4.17 illustrates the sensor value of the tag. It is observed that the sensor value is significantly dropped to the lower frequency when the tag mounted on the transformer as the sensor value depends on the resonance frequency. A read range of approximately 5 m at 868 MHz was obtained, Figure 4.18. The tag read range is increased with the increased frequency as the embedded self-tuning RFID chip covers all worldwide UHF bands (860–960 MHz) which increase the readability of the tag. Despite the mismatch between the tag antenna and the chip when the tag was mounted at the bottom of the transformer, the tag has a good read range at the UHF band because the chip auto tunes its internal impedance to match with the antenna impedance.

Furthermore, the theoretical read range of the normal tag is higher than the measured read range is the result of the following assumptions: (i) the actual sensitivity of the tag chip tends to be smaller than nominal value [11] which can significantly affect the tag read range; (ii) the non-ideal etching mechanism and not properly attaching the tag microchip with the antenna port; (iii) the antenna is bent around the transformer can cause to degrade the tag performance; and (iv) the not-anechoic measurement environment [12].

4.3.5.2 Current Sensing Setup

In the final experiment, to demonstrate the performance of the complete sensing system, the RFID tag, the tuning circuit and the CT were coupled, Figure 4.19, and tested with the measurement setup which included (i) the UHF reader Tagformance Pro System to interrogate the tag system. (ii) the split-core CT clamp around a single current carrying-wire, enclosed in the insulating box (iii) an electrical heater with an adjustable heating setting (low and high) as an electrical load, (iv) a commercial Brennenstuhl PM 231 E current meter with $\pm 1\%$ accuracy [13] to benchmark the tag results.

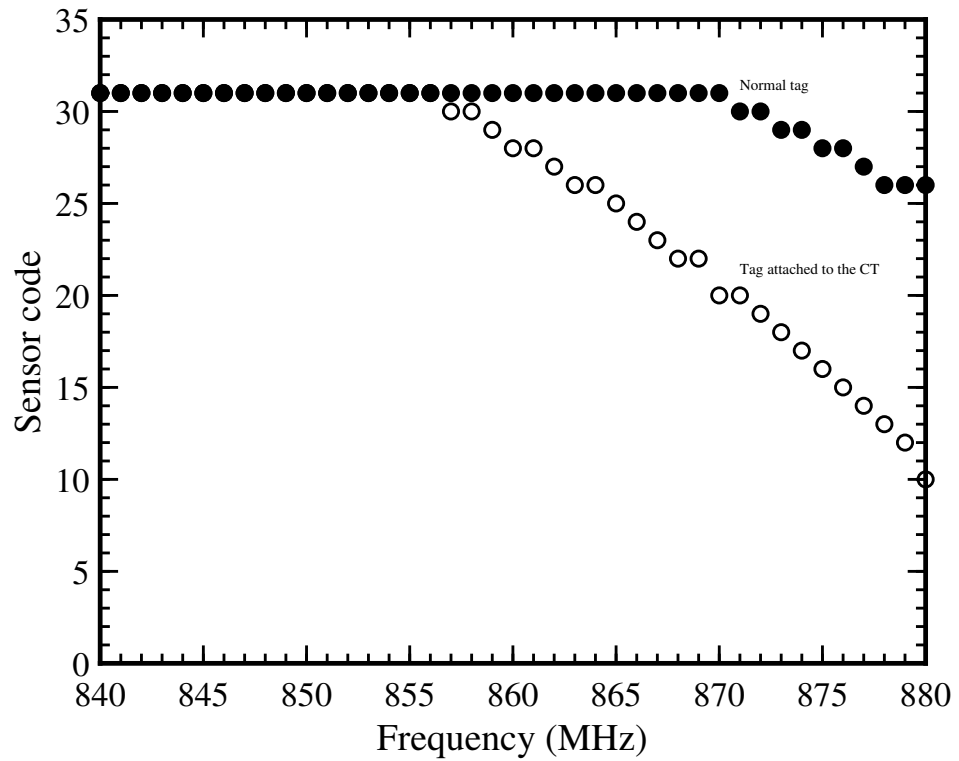


Figure 4.17: Measured sensor code of the tag.

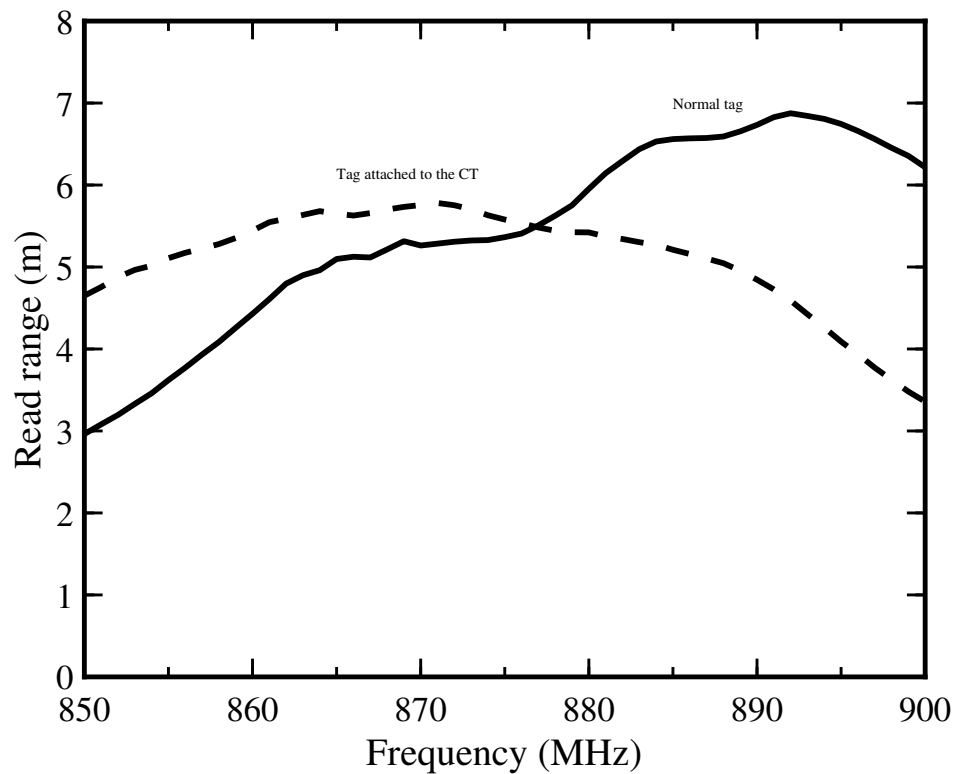


Figure 4.18: Measured read range of the tag.

4.3.5.3 Current to Sensor Code Relationship

The sensing system was clamped around a power cable of an electrical appliance. The electrical appliance draws ac current ranging from 0 A to 10 A. Figure 4.20 shows the measured

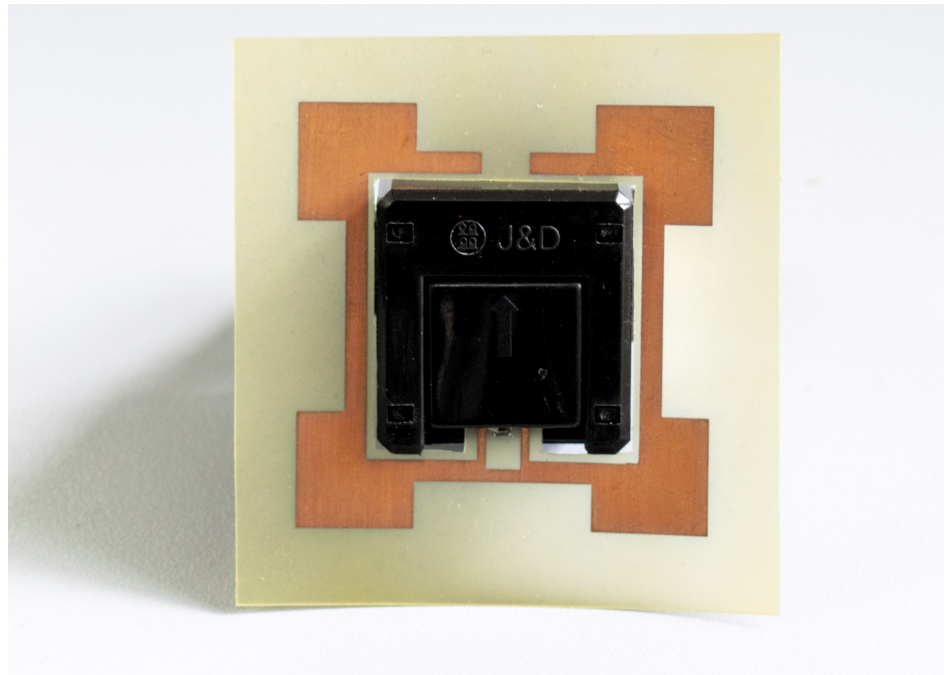


Figure 4.19: A prototype of the tag antenna integrated to the transformer used for experiments to verify the simulated design.

sensor code of the sensing tag. The sensor value for 2 A and 10 A was 1 and 10 respectively where the electric heater consumed 480 W at low setting and 2.4 kW at high setting. There is a lot of fluctuation in the sensor code of the sensing tag, showing that the tag is not well tuned at 868 MHz. Figure 4.21 gives the read range of the sensor for each current level. The lowest read range was recorded at 0 A, because the tag is out of the tuning range as the tuning varactor capacitance reached to its maximum value. There is a decrease in the read range of the tag system as compared to the read range of the normal tag shown in 4.21, as the losses occur due to the tuning circuit attached to the tag.

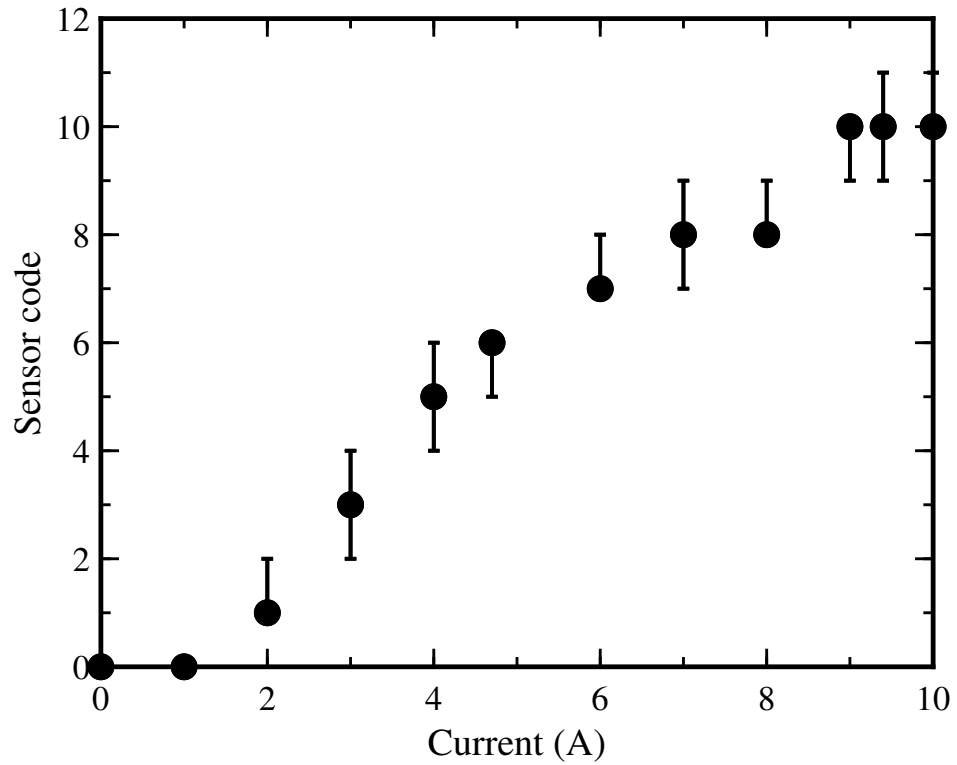


Figure 4.20: Sensor code variations as the current flow changes in the power cable.

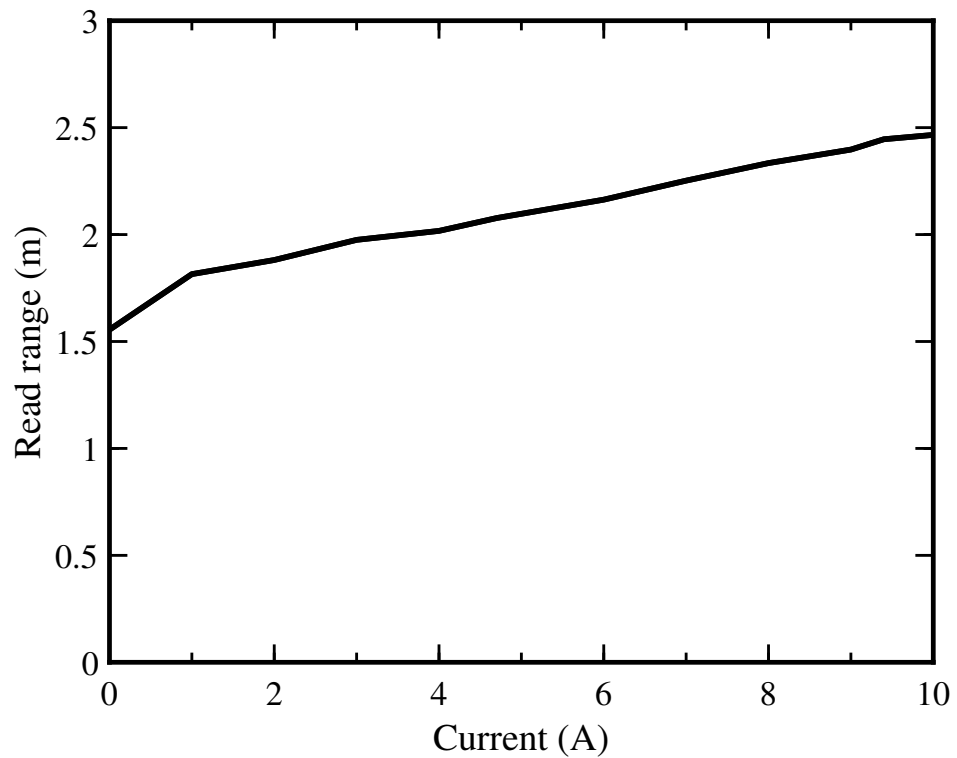


Figure 4.21: Measured read range of the proposed tag system.

To sum up all, a new tag antenna design for a current transformer is demonstrated. The antenna design was bent around the transformer to reduce to the overall size of the tag system. The tag has a good read range at UHF band of about 5 m. The tag was tested for high, low and zero current levels. From measurement results, It is observed that the current detection

range of the tag is very low at 868 MHz, therefore, it was decided to not test the tag system further for the load current. Because of this potential limitation, the same tag antenna will be optimised to increase the current sensing range at 868 MHz.

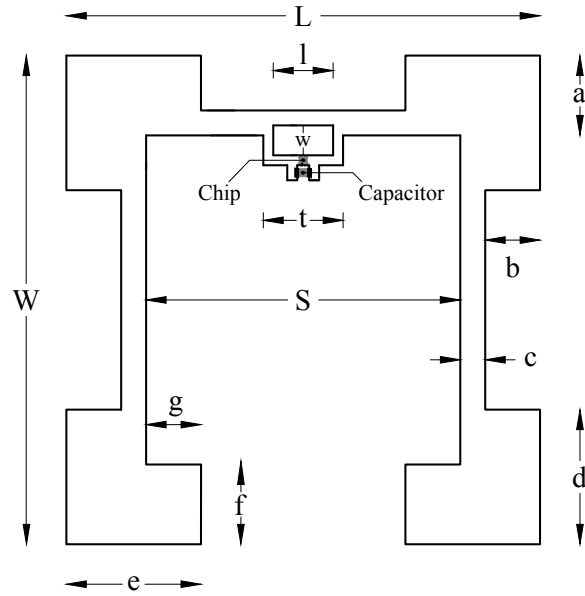
4.4 Optimised Tag Antenna Design

As described earlier that when the tag antenna, Figure 4.2(a), was mounted on the CT, the resonance frequency of the tag was shifted from 863 MHz to 836 MHz. Thus, the transformer detuned the tag antenna which caused to reduce the sensing range of the tag at 868 MHz. To obtain the full 4-bit resolution (0–31) of the chip, the impedance of the tag antenna and the chip need to well match at 868 MHz. Therefore, the tag antenna dimensions, Figure 4.2(a), are optimised to achieve impedance matching at the desired frequency in the UHF band around 868 MHz. The total length and width of the tag antenna was fixed to 0.137λ and 0.141λ respectively, at 868 MHz. The resonance frequency of the tag antenna was adjusted by decreasing the length of the feed loop of the antenna. The end of two coupling arms of the antenna were reduced by 7.5 mm to achieve the best possible impedance match between the tag antenna and the chip. The optimised tag antenna design for the current transformer is depicted in Figure 4.22(a) [14]. The design parameters e , l , and w were optimised to tune the tag antenna at 868 MHz. The values of the other design parameter are identical compared to the design proposed in Figure 4.2. The design parameter e is equal to 13.5 mm. The length l and width w of the food loop are 6 mm and 3 mm, respectively. Other design parameter values are listed in Table 4.8 and 4.9.

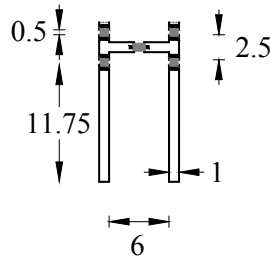
Furthermore, the dimensions of the tuning circuit are shown in Figure 4.22(b). Two 11.75 mm long and 1 mm wide copper traces with a 6 mm gap was used to connect the dc voltage from the CT. The circuit is designed for 0603 size components.

Table 4.8: Feed loop dimensions of the tag antenna.

Parameters (mm).	l	w	t
	6	3	8



(a)



(b)

Figure 4.22: (a) Optimised tag antenna design for the current transformer; and (b) a tuning circuit with dimensions in mm.

4.4.1 Simulation Results

The tag was mounted at the 6 mm above the bottom of the CT, as shown in Figure 4.3 and was simulated in two configurations: (i) the tag with a 0.3 pF capacitor attached across the antenna terminals; (ii) and coupled with the tuning circuit, Figure 4.22(b), was attached at the antenna terminals (excluding the 0.3 pF capacitor). The simulated tag antenna reflection coefficient with the 0.3 pF capacitor and the tag antenna coupled with the tuning circuit are illustrated in Figure 4.24. The antenna in both configurations has a good match at the UHF

Table 4.9: Simulated tag antenna dimensions.

Parameters (mm)	L	W	S	a	b	c	d	e	f	g
	47.5	49	31.5	8	5.5	2.5	13.5	13.5	8	5.5

RFID band (865–868 MHz).

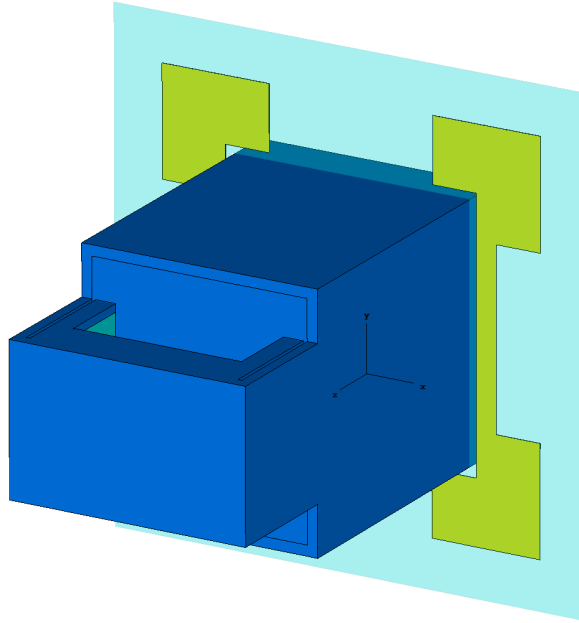


Figure 4.23: 3D model of the tag antenna design attached at the bottom of the transformer.

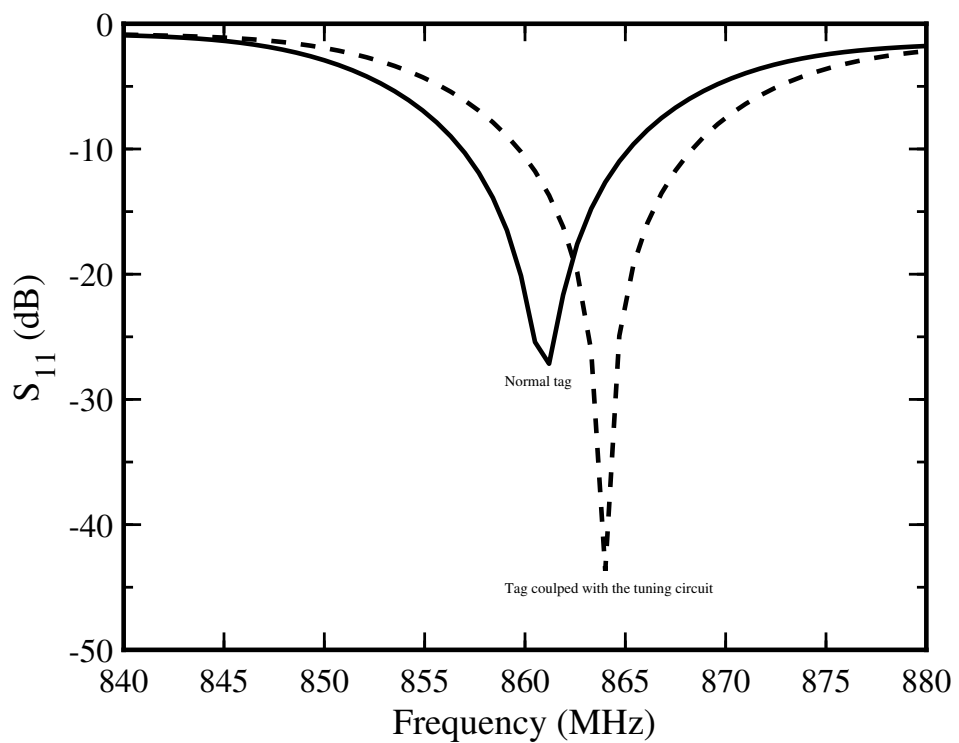


Figure 4.24: Simulated reflection coefficient of the RFID tag design.

4.4.2 Parametric Design Study

Based on the previous design parameters analysis, the main design parameters e , l and w can be optimised to adjust the antenna port impedance and the resonance frequency of the

tag. The antenna comprises of a feed loop for T-matching network and radiating arms for radiation. The length of radiating arms can be optimised to adjust the resonance frequency of the tag antenna, as shown in Figure 4.25. The design parameter e can be used as a tuning parameter. The shorter is e , the higher is the resonant frequency, and vice versa. Furthermore, the size of the feed loop can be optimised to determine the antenna port impedance. The size of the loop mainly influences the input impedance of the antenna port and as a result, the resonance frequency of the tag. With an increase in the loop length l and width w , the resonance frequency shifts to a lower value. However, the shorter is l and w , the lower is the resonant frequency, as shown in Figure 4.26. Table 4.10, 4.11 and 4.12 represent the gain (excluding the impedance mismatch loss), realised gain (including the impedance mismatch loss), and radiation efficiency of the tag at 868 MHz when changing the antenna parameters e , l and w .

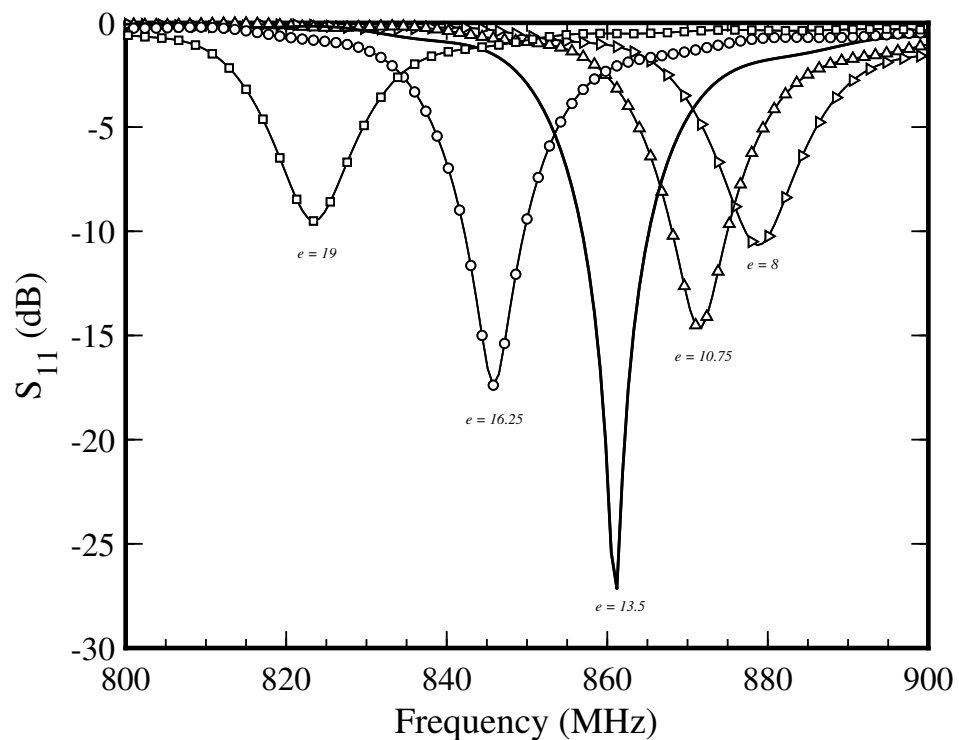


Figure 4.25: Effect of the design parameter e in mm on the tag resonance frequency while other parameters in Table 4.8 and 4.9 were fixed.

Figure 4.27 depicts the normalised magnitude of the current distribution of the tag antenna at 868 MHz. It is observed that the maximum current distribution is located in the two radiating arms that extend outward from the feed loop, as well as in the two vertical axes and the most power radiate from these parts of the antenna. The corners of the antenna contribute to less current distribution.

Table 4.10: Simulated gain (G_t), realised gain ($rlsd.G_t$) and radiation efficiency (η_e) of the proposed tag at 868 MHz by varying the design parameter e .

e (mm)	8	10.75	13.5	16.25	19
$G_t(dB)$	0.46	0.12	0.74	0.34	0.84
$rlsd.G_t(dB)$	-2.95	-0.35	-0.45	-5.12	-9.17
$\eta_e(dB)$	-1.01	-1.37	-0.72	-0.98	-0.54

Table 4.11: Simulated gain (G_t), realised gain ($rlsd.G_t$) and radiation efficiency (η_e) of the proposed tag at 868 MHz by varying the design parameter l .

l (mm)	5	5.5	6	6.5	7
$G_t(dB)$	-0.17	0.77	0.74	0.42	0.63
$rlsd.G_t(dB)$	-9.03	-2.16	-0.45	-6.09	-9.72
$\eta_e(dB)$	-1.59	-0.65	-0.72	-0.98	-0.8

Figure 4.28 displays the radiation patterns of the tag configurations with a realised gain (including the reflection coefficient losses) at 868 MHz of 0.159 dB and -0.455 dB, respectively. Additionally, the tag antenna simulated radiation efficiency was -0.9 dB and the radiation efficiency of the tag antenna with the tuning circuit was 0.7 dB.

4.4.3 Theoretical Read Range

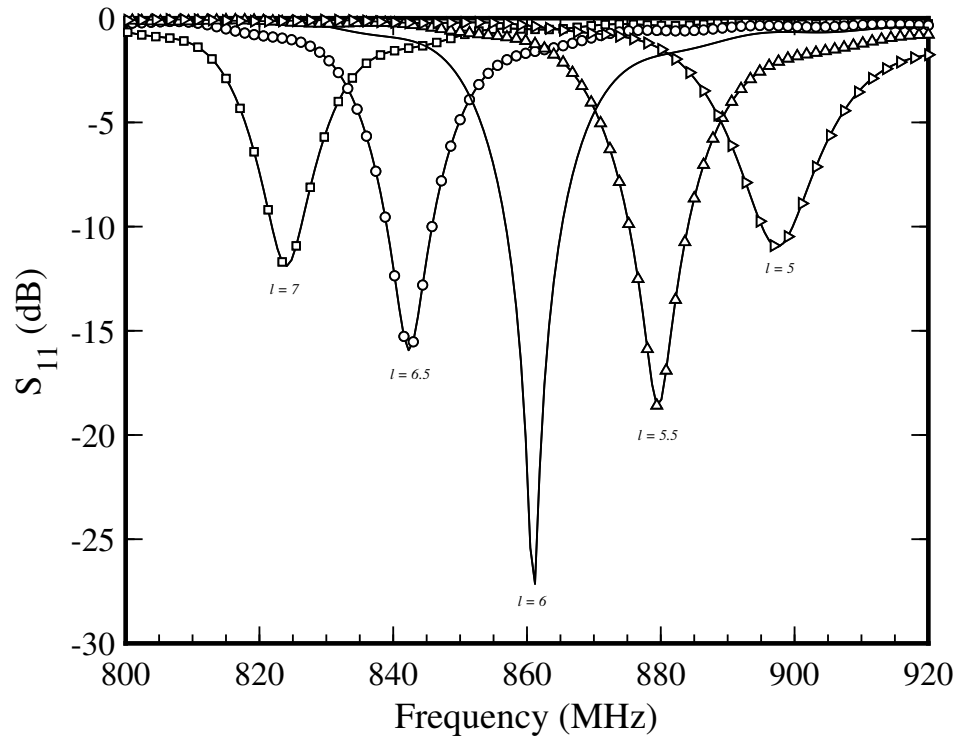
4.4.3.1 Normal Tag

Theoretical read range of the tag can be calculated using the Friis free-space formula:

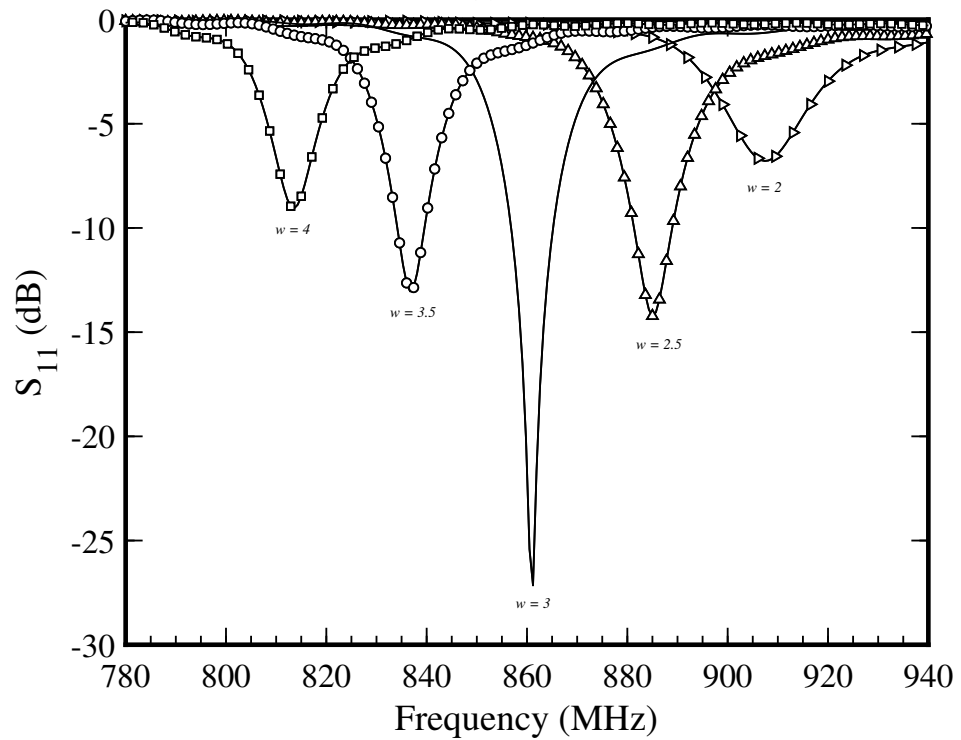
$$r_{max} = \frac{\lambda_0}{4\pi} \cdot \sqrt{\frac{EIRP \cdot G_r \cdot \tau}{P_{IC}}} \quad (4.2)$$

Table 4.12: Simulated gain (G_t), realised gain ($rlsd.G_t$) and radiation efficiency (η_e) of the proposed tag at 868 MHz by varying the design parameter w .

w (mm)	2	2.5	3	3.5	4
$G_t(dB)$	0.73	0.99	0.74	1.41	-0.22
$rlsd.G_t(dB)$	-11.56	-4.59	-0.45	-7.49	-11.71
$\eta_e(dB)$	-0.68	-0.37	-0.72	-0.03	-1.59



(a)



(b)

Figure 4.26: Simulated power reflection coefficient against frequency: (a) with different values of l in mm; and (b) w in mm while other parameters in Table 4.8 and 4.9 were fixed.

where λ_0 is the wavelength, EIRP is the effective isotropic radiative power transmitted by the reader antenna, and P_{IC} is the tag chip sensitivity which is the minimum threshold power

required to turn on the tag chip. The values of these parameters are following:

$$\lambda_0 = 345.62 \text{ mm } (f_0 = 868 \text{ MHz})$$

$$P_{IC} = -16.1 \text{ dBm } (= 0.0245 \text{ mW})$$

$$EIRP = 3.28 \text{ W}$$

The simulated value of the tag realised gain (G_r) and reflection coefficient (S_{11}) are:

$$G_r = 0.159 \text{ dB } (= 1.03)$$

$$S_{11} = -6 \text{ dB } (= 0.2511)$$

$$\tau = 1 - |S|^2 (= 0.9369)$$

The maximum theoretical distance between tag and reader can be calculated to be:

$$r_{max} = 9.92 \text{ m}$$

4.4.3.2 Tag with Tuning Circuit

The simulated value of the tag realised gain (G_r) and reflection coefficient (S_{11}) are:

$$G_r = -0.455 \text{ dB } (= 0.9005)$$

$$S_{11} = -10.25 \text{ dB } (= 0.0944)$$

$$\tau = 1 - |S|^2 (= 0.9910)$$

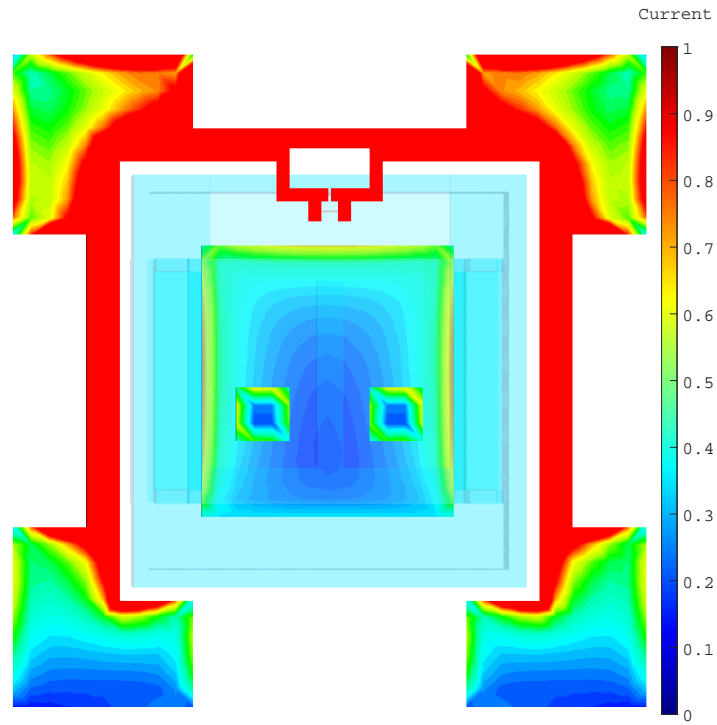
The maximum theoretical distance between tag and reader can be calculated to be:

$$r_{max} = 9.5 \text{ m}$$

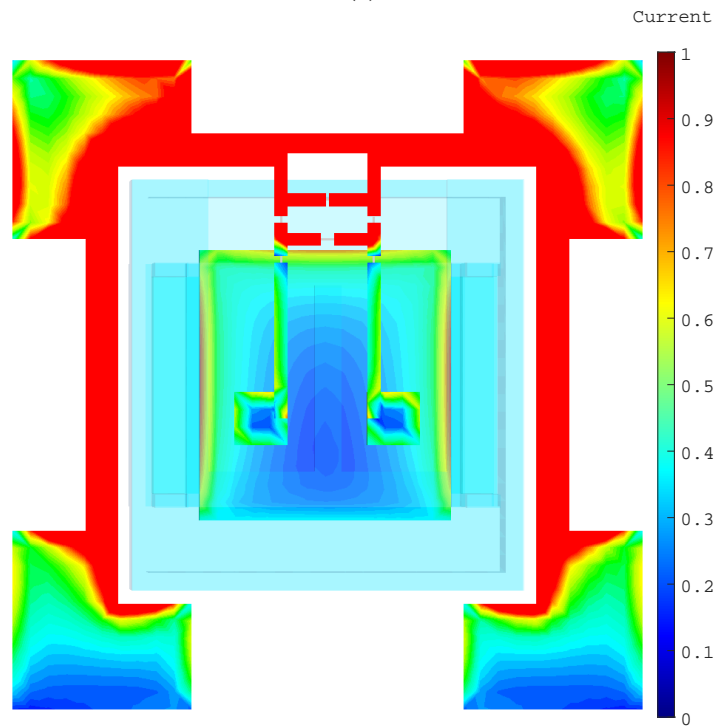
4.4.4 Measurement Results

4.4.4.1 Sensor Code and Read Range

In the first experiment, the antenna was etched onto the Mylar film, of copper thickness 0.18 mm, Figure 4.22(a). A 0.3 pF capacitor was soldered across the antenna terminals. The tag was mounted at the bottom of the current transformer. The UHF RFID reader Tagformance Pro System was used to measure the tag performance. The tag was placed 30 cm



(a)



(b)

Figure 4.27: Normalised magnitude of the surface current distribution of the tag antenna mounted on the transformer: (a) the tag antenna with a 0.3 pF capacitor across the terminals; and (b) the tag connected with the tuning circuit.

away from a linear polarised antenna of 6 dBi gain, as mentioned above.

Figure 4.29 illustrates the measured sensor code of the tag. The sensor code of the tag is fine-tuned to 868 MHz to achieve the maximum sensing range (0–31) of the tag. The read range of the tag across different frequencies, Figure 4.29 and a good read range of about 3 m

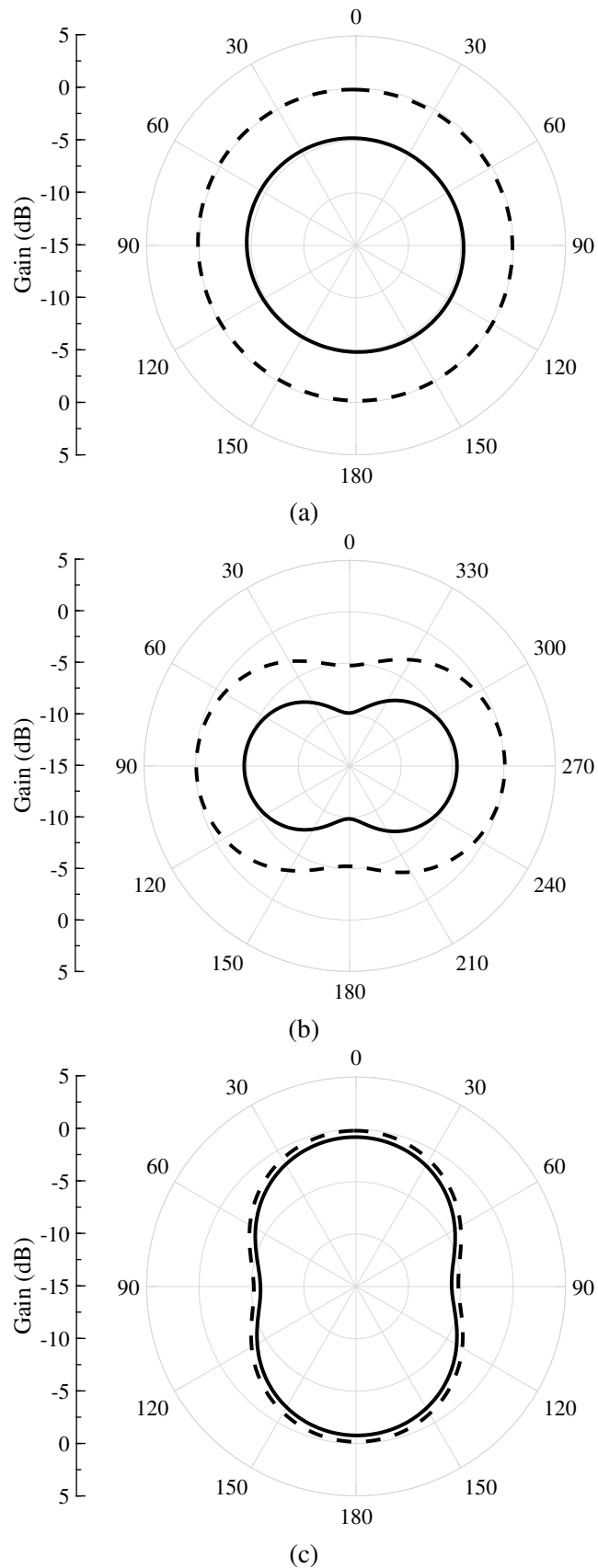


Figure 4.28: Polar plot of CST simulated tag system realised gain: (a) yz -plane; (b) azimuth plane; and (c) xz -plane. Solid line: normal tag antenna with a 0.3 pF capacitor across the terminals. Dashed line: tag connected with the tuning circuit.

is observed at the UHF band (860–868 MHz).

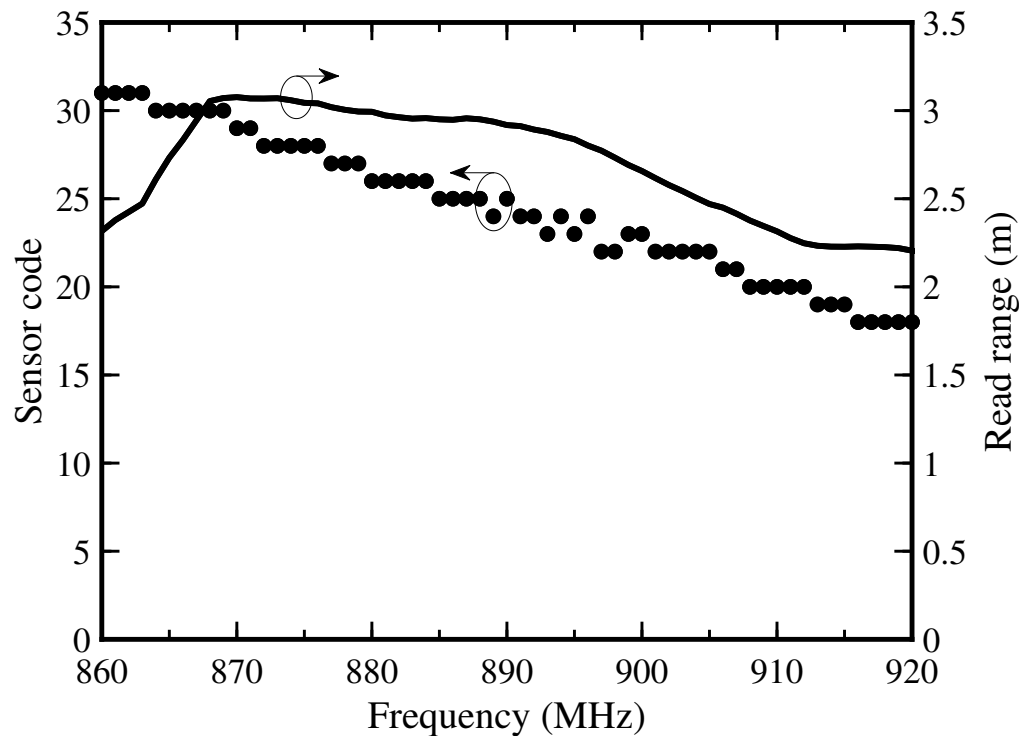


Figure 4.29: Measured sensor code and read range of the tag with a 0.3 pF capacitor across the antenna terminals.

4.4.4.2 Current Sensing Setup

In the final experiment, the tag was linked with the tuning circuit and fabricated on the Mylar film. The lumped elements were soldered across the slots. The end of the copper tracks of the tuning circuit was connected to the output terminals of the CT via M3 screws, Figure 4.30. The tag was tested with the Tagformance Pro system as described earlier and the reader antenna was placed 30 cm away from the tag. The CT was clamped around a single electrical conductor and the split-core part of the CT was enclosed in an insulated box. A switchable electrical load was used to draw ac current from 1 A to 13 A and the electrical load was powered from a 240 V ac power outlet with the operating frequency of 50/60 Hz. A current meter was included in the set up to measure the ac current drawn by the electrical load and standardised the sensor code of the tag device.



Figure 4.30: Manufactured prototype of the RFID tag system.

4.4.4.3 Current to Sensor Code Relationship

The ac current measurements were performed from 0 A to 13 A with a step of 0.5 A and each measurement was made 10 times for a single tag. Figure 4.31 illustrates the measured sensor code and is compared with the ac current flow in the power cable to an electrical load. The measurement results suggest that the tag system can detect ac current in the range of 1 A to 13 A with a resolution of 0.5 A. At 0 A the output capacitance of the tuning circuit is maximum and therefore the tag is detuned from 868 MHz.

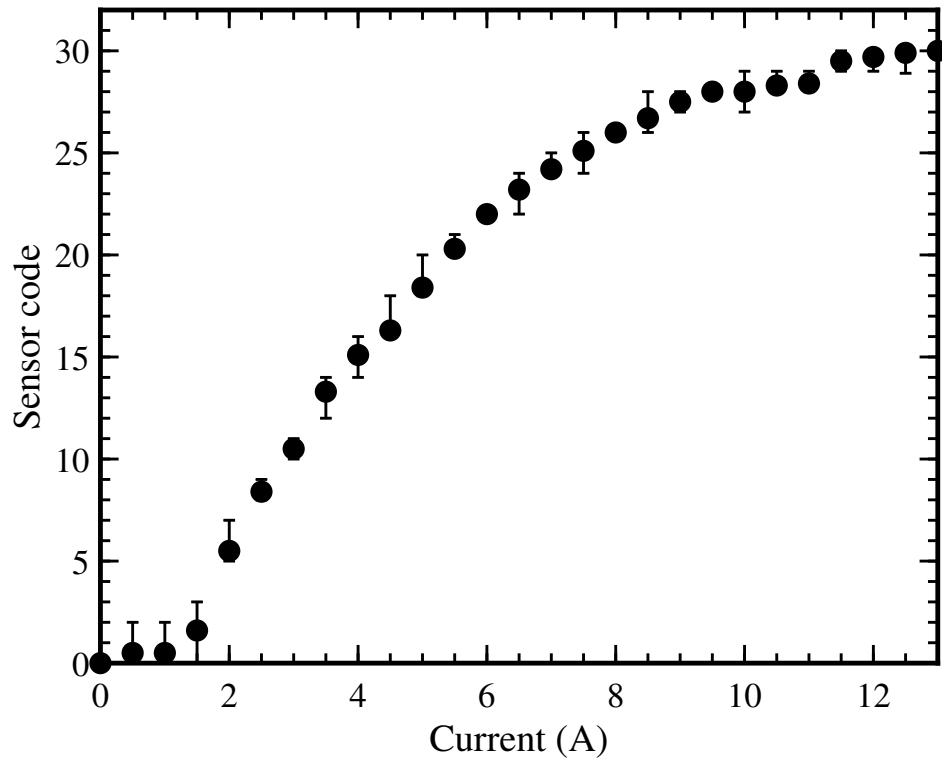


Figure 4.31: Measured sensor code of the tag system at 868 MHz.

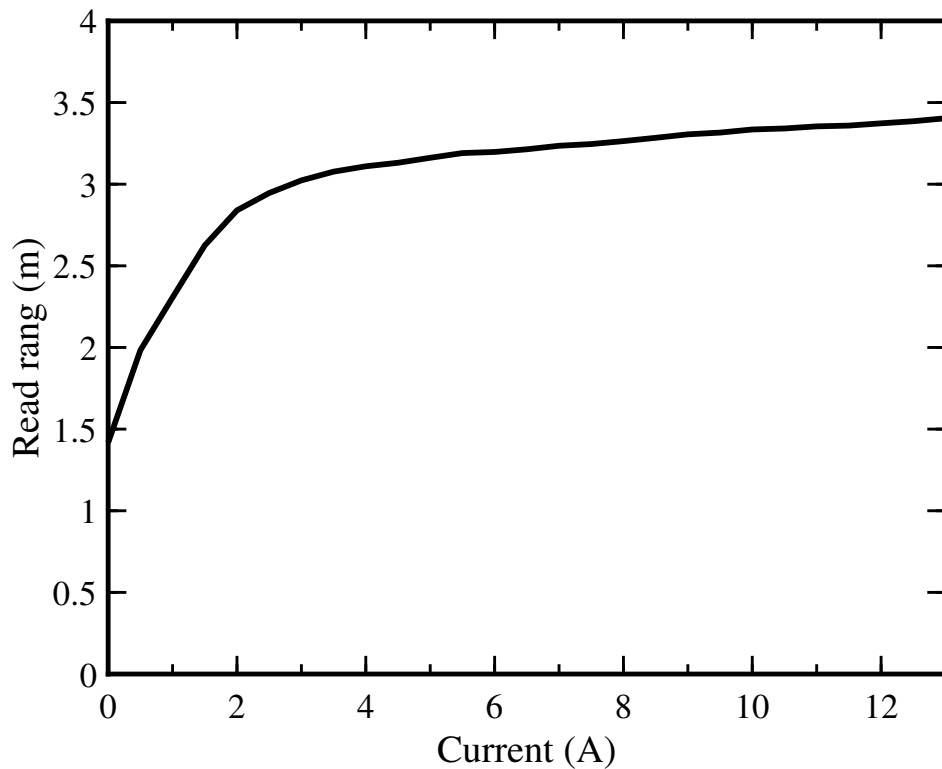


Figure 4.32: Measured read range of the tag system at 868 MHz.

Furthermore, the tag device response is saturated at 12 A, because the reactance of the tuning diode becomes saturated when the bias voltage reached to 12 V. However, the input current sensing range of the tag devices can be increased above 13 A by adjusting the reac-

tance of the tuning circuit of the system. Furthermore, Figure 4.32 shows the measured read range of the tag of about 3 m to 3.5 m across the all current reading at 868 MHz. The lowest read range of 1.4 m was recorded at 0 A because the tuning circuit reactance is at its peak and detune the tag from 868 MHz.

The tag was placed at a different distance away from the reader antenna to assess if non-linearities occurred at the short range. At 2 cm the tag response was 22, which is just 2 sensor values less than the value measured at 30 cm. Additionally, the distance between the tag and the reader antenna was gradually increased and at 7 cm the tag response returned to the original value for 30 cm. The effect of distance difference between the tag and the interrogator antenna on the sensor value of the tag system can be seen in Figure 4.33.

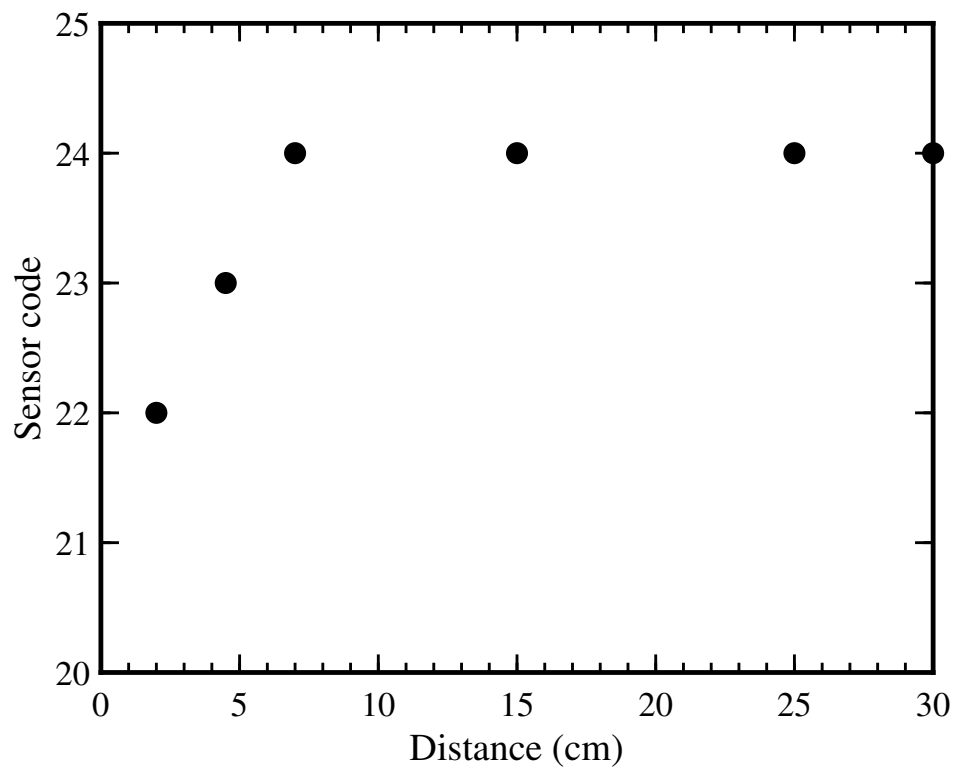


Figure 4.33: The effect of distance variation between the tag system and the reader antenna on the sensor code of the tag system at 868 MHz.

4.5 Further Tag Antenna Optimisation

In order to maximise the tag read range, further simulations were carried out to improve the realised gain of the tag antenna (Figure 4.2). The high-gain antenna will help to increase the read range of the tag antenna. It was observed that adding more copper to the two radiating arms of the antenna bent around the transformer can increase the antenna gain by 0.3 dB.

The new optimised tag antenna with increased antenna gain is depicted in Figure 4.34. The dimensions of the tag antenna are identical to the tag antenna shown in Figure 4.2(a) excluding extra copper added to both radiating arms of the tag antenna. However, the resonance frequency of the tag antenna, Figure 4.35, remain the same when compared to the resonance frequency of the tag antenna shown in Figure 4.24.

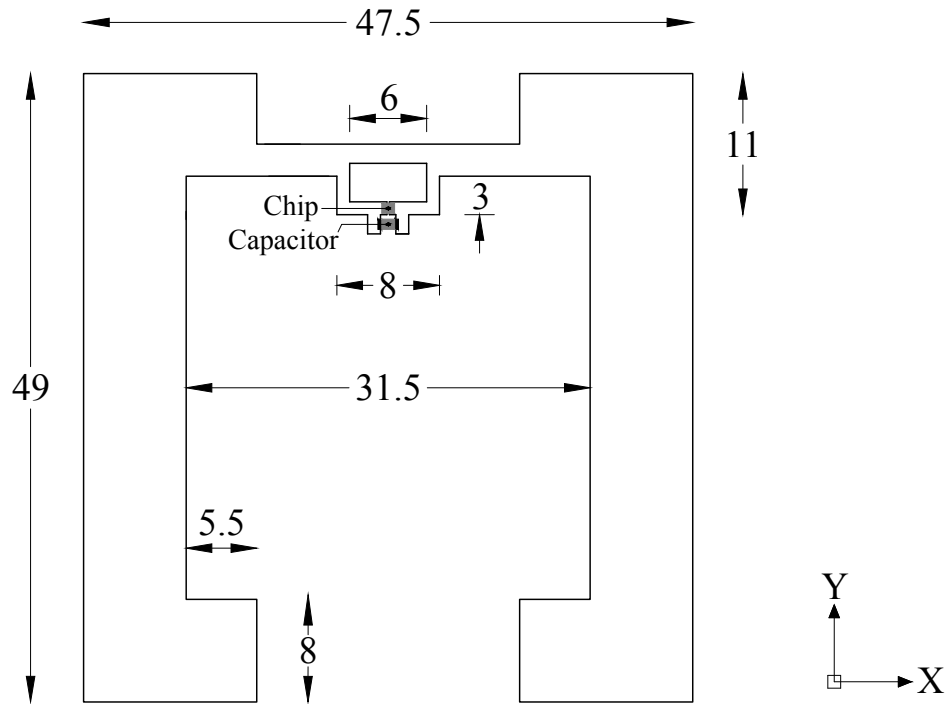


Figure 4.34: Geometry of the tag antenna with increased realised gain.

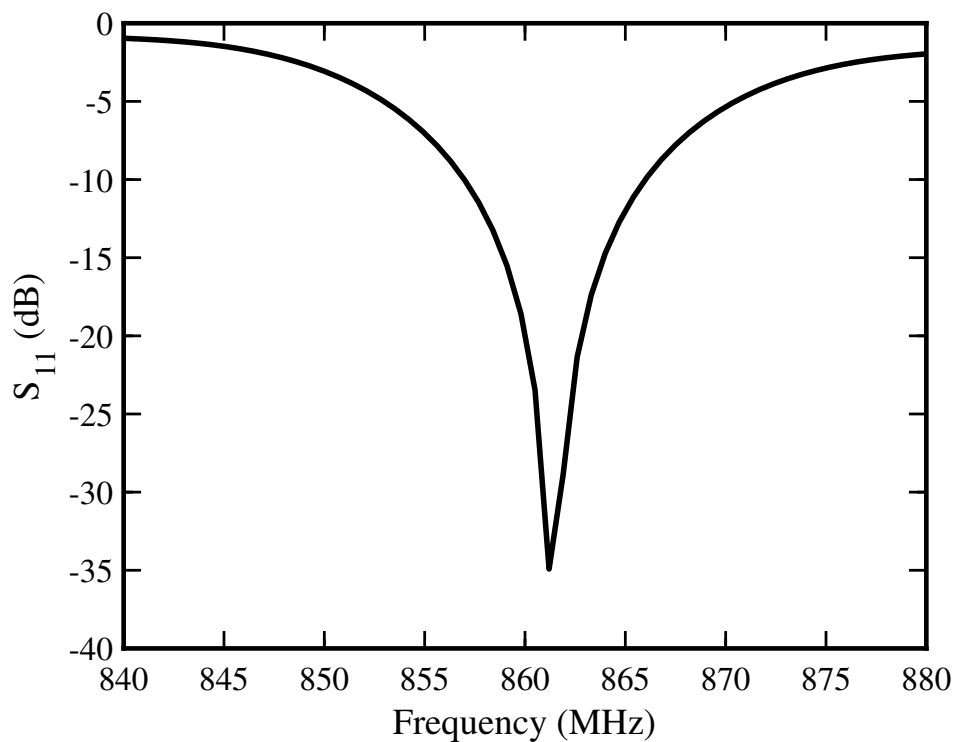


Figure 4.35: Simulated reflection coefficient of the tag antenna with increased realised gain.

4.5.1 Measurement Results

The tag antenna (Figure 4.34) was etched on the Mylar film and the manufactured tag prototype is depicted in Figure 4.36. A tag chip and a capacitor of 0.3 pF was attached across the terminals. The tag was interrogated with the RFID reader, as described earlier.

Figure 4.37 shows the measured sensor code and read range of the sensing tag. It is observed that the read range of the tag is 4 m at 868 MHz which is 1 m greater when compared to the previous sensing tag. Furthermore, the sensor code of the sensing tag is 27 at 868 MHz, indicating the tag is well tuned.

Moreover, the self-tuning action of the chip is activated at 855 MHz (Figure 4.37), which means that the tuning of the tag can be further optimised to alter the sensor response right at 868 MHz.

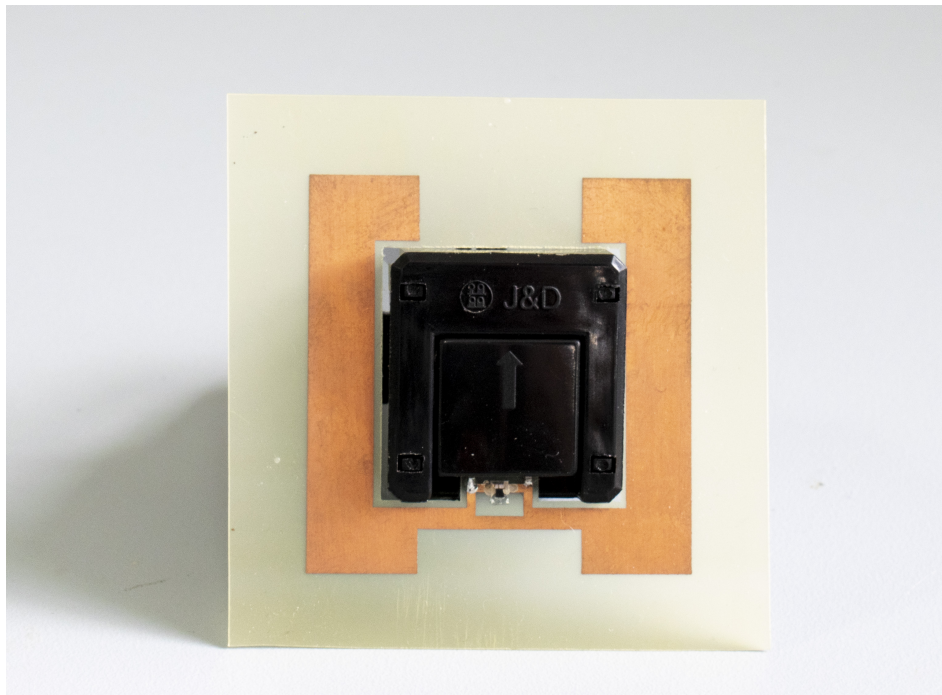


Figure 4.36: A prototype of the tag antenna with increased realised gain.

4.5.2 Sensor Comparison

Table 4.13 shows the comparison of the proposed tag system with the commercial alternative ac current meters. The total cost of the tag device is inclusive of the cost of the CT (\$45.00) and the estimated cost of the tag (\$5.00). In order to be cost-effective for a domestic setting the RFID reader should be redeveloped for domestic use and price range.

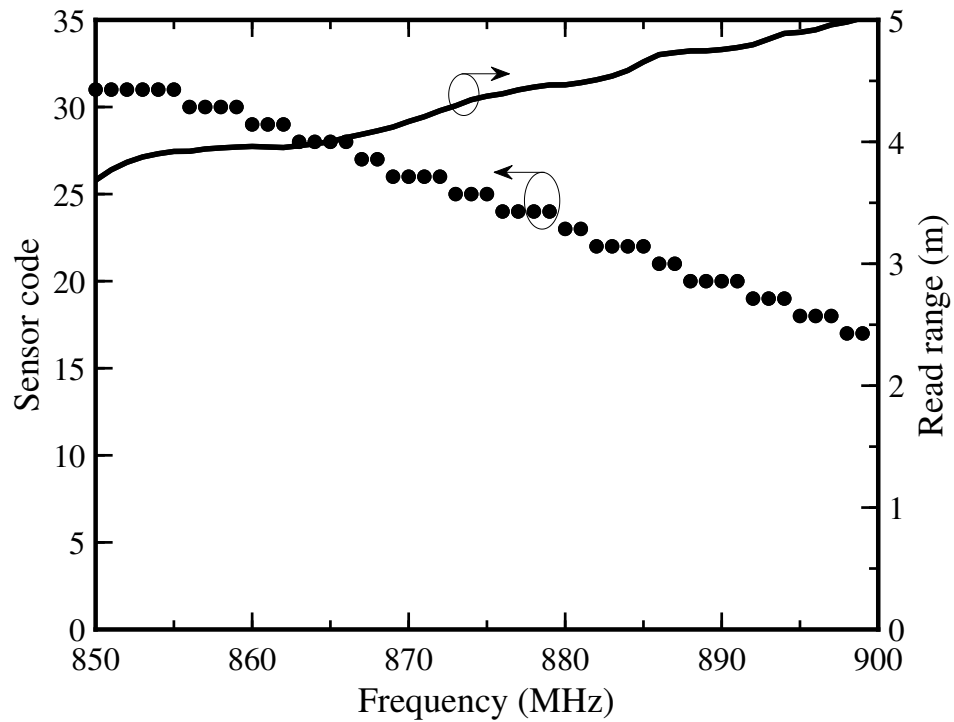


Figure 4.37: Measured sensor code and read range of the tag antenna with increased realised gain.

Figure 4.38 shows the comparison between the optimised tag antenna and previously proposed tag antenna design for ac current sensing system. The optimised tag antenna is formed of balanced lines wrapped around transformer housing occupies a small volume of $47.5 \times 49 \text{ mm}^2$ compares to the previously proposed antenna design which occupies area of $94 \times 24 \text{ mm}^2$.

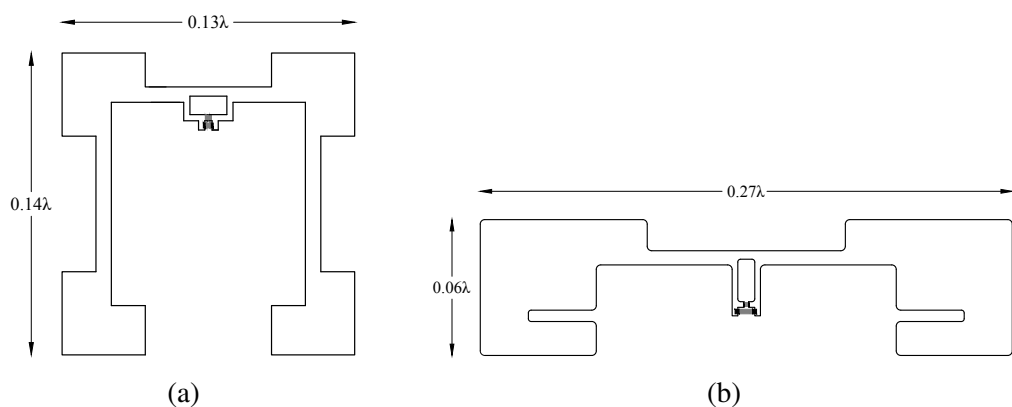


Figure 4.38: Comparison between the tag antenna designs for ac current sensing system: (a) optimised tag antenna; and (b) previously proposed tag antenna design.

Table 4.13: Comparison between the proposed tag system and commercial alternative ac current meters in terms of communication, cost, current range and power type.

Ref.	Sensors	Communication	Cost (\$)	Current Range (A)	Power Type
[15]	IoT long range wireless ac current monitor	DigiMesh protocol	179.95	0–100	Active
[16]	Alta wireless ac current meter - 20 A - AA battery powered	Monnit proprietary protocol	150.00	0–20	Active
[17]	Pressac current sensor: one channel	Enocean wireless radio protocol	98.00	0–60	Passive
[18]	SCT-125W-100 by Mag-nelab	IEEE 802.15.4, 2.4 GHz technology	245.00	0–100	Active
[19, 20]	AC power meter	Universal serial bus	–	0–100	Active
[32]	Web based smart meter	WiFi network	–	0–100	Active
[22]	Piezoelectromagnetic wireless current monitoring system	Digi XBee radio	–	0–20	Active
[23]	Smart power meter	Wired network	–	0–20	Active
[1]	Single tag system	Radio frequency Identification	50.00	2–10	Passive
—	Optimised single tag system	Radio frequency Identification	50.00	1–13	Passive

4.6 Conclusion

In this chapter, we demonstrated novel UHF RFID tags and antenna designs for an ac current transformer for measuring real-time ac current in smart power metering systems. The tags and antenna designs were experimentally tested with a switchable electrical load and the measured results show that the sensing tag can detect ac current in the range of 1 A to 13 A with a resolution of 0.5 A and has a good read range of between 3 and 3.5 m through all current readings at 868 MHz. However, the input current sensing range of the tag devices can be increased above 13 A by adjusting the reactance of the tuning circuit of the sensing system. The tag system has a very simple structure as compared to microcontroller-based smart electricity metering and can be used for real-time monitoring of power consumption

of multiple appliances with a single RFID reader at smart homes.

The main contribution of this chapter has been,

- Demonstration of a tag antenna designing technique for a current transformer.
- Three novel tag antennas designs for a current transformer.
- Increase in the current sensing range of the tag system.

In the next chapter, a dual tag system for ac current sensing is presented.

References

- [1] I. Ullah, R. Horne, B. Sanz-Izquierdo and J. C. Batchelor, “RFID AC Current Sensing Technique,” in *IEEE Sensors Journal*, vol. 20, no. 4, pp. 2197–2204, Feb.15, 2020, doi: 10.1109/JSEN.2019.2949856.
- [2] I. Ullah, R. Horne, B. Sanz-Izquierdo and J. C. Batchelor, “UHF RFID Tag Design for AC Current Sensing,” *IET’s Antennas and Propagation Conference (APC–2019)*, Birmingham, UK, Nov. 11–12, 2019, pp. 1–4, doi: 10.1049/cp.2019.0728.
- [3] Computer Simulation Technology (CST) Microwave Suite 2017. [Online]. Available: <https://www.cst.com>
- [4] GTS flexible by design (2020, Apr. 20), [Online]. Available: <https://www.gts-flexible.com/home/>
- [5] Axzon Sensing Data Insights (2020, Apr. 01). Chameleon Sensor Engine [Online]. Available: <http://rfmicron.com/technology/chameleon/>
- [6] Axzon (2019, Feb. 10). RFM2100 wireless flexible moisture sensor [Online]. Available: <https://axzon.com/rfm2100-wireless-flexible-moisture-sensor/>
- [7] Magnelab (2019, Feb. 10). DCT-0016-10/10Vdc split-core current sensor [Online]. Available: <http://www.magnelab.com/products/ac-splitcore-current-sensor-dct-0016-100/>
- [8] Skyworks (2019, Feb. 5). SMV2019 series hyperabrupt junction tuning varactors [Online]. Available: https://www.skyworksinc.com/Product/668/SMV2019_Series

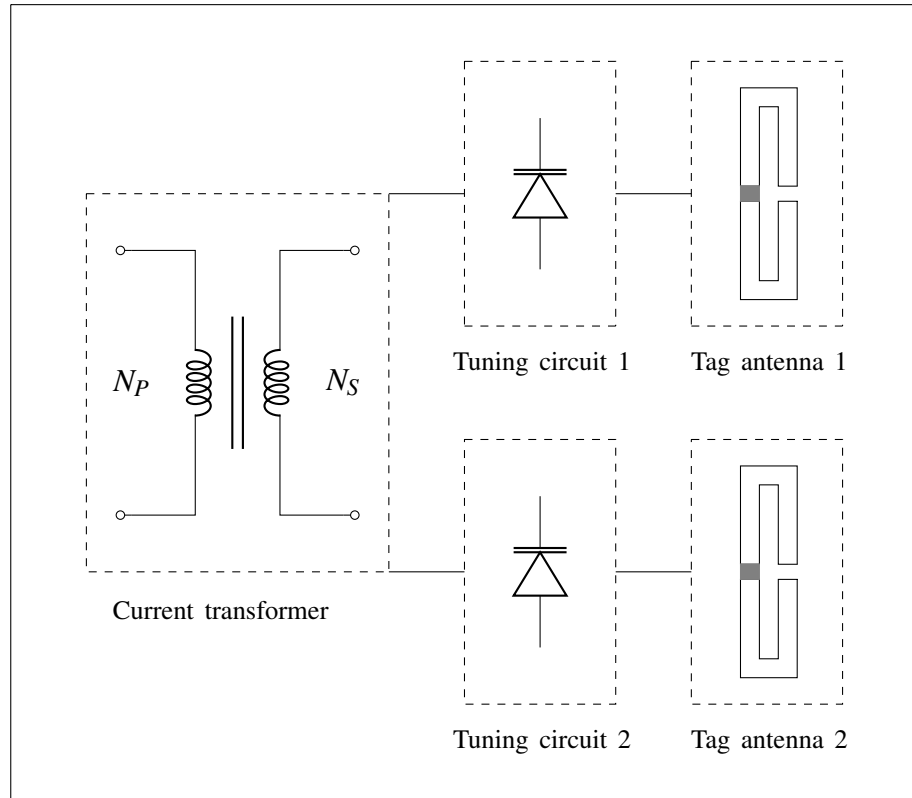
- [9] Skyworks, “SMV2019 to SMV2023 series: hyperabrupt junction tuning varactors,” SMV2019 to SMV2023 varactors datasheet, Aug. 2015.
- [10] Voyantic (2019, Feb. 10). Tagformance Pro [Online]. Available: <http://voyantic.com/products/tagformance-pro>
- [11] S. Zuffanelli, P. Aguila, G. Zamora, F. Paredes, F. Martin, J. A. Bonache, “High-Gain Passive UHF-RFID Tag with Increased Read Range.” *Sensors* 2016, 16, 1150. <https://doi.org/10.3390/s16071150>
- [12] C. Calabrese and G. Marrocco, “Meandered-Slot Antennas for Sensor-RFID Tags,” in *IEEE Antennas and Wireless Propagation Letters*, vol. 7, pp. 5–8, 2008, doi: 10.1109/LAWP.2007.914123.
- [13] Brennenstuhl smart technology (2018, Feb. 9). Primera-line wattage and current meter PM 231 E [Online]. Available: <https://www.brennenstuhl.co.uk/en-GB/products/adapter-plugs/primera-line-wattage-and-current-meter-pm-231-e-gb>
- [14] I. Ullah, R. Horne, B. Sanz-Izquierdo and J. C. Batchelor, “Tag Design for RFID AC Current Sensing System,” *14th European Conference on Antennas and Propagation (EuCAP)*, Copenhagen, Denmark, 2020, pp. 1–5, doi: 10.23919/EuCAP48036.2020.9135550.
- [15] NCD (2019, Aug. 26). IoT long range wireless ac current monitor [Online]. Available: <https://store.ncd.io/product/wireless-ac-current-monitor/>
- [16] Monnit (2019, Aug. 26). Alta wireless ac current meter - 20 A - AA battery powered [Online]. Available: <https://www.monnit.com/Product/MNS2-9-W2-CM-020/>
- [17] Pressac (2019, Aug. 26). Current sensor: one channel [Online]. Available: <https://www.pressac.com/current-monitoring-sensors/>
- [18] Magnelab (2019, Aug. 26). SCT-125w-100 by Magnelab [Online]. Available: <https://www.magnelab.com/products/wireless-ac-current-sensor-system-sct-125w/>
- [19] N. Tamkittikhun, T. Tantidham and P. Intakot, “AC power meter design based on Arduino: Multichannel single-phase approach,” in *2015 International Computer Science*

- and Engineering Conference (ICSEC)*, Chiang Mai, 2015, pp. 1–5, doi: 10.1109/IC-SEC.2015.7401422.
- [20] N. Tamkittikhun, T. Tantidham and P. Intakot, “AC power meter design for home electrical appliances,” in *2015 12th International Conference on Electrical Engineering/Electronics, Computer, Telecommunications and Information Technology (ECTI-CON)*, Hua Hin, 2015, pp. 1–6, doi: 10.1109/ECTICon.2015.7207005.
- [21] S. Yildiz and M. Burunkaya, “Web Based Smart Meter for General Purpose Smart Home Systems with ESP8266,” in *2019 3rd International Symposium on Multidisciplinary Studies and Innovative Technologies (ISMSIT)*, Ankara, Turkey, 2019, pp. 1–6, doi: 10.1109/ISMSIT.2019.8932931.
- [22] Q. R. Xu, I. Paprotny, M. Seidel, R. M. White and P. K. Wright, “Stick-On Piezoelectromagnetic AC Current Monitoring of Circuit Breaker Panels,” in *IEEE Sensors Journal*, vol. 13, no. 3, pp. 1055–1064, March 2013, doi: 10.1109/JSEN.2012.2234738.
- [23] R. Morello, C. De Capua, G. Fulco and S. C. Mukhopadhyay, “A Smart Power Meter to Monitor Energy Flow in Smart Grids: The Role of Advanced Sensing and IoT in the Electric Grid of the Future,” in *IEEE Sensors Journal*, vol. 17, no. 23, pp. 7828–7837, 1 Dec.1, 2017, doi: 10.1109/JSEN.2017.2760014.

Dual RFID Tag System

5.1 Introduction

IN this chapter, a novel dual tag system with an increased current sensing range from 0 A to 13 A is described. The dual tag system consists of a current transformer, two tuning circuits and two RFID tags, as shown in Figure 5.1. The total reactance of the tuning circuit 1 and tuning circuit 2 is different from each other. However, the tag antennas design are identical. The tag antennas are designed in close proximity to reduce the overall size of the tag device while achieving lower mutual coupling between the tag antennas. Each tag antenna terminals are linked with the respective tuning circuit and integrated with a single transformer. Because of the limited sensing resolution of the tag chip, the tuning circuits with the different reactance configuration, fed by the same transformer will help to sense the low or high level current (referring to 0–13 A) whereas the previously proposed single tag system [1–3] was not able to detect. Therefore, the tag system resolution can be increased by using multiple tag chips in a single design. This study aims to analyse how the current sensing range of the tag system can be increased by using multiple tag chips in a single design. In addition, the study also explores how two RFID tags can be detected and read with a single UHF RFID reader. This chapter is organised as follows: In Section 5.2, a novel two tag antennas design is proposed. The two tag antennas are further optimised and presented in Section 5.3. Followed by Section 5.3.4 in which the theoretical read range of the tags is discussed. Finally, Section 5.4 concludes the chapter.



Dual tag system

Figure 5.1: Schematic diagram of the proposed dual RFID tag system.

5.2 Two Tag Antennas Design

Figure 5.2 shows the geometry of the proposed tag antenna labelled with the design parameters. The values of the antenna parameters are listed in Table 5.1. The tag antenna consists of a loop for feeding and two dipole arms for radiation. The antenna design incorporates with the Magnus S2 tag chip, which has an input impedance of $1.63 \Omega - j 61.07 \Omega$, at 868 MHz. The antenna is printed on a Mylar substrate. The antenna lengths L and width W are 78 mm and 27.5 mm, respectively which can be optimised to obtain an optimal tag performance at the UHF band. The feed loop is used to achieve a good impedance matching between the antenna and the tag chip.

Table 5.1: Simulated tag dipole antenna dimensions.

Parameters (mm)	L	W	S	a	b	c	d	e	f	l	w
	78	27.5	32	23	15	13	9.5	35	48	7	2.7

The antenna shown in Figure 5.2 is integrated to the current transformer, forming a dual

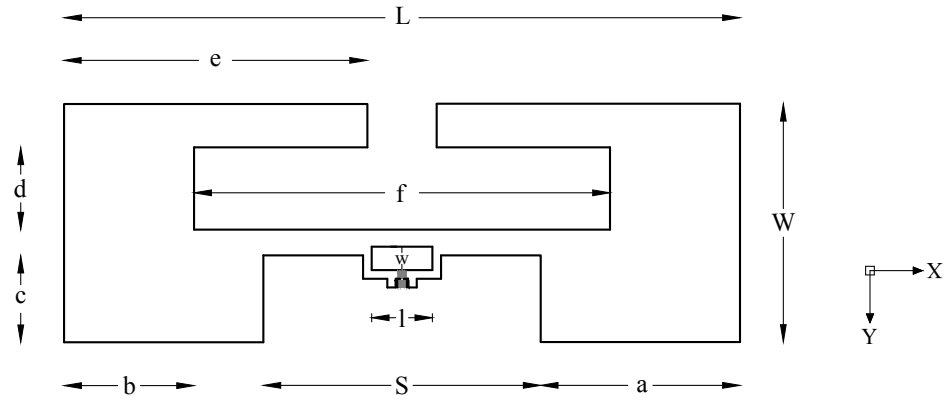


Figure 5.2: Geometry of the proposed tag dipole antenna for dual RFID tag system.

RFID tag system, as shown in Figure 5.3. The geometry of both tag antennas is symmetrical. The total length of the tag antenna is 0.225λ and with the total width of 0.079λ at 868 MHz. The feed loop is 7 mm long and 2.70 mm wide. The width of the copper trace of the feed loop is 1 mm. There is a slot of 0.20 mm in the copper trace of the feed loop where the discrete ports are created. The antennas are well integrated with the transformer by sparing a space of 32 mm long and 10 mm wide in the antennas design. The antennas were simulated on the Mylar substrate with a dielectric constant (ϵ_r) of 2.8, loss tangent ($\tan \delta$) of 0.003 and thickness of 0.18 mm including the copper thickness of 0.04 mm [4], using CST microwave studio [8]. A 0.3 pF capacitor was attached at the antennas terminals. The tag antennas are mounted at the bottom of the transformer. Furthermore, the two identical tag antennas lie on the z -axes and opposite to each other in a symmetrical fashion along y -axes, as shown in Figure 5.3. The transformer lies in between the tag antennas. There is air bridge of 13.68 mm between the tag antennas. By integrating the two RFID tag antennas to the transformer and the overall size of the tag system is $78 \times 68.68 \times 55 \text{ mm}^3$. The Magnus S2 [7] tag chip input impedance is used to simulate the tag antennas in two configurations: (i) single tag antenna mounted at the bottom of the transformer; and (ii) two identical tag antennas are integrated to the transformer (opposite to each other), as shown in Figure 5.3.

5.2.1 Simulation Results

Figure 5.4 illustrates the S-parameters of the tags when they are simulated in two configurations, as described above. It is observed that the reflection coefficient of the signal tag attached to the transformer is -35 dB , which shows a good matching for the antenna impedance to the tag chip impedance at 864 MHz. Furthermore, the resonance frequency of

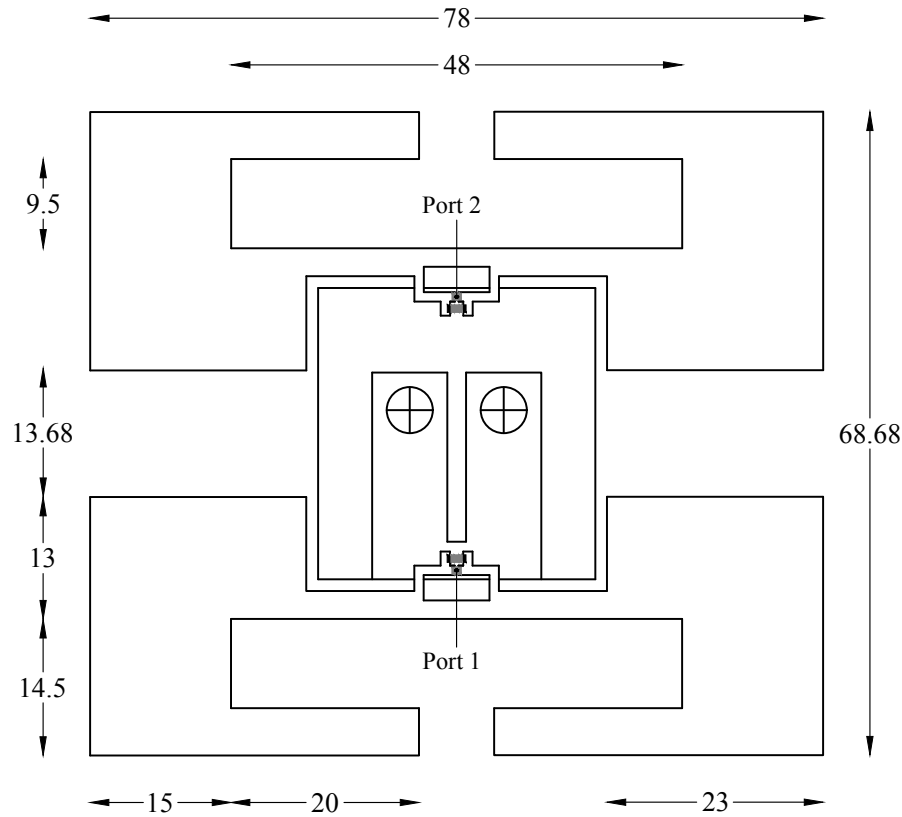


Figure 5.3: Geometry of the proposed two RFID tag antennas design mounted at the bottom of the current transformer. (All dimensions are in mm)

the two tag antennas design is about 858 MHz. However, the tag antenna with the port 1 has less losses as compared to the tag antenna with the port 2. There is a 6 MHz shift in the resonance frequency of the two tag antennas design when compared to the resonance frequency of the single tag antenna design. The S_{21} of -5 dB and S_{12} of -5 dB show the mutual coupling between the radiating elements of the tags at the UHF band. It is observed that there is a strong mutual coupling between the tag antennas. These couplings are mainly due to the two reasons: (i) the tag antennas are located in the same plane; and (ii) the tag antennas are in close proximity and copolarised. However, the resonance frequency of the tags was not shifted of the UHF band because of the strong mutual coupling between the tag antennas, which can degrade the tag antennas performance. Therefore, it was concluded that the tag antennas geometry must be optimised to reduce the coupling between them. Figure 5.5 depicts the normalised magnitude of the current distribution of the tag antennas at 868 MHz. It is observed from Figure 5.5(a) that the maximum current distribution is located in the radiating arms near the feed loop, which radiate more power. The corners of the antennas contribute to less current distribution. Figure 5.5(b) shows the magnitude of the current distribution of the tag antenna with the port 1, as well as the current distribution of the tag antenna with the

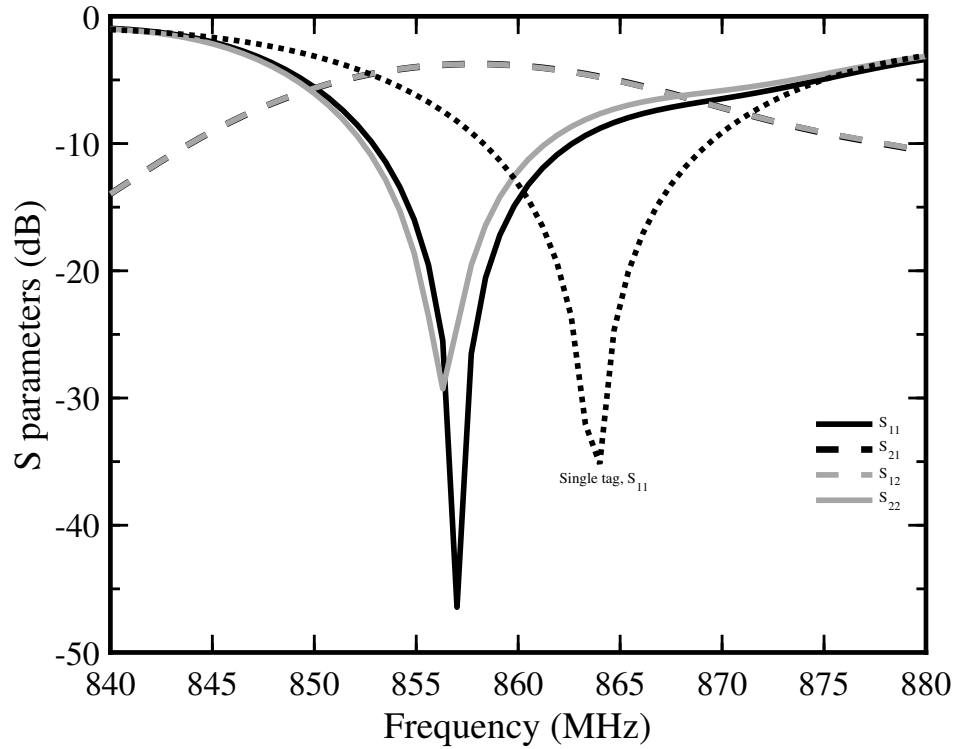
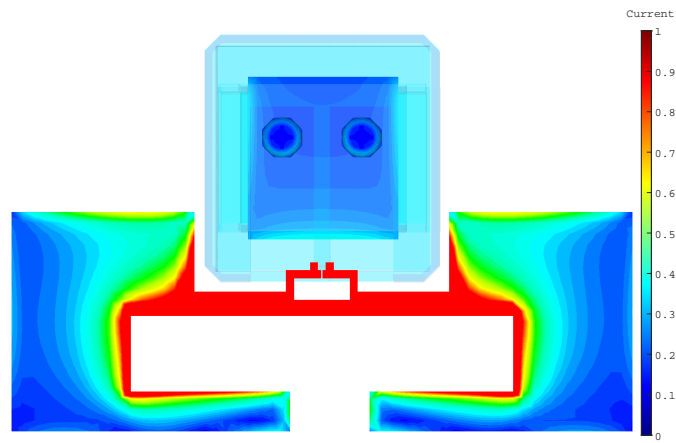
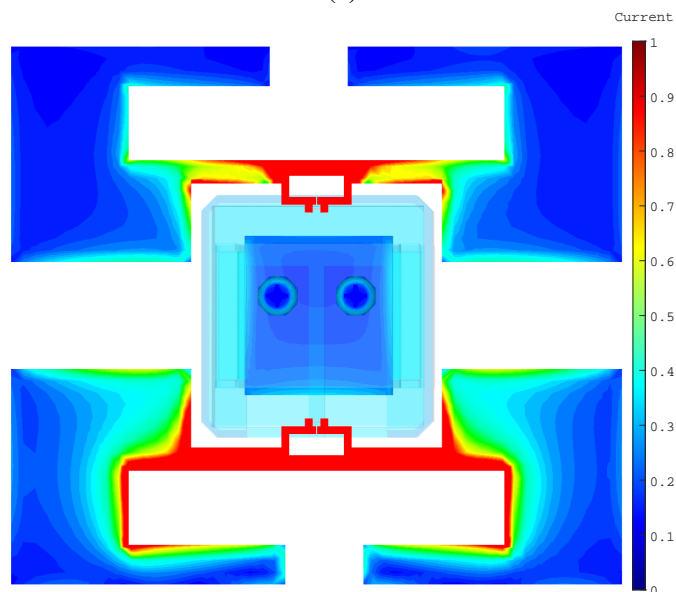


Figure 5.4: Simulated S-parameters. All power reflection coefficients are below -10 dB. The coupling between the radiating elements are above -10 dB.

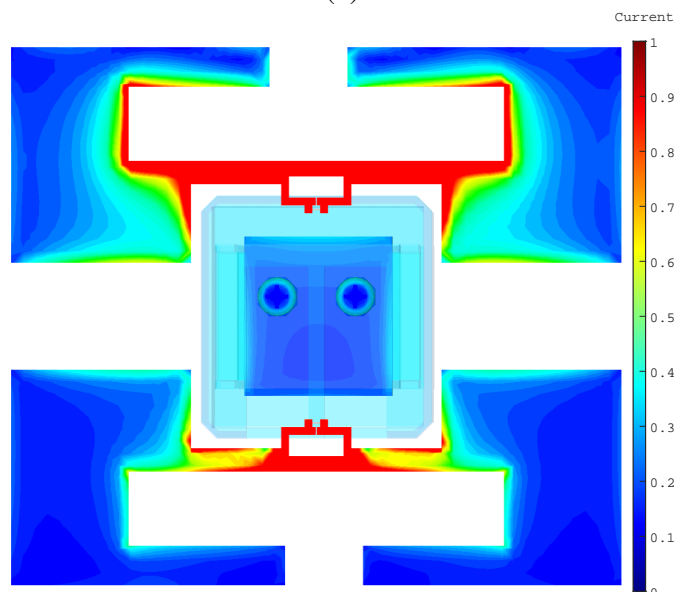
port 2. Similarly, Figure 5.5(c) displays the magnitude of the current distribution of the tag antenna with the port 2. Figure 5.6 illustrates the radiation pattern of the single tag antenna and two tag antennas design. The realised gain of the single tag is 1.15 dB. The realised gain of the two tag antennas design is 0.918 dB for the tag antenna with the port 1 and 0.694 dB for the tag antenna with the port 2. It is observed from the Figure 5.6 that the single tag antenna has a good omnidirectional radiation. However, the radiation pattern of the two tag antennas design has a maximum radiation when the theta (θ) is 90° .



(a)



(b)



(c)

Figure 5.5: The normalised surface current distribution of the tag antennas configurations at 868 MHz: (a) single tag antenna attached to the transformer; (b) tag antenna with the port 1; and (c) tag antenna with the port 2.

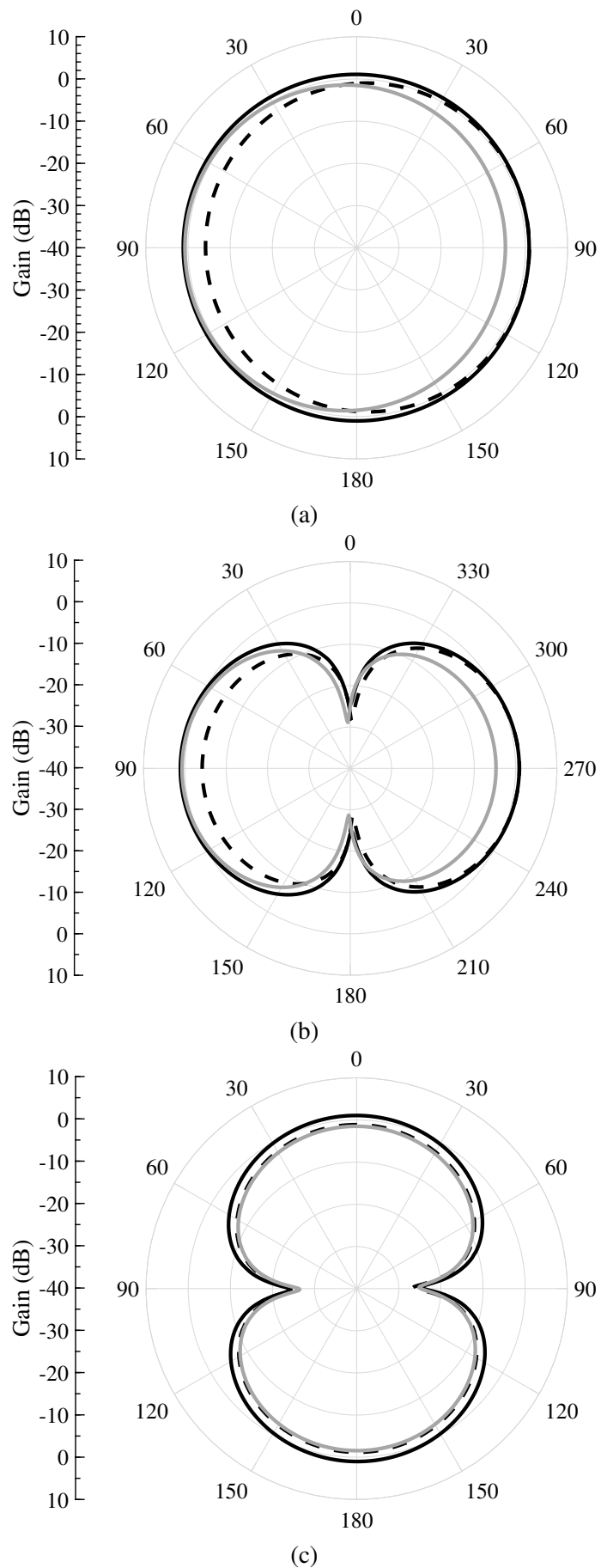


Figure 5.6: Realised gain of the single tag and the two tag antennas design at 868 MHz: (a) yz -plane; (b) xy -plane; and (c) xz -plane. Black solid line: single tag antenna design. Dashed black line: tag antenna design with the port 1. Gray solid line: tag antenna design with the port 2.

5.2.2 Parametric Design Study

A parametric analysis of the tag antenna shown Figure 5.2 is performed using Computer Simulation Technology (CST) Studio Suite to illustrate how the various design parameters listed in Table 5.1 can affect the antenna performance. The tag antenna, Figure 5.2, illustrates the design parameters influencing the tag antenna port impedance, namely, L , W , l , and w . Several simulations were performed to analyse the affect of L , W and the loop length l and width w on the antenna port impedance and the tag resonance frequency. Other parameters shown in Figure 5.2 are kept the same while examining the affect of one of the main parameters.

When the antenna length L gets longer, it is expected that the resonance frequency of the tag will shift toward a lower frequency range. Figure 5.7 presents the antenna port impedance against frequency. The real magnitude of the antenna increases drastically with little change observed in the imaginary magnitude. Figure 5.8 presents the reflection coefficient S_{11} of the tag, indicating an increase in the antenna length L yields to move the resonance frequency of the tag toward a lower frequency range, and vice versa. However, the return losses are decreased and as a result, reducing the power available to the tag chip and degrade the tag performance, i.e read range.

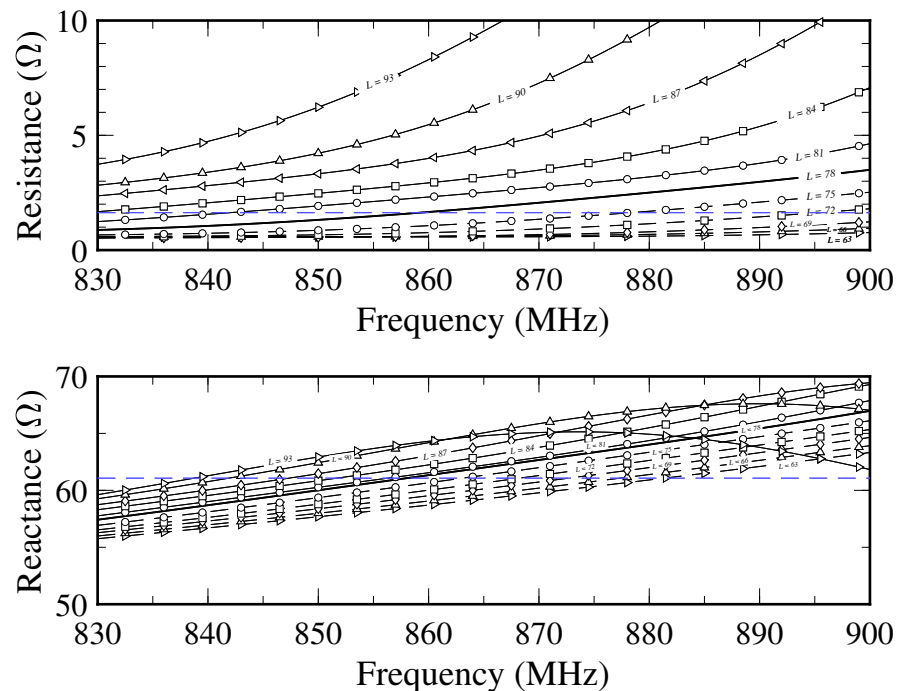


Figure 5.7: Effect of the design parameter L in mm on the antenna port impedance while other parameters in Table 5.1 were fixed.

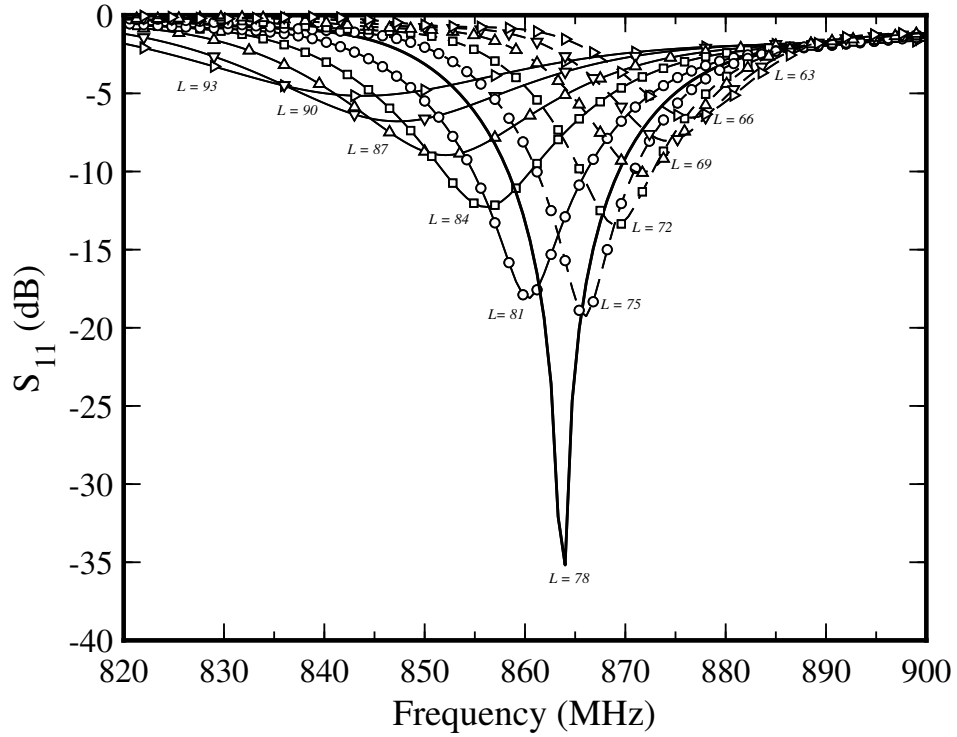


Figure 5.8: Effect of the design parameter L in mm on the reflection coefficient S_{11} of the tag while other parameters in Table 5.1 were fixed.

Moreover, Table 5.2 presents the antenna port impedance ($Z_{ant.}$), gain (G_t , excluding the impedance mismatch loss), realised gain ($rlsd.G_t$, including the impedance mismatch loss) and radiation efficiency (η_e) of the proposed tag at 868 MHz by varying the design parameter L . As the antenna length L increases, the tag antenna gain is increased as well. The antenna length and width mainly determine the antenna gain, in other words, the bigger the antenna, the higher the antenna gain, resulting in a higher read range.

Table 5.2: Simulated antenna port impedance, gain, realised gain and radiation efficiency of the proposed tag at 868 MHz by varying the design parameter L .

L (mm)	63	66	69	72	75	78	81	84	87	90	93
$Z_{ant.} (\Omega)$	0.57 +j59.62	0.61 +j60.02	0.65 +j60.55	0.89 +j61.10	1.2 +j61.79	1.92 +j62.42	2.66 +j62.69	3.39 +j63.53	4.79 +j64.53	6.96 +j65.62	10.47 +j65.01
$G_t (dB)$	0.61	0.63	0.78	1.01	1.2	1.57	1.7	1.9	2.08	2.13	2.12
$rlsd.G_t (dB)$	-2.5	-1.12	0.02	0.77	1.15	1.14	1.01	0.45	-0.17	-0.91	-1.45
$\eta_e (dB)$	-1.42	-1.4	-1.2	-1.07	-0.79	-0.49	-0.29	-0.09	0.01	0.05	0.06

Furthermore, Figure 5.9 depicts the antenna port impedance against frequency when the width W of the antenna changes from 18.5 mm to 36.5 mm. As expected, the real magnitude of the antenna increases with an increase in the antenna width W , while a little variation

observed in the imaginary magnitude. Figure 5.10 depicts the reflection coefficient S_{11} of the tag when the antenna width W changes from 18.5 mm to 36.5 mm. When the width $W = 36.5$ mm, the tag resonance frequency has shifted to 835 MHz. Alternatively, when the width $W = 18.5$ mm, the tag resonance frequency has shifted to about 880 MHz. Therefore, it is concluded that the width W influences the resonance frequency of the tag and can be adjusted for achieving a resonance within the band of interest. Additionally, as the antenna width W increases, the antenna gain increases at first and then decreases, as summarised in Table 5.3.

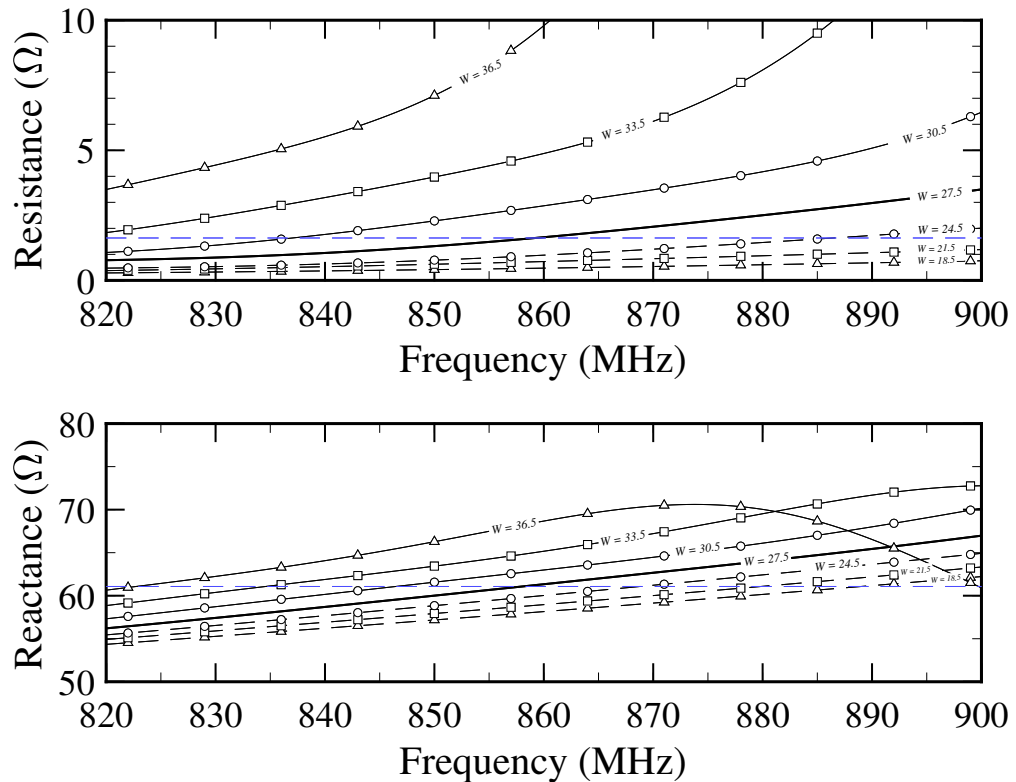


Figure 5.9: Simulated antenna port impedance with varying the antenna width W in mm while other parameters in Table 5.1 were fixed.

Table 5.3: Simulated antenna port impedance, gain, realised gain and radiation efficiency of the proposed tag at 868 MHz by varying the design parameter W .

W (mm)	18.5	21.5	24.5	27.5	30.5	33.5	36.5
$Z_{ant.}(\Omega)$	$0.52+j58.97$	$0.81+j59.83$	$1.15+j61.01$	$1.92+j62.42$	$3.37+j64.20$	$5.86+j66.84$	$13.26+j70.23$
$G_t(dB)$	1.34	1.04	1.13	1.57	1.98	1.86	1.65
$rlsd.G_t(dB)$	-3.80	-0.77	0.95	1.14	-0.10	-2.06	-3.55
$\eta_e(dB)$	-0.75	-1.04	-0.96	-0.49	-0.04	-0.12	-0.34

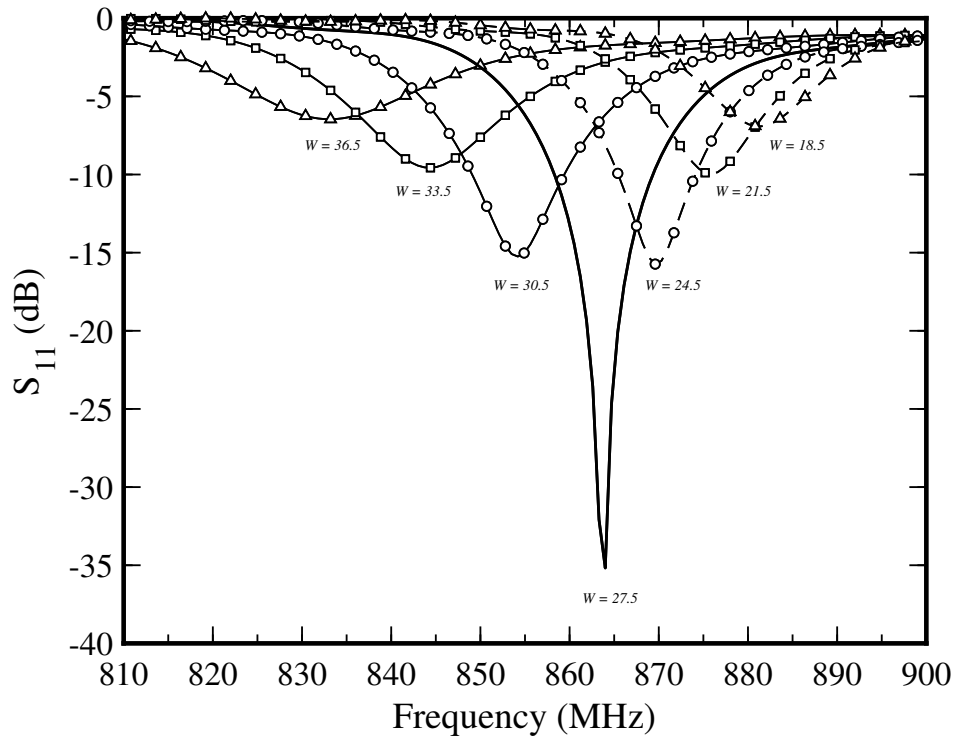


Figure 5.10: Simulated power reflection coefficient of the tag with varying the antenna width W in mm while other parameters in Table 5.1 were fixed.

As mentioned earlier that the feeding loop strongly affects the tag performance. The size of the loop can be adjusted for shifting the resonance frequency of the tag as well as for aligning the antenna impedance within the band of interest. Figure 5.11(a) and 5.12(a) illustrate the input impedance of the antenna and the reflection coefficient of the tag, respectively when the length of the feed loop varies from 6 mm to 8 mm. It is found that the shorter is l or w , the higher is the resonance frequency. As the length l increases from 6 mm to 8 mm, the resonance frequency moves toward a lower frequency regime, as shown in Figure 5.12(a). Referring to Figure 5.11(a), it is noted that an increase in l yields an increase in the antenna reactance with little change in the resistance. It is expected that l can be as effective as w to align the antenna port impedance. Figure 5.11(b) and 5.12(b) show the input impedance of the antenna ports and reflection coefficient of the tag, respectively when the loop width w varies from 1.7 mm to 3.7 mm. There is a slight variation in the real magnitude of the antenna when the width of the loop changes. However, the imaginary magnitude significantly changes with the change in w . Therefore, the size of the loop can be adjusted to cancel the reactance of the tag chip for aligning the antenna impedance. Moreover, Table 5.4 and 5.5 summarise the tag performance in term of gain, realised gain and radiation efficiency at 868 MHz.

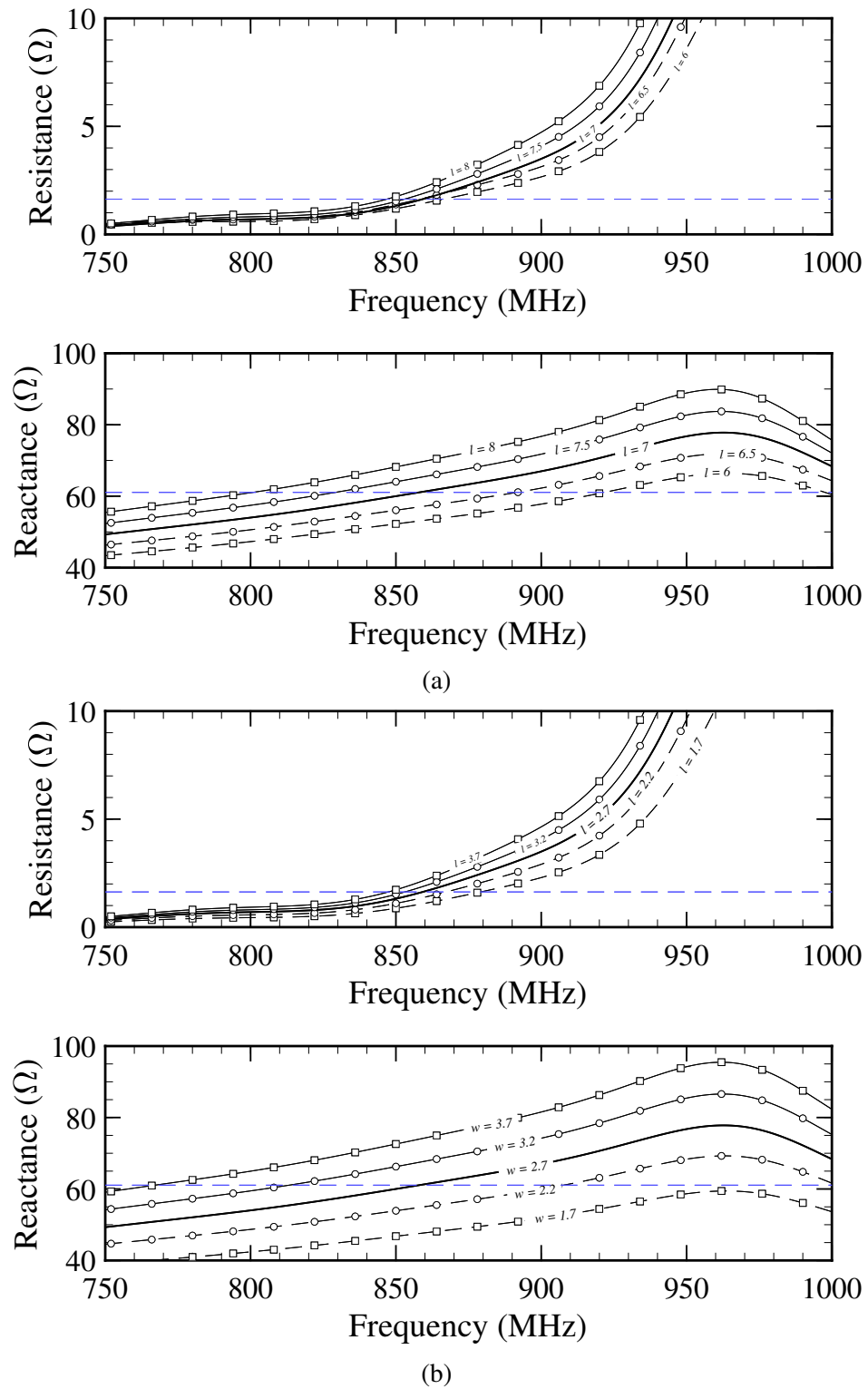
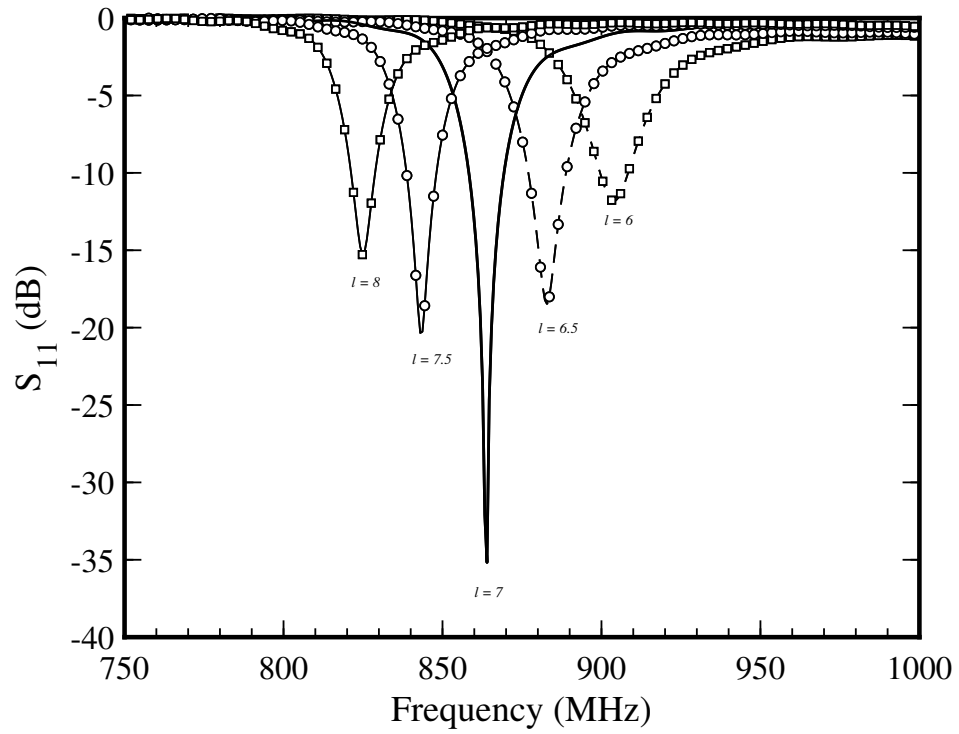
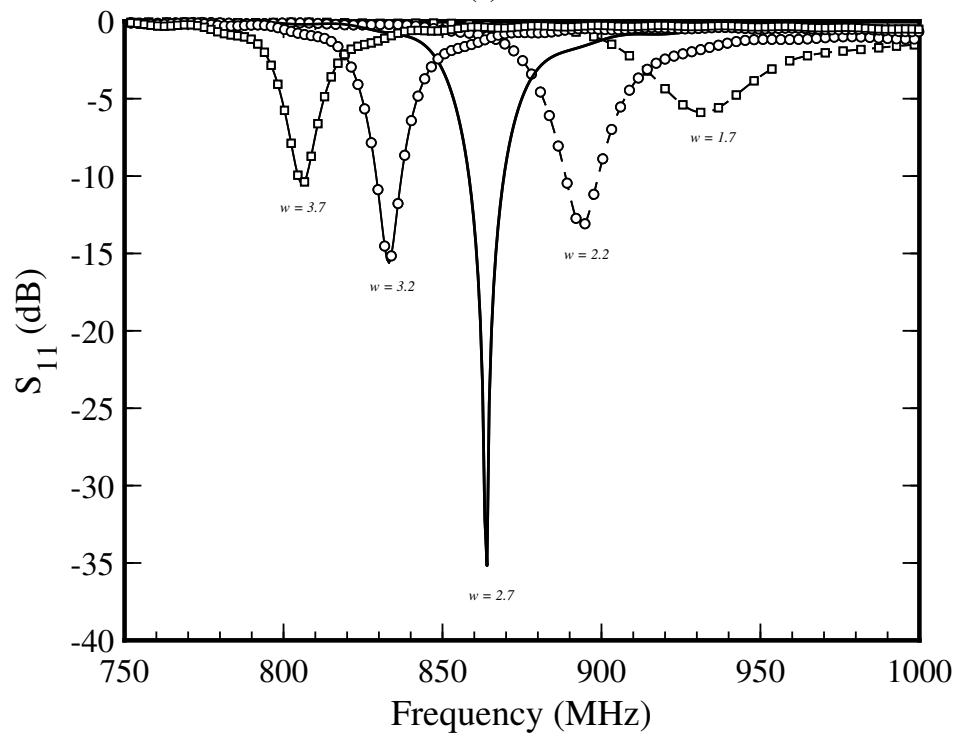


Figure 5.11: Simulated antenna port impedance against frequency: (a) by varying the length l in mm of the feed loop; (b) by varying the width w in mm of the feed loop while other parameters in Table 5.1 were fixed.



(a)



(b)

Figure 5.12: Simulated power reflection coefficient of the tag: (a) at different values of the loop length l in mm; (b) at the different values of the loop width w in mm while other parameters in Table 5.1 were fixed.

Table 5.4: Simulated antenna impedance, gain, realised gain and radiation efficiency of the proposed tag at 868 MHz by varying the design parameter l .

l (mm)	6	6.5	7	7.5	8
$Z_{ant.}(\Omega)$	1.68 + j54.13	1.96 + j58.18	1.92 + j62.42	2.31 + j66.76	2.66 + j71.20
$G_t(dB)$	1.35	1.73	1.57	1.23	1.42
$rlsd.G_t(dB)$	-7.08	-0.97	1.14	-3.67	-7.26
$\eta_e(dB)$	-0.69	-0.30	-0.49	-0.77	-0.63

Table 5.5: Simulated antenna impedance, gain, realised gain and radiation efficiency of the proposed tag at 868 MHz by varying the design parameter w .

w (mm)	1.7	2.2	2.7	3.2	3.7
$Z_{ant.}(\Omega)$	1.32 + j48.53	1.66 + j55.99	1.92 + j62.42	2.28 + j68.99	2.60 + j75.66
$G_t(dB)$	11.05	1.99	1.57	2.12	0.88
$rlsd.G_t(dB)$	-11.54	-4.19	1.14	-5.65	-10.18
$\eta_e(dB)$	-0.99	-0.02	-0.49	0.07	-1.18

5.3 Optimised Two Tag Antennas Design

The new optimised tag antenna design for the dual tag system is presented in Figure 5.13, consisting of a feed loop for T-matching network and two dipole arms for radiation. To reduce the size of the antenna, the radiating arms are bent around, forming a rectangular shape. Both dipole arms that extent from the feed loop have the same length and width. The total length of the antenna $(L_L + W_L + T_L) + (L_R + W_R + T_R)$ is equal to 167 mm. The length of the antenna determines the tag resonance frequency. Design parameters T_L and T_R can be used as the tuning parameters for tuning the resonance frequency of the antenna. The tag chip Magnus S2 has high capacitive input reactance, therefore the feed loop is used to achieve the inductive input reactance required for the tag chip impedance matching. The feed loop length l and width w of the feed loop are 7 mm and 2.75 mm, respectively. The dimensions of the feed loop are the most important design factor to adjust the tag antenna port impedance. The dimensions of the antenna parameters are tabulated in Table 5.6.

Since the previously proposed two tag antennas design have strong mutual coupling between the radiating elements, which may degrade the tag system performance. Therefore,

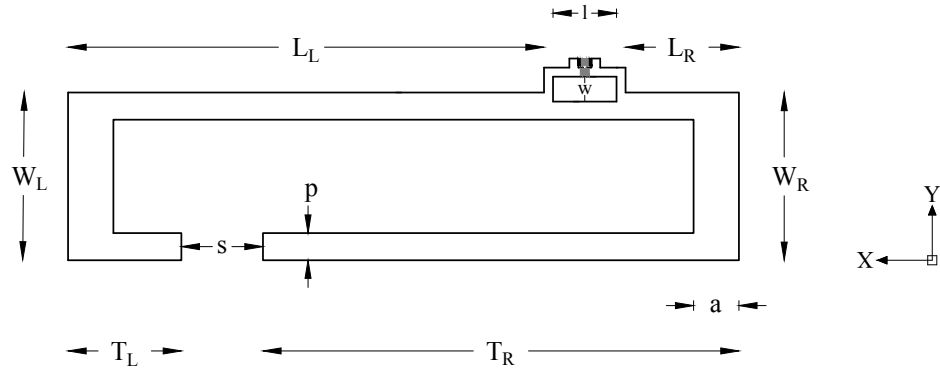


Figure 5.13: Geometry of the proposed tag antenna for dual tag system.

Table 5.6: Simulated dipole antenna dimensions.

Parameters (mm)	L_L	W_L	T_L	L_R	W_R	T_R	s	p	a	l	w
	52.5	18.5	12.5	12.5	18.5	52.5	9	3	5	7	2.75

new tag antennas have been designed to reduce the mutual coupling between the coupling elements. Two identical tag antennas design shown in Figure 5.13 are integrated to the current transformer, forming the dual RFID tag system, as shown in Figure 5.14. The antenna is designed in the form of a rectangular shape. The tag antennas are placed in the horizontal and vertical orientation. The feed loop is located at 12.5 mm away from the right end of the antenna. So, both tag antennas to be well integrated with the transformer. The geometry of both tag antennas is symmetrical. The tag antenna is 74 mm long and 18.5 mm wide. The radiating arms of the tag antenna that extends for the feed loop are equal in length. There is a slot of 9 mm which disconnects the radiating arms.

The length of the feed loop is 7 mm and with the width of 2.75 mm without including the width of the copper trace. The width of the copper trace of the feed loop is 1 mm. There is a gap of 0.2 mm in the copper trace of the feed loop where the discrete ports are created. Right across the antennas terminals, a 0.3 pF capacitor is connected which represents the minimum reactance of the tuning circuit. There is an air bridge of 10 mm between the coupling elements of the tags. The tags were placed right at the bottom of the transformer. Two M3 screws are located about 6 mm above the bottom of the transformer. Therefore, 5 mm M3 metal standoff spacers were employed to fill the gap so that the terminals of the tuning circuits of the tags can be connected to the terminals of the transformer.

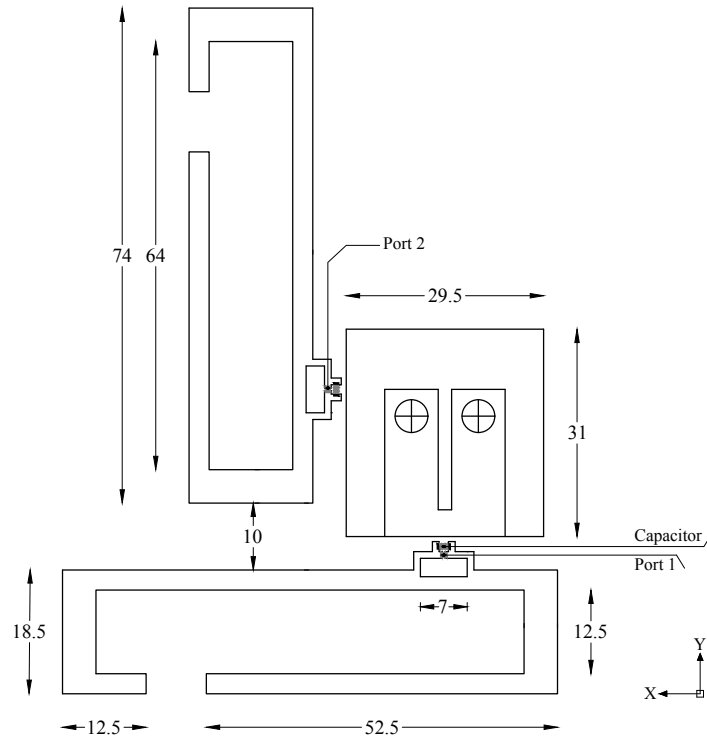


Figure 5.14: Layout of the optimised two tag antennas design with the current transformer mounted in the centre. (All dimensions are in mm)

5.3.1 Simulation Results

Figure 5.16 illustrates the reflection coefficient and the mutual coupling between the radiating elements of the two tag antennas design. The resonance frequency of the tags is 864 MHz. The reflection coefficient of the tag antenna with the port 1 (S_{11}) and the tag antenna with the port 2 (S_{22}) are -21 dB and -23 dB, respectively. Despite the close proximity, the mutual coupling S_{21} and S_{12} between the radiating elements are -16 dB.

5.3.2 Parametric Design Study

Antenna parametric analysis is performed using CST Microwave Studio. The main parameters that affect the tag resonance frequency are: (i) the length of the dipole; and (ii) the size of the feed loop. The feed loop acts as an input transformer and strongly affects the antenna port impedance and consequently, the tag resonance frequency. A slot s of 9 mm disconnects the radiating arms from each other. The length of the design parameter s can be adjusted to increase and decrease the length of dipole arms of the antenna to tune its resonance frequency. Figure 5.17 and 5.18 show the antenna port impedance and the power reflection coefficient of the tag against frequency, respectively when s varies from 3 mm to 21 mm.

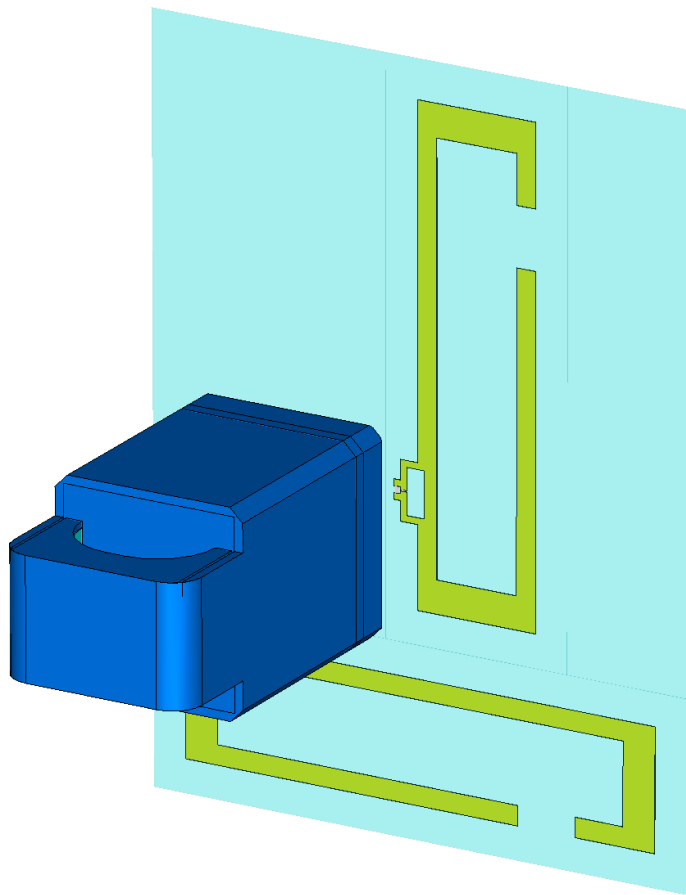


Figure 5.15: 3D model of the optimised two tag antennas design with the current transformer mounted in the centre.

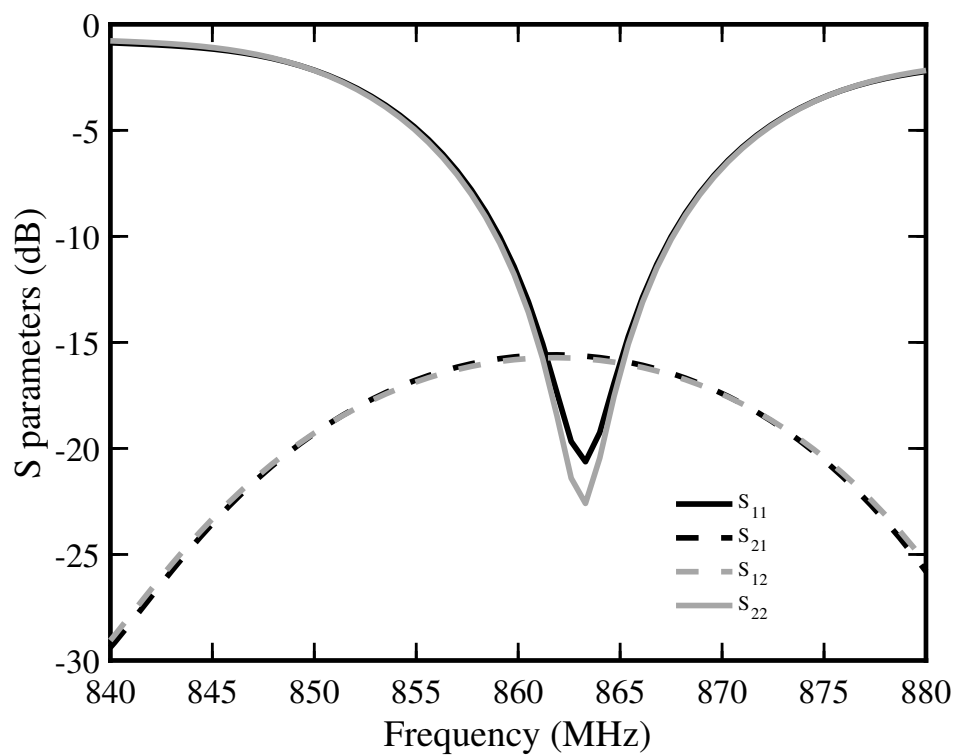


Figure 5.16: Simulated S-parameters of the two tag antennas design. All power reflection coefficients are below -10 dB. The coupling between the radiating elements is below -15 dB.

The parameter s can be used a tuning parameter for tuning the antenna resonance frequency. When the length of the slot s increases, as a result, the length of the radiating arms T_L and T_R decrease, causing to shift the resonance frequency to a higher range. Moreover, Figure 5.19 and 5.20 illustrate the effect of design parameter p on the input impedance of the antenna and tag reflection coefficient. It is observed that an increase in the width of radiating arms T_L and T_R , causes to shift the resonance frequency to a lower frequency band. Furthermore, Table 5.7 and Table 5.8 summarise the tag performance in term of gain, realised gain and radiation efficiency at 868 MHz for the design parameters s and p , respectively.

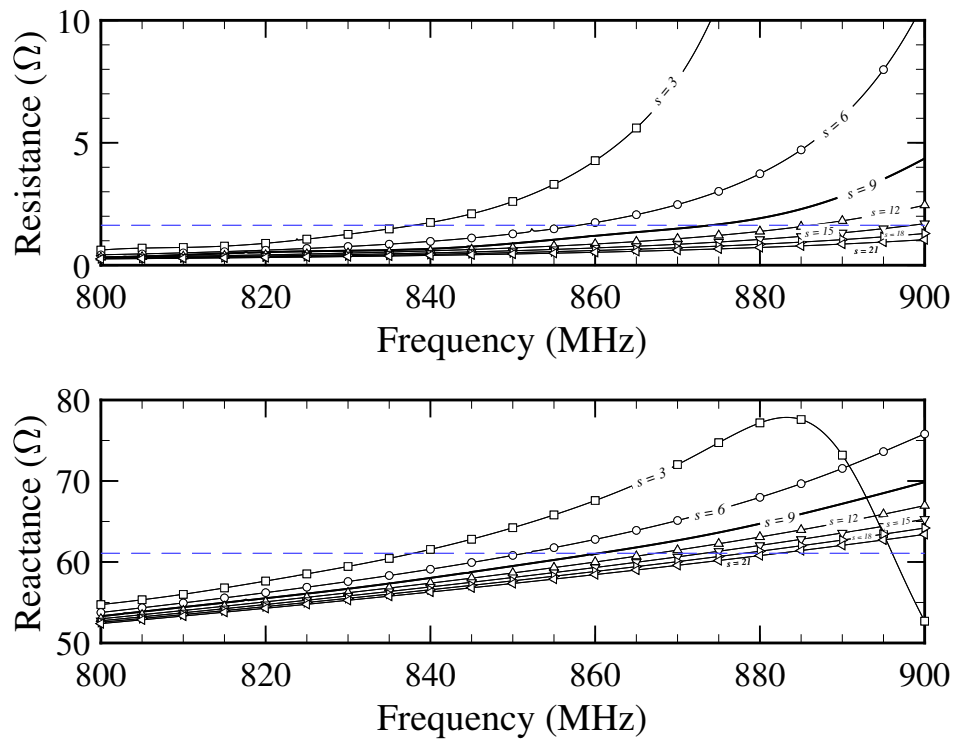


Figure 5.17: Simulated antenna port impedance by varying the parameter s in mm while other parameters in Table 5.6 were fixed.

Table 5.7: Simulated gain, realised gain and radiation efficiency of the tag when s varies from 3 mm to 21 mm at 868 MHz.

s (mm)	3	6	9	12	15	18	21
$Z_{ant.}(\Omega)$	6.68 +j71.01	2.29 +j64.62	1.42 +j62.30	1.03 +j61.16	0.82 +j60.36	0.68 +j59.76	0.59 +j59.35
$G_t(dB)$	1.18	1.94	1.52	1.17	1.05	1.09	1.19
$rlsd.G_t(dB)$	-4.38	-0.84	0.83	0.85	0.14	-0.85	-1.95
$\eta_e(dB)$	-0.61	-0.04	-0.61	-0.98	-1.09	-1.03	-0.9

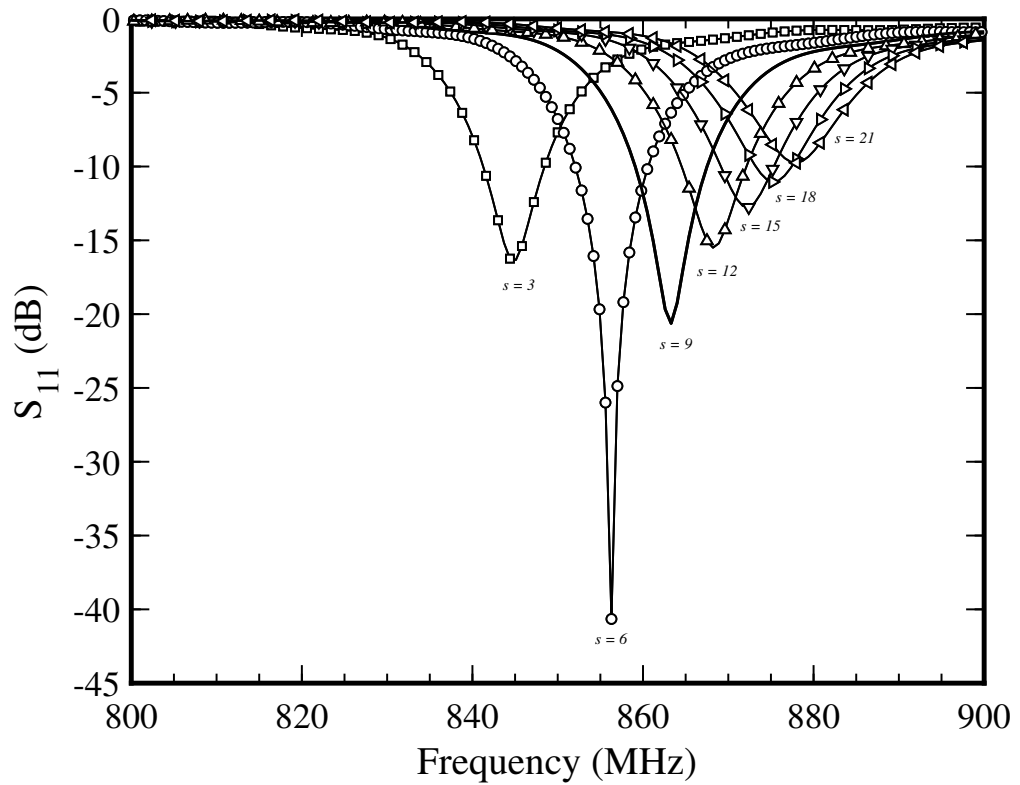


Figure 5.18: Simulated power reflection coefficient of the tag by varying the parameter s in mm while other parameters in Table 5.6 were fixed.

Table 5.8: Simulated gain, realised gain and radiation efficiency of the tag when the p varies from 2 mm to 5 mm at 868 MHz while other parameters in Table 5.6 were fixed.

p (mm)	2	3	4	5
$Z_{ant.}(\Omega)$	$0.84 + j60.64$	$1.42 + j62.30$	$2.71 + j65.09$	$6.67 + j69.76$
$G_t(dB)$	0.98	1.52	1.95	1.26
$rlsd.G_t(dB)$	-0.34	0.83	-1.1	-3.75
$\eta_e(dB)$	-1.15	-0.61	-0.02	-0.52

The affect of the feed loop on the antenna performance is also investigated. The antenna was simulated in two configurations: (i) by changing the length l of the loop; and by changing the width w of the loop. Figure 5.21 depicts the input impedance observed at the antenna port. It is observed that as the length of the feed loop decrease, the resistance and reactance of the antenna decreases as well, and consequently, the resonance frequency of the antenna moves toward a higher band. Similarly, as the loop width w decrease, the resistance and reactance of the antenna decreases, and vice versa.

Figure 5.22(a) and 5.22(b) show the reflection coefficient of the tag for different loop sizes. As expected, the increases in the length l and width w of the feed loop yield a shift in

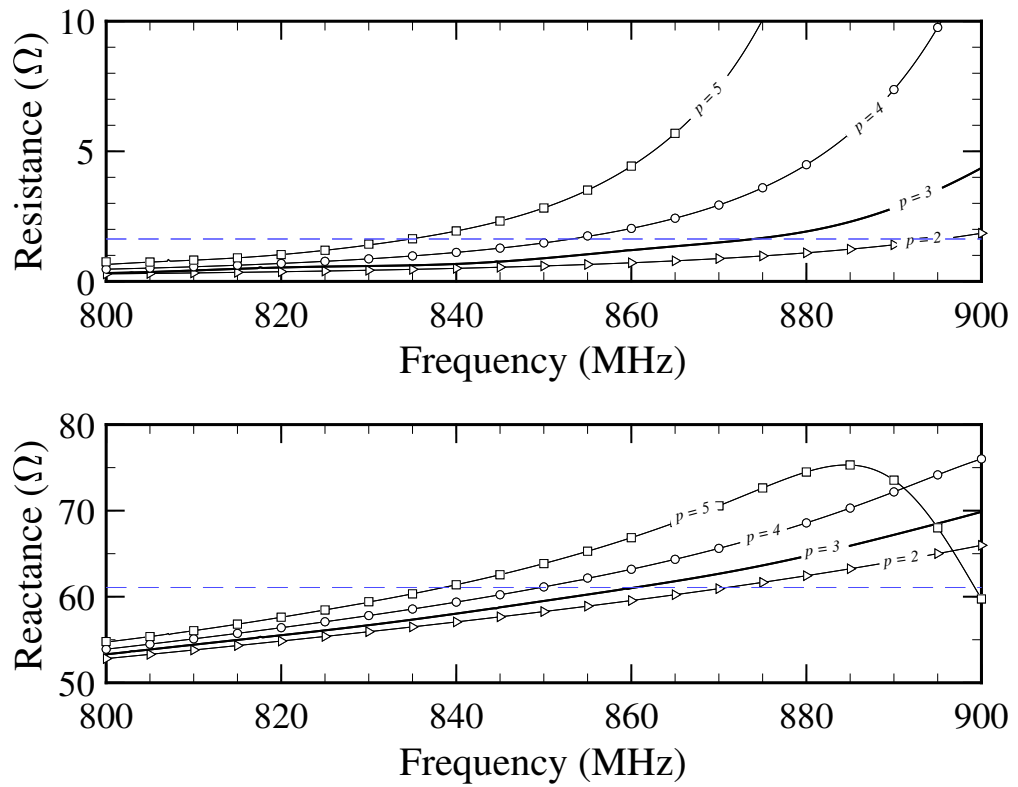


Figure 5.19: Simulated antenna input impedance by varying the parameter p in mm while other parameters in Table 5.6 were fixed.

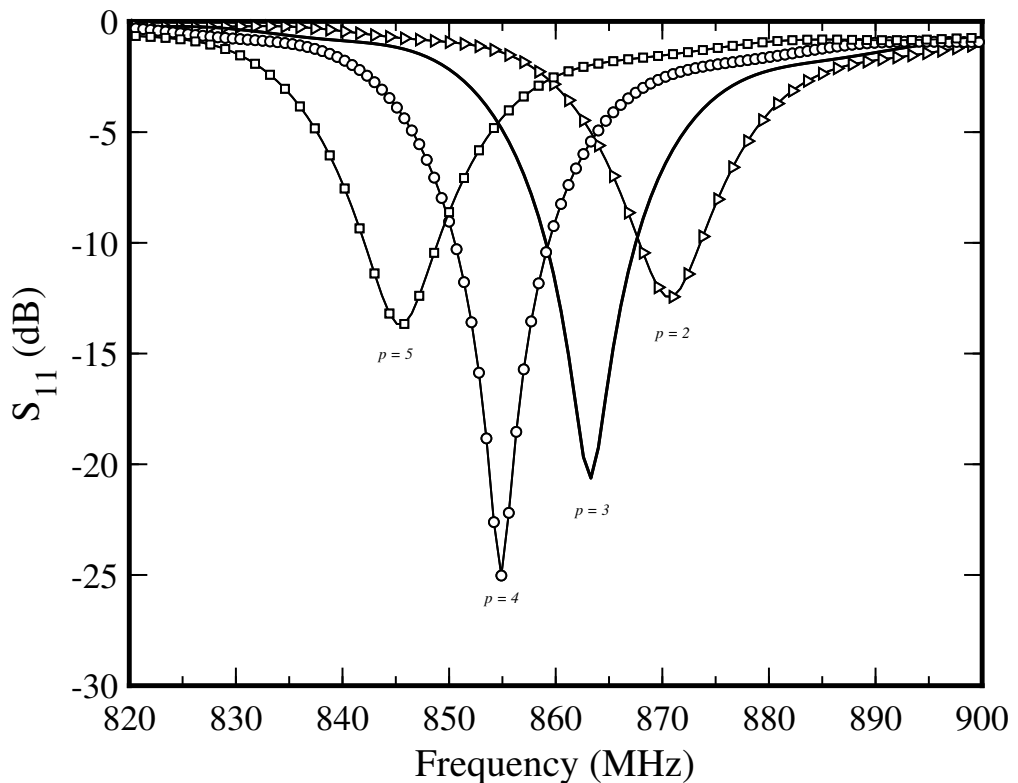


Figure 5.20: Simulated power reflection coefficient of the tag by varying the parameter p in mm while other parameters in Table 5.6 were fixed.

the resonance frequency of the tag to a lower frequency range, and with the decrease in l and width w move the resonance frequency to the higher frequency band. Furthermore, Table 5.9

and Table 5.10 summarise the tag performance in term of gain, realised gain and radiation efficiency at 868 MHz for the design parameters l and w , respectively.

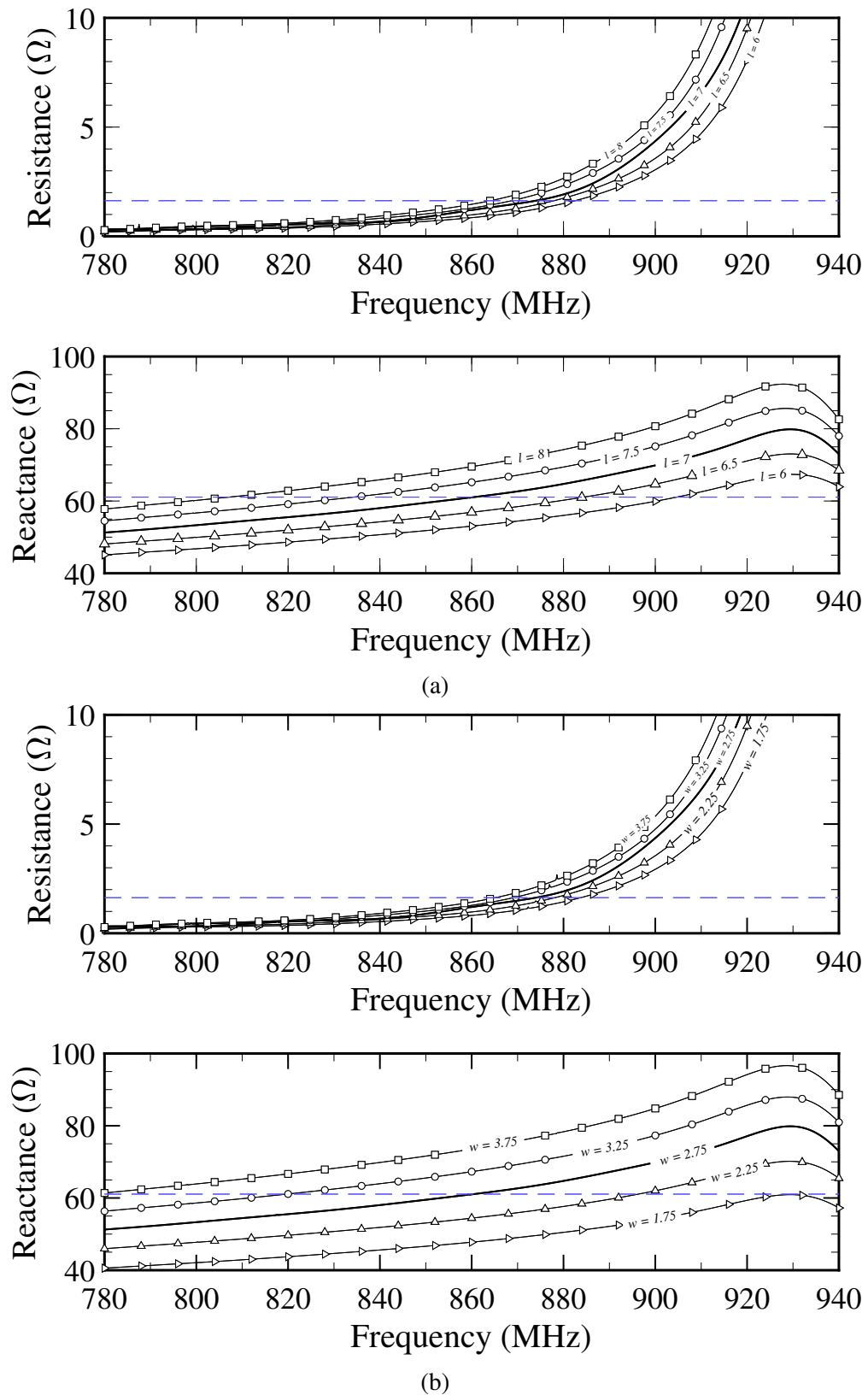
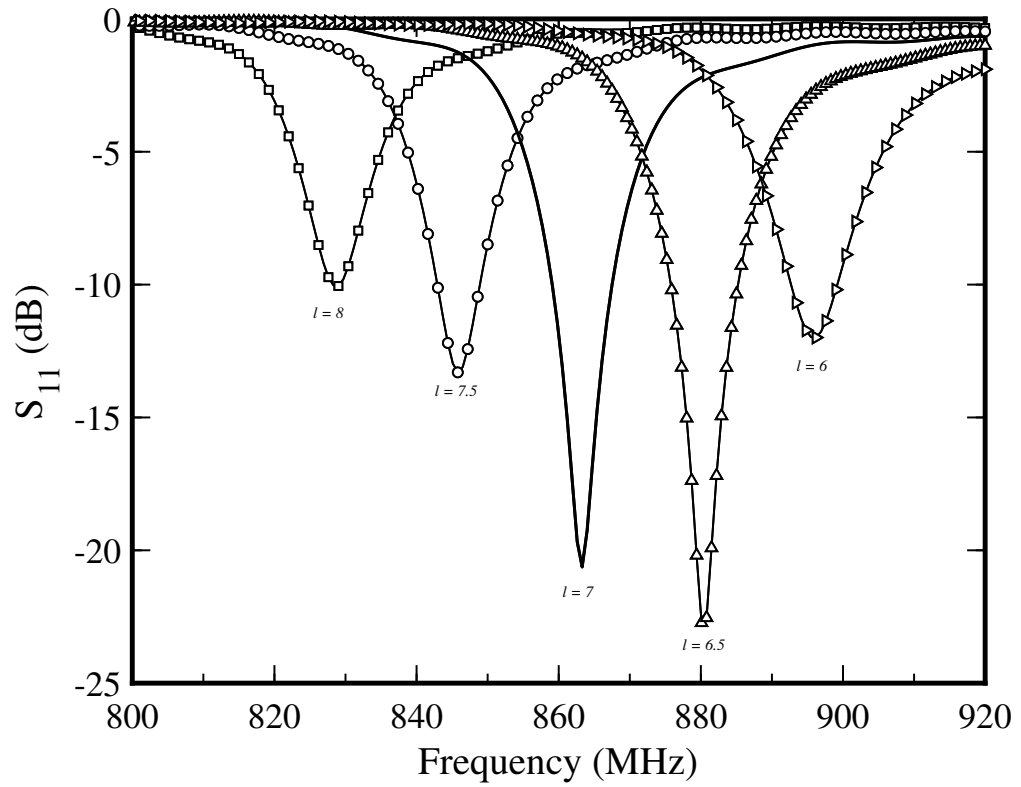
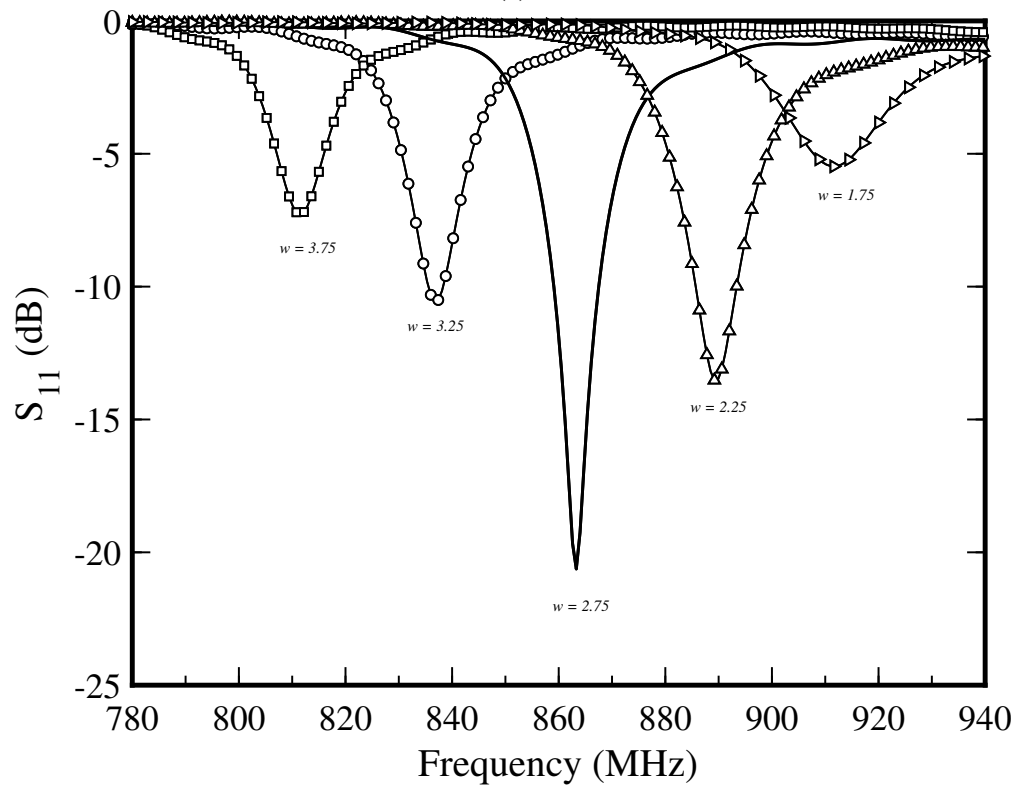


Figure 5.21: Simulated power reflection coefficient of the tag: (a) at the different values of l in mm; (b) at the different values of w in mm while other parameters in Table 5.6 were fixed.



(a)



(b)

Figure 5.22: Simulated power reflection coefficient of the tag: (a) at the different values of l in mm; (b) at the different values of w in mm while other parameters in Table 5.6 were fixed.

Table 5.9: Simulated gain, realised gain and radiation efficiency of the tag when l varies from 6 mm to 8 mm at 868 MHz.

l (mm)	6	6.5	7	7.5	8
$Z_{ant.}(\Omega)$	$1.04 + j54.14$	$1.20 + j58.11$	$1.42 + j62.30$	$1.59 + j66.73$	$1.81 + j71.24$
$G_t(dB)$	0.67	1.68	1.52	0.95	0.84
$rlzd.G_t(dB)$	-8.15	-1.59	0.83	-4.62	-8.43
$\eta_e(dB)$	-1.17	-0.31	-0.61	-0.96	-1.08

Table 5.10: Simulated gain, realised gain and radiation efficiency of the tag when w varies from 1.75 mm to 3.75 mm at 868 MHz.

w (mm)	1.75	2.25	2.75	3.25	3.75
$Z_{ant.}(\Omega)$	$1.0 + j48.77$	$11.19 + j55.61$	$11.42 + j62.30$	$11.57 + j68.85$	$11.76 + j75.31$
$G_t(dB)$	1.86	1.6	1.51	2.09	0.65
$rlzd.G_t(dB)$	-12.19	-5.69	0.83	-6.73	-11.22
$\eta_e(dB)$	-0.03	-0.25	-0.61	0.11	-1.24

5.3.3 Tags with Tuning Circuits

Furthermore, in the final simulation, two tuning circuits were designed and coupled with the terminals of the tag antennas and simulated. The total reactance of the tuning circuits was fixed to 0.3 pF. The dimensions of the tuning circuits are given in Figure 5.23. The maximum length of the tuning circuit 1 and 2 are 28.75 mm and 21.5 mm respectively. The minimum length of the tuning circuit 1 and 2 are 17.85 mm and 9.6 mm respectively. The width of the copper traces of the tuning circuits is 1.5 mm. There are two air bridges of 1 mm long for mounting the tuning diodes. Air gaps of 0.5 mm are introduced for mounting the lumped elements of a size of 0603. The edge-to-edge distance between the copper traces in the tuning circuits is 6 mm. Figure 5.25 illustrates the reflection coefficient of the tag antennas linked with the tuning circuits and the mutual coupling between the radiating elements. Both tag antennas are well matched at the UHF band, as well as the mutual coupling S_{21} and S_{12} between the radiating elements is below -15 dB. It is observed that there is a slight shift in the resonance frequency of the tag antennas.

Figure 5.26 depicts the normalised magnitude of the current distribution of the two tag

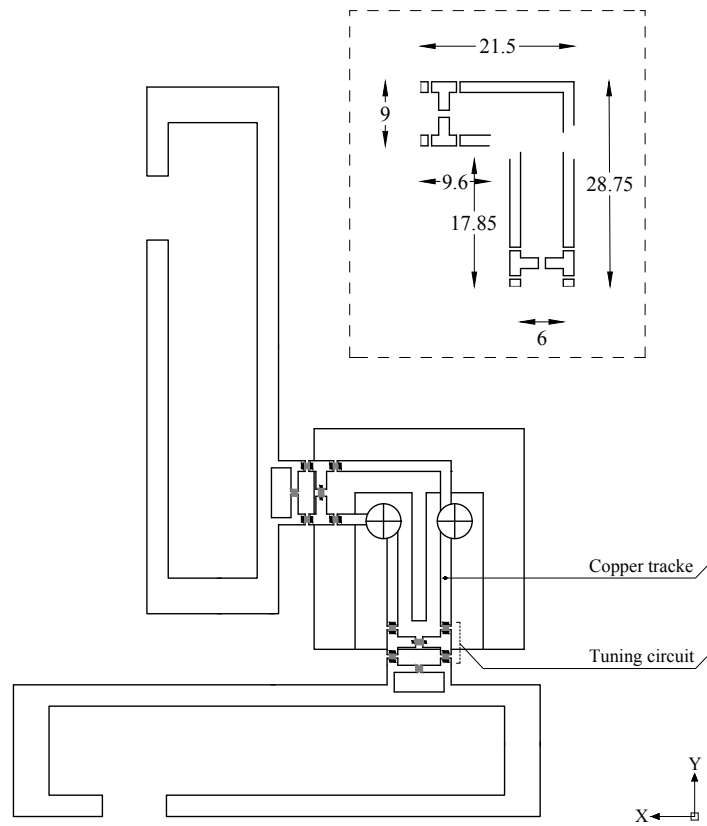


Figure 5.23: Proposed two RFID tag antennas coupled with the tuning circuits and integrated with the current transformer. (All dimensions are in mm)

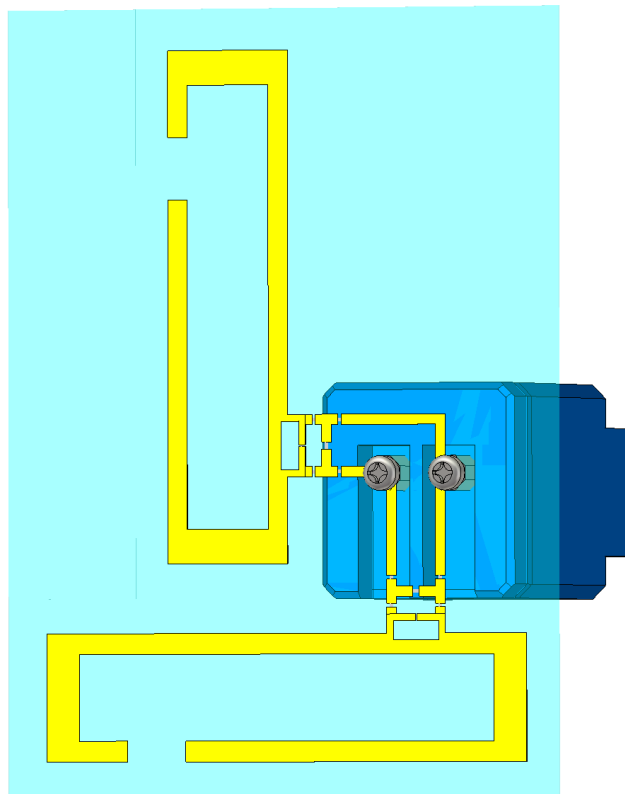


Figure 5.24: 3D model of the two RFID tag antennas coupled with the tuning circuits and integrated with the current transformer.

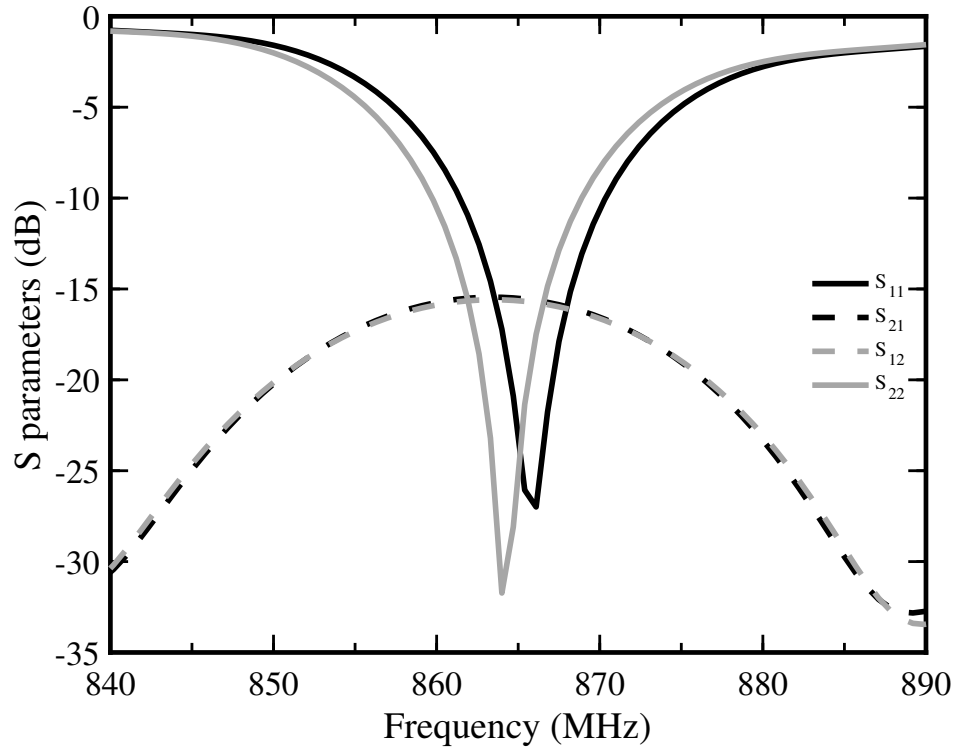
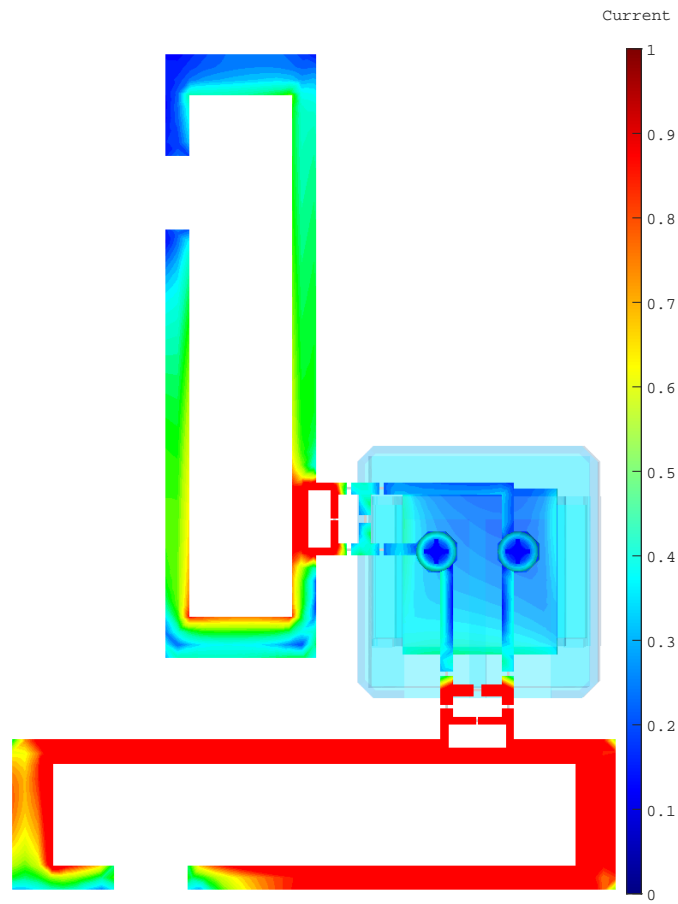


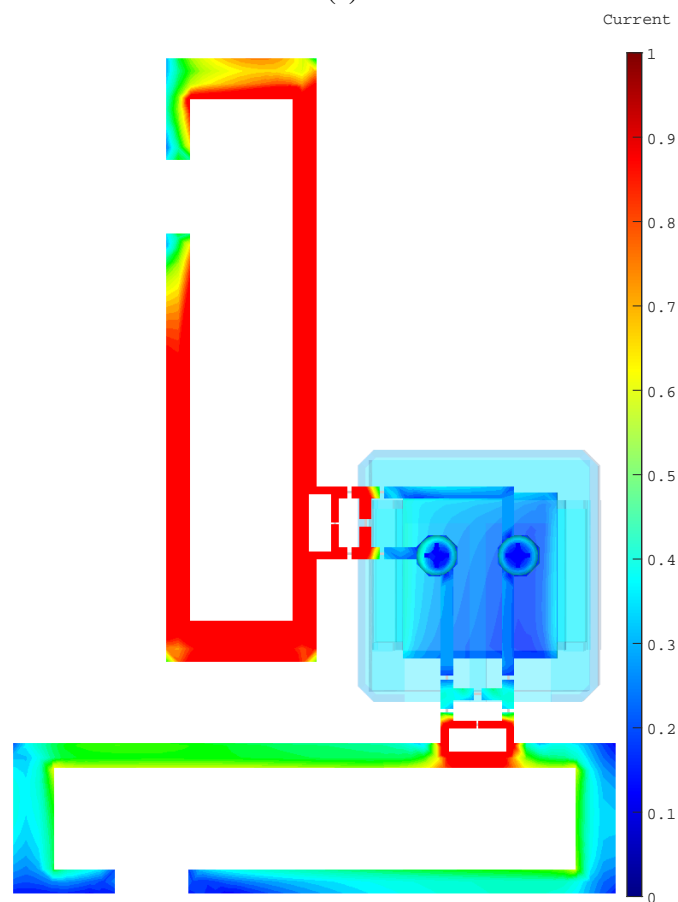
Figure 5.25: Simulated S-parameters of the two tag antennas linked with the tuning circuits. All power reflection coefficients are below -10 dB. The coupling between the radiating elements is below -15 dB.

antennas design at 868 MHz. It is observed that the maximum current distribution is located in the two radiating arms that extend from the feed loop, which are responsible for radiating more power. However, there is less current distribution at the end of the radiating arms. Figure 5.26(a) shows the normalised magnitude of the current distribution of the tag antenna with the port 1, and there is less current distribution observed at feed loop of the tag antenna with the port 2. Similarly, Figure 5.26(b) demonstrates the magnitude of the current distribution of the tag antenna with the port 2.

Figure 5.27 depicts the radiation pattern of the two tag antennas in yz -plane, xy -plane, and xz -plane. The realised gain of the two tag antennas design is 0.964 dB for the tag antenna with the port 1 and 0.64 dB for the tag antenna with the port 2. It is observed from the Figure 5.6 that the tag antenna with the port 1 has a good omnidirectional radiation however the tag antenna with the port 2 has a maximum of radiation when the theta (θ) is equal to 0° and 180° .



(a)



(b)

Figure 5.26: The normalised surface current distribution of the two tag antennas design at 868 MHz: (a) tag antenna with the port 1; and (b) tag antenna with the port 2.

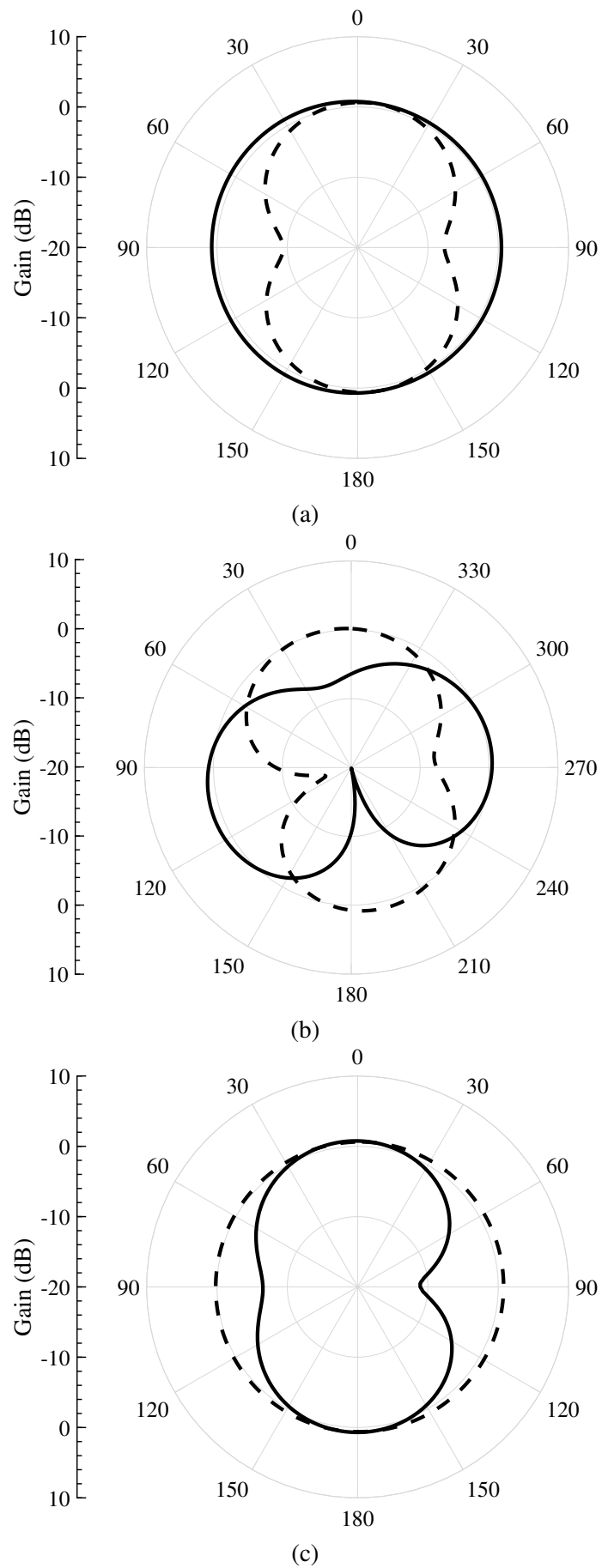


Figure 5.27: Simulated radiation pattern of the two tag antennas design at 868 MHz: (a) yz -plane; (b) xy -plane; and (c) xz -plane. Black solid lines: tag antenna design with the port 1. Dashed black lines: tag antenna design with the port 2.

5.3.4 Theoretical Read Range

5.3.4.1 Tag with the Port 1

Theoretical read range of the tag can be calculated using the Friis free-space formula:

$$r_{max} = \frac{\lambda_0}{4\pi} \cdot \sqrt{\frac{EIRP \cdot G_r \cdot \tau}{P_{IC}}} \quad (5.1)$$

where λ_0 is the wavelength, EIRP is the effective isotropic radiative power transmitted by the reader antenna, and P_{IC} is the tag chip sensitivity which is the minimum threshold power required to turn on the tag chip. The values of these parameters are following:

$$\lambda_0 = 345.62 \text{ mm } (f_0 = 868 \text{ MHz})$$

$$P_{IC} = -16.1 \text{ dBm } (= 0.0245 \text{ mW})$$

$$EIRP = 3.28 \text{ W}$$

The simulated value of the tag realised gain (G_r) and reflection coefficient (S_{11}) are:

$$G_r = 0.964 \text{ dB } (= 1.2485)$$

$$S_{11} = -15.14 \text{ dB } (= 0.0306)$$

$$\tau = 1 - |S_{11}|^2 (= 0.9990)$$

The maximum theoretical distance between tag and reader can be calculated to be:

$$r_{max} = 10.47 \text{ m.}$$

5.3.4.2 Tag with the Port 2

The simulated value of the tag realised gain (G_r) and reflection coefficient (S_{22}) are:

$$G_r = 0.64 \text{ dB } (= 1.1587)$$

$$S_{22} = -11.28 \text{ dB } (= 0.0744)$$

$$\tau = 1 - |S_{22}|^2 (= 0.9944)$$

The maximum theoretical distance between tag and reader can be calculated to be:

$$r_{max} = 10.80 \text{ m.}$$

5.3.5 Current Transformer

The split-core current transformer [7] can detect ac current in the range of 0 A to 13 A from an power cable of an electrical load and transform it into 0 V to 13 V dc proportionally was connected to the terminals of the tuning circuits of the capacitance RFID tags to evaluate the performance of the dual tag system. The transformer has a full-scale accuracy of $\pm 2\%$ with the operating frequency of 50/60 Hz. The transformer comes with two M3 screw terminals, which were used to connect the transformer with the tuning circuits, as described earlier.

5.3.6 Tuning Circuit 1

The tuning circuit 1 consists of two inductors of 400 nH, a varactor tuning diode from MA-COM [8] and two 36 pF capacitors, as shown in Figure 5.28. The relationship of the reverse voltage and capacitance of the tuning diode is derived from the diode datasheet [9]. The input terminals of the tuning circuit were connected to the transformer, while the output terminals of the tuning circuit were linked to the tag antennas terminals with the port 1. The tuning circuit used 0603 size components with a pitch of 0.5 mm between contacts, and was fabricated along with the tag antennas on a 0.18 mm thick Mylar substrate.

5.3.7 Tuning Circuit 2

The tuning circuit 2 consists of two inductors of 400 nH, a varactor tuning diode from Sky-works [10] and two 15 pF capacitors, as shown in Figure 5.29. The relationship of the reverse voltage and capacitance of the tuning diode is derived from the diode datasheet [11]. The input terminals of the tuning circuit were connected to the transformer, while the output terminals of the tuning circuit were linked to the tag antennas terminals with the port 2. The tuning circuit used 0603 size components with a pitch of 0.5 mm between contacts, and was fabricated along with the tag antennas on a 0.18 mm thick Mylar substrate.

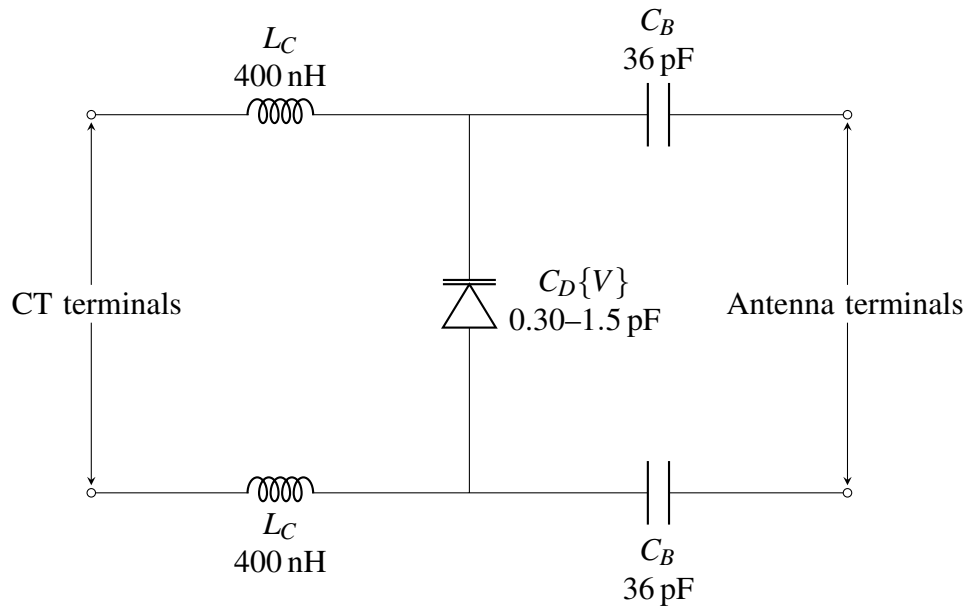


Figure 5.28: Schematic diagram of the tuning circuit 1. The input terminals of the circuit are connected to the transformer and the output terminals are connected to the antenna ports of the tag.

5.3.8 Measurement Results

5.3.8.1 Measurement Setup

The tags were etched on the Mylar film. The tag chips were attached to the antenna terminals using conductive silver paint [12]. A 0.3 pF capacitor was soldered near the antenna terminals. Both tags were interrogated with the UHF reader Tagformance Pro System, comprising of a linear polarised antenna of 6 dBi gain and placed at a fixed distance of 30 cm away from the tags. The tags are capable of operation at distances greater than 30 cm, and the calibrated Tagformance Pro System was able to assess the maximum read distance achievable in each measurement. The set up was also able to record the sensor code as well as provide tag threshold power analysis.

5.3.8.2 Sensor Code and Read Range

Figure 5.30 and Figure 5.31 represents the measured sensor value and read range of the two tags design when a 0.3 pF capacitor was attached across each tag antenna terminals. It is observed that the two tags are well-tuned to the 868 MHz frequency band. The tag antenna with the port 1 has a sensor value of 22, and the tag antenna with the port 2 has a sensor value of 20. There is a difference of two sensor value between the tags at 868 MHz. A small discrepancy between the measured sensor codes may be caused by the non-ideal etching

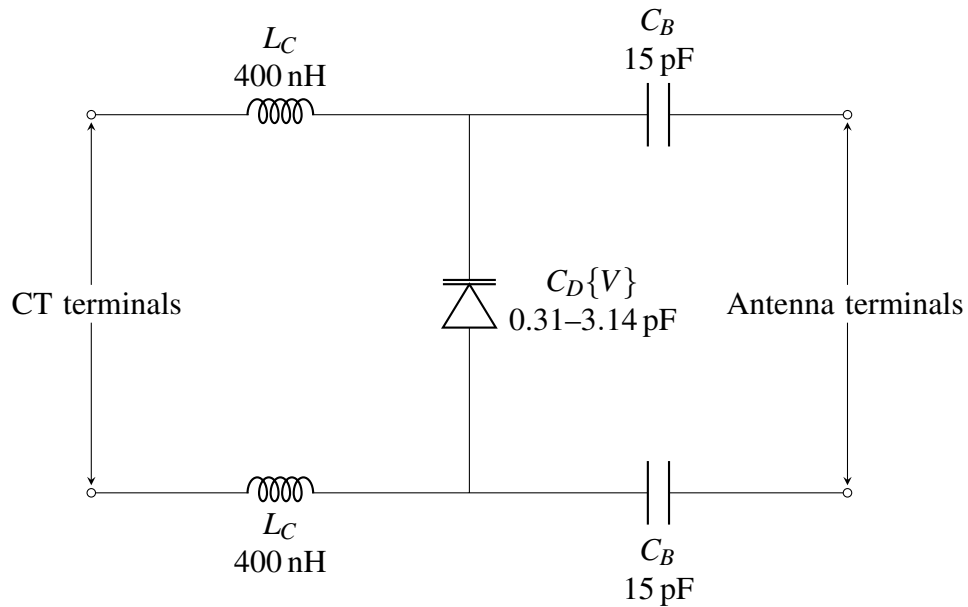


Figure 5.29: Schematic diagram of the tuning circuit 2. The input terminals of the circuit are connected to the transformer and the output terminals are connected to the antenna ports of the tag.

mechanism and not properly connecting the tag chip ports with the antenna ports during the manufacturing process. With the reference to Figure 5.31, It can be observed that the tag antenna with the port 2 has a higher read range of 4.4 m as compared to the read range of the tag antenna with the port 1 which is 2.6 m. The long radiating arm of the tag antenna with the port 1 that extends from the feed loop which is responsible for radiating more power is located near to the edge of tag antenna with the port 2. So, It could be concluded that the 5 mm width radiating arm of the tag antenna with the port 2 has significantly degraded the tag antenna performance with the port 1.

5.3.8.3 Current Sensing Setup

In the final set of experiments, the two RFID tags were connected with the tuning circuits and etched on flexible Mylar sheet. Tag chips and lumped components were mounted on the tags and tuning circuits using conductive silver paint and soldering iron. The copper straps of the tuning circuits were linked with the M3 screw terminals of the transformer. The magnetic circuit of the transformer encircled a single split-core cable that was enclosed in an insulating box as the current transformer must be installed on a single live or neutral current carrying wire, as shown in Figure 5.32. The sensor response was measured with the Tagformance Pro System UHF RFID reader and with the same sensing setup described in Chapter 3.

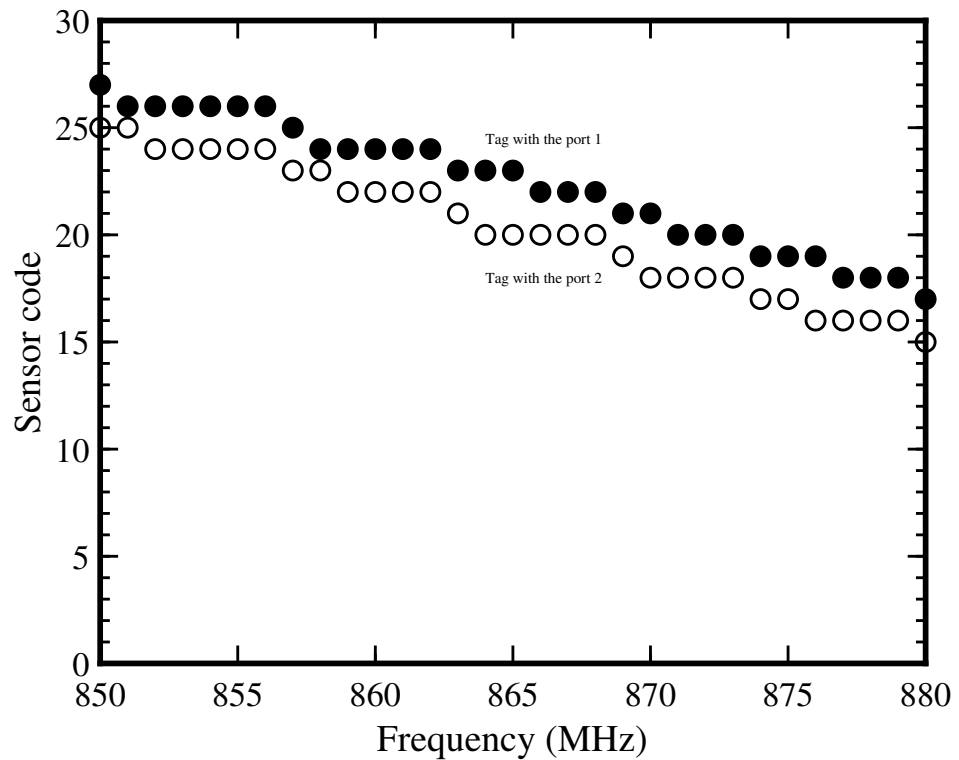


Figure 5.30: Measured sensor code of the two tag antennas configured in the horizontal and vertical orientation.

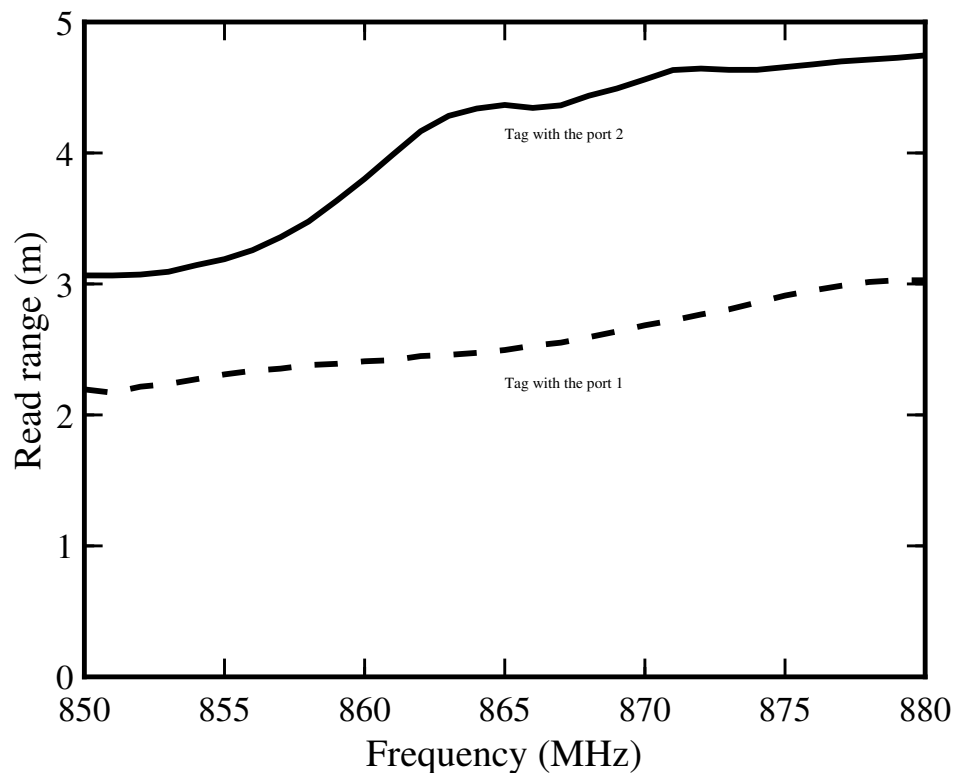


Figure 5.31: Measured read range of the two tag antennas configured in the horizontal and vertical orientation.

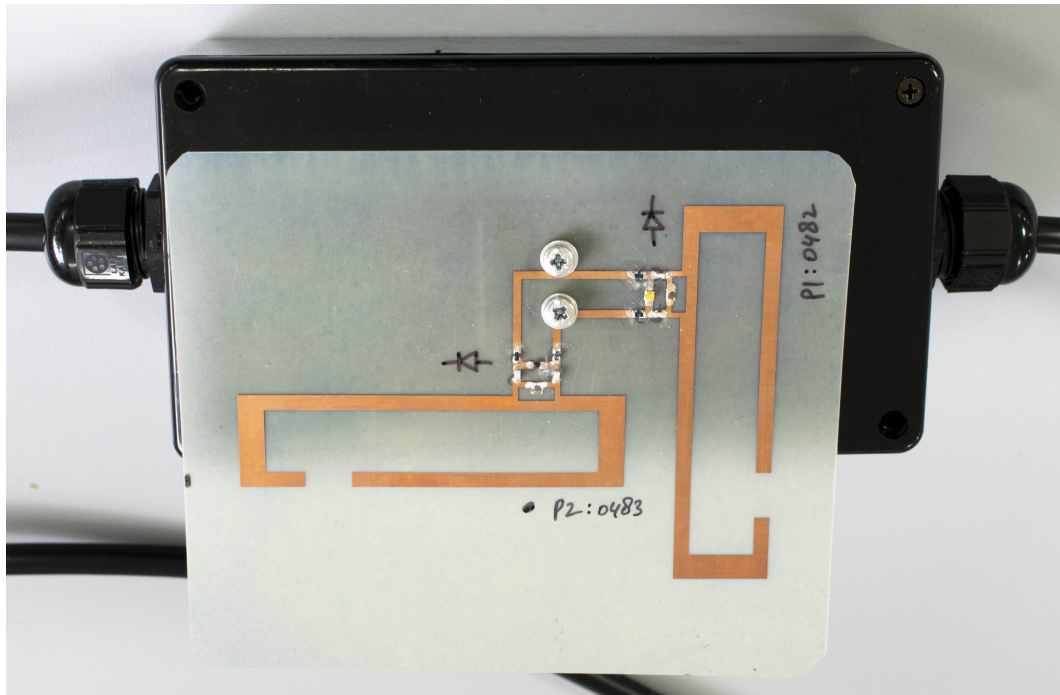


Figure 5.32: Final manufactured prototype of the dual RFID tag system.

5.3.8.4 Current to Sensor Code Relationship

Figure 5.33 illustrates the measured sensor value of the two tags design at 868 MHz when ac current changes in the primary winding of the transformer from 0 A to 13 A. The tag antenna with the port 1 covers the ac current range from 0 A to 5 A and the tag antenna with the port 2 covers the ac current range from 5.5 A to 13 A. Figure 5.34 shows the measured read range of the two tag antennas design across the all current readings in the range from 0 A to 13 A at 868 MHz. It is observed that the tag antenna with the port 1 has a lower read range of about 3 m as compared to the tag antenna with the port 2 which has a read range of about 5 m across all current readings.

Furthermore, the theoretical read range of the sensing tags is higher than the measured read range is the result of the following assumptions: (i) the actual sensitivity of the tag chip tends to be smaller than nominal value which can significantly affect the tag read range; (ii) the non-ideal etching mechanism and not properly attaching the tag microchip with the antenna port; (iii) the losses occur in the tuning circuits attached to the sensing tags; and (iv) the not-anechoic measurement environment.

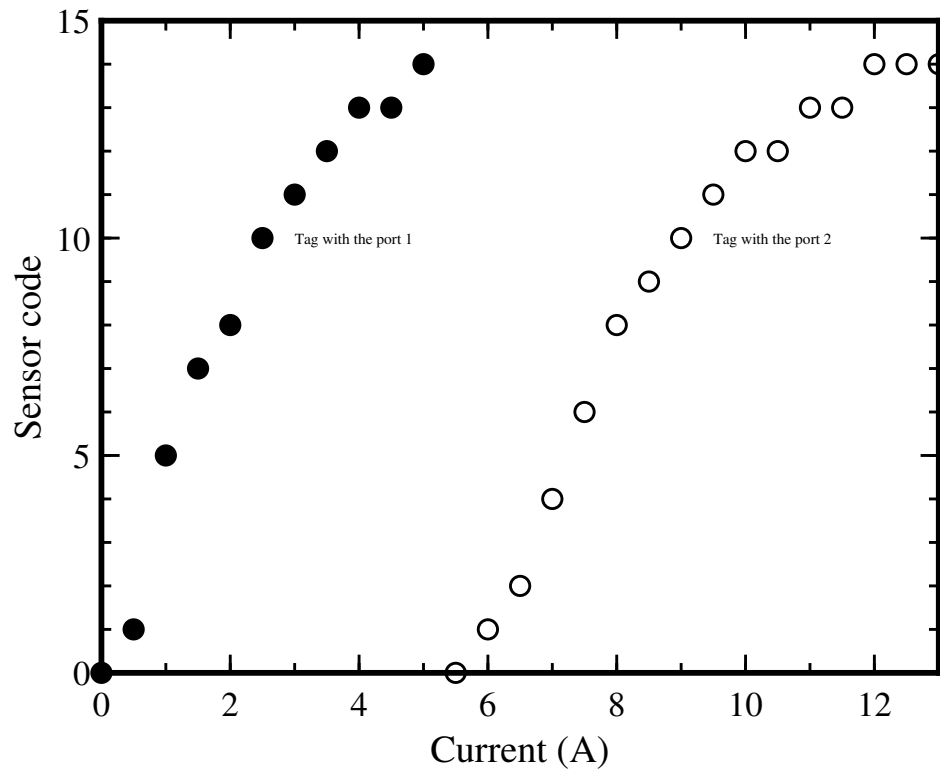


Figure 5.33: Measured sensor code of the dual tag system when the current in the primary winding of the transformer changes from 0 A to 13 A.

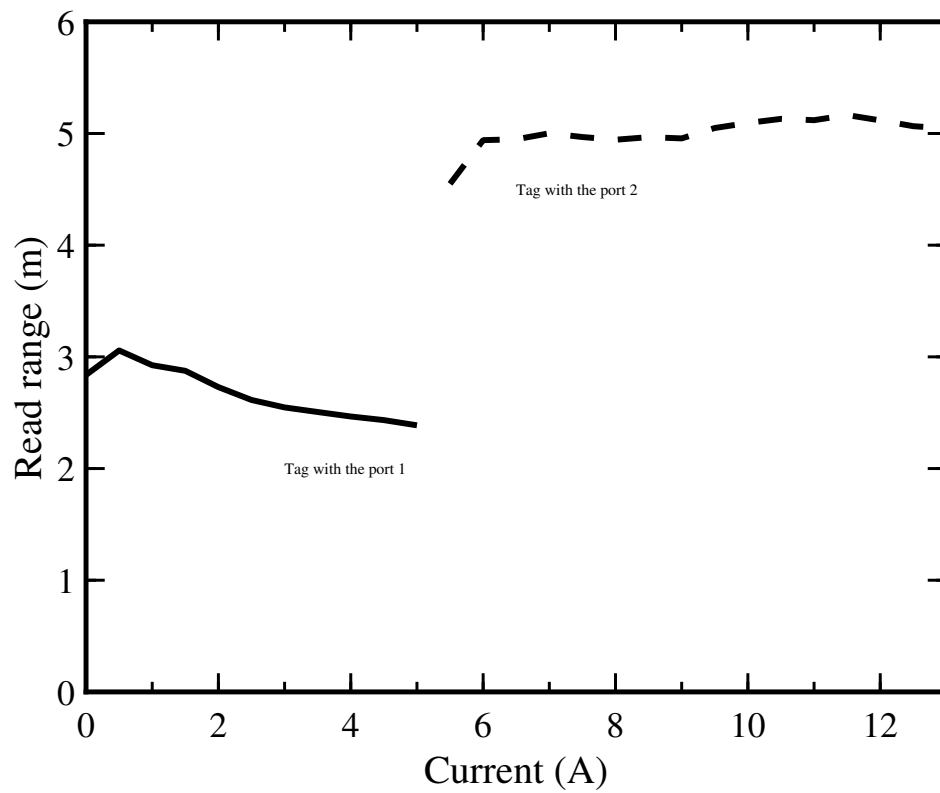


Figure 5.34: Measured read range of the two tag antennas across the current reading in the range from 0 A to 13 A.

5.3.9 Sensor Comparison

Table 5.11 shows the comparison of the proposed tag system with the commercial alternative ac current meters. The total cost of the tag device is inclusive of the cost of the current transformer (\$45.00) and the estimated cost of the tag (\$5.00). In order to be cost-effective for a domestic setting the RFID reader should be redeveloped for domestic use and price range.

Table 5.11: Comparison between the proposed tag system and commercial alternative ac current meters in terms of communication, cost, current range and power type.

Ref.	Sensors	Communication	Cost (\$)	Current Range (A)	Power Type
[13]	IoT long range wireless ac current monitor	DigiMesh protocol	179.95	0–100	Active
[14]	Alta wireless ac current meter - 20 A - AA battery powered	Monnit proprietary protocol	150.00	0–20	Active
[15]	Pressac current sensor: one channel	Enocean wireless radio protocol	98.00	0–60	Passive
[16]	SCT-125W-100 by Mag-nelab	IEEE 802.15.4, 2.4 GHz technology	245.00	0–100	Active
[17, 18]	AC power meter	Universal serial bus	–	0–100	Active
[19]	Web based smart meter	WiFi network	–	0–100	Active
[20]	Piezoelectromagnetic wireless current monitoring system	Digi XBee radio	–	0–20	Active
[21]	Smart power meter	Wired network	–	0–20	Active
[1]	Single tag system	Radio frequency Identification	50.00	2–10	Passive
[3]	Optimised single tag system	Radio frequency Identification	50.00	1–13	Passive
—	Dual RFID tag system	Radio frequency Identification	55.00	0–13	Passive

5.4 Conclusion

In this chapter, a dual tag system for ac current sensing is proposed. The proposed system consists of two antennas, two tuning circuits and a current transformer. The total reactance of the tuning circuits is different from each other. However, the tuning circuits are linked with the separate tag antenna and integrated into a single current transformer. Such a configuration will help to measure low and high current level (with reference to 0 A to 13 A). To implement the proposed mechanism, three types of tag antennas designs were designed and fabricated. The measured results of the tag antennas show a good agreement with the simulation results. The two tag antennas are designed in closed proximity to reduce the overall size of the tag system. The mutual coupling S_{21} and S_{12} between the tag antennas is also demonstrated. The dual tag system was experimentally tested with a switchable electrical load, and the measured results show that the sensing tags can detect ac current in the range from 0 A to 13 A.

The main contributions of this chapter has been,

- A novel dual tag system for ac current sensing.
- Three different types of two tag antennas designs for a current transformer.
- Increase in the current sensing range of the tag system.

In the next chapter, a miniaturised tag antenna for the dual RFID tag system will be proposed.

References

- [1] I. Ullah, R. Horne, B. Sanz-Izquierdo and J. C. Batchelor, "RFID AC Current Sensing Technique," in *IEEE Sensors Journal*, vol. 20, no. 4, pp. 2197–2204, Feb.15, 2020, doi: 10.1109/JSEN.2019.2949856.
- [2] I. Ullah, R. Horne, B. Sanz-Izquierdo and J. C. Batchelor, "UHF RFID Tag Design for AC Current Sensing," *IET's Antennas and Propagation Conference (APC–2019)*, Birmingham, UK, Nov. 11–12, 2019, pp. 1–4, doi: 10.1049/cp.2019.0728.
- [3] I. Ullah, R. Horne, B. Sanz-Izquierdo and J. C. Batchelor, "Tag Design for RFID AC Current Sensing System," *14th European Conference on Antennas and Propagation (EuCAP)*, Copenhagen, Denmark, 2020, pp. 1–5, doi: 10.23919/Eu-CAP48036.2020.9135550.
- [4] GTS flexible by design (2020, Apr. 20), [Online]. Available: <https://www.gts-flexible.com/home/>
- [5] Computer Simulation Technology (CST) Microwave Suite 2017. [Online]. Available: <https://www.cst.com>
- [6] Axzon Sensing Data Insights (2020, Apr. 01). Chameleon Sensor Engine [Online]. Available: <http://rfmicron.com/technology/chameleon/>
- [7] Magnelab (2019, Feb. 10). DCT-0016-10/10Vdc split-core current sensor [Online]. Available: <http://www.magnelab.com/products/ac-splitcore-current-sensor-dct-0016-100/>

- [8] Macom partners from RF to light (2020, Aug. 10). Varactor tuning diodes, MA46H070–1056 [Online]. Available: <https://www.macom.com/products/product-detail/MA46H070-1056>
- [9] Macom partners from RF to light, “Surface Mount GaAs Tuning Varactors 0.75, 1.25, & 1.5 Gamma Hyperabrupt,” MA46 series datasheet, Aug. 2020
- [10] Skyworks (2020, Aug. 10). SMV2202-040LF Surface Mount, 0402 Silicon Hyperabrupt Tuning Varactor Diodes[Online]. Available: <https://www.skyworksinc.com/en/Products/Diodes/SMV2202-040LF>
- [11] Skyworks, “SMV2201-SMV2205 Series: Surface Mount, 0402 Silicon Hyperabrupt Tuning Varactor Diodes,” SMV2019 to SMV2023 varactors datasheet, May 23, 2012.
- [12] RS components (2020, Apr. 20). RS pro silver conductive paint [Online]. Available: <https://uk.rs-online.com/web/p/conductive-adhesives/1863600/>
- [13] NCD (2019, Aug. 26). IoT long range wireless ac current monitor [Online]. Available: <https://store.ncd.io/product/wireless-ac-current-monitor/>
- [14] Monnit (2019, Aug. 26). Alta wireless ac current meter - 20 A - AA battery powered [Online]. Available: <https://www.monnit.com/Product/MNS2-9-W2-CM-020/>
- [15] Pressac (2019, Aug. 26). Current sensor: one channel [Online]. Available: <https://www.pressac.com/current-monitoring-sensors/>
- [16] Magnelab (2019, Aug. 26). SCT-125w-100 by Magnelab [Online]. Available: <https://www.magnelab.com/products/wireless-ac-current-sensor-system-sct-125w/>
- [17] N. Tamkittikhun, T. Tantidham and P. Intakot, “AC power meter design based on Arduino: Multichannel single-phase approach,” in *2015 International Computer Science and Engineering Conference (ICSEC)*, Chiang Mai, 2015, pp. 1–5, doi: 10.1109/ICSEC.2015.7401422.
- [18] N. Tamkittikhun, T. Tantidham and P. Intakot, “AC power meter design for home electrical appliances,” in *2015 12th International Conference on Electrical Engineering/Electronics, Computer, Telecommunications and Information Technology (ECTI-CON)*, Hua Hin, 2015, pp. 1–6, doi: 10.1109/ECTICon.2015.7207005.

-
- [19] S. Yildiz and M. Burunkaya, “Web Based Smart Meter for General Purpose Smart Home Systems with ESP8266,” in *2019 3rd International Symposium on Multidisciplinary Studies and Innovative Technologies (ISMSIT)*, Ankara, Turkey, 2019, pp. 1–6, doi: 10.1109/ISMSIT.2019.8932931.
- [20] Q. R. Xu, I. Paprotny, M. Seidel, R. M. White and P. K. Wright, “Stick-On Piezoelectromagnetic AC Current Monitoring of Circuit Breaker Panels,” in *IEEE Sensors Journal*, vol. 13, no. 3, pp. 1055–1064, March 2013, doi: 10.1109/JSEN.2012.2234738.
- [21] R. Morello, C. De Capua, G. Fulco and S. C. Mukhopadhyay, “A Smart Power Meter to Monitor Energy Flow in Smart Grids: The Role of Advanced Sensing and IoT in the Electric Grid of the Future,” in *IEEE Sensors Journal*, vol. 17, no. 23, pp. 7828–7837, 1 Dec.1, 2017, doi: 10.1109/JSEN.2017.2760014.

Miniaturised RFID Tag Antenna Design

6.1 Introduction

THIS chapter describes a new tag antenna design for the dual RFID tag system. The meander line technique is utilised to reduce the size of the tag antenna without affecting the reading range. The tag antenna occupies a total area of $46 \times 33 \text{ mm}^2$. The antenna port impedance is conjugately matched with the tag chip impedance of $1.63 \Omega - j 61.07 \Omega$, at 868 MHz and the resultant reflection coefficient is less than -10 dB and the realised gain is 0.368 dB. A prototype tag is tested to validate the miniaturised tag antenna that streams current measurement data over a read range over 5 m using the European RFID UHF band at 868 MHz. A detailed parametric analysis of various design parameters such as the length and width of the meander line and the size of the feed loop is presented, illustrating how the main design parameters can affect the antenna gain and impedance which determine the tag resonance frequency and read range. The antenna design discussed in the previous chapter has a low read range when two tag antennas were integrated to a single transformer. Because the tag antennas were located nearby and they strongly effected each other performance. Therefore, in order to improve the read range of both tags, in this chapter, a new meander-line antenna is designed in such way that it occupies a small space as well as to be easily integrated with the current transformer. The remainder of the chapter is organised as follow: In Section 6.2, the proposed miniaturised tag antenna is outlined. Section 6.2.1 describes the simulation results and Section 6.2.2 presents the parametric design study. In Section 6.2.3, the theoretical read range of the tag is discussed. The experimental results are reported in Section 6.2.4. Finally, Section 6.3 concludes the chapter.

6.2 Miniaturised Tag Antennas Design

The geometry of the miniaturised tag antenna with a bending structure to reduce the size of the antenna is shown in Figure 6.1. The design parameter values are listed in Table 6.1 and 6.2. The proposed tag antenna design is similar to an electrical dipole but the meander line technique [1–6] is utilised to reduce the size of the antenna. Additionally, a T-matching structure is introduced to enable efficient matching. The meander line dipole antenna was chosen due to the following reasons: (i) the antenna can be easily tuned by simply trimming its radiating arms; (ii) to be compact in size and has a simple structure; and (ii) provide omnidirectional performance. The antenna dimensions were optimised to align its input impedance with the tag chip impedance of $1.63 \Omega - j 61.07 \Omega$, at 868 MHz. The antenna occupies total area of $46 \times 33 \text{ mm}^2$ (including the size of the T-matching network). The fine tuning and conjugate impedance matching between the antenna and the tag chip is achieved by adjusting the feed loop size.

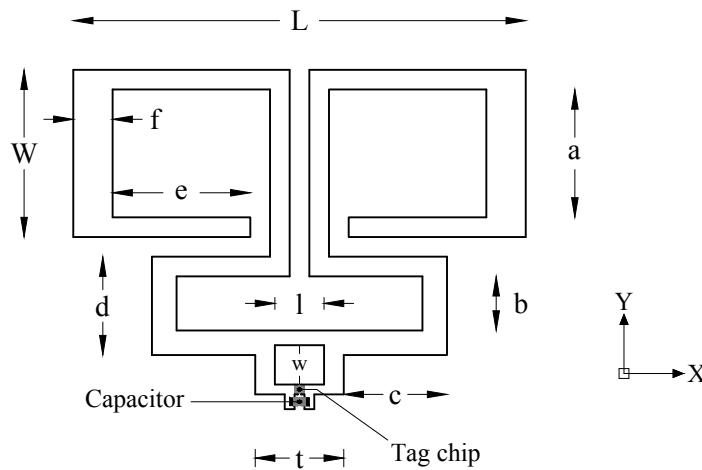


Figure 6.1: Geometry of the proposed miniaturised tag antenna.

Table 6.1: Feed loop dimensions of the miniaturised tag antenna.

Parameters (mm)	l	w	t
	5	4	9

Two identical miniaturised tag antennas design, Figure 6.1, integrated to the current transformer, forming a dual tag system, as shown in Figure 6.2. The tag antennas are placed in the horizontal and vertical orientation in order to keep the antennas well isolated from each other. Good isolation between the radiating elements of the tag antennas will help to

Table 6.2: Simulated miniaturised tag antenna dimensions.

Parameters (mm)	L	W	a	b	c	d	e	f
	46	17	13	5.5	10.5	10	14	4

improve the performance of both tags. The total length L of the antenna is 46 mm, and the total width is 29 mm. The length l of the feed loop is 5 mm with the total width w of 4 mm, excluding the width of the copper traces. The width of the horizontal and vertical traces of the feed loop is 2 mm and 1 mm, respectively. The antenna terminals are created by inserting an air gap of 0.2 mm in the feed loop where a tag chip will be attached. The length of the radiating arms that extend from the feed loop in x-axis is 30 mm. Air bridge of 2 mm disconnects the two radiating arms of the tag antenna. The length of the square loop of the radiating arms as well as the length of the feed loop of the tag antenna can be used as tuning parameters. The geometry of both tag antennas is symmetrical.

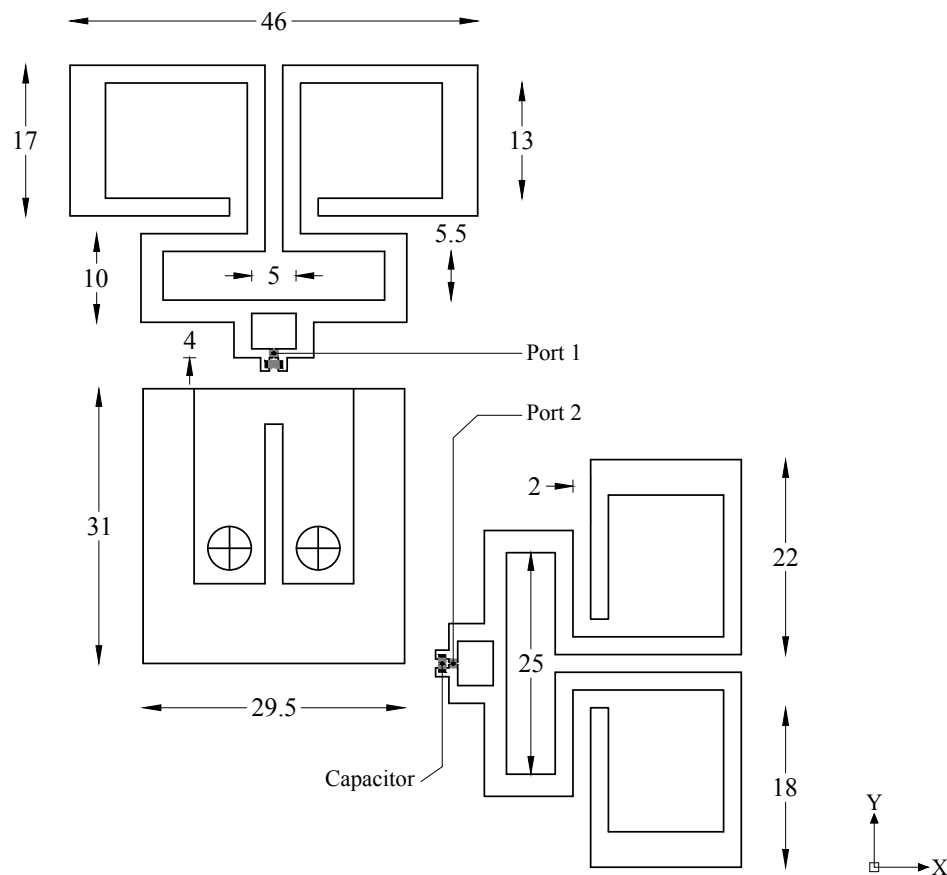


Figure 6.2: Geometry and configuration of the miniaturised two tag antennas design for the current transformer. (All dimensions are in mm)

6.2.1 Simulation Results

The Axzon Magnus S2 chip [7] requiring input power of -16 dBm and has the impedance of 2 pF to 3 pF in parallel with 2284Ω was used in the simulations for designing tag antennas. The tag was designed on a Mylar substrate with a dielectric constant (ϵ_r) of 2.8 , loss tangent (δ) of 0.003 , and with a total height of 0.18 mm including the copper thickness of 0.04 mm. The tag antennas were simulated in CST Microwave Studio [8], and the S-parameters of both tag antennas are given in Figure 6.4. The reflection coefficient S_{11} and S_{22} are well below -10 dB, showing that the tag antennas are well matched at the UHF band 868 MHz. It can be observed that the both tag antennas resonate at the same frequency. However, the mutual coupling between the tag antennas S_{21} and S_{12} are above -10 dB, indicating that the isolation between the ports of the antennas may need to improve further. The mutual coupling may or may not affect the performance of the tag antennas. Therefore, the tag antennas will be fabricated and tested with an RFID reader to evaluate the effect of the mutual coupling on the tag antenna performance, i.e. read range.

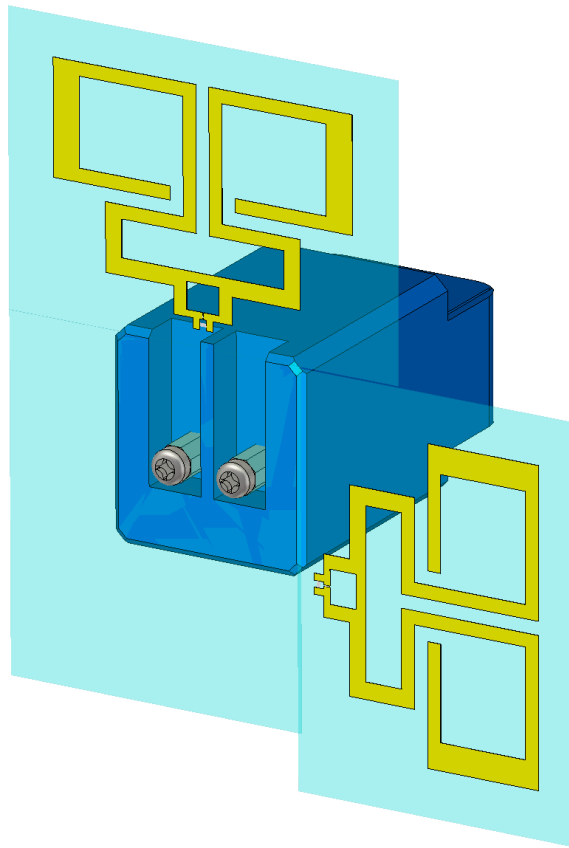


Figure 6.3: 3D model of the tag antennas attached to the transformer in CST Microwave Studio.

Figure 6.5 shows the normalised surface current distribution of the miniaturised two tag antennas design at 868 MHz, and a high concentration of the surface current is observed in both meandered radiating arms of the antennas. Furthermore, Figure 6.6 presents the radiation pattern of the tag antennas in yz -plane, xy -plane, and xz -plane at 868 MHz. It is observed that the realised gain of the tag antenna with the port 1 is 0.368 dB while the realised gain of the tag antenna with the port 2 is 0.336 dB at 868 MHz. Moreover, from Figure 6.6(b), it can be seen that the tag antenna with the port 1 has a high gain when the theta (θ) is equal to 120° and 260° , which tag antenna with the port 2 has a high gain when the theta (θ) is equal to 200° and 330° .

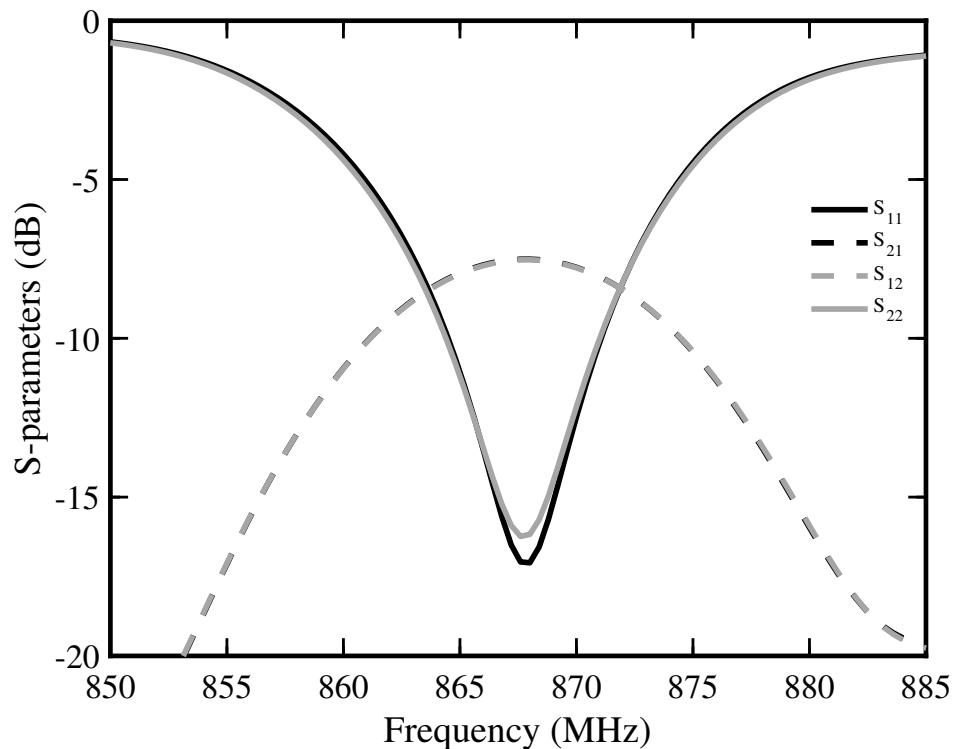


Figure 6.4: Simulated S-parameters of the miniaturised two tag antennas design.

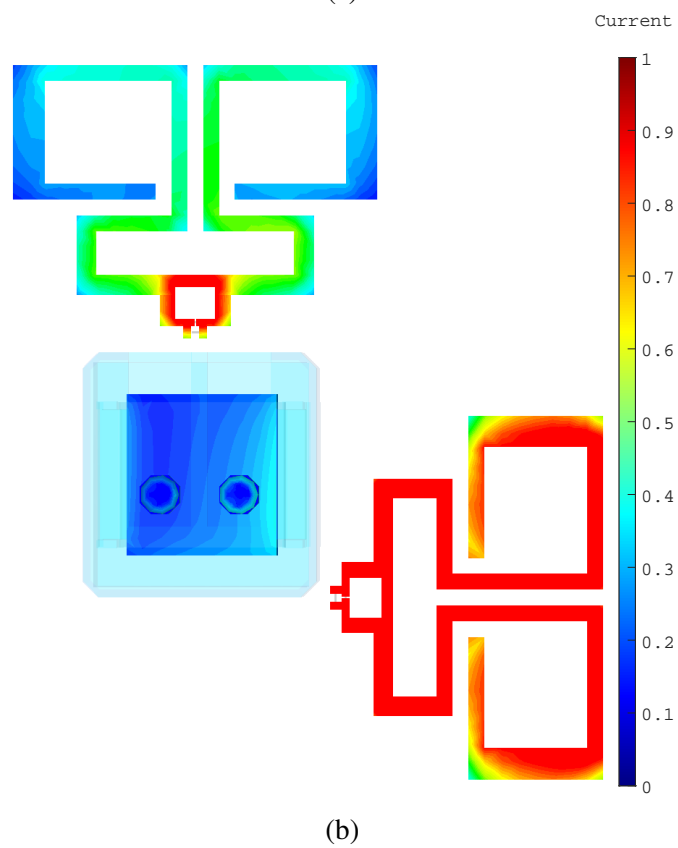
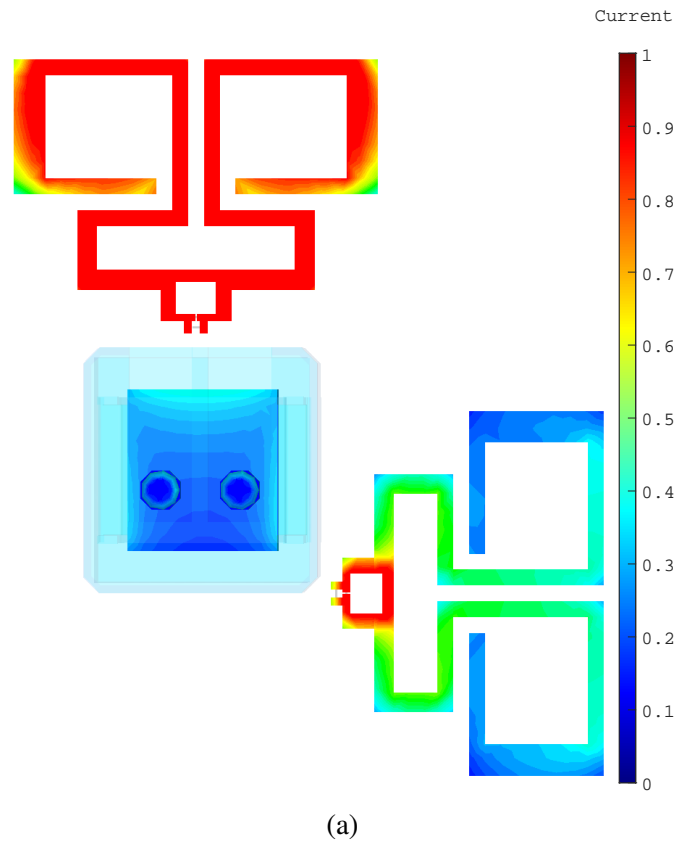


Figure 6.5: The normalised surface current distribution of the miniaturised two tag antennas at 868 MHz: (a) tag antenna with the port 1; and (b) tag antenna with the port 2.

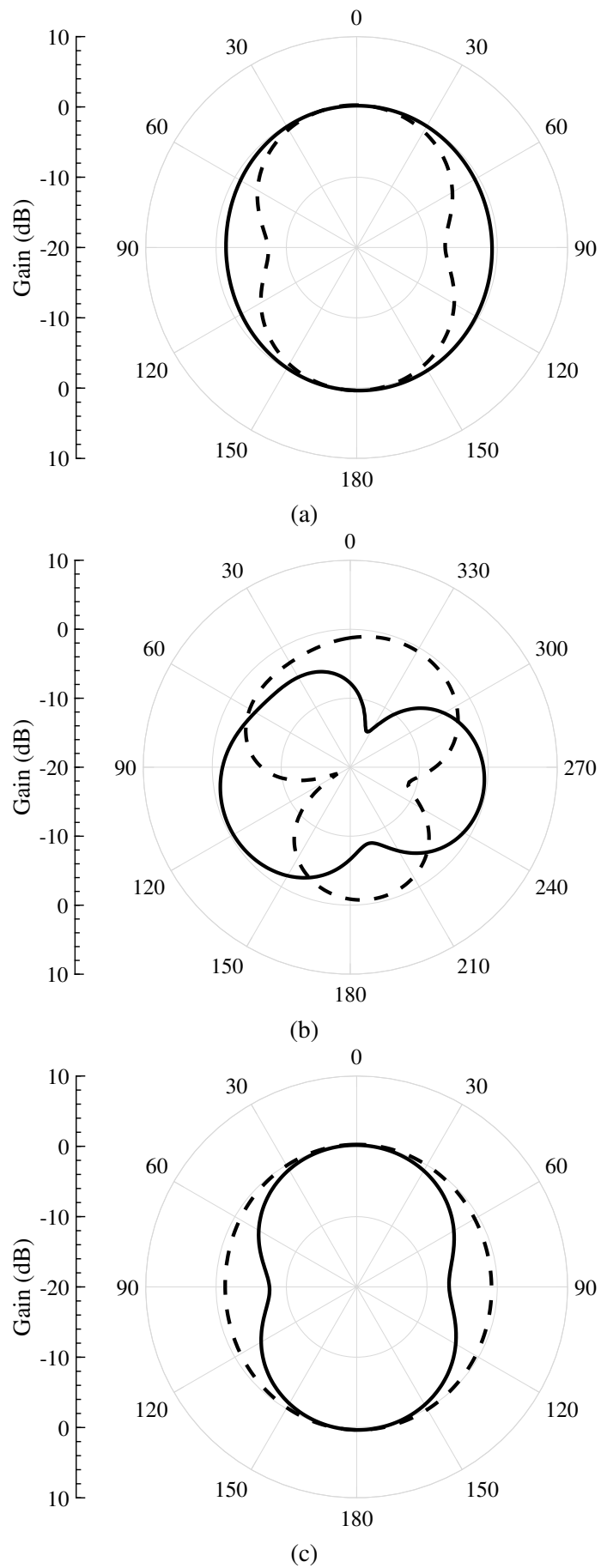


Figure 6.6: Simulated radiation pattern of the miniaturised two tag antennas at 868 MHz: (a) yz -plane; (b) xy -plane; and (c) xz -plane. Black solid lines: tag antenna with the port 1. Dashed black lines: tag antenna with the port 2.

6.2.2 Parametric Design Study

A parametric analysis is performed in CST Microwave Studio to analyse the affect of the antenna design parameters specified in Table 6.1 and 6.2 on the tag antenna performance. The antenna was simulated in three configurations: reducing the length of the antenna; (ii) changing the width of the parameter f ; and (iii) changing the size of the loop, the length l and the width w .

The antenna impedance can be controlled by reducing the length of the meander trace. For example, the parameter e can be used as a tuning parameter to tune the tag antenna. Figure 6.7 and 6.8 show the input impedance of the antenna and the reflection coefficient of the tag with different values of e . It can be observed that as the length of e decreases, the tag resonance frequency moves toward a higher frequency range, as expected. When e is equal to 2 mm, the tag resonates at 895 MHz. However, trimming the meander line leads to impedance mismatching. Therefore, the loop size can be adjusted to achieve optimum resistance and reactance matching.

Furthermore, Table 6.3 summarises the antenna port impedance ($Z_{ant.}$), gain (G_t), realised gain ($rlsd.G_t$) and radiation efficiency (η_e) of the tag for different values of e at 868 MHz. It is observed that the tag gain and the radiation efficiency are degraded as the antenna length decreases.

Table 6.3: Simulated antenna port impedance ($Z_{ant.}$), gain (G_t , excluding input impedance mismatch losses), realised gain ($rlsd.G_t$, including input impedance mismatch losses) and radiation efficiency (η_e) of the tag when e varies from 14 mm to 2 mm at 868 MHz.

e (mm)	14	11	8	5	2
$Z_{ant.}(\Omega)$	2.17 + j62.33	1.08 + j59.38	0.56 + j57.76	0.46 + j56.81	0.36 + j56.26
$G_t(dB)$	1.32	1.15	0.8	0.23	0.68
$rlsd.G_t(dB)$	0.36	-1.9	-6.03	-8.94	-10.68
$\eta_e(dB)$	-0.84	-0.8	-1.16	-1.77	-1.31

Figure 6.9 depicts four tag antenna designs having different values of the parameter f . Each tag was simulated to evaluate the affect of adding more copper at the end of radiating arms on the antenna input impedance. Figure 6.10 and 6.11 illustrate the antenna impedance and the tag reflection coefficient when f varies from 4 mm to 18 mm. It can be observed

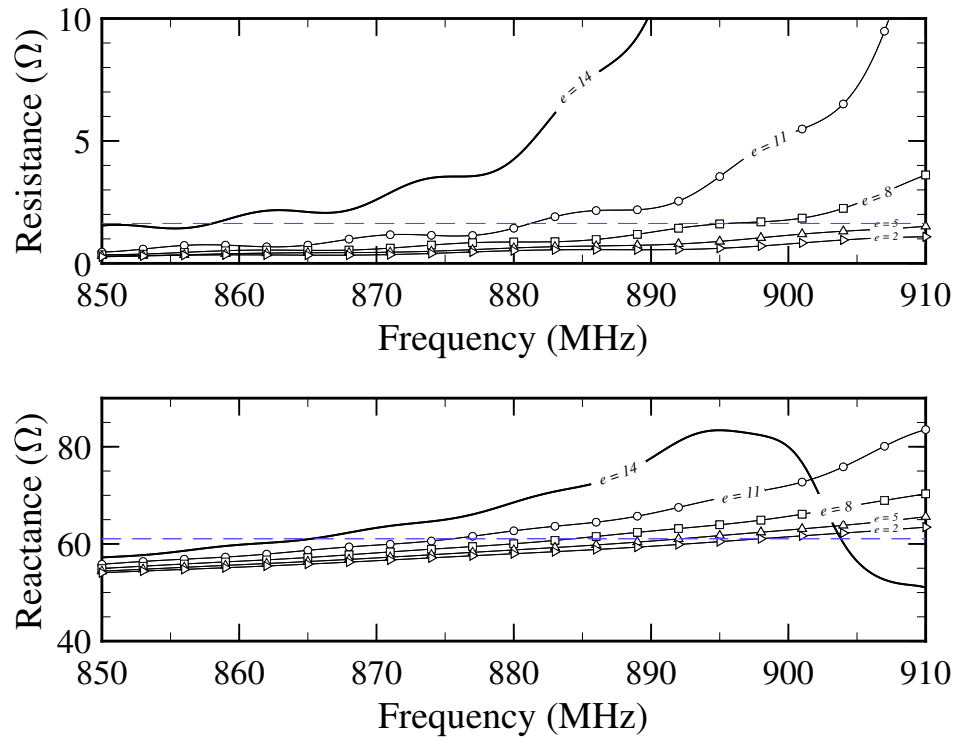


Figure 6.7: Simulated antenna port impedance with different values of the parameter e in mm. The other sizes are fixed to the values in Table 6.2.

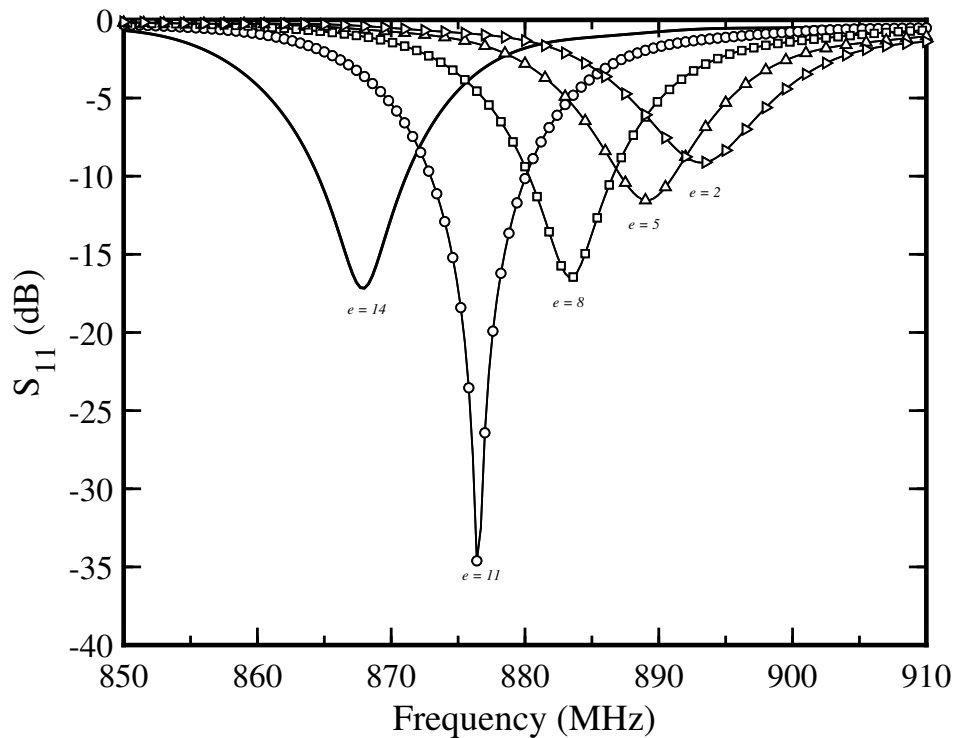


Figure 6.8: Power reflection coefficient of the tag with different values of the parameter e in mm. The other sizes are fixed to the values in Table 6.2.

from Figure 6.11 that increasing the width of f is not significantly influencing the resonance frequency of the tag. Furthermore, there is a slight variation observed in the tag gain and radiation efficiency, as shown in Table 6.4.

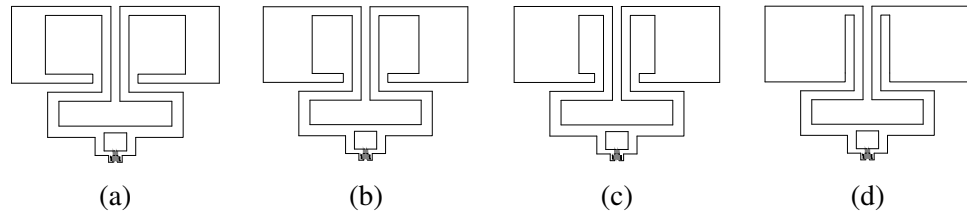


Figure 6.9: Simulated tag antenna design with different values of the parameter f : (a) $f = 7.5$ mm; (b) $f = 11$ mm; (c) $f = 14.5$ mm; and (d) $f = 18$ mm.

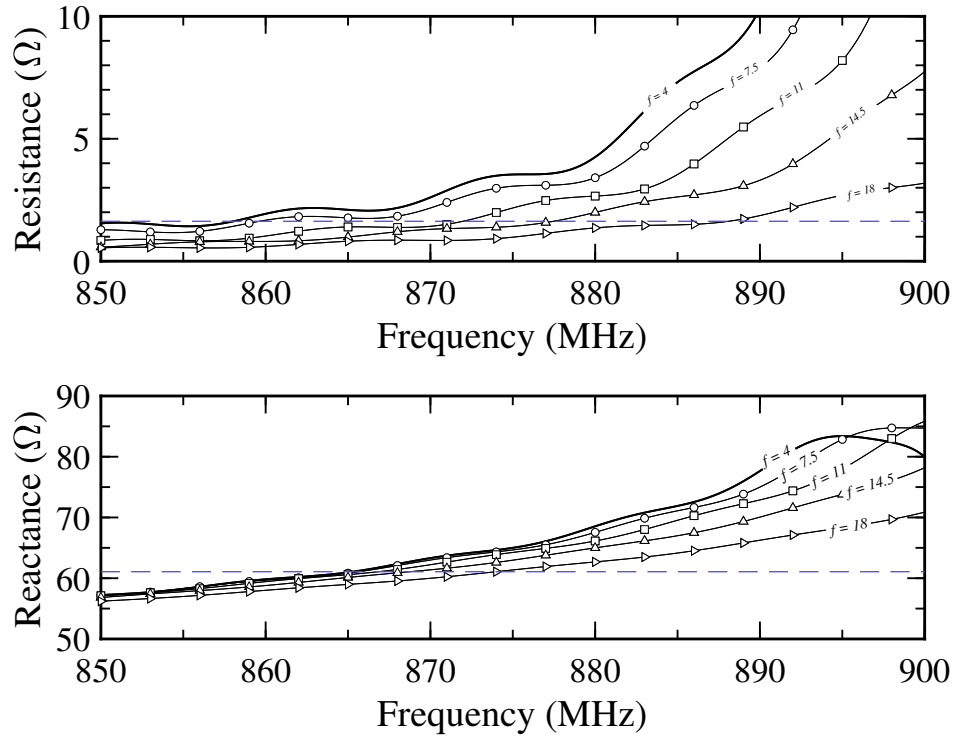


Figure 6.10: Simulated antenna port impedance with different values of the parameter f in mm. The other sizes are fixed to the values in Table 6.2.

As described earlier, the length l and width w of the feed loop strongly affect the antenna input impedance. The effect of the loop size on the antenna impedance is investigated in two configurations: (i) changing the length l of the loop while keeping the width w constant; and (ii) changing the width w of the loop while the length l remains constant.

Figure 6.12 shows the input impedance of the antenna as l and w of the feed loop vary from 4 mm to 6 mm and 3 mm to 5 mm, respectively. It is observed that there is a slight variation in the real magnitude of the antenna. However, the reactance part is significantly changed with the change in l and w . At 915 MHz, the simulated input impedance of the antenna when the $l = 5$ and $w = 4$, is $2.17 \Omega + j 62.33 \Omega$, at 868 MHz, indicating the antenna impedance is well matched with the chip impedance.

Furthermore, as the antenna impedance varies with the parameters l and w and it directly affect the tag resonance frequency. Figure 6.13 shows the reflection coefficient of the tag

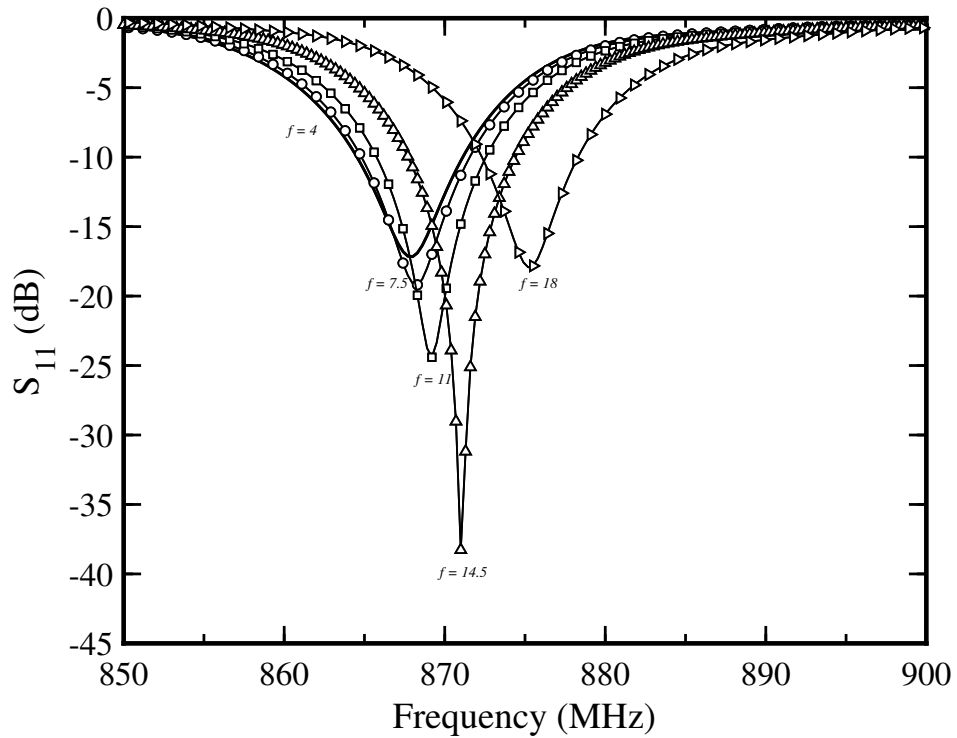


Figure 6.11: Simulated power reflection coefficient of the tag with different values of the parameter f in mm. The other sizes are fixed to the values in Table 6.2.

Table 6.4: Simulated antenna port impedance ($Z_{ant.}$), gain (G_t), realised gain ($rlzd.G_t$), and radiation efficiency (η_e) of the tag when f varies from 4 mm to 18 mm at 868 MHz.

f (mm)	4	7.5	11	14.5	18
$Z_{ant.}(\Omega)$	$2.17 + j62.33$	$1.81 + j62.08$	$1.52 + j61.44$	$1.27 + j60.88$	$0.88 + j59.54$
$G_t(dB)$	1.32	1.31	1.26	1.19	1.25
$rlzd.G_t(dB)$	0.36	0.45	0.48	0.2	-1.52
$\eta_e(dB)$	-0.84	-0.82	-0.86	-0.92	-0.84

when l and w vary from 4 mm to 6 mm and 3 mm to 5 mm, respectively. As can be observed the size of the feed loop has a strong impact on the reflection coefficient of the tag. As the value of l and w increase, the resonance frequency moves toward a lower frequency range, and vice versa. Simulation indicated that decreasing the loop size causes the antenna port impedance to be no longer inductive.

Table 6.5 and 6.6 summarise the antenna input impedance, gain, realised gain and radiation efficiency of the tag with different values of l and w , at 868 MHz. By decreasing the length l and width w , the tag gain and radiation efficiency decrease as well. However, by increasing the length l and width w , the tag gain and radiation efficiency initially increase, afterward when $l = 6$, the tag gain and radiation efficiency are decreased to 1 dB and -1.13 dB,

respectively and when $w = 5$, the tag gain and radiation efficiency are decreased to 1.21 dB and -0.93 dB, respectively.

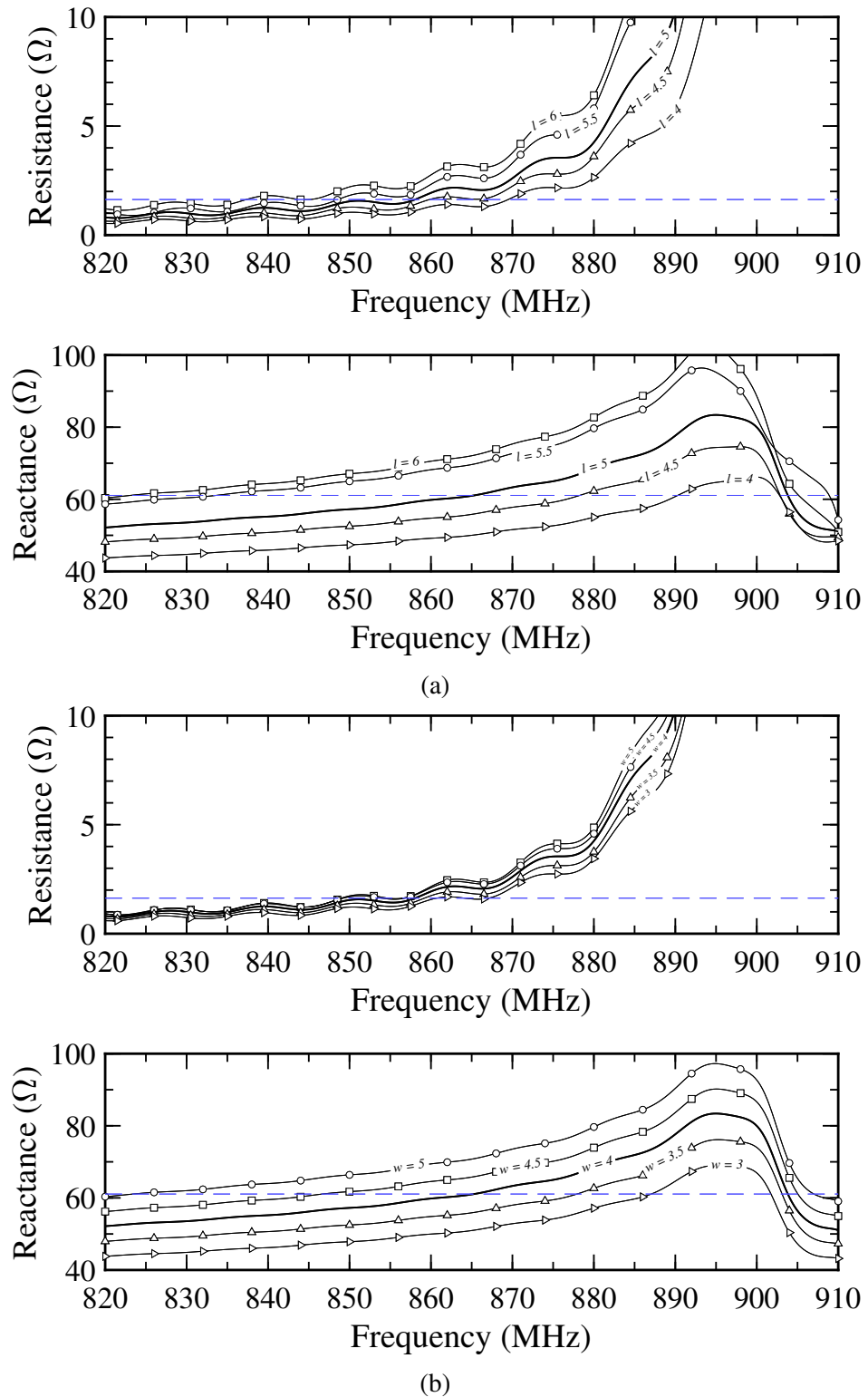
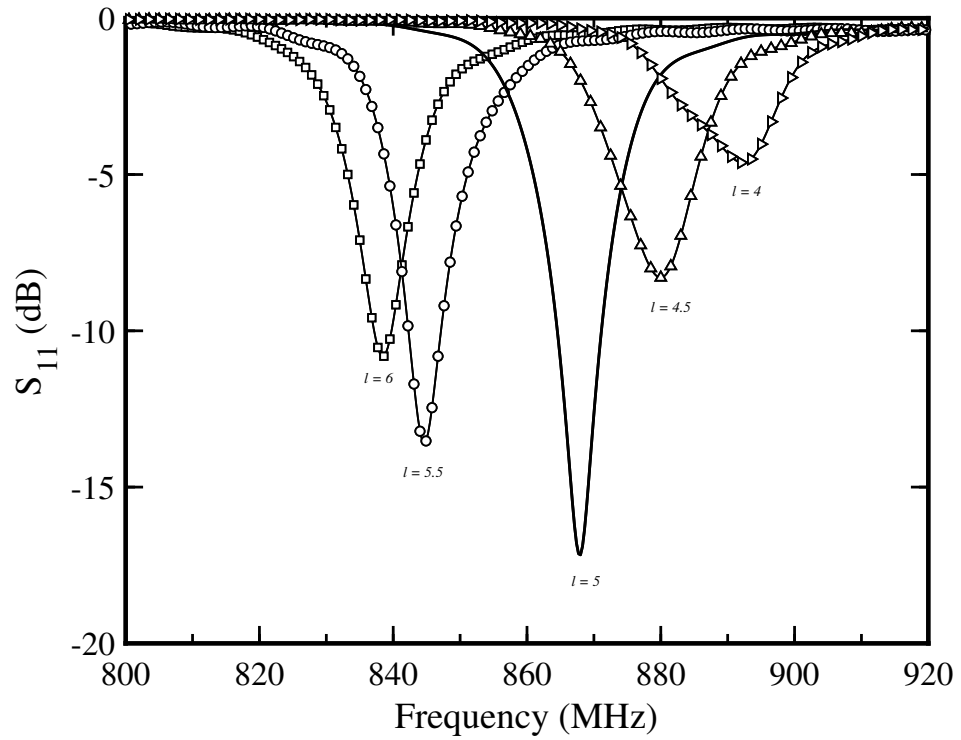
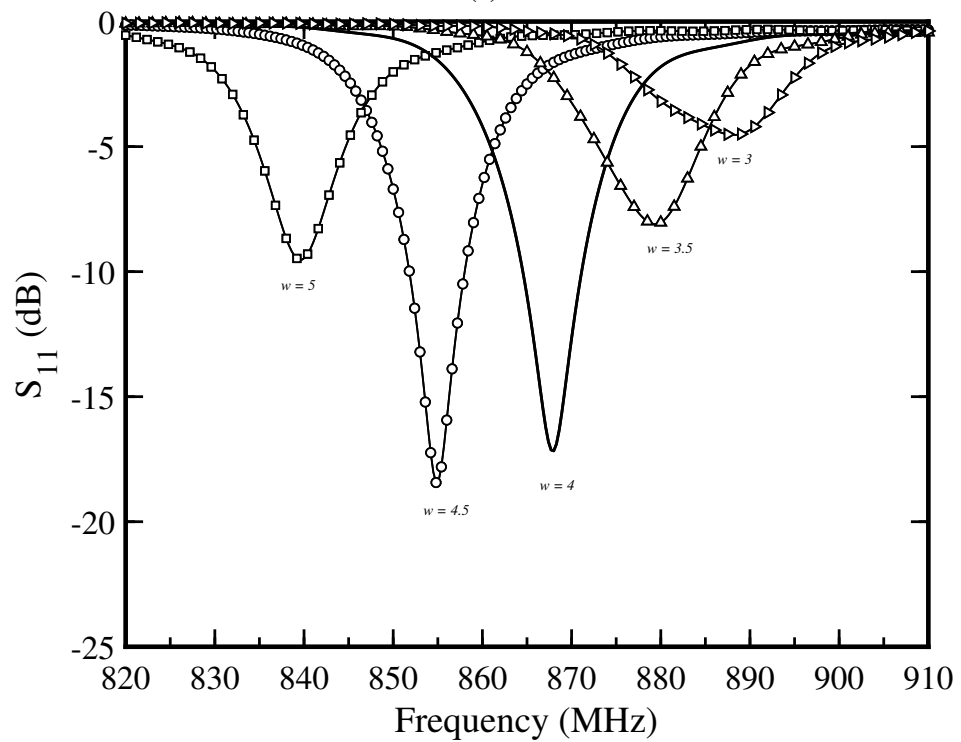


Figure 6.12: Simulated tag antenna input impedance: (a) at the different values of l in mm; and (b) w in mm. The other sizes are fixed to the values in Table 6.2.



(a)



(b)

Figure 6.13: Simulated power reflection coefficient of the tag: (a) at different values of l in mm; and (b) w in mm. The other sizes are fixed to the values in Table 6.2.

Table 6.5: Simulated antenna port impedance ($Z_{ant.}$), gain (G_t), realised gain ($rlsd.G_t$), and radiation efficiency (η_e) of the tag when l varies from 4 mm to 6 mm at 868 MHz.

l (mm)	4	4.5	5	5.5	6
$Z_{ant.}(\Omega)$	$1.49 + j50.97$	$1.82 + j57.03$	$2.17 + j62.33$	$2.99 + j71.38$	$3.05 + j73.89$
$G_t(dB)$	0.88	1.27	1.32	1.61	1
$rlsd.G_t(dB)$	-10.73	-3.41	0.36	-7.31	-8.95
$\eta_e(dB)$	-1.09	-0.66	-0.84	-0.59	-1.13

Table 6.6: Simulated antenna port impedance ($Z_{ant.}$), gain (G_t), realised gain ($rlsd.G_t$), and radiation efficiency (η_e) of the tag when w varies from 3 mm to 5 mm at 868 MHz.

w (mm)	3	3.5	4	4.5	5
$Z_{ant.}(\Omega)$	$1.80 + j52.10$	$2.00 + j57.12$	$2.17 + j62.33$	$2.31 + j67.23$	$2.56 + j72.33$
$G_t(dB)$	1.1	1.21	1.32	1.48	1.21
$rlsd.G_t(dB)$	-9.02	-3.07	0.36	-3.94	-8.68
$\eta_e(dB)$	-0.87	-0.73	-0.84	-0.73	-0.93

6.2.3 Theoretical Read Range

6.2.3.1 Tag with the Port 1

Theoretical read range of the tag can be calculated using the Friis free-space formula:

$$r_{max} = \frac{\lambda_0}{4\pi} \cdot \sqrt{\frac{EIRP \cdot G_r \cdot \tau}{P_{IC}}} \quad (6.1)$$

where λ_0 is the wavelength, EIRP is the effective isotropic radiative power transmitted by the reader antenna, and P_{IC} is the tag chip sensitivity which is the minimum threshold power required to turn on the tag chip. The values of these parameters are following:

$$\lambda_0 = 345.62 \text{ mm } (f_0 = 868 \text{ MHz})$$

$$P_{IC} = -16.1 \text{ dBm } (= 0.0245 \text{ mW})$$

$$EIRP = 3.28 \text{ W}$$

The simulated value of the tag realised gain (G_r) and reflection coefficient (S_{11}) are:

$$G_r = 0.368 \text{ dB} (= 1.0884)$$

$$S_{11} = -16.17 \text{ dB} (= 0.0241)$$

$$\tau = 1 - |S_{11}|^2 (= 0.9994)$$

The maximum theoretical distance between tag and reader can be calculated to be:

$$r_{max} = 10.49 \text{ m.}$$

6.2.3.2 Tag with the Port 2

The simulated value of the tag realised gain (G_r) and reflection coefficient (S_{22}) are:

$$G_r = -0.336 \text{ dB} (= 1.0804)$$

$$S_{22} = -17.07 \text{ dB} (= 0.0196)$$

$$\tau = 1 - |S_{22}|^2 (= 0.9996)$$

The maximum theoretical distance between tag and reader can be calculated to be:

$$r_{max} = 10.45 \text{ m.}$$

6.2.4 Measurement Results

The two tag antennas shown in Figure 6.2 were etched on a Mylar sheet. Figure 6.14 shows the prototype of the miniaturised tag antenna. A 0.3 pF capacitor was mounted on both tag antennas terminals. The two tag antennas were attached to the bottom of the transformer with the same configuration outlined in Figure 6.2 and interrogated by a UHF reader Tagformance Pro System [9], comprising of a linear polarised antenna of 6 dBi gain and placed a fixed distance of 30 cm away from the dual tag system [9]. The tag is capable of operation at distances greater than 30 cm, and the calibrated Tagformance system was able to assess the maximum read distance achievable in each measurement. The set up was also able to record the sensor code as well as provide tag threshold power analysis. Figure 6.15 illustrates the measured sensor code of the tag antennas. The sensor value of both tags is 14 at 868 MHz. It is observed that the tuning of the tags can be improved further. Figure 6.16 represents the

measured read range of the tag antennas. Both tags have a good read range as compared to the previous two tag antennas design. The increased in the read range may be due to the isolation between the antennas. The read range of the tag antenna with the port 1 is 5.2 m while the read range of the tag antenna with the port 2 is 6.5 m which about 1.5 m greater than the tag antenna with the port 1. The measured results suggest that by properly isolating the tag antennas, a good read range performance can be achieved for both tag antennas. Furthermore, the theoretical read range of both tags is higher than the measured read range is the result of the following assumptions: (i) the actual sensitivity of the tag chip tends to be smaller than nominal value which can significantly affect the tag read range; (ii) the non-ideal etching mechanism as well as not properly attaching the tag microchip with the antenna port; and (iii) the not-anechoic measurement environment. In future work, the tag antennas will be linked with the tuning circuits and will be tested with an electrical load.

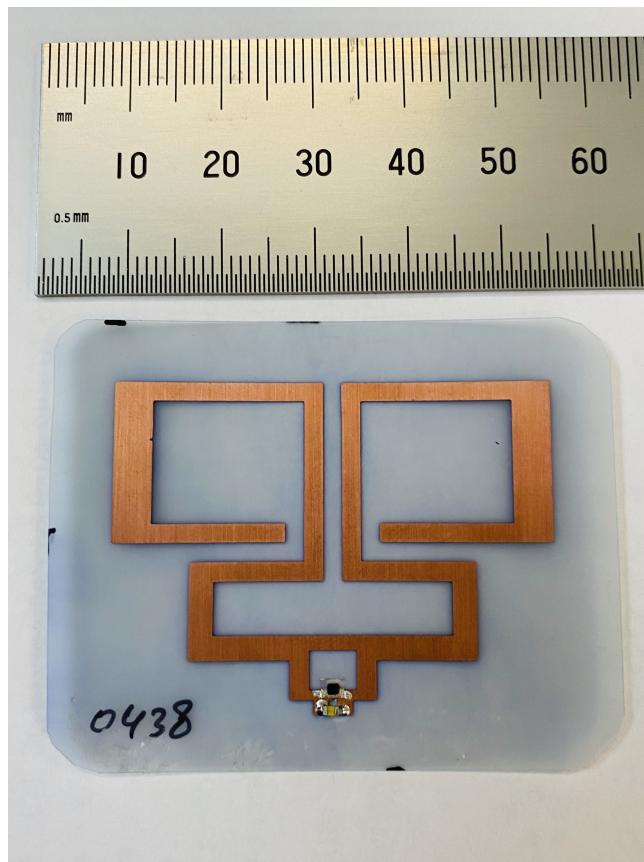


Figure 6.14: Final prototype of the proposed miniaturised tag antenna.

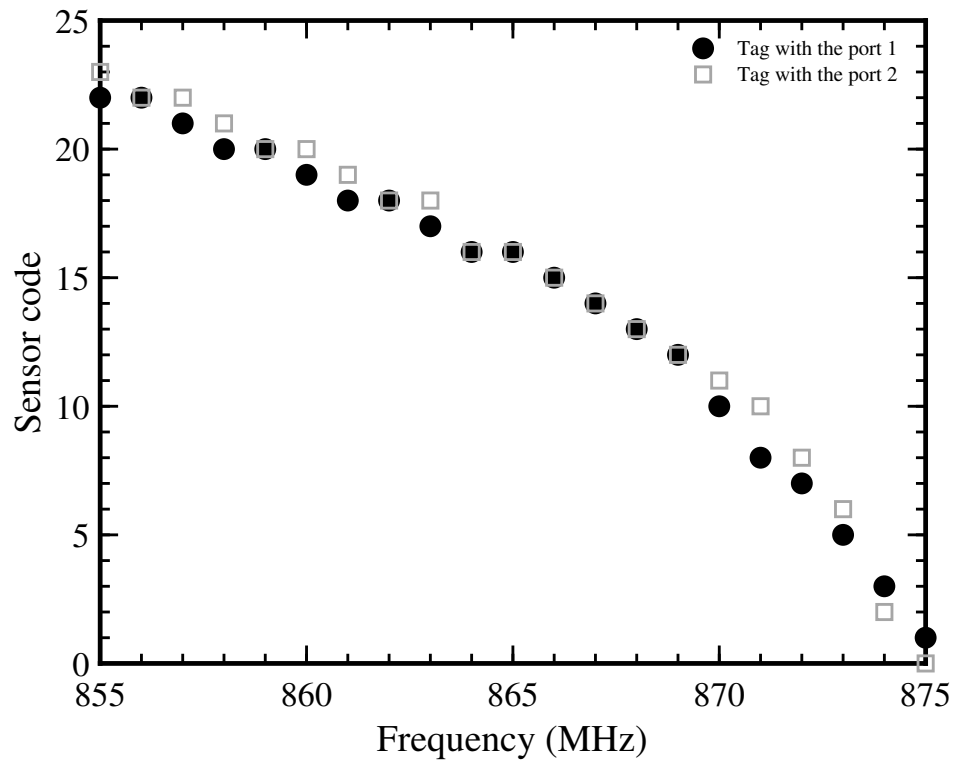


Figure 6.15: Measured sensor value of the miniaturised two tag antennas design.

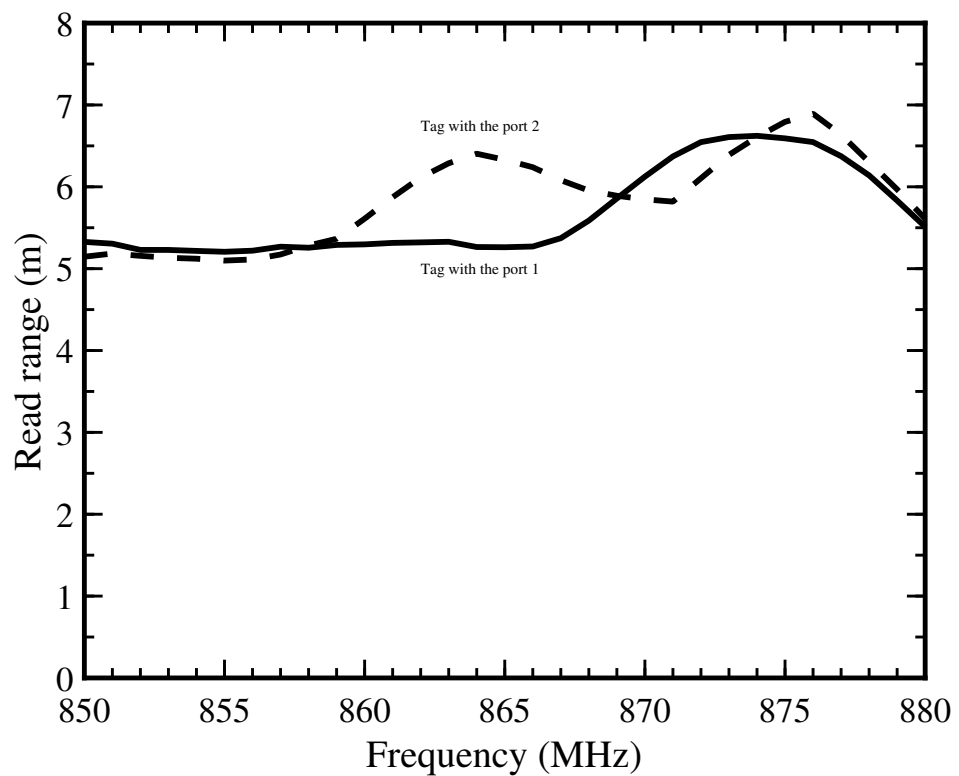


Figure 6.16: Measured read range of the miniaturised two tag antennas design.

6.3 Conclusion

This chapter introduced a new miniaturised tag antenna design for the dual tag system. The meander line antenna is used to reduce the size of the antenna while maintaining the tag link. The overall size of the proposed tag antenna is tuned to operate at 868 MHz and occupies a total area of $46 \times 33 \text{ mm}^2$. The parametric analysis shows that it is possible to tune the tag antenna by trimming its meander trace. The tuning T-match section of the antenna design strongly impacts the antenna port impedance and consequently, the resonance frequency of the tag. It has been found out that the feed loop dimensions can be adjusted to achieve the desired impedance matching. Prototypes of the tag antennas were tested and measured results show that both tags have good read range when integrated to the current transformer. Despite the close proximity and small in size, the tag with the port 1 has a good read range of 5 m and the tag with port 2 has a read range of 6 m at the UHF band of 868 MHz.

The main contribution of this chapter has been,

- A novel miniaturised tag antenna design for the dual RFID tag system.

In the next chapter, a summary, conclusion and recommendations for future work is provided.

References

- [1] E. A. Soliman, M. O. Sallam, W. De Raedt and G. A. E. Vandenbosch, "Miniaturized RFID Tag Antenna Operating at 915 MHz," in *IEEE Antennas and Wireless Propagation Letters*, vol. 11, pp. 1068-1071, 2012, doi: 10.1109/LAWP.2012.2215951.
- [2] K. V. S. Rao, P. V. Nikitin and S. F. Lam, "Antenna design for UHF RFID tags: a review and a practical application," in *IEEE Transactions on Antennas and Propagation*, vol. 53, no. 12, pp. 3870-3876, Dec. 2005, doi: 10.1109/TAP.2005.859919.
- [3] F. Paredes, G. Zamora, F. J. Herraiz-Martinez, F. Martin and J. Bonache, "Dual-Band UHF-RFID Tags Based on Meander-Line Antennas Loaded With Spiral Resonators," in *IEEE Antennas and Wireless Propagation Letters*, vol. 10, pp. 768-771, 2011, doi: 10.1109/LAWP.2011.2162716.
- [4] C. Occhiuzzi, C. Paggi and G. Marrocco, "Passive RFID Strain-Sensor Based on Meander-Line Antennas," in *IEEE Transactions on Antennas and Propagation*, vol. 59, no. 12, pp. 4836-4840, Dec. 2011, doi: 10.1109/TAP.2011.2165517.
- [5] B. D. Braaten, M. Reich and J. Glower, "A Compact Meander-Line UHF RFID Tag Antenna Loaded With Elements Found in Right/Left-Handed Coplanar Waveguide Structures," in *IEEE Antennas and Wireless Propagation Letters*, vol. 8, pp. 1158-1161, 2009, doi: 10.1109/LAWP.2009.2034990.
- [6] C. Calabrese and G. Marrocco, "Meandered-Slot Antennas for Sensor-RFID Tags," in *IEEE Antennas and Wireless Propagation Letters*, vol. 7, pp. 5-8, 2008, doi: 10.1109/LAWP.2007.914123.

-
- [7] Axzon Sensing Data Insights (2020, Apr. 01). Chameleon Sensor Engine [Online]. Available: <http://rfmicron.com/technology/chameleon/>
- [8] Computer Simulation Technology (CST) Microwave Suite 2017. [Online]. Available: <https://www.cst.com>
- [9] Voyantic (2019, Feb. 10). Tagformance Pro [Online]. Available: <http://voyantic.com/products/tagformance-pro>

Conclusions and Future Work

7.1 Introduction

THIS chapter presents a summary of the work covered in this thesis. This will be followed by a discussion of the research findings of this study and provides recommendations for future research directions.

7.2 Summary and Conclusion

The main aim of the research was to explore the RFID technology for real-time ac current sensing to enhance energy-saving solutions in smart homes. This aim is achieved by designing a capacitance sensing UHF RFID tag and transformed it into an ac current sensor. The sensing mechanism is based on the tuning of the tag antenna via a tuning circuit. Therefore, this study also focused on designing a tuning circuit using a varactor tuning diode. The sensing mechanism was described by which the tuning circuit was coupled with the capacitance sensing UHF RFID tag and integrated with the current transformer for sensing ac current in an electrical wire for smart power monitoring of individual appliances. A switchable electrical load was used to evaluate the performance of the proposed tag system.

A novel tag antenna for the current transformer is presented, fabricated and measured in this work. To reduce the tag antenna size, the radiating arms of the antenna was bent around the transformer to achieve a compact form integration with the transformer. Self-tuning RFID chips were used to design antennas to achieve optimum tag performance. The self-tuning properties of the Axzon Magnus S2 chip were exploited for low-cost sensing

applications, and several simulations and experiments were performed to analyse the relationship between the capacitance and the sensor code of the self-tuning RFID tags. The design of the single tag system was further extended, and a novel dual tag system for ac current measurement is introduced. The dual tag system consists of two tag antennas, designed in close proximity and integrated into a single current transformer.

In addition, a miniaturised tag antenna for the dual tag system is also investigated. The overall size of the tag is significantly reduced by applying the antenna meander-line technique while maintaining the link. The geometrical parameters of the antenna were optimised to have the best conjugate matching to the Magnus S2 chip with the impedance of $1.63 \Omega - j 61.07 \Omega$, at 868 MHz. The tag occupies a total volume of $46 \times 33 \text{ mm}^2$. Despite small in size, the tag has a good read range of 6 m at the UHF band.

In this work, we only focused on developing the sensing mechanism for small ac current measurement in the range of 0 A to 13 A for domestic applications. However, the proposed current sensing mechanism can be optimised for sensing ac current higher than 13 A. This can be done by adjusting the reactance of the tuning circuit or a current transformer with a different turns ratio could be employed. As well as indicating the current level, the technique can also be used to detect the ON and OFF state of an electrical device and is demonstrated to work for a rapidly switching load. Furthermore, the sensing tag system was tuned for the Electronic Product Code (EPC) Class 1 Generation 2 UHF RFID readers at 868 MHz. However, the study did not explore the sensing tag system for other RFID UHF bands, such as 902–928 MHz (US), and 950–956 MHz (Japan).

Chapter 2 presented a review of the literature on passive UHF RFID tags and antenna designs and their applications. This chapter provides a brief overview of RFID systems and the principle operation of the UHF passive RFID system. RFID tags were grouped into three main categories: (i) active; (ii) passive; and (iii) semipassive. A number of conjugate input impedance matching techniques have been reported in the literature for designing RFID tags are demonstrated. Several types of tag antenna designs and the size reduction techniques for RFID applications were also discussed. Finally, this chapter covers the previous work related to the RFID sensing and RFID based ac current sensing solution for power monitoring.

The development of a novel RFID ac current sensing mechanism for smart power monitoring systems was introduced in Chapter 3. We outlined the operating principle of the pro-

posed sensing tag system. We also provided a detail explanation of the design of a current transformer, a tuning circuit and a capacitance sensing RFID tag. The system was experimentally tested with an electrical load to evaluate the performance of the tag system. The measured results suggest that the sensing tag can measure ac current in the range from 1.5 A to 10 A and had a good read range of about 4 m across all current readings. A brief overview of commercially available smart current meters was presented and compared them with the proposed RFID sensing system in term of cost, communication and power type.

Chapter 4 explored a novel tag antenna design for the current transformer. The tag antenna was designed with the aim to reduce the size of the antenna as well as to increase the current sensing range of the tag system. This chapter also described a 3D model of a current transformer designed in CST for assessing the impact of the current transformer on the tag antenna performance. The measurement results show that the optimised tag antenna can measure ac current in the range from 1 A to 13 A and had a good read range of about 3.5 m across all current readings.

Chapter 5 presented a dual tag system for ac current sensing. It consists of two tag antennas coupled with two tuning circuits and integrated into a single current transformer. The system is developed with the aim to increase the current sensing range of the sensor using multiple tag chips in a single design. The measurement results show that the dual tag system can measure ac current in the range from 0 A to 13 A with a good read range of about 2.5 m to 5 m. This chapter investigated the mutual coupling between the antenna elements in designing two tag antennas in close proximity.

A design of a miniaturised tag antenna for a dual tag system was presented in Chapter 6. The meander line antenna is described to reduce the size of the antenna while maintaining the tag link. The tag antenna occupies a total area of $46 \times 33 \text{ mm}^2$. I provided the detail of the antenna design parameters influencing the tag antenna performance. Measurement results were also discussed. When two tags are integrated with the current transformer, it was observed that both tags have a good read range from 5 m to 6 m at the UHF band of 868 MHz.

Chapter 7 concluded the thesis, and we provided some suggestions for future work for researchers in the field.

7.3 Recommendations for Future Work

The results suggest that the read range of the tag was decreased when the tag antenna was bent around the current transformer. It would be worth to investigate how the impact of the current transformer on the tag antenna can be further decreased to improve the performance of the tag antenna.

The tuning diode used in this study exhibits non-linear capacitance-voltage characteristics. Therefore, the sensor code and current curve of the tag system was non-linear. Because of the limited tag chip resolution and the non-linearity response of the tuning circuit make it difficult to detect low and high ac current level (referring to 0–13 A) with the single tag system. A new ultra-linear tuning diode and multiple tuning diodes can be employed in the tuning circuit to improve the non-linear capacitance-voltage characteristics.

A mountable tag antenna for the current transformer can be explored. The advantage of such an antenna will be a compact form integration with the current transformer. The main challenge in the mountable antenna design is the read range of the tag as the tag performance significantly degrades when it mounted on a device like a transformer which contains detuning elements.

The size of the two tag antennas design can be further optimised to reduce the overall size of the dual tag system. Furthermore, mutual coupling reduction techniques can be applied to reduce the mutual coupling between the radiating elements, which may lead to increase the read range of the tags. The mutual coupling between the two tag antennas can be further explored to assess the affect of the mutual coupling on the tag antenna performance.

In future, the self-tuning Axzon Magnus S2 tag chip can be replaced with the new Axzon Xerxes tag chip. The Xerxes tag chip is a multi-state tag chip and has a high resolution. The capacitance sensing range of the chip lie between 0.5 pF to 50 pF. The sensor code of the chip can be tuned between 0 to 554, as well as the chip has two analogue ports which can be used for various measurements include temperature, resistance, capacitance and voltage.

24 V DC Wireless Energy Logger

A.1 Introduction

THIS chapter describes the development of a 24 V dc smart power monitoring system. The system can simultaneously monitor three electrical parameters: (i) current; (ii) voltage; and (iii) power consumption of electrical devices in 24 V dc power distribution systems. Unlike plug-in dc meters [1], the proposed system can stream data to a data acquisition module via WiFi network where the data can be displayed in a dashboard, as well as to be viewed in a graph. The proposed system consists of a dc current sensor for sensing current in a power cable, a dc power extension cable for supplying a dc voltage sample to a central processing unit for measurements, a central processing unit, and a 5 V dc power adapter for supplying power to the central processing unit. The central processing unit consists of an Atmel ATmega328P microcontroller with 5 input channels of 10-bit analogue to digital converter (adc) on board. Additionally, an external 24-bit adc is integrated into the system board for very low voltage measurements with high accuracy. A Hall effect split-core current transducer is used to measure current in the range of 0 A to 100 A dc from the power cable, however, 0 V to 24 V dc voltage sample will directly feed from a dc power supply via a dc power extension cable to the central processing unit for real-time voltage measurements. The system is integrated with a Raspberry Pi Model B which uses wireless LAN for transmitting electrical data to the data acquisition module. The design of the proposed dc smart power monitoring system is not novel but can play an important role in tracking the power consumption of individual electrical appliances in solar power systems for smart homes, as well as in 24 V power distribution system in industries. This work is the part of the Interreg

V Seas Project INCASE (Industry 4.0 via Networked Control Applications and Sustainable Engineering) [2]. The main objective of the INCASE was preparing the industry (automation and manufacturing industry) for the future Industry 4.0 (I4.0) and Industrial Internet of Things (IIoT). In Section A.2, the proposed system is outlined. Section A.3 describes the central processing unit and Section A.4 presents the PCB layout. In Section A.5, the software part of the system is discussed. The experimental results are reported in Section A.6. Finally, Section A.8 concludes the chapter.

A.1.1 System Specification

The basic features of the proposed dc power monitoring system are:

- Current dc: 1–100 A
- Voltage dc: 0–24 V
- Power measurement range: 0–2.4 kW
- Data transmission: WiFi and ethernet connection
- Low-cost and portable device

A.2 Proposed System

The block diagram of the proposed system consists of a 5 V dc power adapter, a dc current sensor, a dc voltage sensor node and a central processing unit, as shown in Figure A.1. The central processing unit consists of an Atmel ATmega328P microcontroller, a 24-bit A/D converter, a real-time clock integrated circuit (IC), a UBS to URT IC, an ID EEPROM microchip, a Raspberry Pi with on-board WiFi, a 3.3 V voltage regulator, and a mini USB connector. The 5 V dc power adapter is used to power up the system board. The dc current sensor used to detect the current from a power cable of an electrical appliance and transform into dc voltage proportionally. The voltage feed to the filtered voltage divider circuit in the Printed Circuit Board (PCB) board, where the voltage is scaled-down and feed to the adc input channels of the microchips (microcontroller and 24-bit adc). The adc allows converting

an analogue signal into a digital signal. Finally, the measured signals will be displayed on a PC and to be transmitted to a web server.

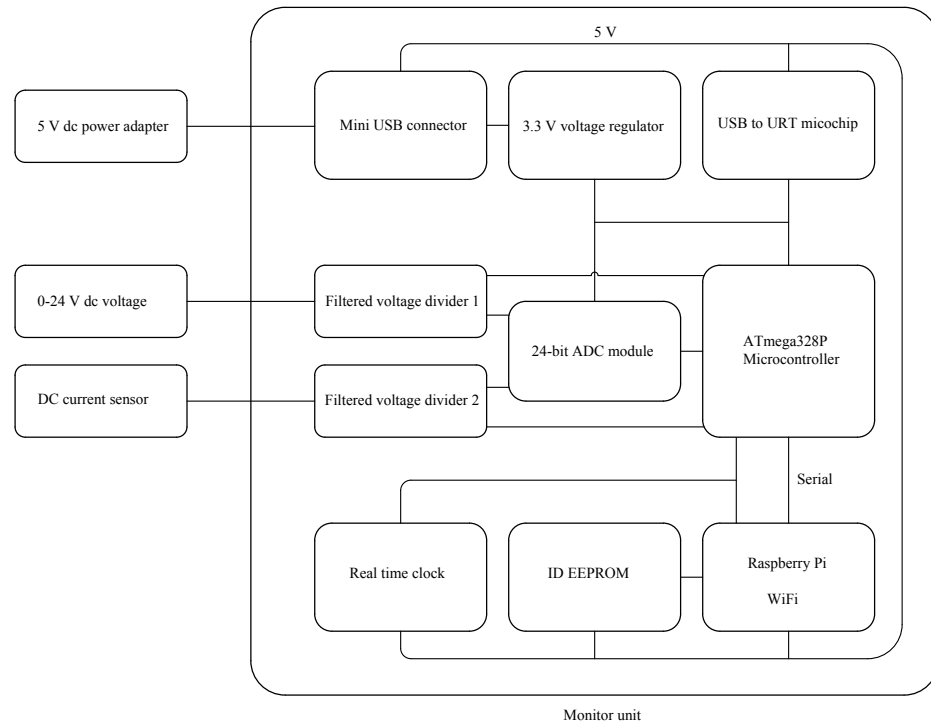


Figure A.1: Block diagram of the 24 V dc smart power monitoring system.

A.2.1 DC Current Sensor

The Hall effect split-core current transducer [3], with an input current range of 0 A to 100 A dc and transform it into 0 V to 4 V dc proportionally with the accuracy of 1% is used to sense dc current from the power cable. The sensor needs a power source of ± 15 V for operation. The transducer can be clipped around a single electrical cable, either live or neutral. The sensor works on the Hall effect principle [4]. The schematic diagram of the sensor, Figure A.2, consists of a primary winding, a magnetic core, a Hall element, a reference current amplifier with an offset adjustment potentiometer, and a high gain output amplifier connected to R_1 , R_2 and R_3 .

A.2.2 DC Voltage

DC voltage can be directly supplied from the power supply to the central monitoring unit via dc power extension cable for measurements. The system can measure dc voltage from 0 V to 24 V. The maximum voltage that the adc input channels of the microcontroller and the adc

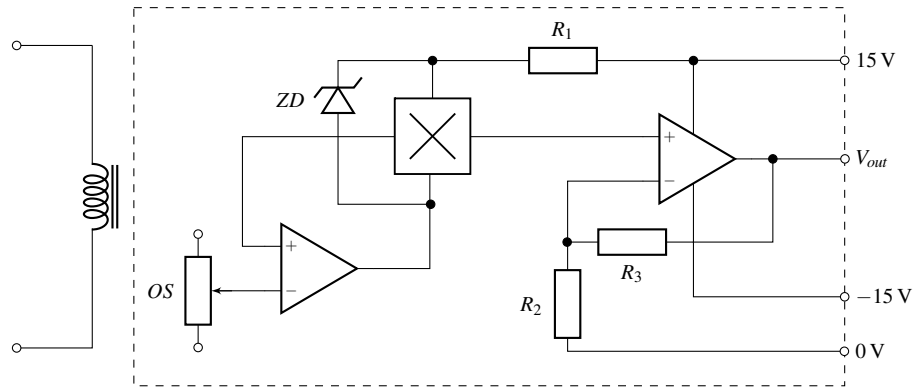


Figure A.2: Schematic diagram of the Hall effect split-core current transducer [3].

input channels of the 24-bit adc board can measure between 3.3 V and 2.5 V respectively. Therefore, a voltage divider is used to convert a higher voltage to a lower voltage.

A.2.3 Filtered Voltage Divider

The circuit diagrams of the filtered voltage divider for the dc current sensor and 0 V to 24 V dc voltage sample are shown in Figure A.3 and Figure A.4 respectively. The circuit consists of a voltage divider, a current limiting resistor, a smoothing capacitor and a zener diode. The voltage divider is used to step down high voltage to 2.5 V. The output voltage of the potential divider can be controlled by adjusting the resistor value of the R_1 and R_2 . The 1 k Ω resistance is used to limit the current flow and the 100 nF capacitor is used to reduce the noise in signals. The zener diode is used to protect the adc input of the microcontroller from voltage spikes. The output voltage of the potential divider can be calculated from (A.1).

$$V_{out} = V_{in} \left(\frac{R_2}{R_1 + R_2} \right) \quad (\text{A.1})$$

where V_{out} is the output voltage and V_{in} is the input voltage of the voltage divider.

A.2.4 5 V DC Power Adapter

A 5 V dc usb power adapter [5] is used to power the system board. The input voltage range of the adapter is 100 V to 240 V ac at the operating frequency of 50 Hz to 60 Hz and transform into the output voltage of 5 V dc. The transformer rated load current is 2 A and the maximum output power is 10 W.

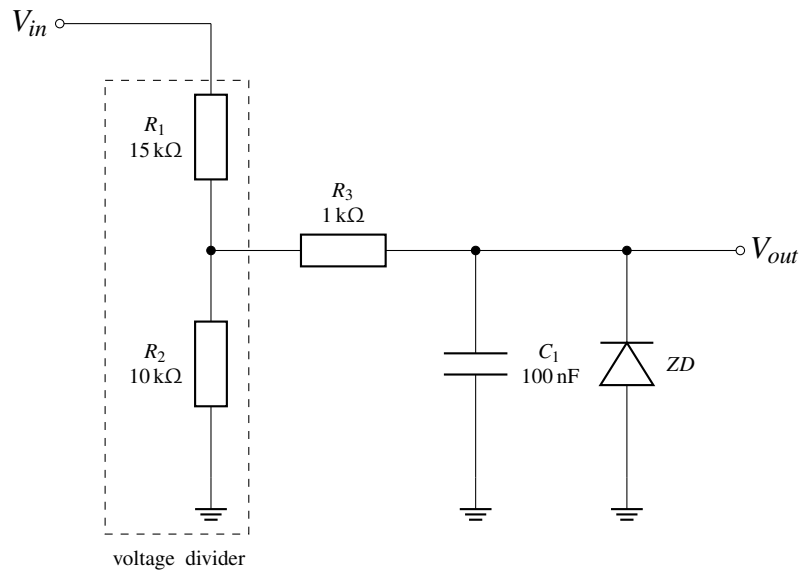


Figure A.3: Filtered voltage divider for dc current sensing in the PCB schematic.

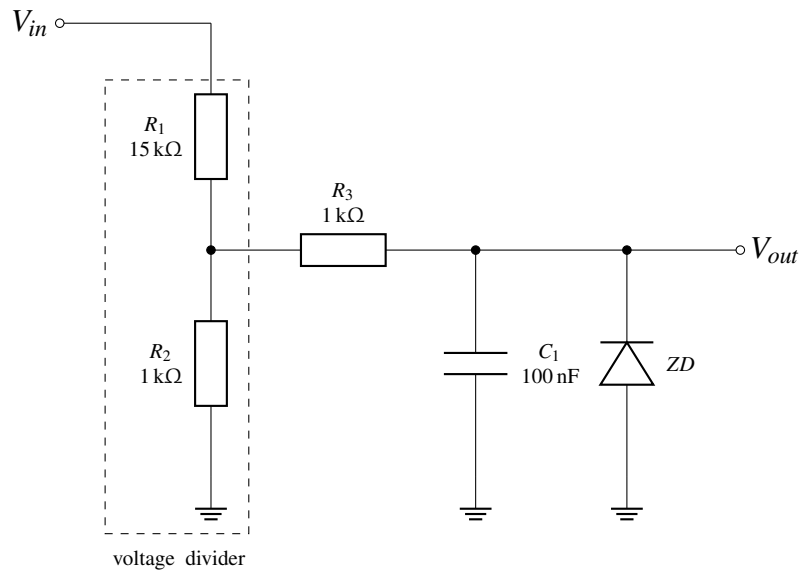


Figure A.4: Filtered voltage divider for dc voltage sensing in the PCB schematic.

A.3 Central Processing Unit

A.3.1 PCB Design

The Autodesk Eagle [6] is used to design the schematic diagram and layout of the main circuit board. The schematic diagram of the central processing unit is based on [7] and consists of operating circuits of a microcontroller, a USB to UART interface integrated circuit devices, a serial Real-Time Clock (RTC), a Raspberry Pi on-board WiFi, a 32 kB serial CMOS Electrically Erasable Programmable Read-Only Memory (EEPROM), a 3.3 V voltage regulator, a mini usb connector, and two filtered voltage divider circuits.

A.3.2 Microcontroller

The Atmel ATmega328P [8] is a high performance, low power CMOS 8-bit microcontroller based on the AVR enhanced Reduced Instruction Set Computer (RISC) architecture. It provides six input channels of 10-bit adc and 1 K byte of data EEPROM memory. The operating voltage of the microchip lies between 2.7 V to 5.5 V. Figure A.5 illustrates the configuration of the pins of the microcontroller which are configured as inputs or outputs.

- The operating voltage of the microcontroller and the analogue reference voltage for the adc input channel is 3.3 V.
- A resistor of 10 k Ω is used as a pull-up resistor on the RESET pin and decoupling capacitors of 100 nF are connected across the V_{CC} pins and ground to improve the noise immunity.
- A 16 MHz crystal [9] is attached across the XTAL1 and the XTAL2 pins for generating a clock signal to the microcontroller.
- The pin 17 (SCK), 16 (MISO), 15 (MOSI), and 29 (RESET) are the SPI pins which are used to communicate the host device with an external device, such as a 24-bit adc board.
- The pin 11 (D7) is a digital input/output pin and used to drive an LED.
- The pin 30 (RXD) is a receive data input pin for the Universal Synchronous/Asynchronous Receiver/Transmitter (USART) while the pin 31 (TXD) is the transmit data output pin for USART.
- The pin 27 (SDA) and pin 28 (SCL) are the serial data and clock pins for an I2C interface.
- The pin 23 (ADCO), 24 (ADC1), 25 (ADC2), 26 (ADC3), 19 (ADC6), and 22 (ADC7) are the 10-bit analogue to digital converter input channels with the sampling rate of 15 kSPS (sample per second).

The output code of the adc of the ATmega328P is:

$$ADC = \frac{V_{IN} \times 1024}{V_{REF}} \quad (A.2)$$

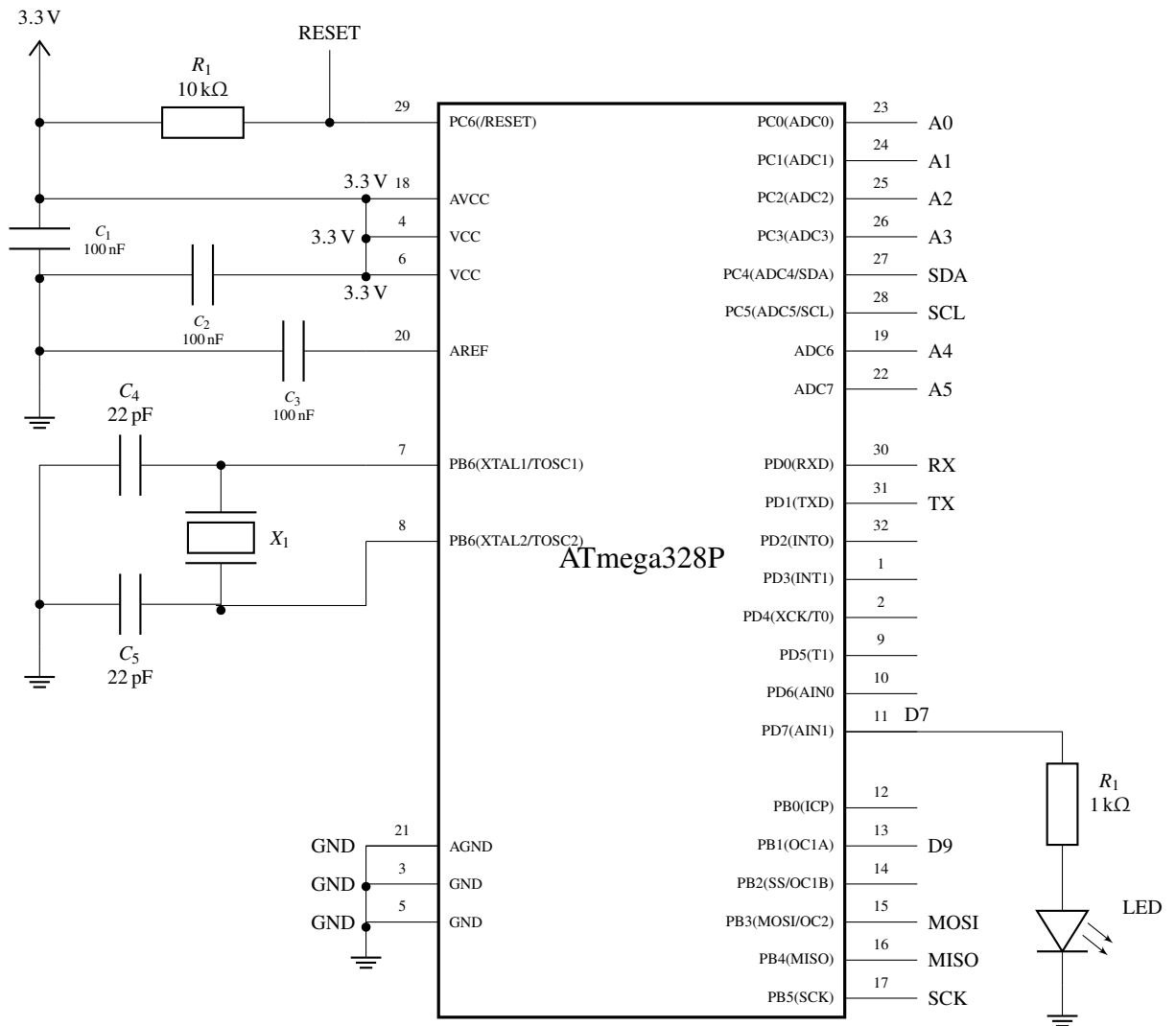


Figure A.5: Schematic overview of the Atmel Atmega328P microcontroller [7, 10, 11].

where V_{IN} is the input voltage and V_{REF} is the reference voltage of 3.3 V. The analogue signals of the dc current sensor and 24 V dc sample from the power supply are connected to the ADC0 and ADC3 pins of the microcontroller, as well as to the analogue input channel 1 and 3 of the 24-bit adc circuit board. In software, either analogue input pins of the microcontroller or analogue input pins of the external 24-bit adc board can be selected for determining the current and voltage values.

A.3.3 USB UART Integrated Circuit

The FT232R [12] is a USB to asynchronous serial data transfer interface which is used to develop a serial communication between the system board and a computer. The functional circuit of the USB UART IC is shown in Figure A.6.

- The device core is powered of 5 V and decoupling capacitors of 100 nF are used to

reduce the noise at the voltage supply pins of the microchip.

- Any of the CBUS [0–4] pins can be configured to drive an LED. In this design, the CBUS0 and CBUS1 have been configured to drive transmit LED (TXLED) and receive LED (RXLED). The CBUS0 indicates when data is being transmitted and the CBUS1 indicates when data is being received by the system board.
- The TXD and RXD pins are used for transmission and reception of data via the 2-wire serial interface. The pins are connected into RX and TX of the microcontroller respectively.
- The USBDP and USBDM pins of FT232R have been connected to USB connector D negative and D positive respectively.

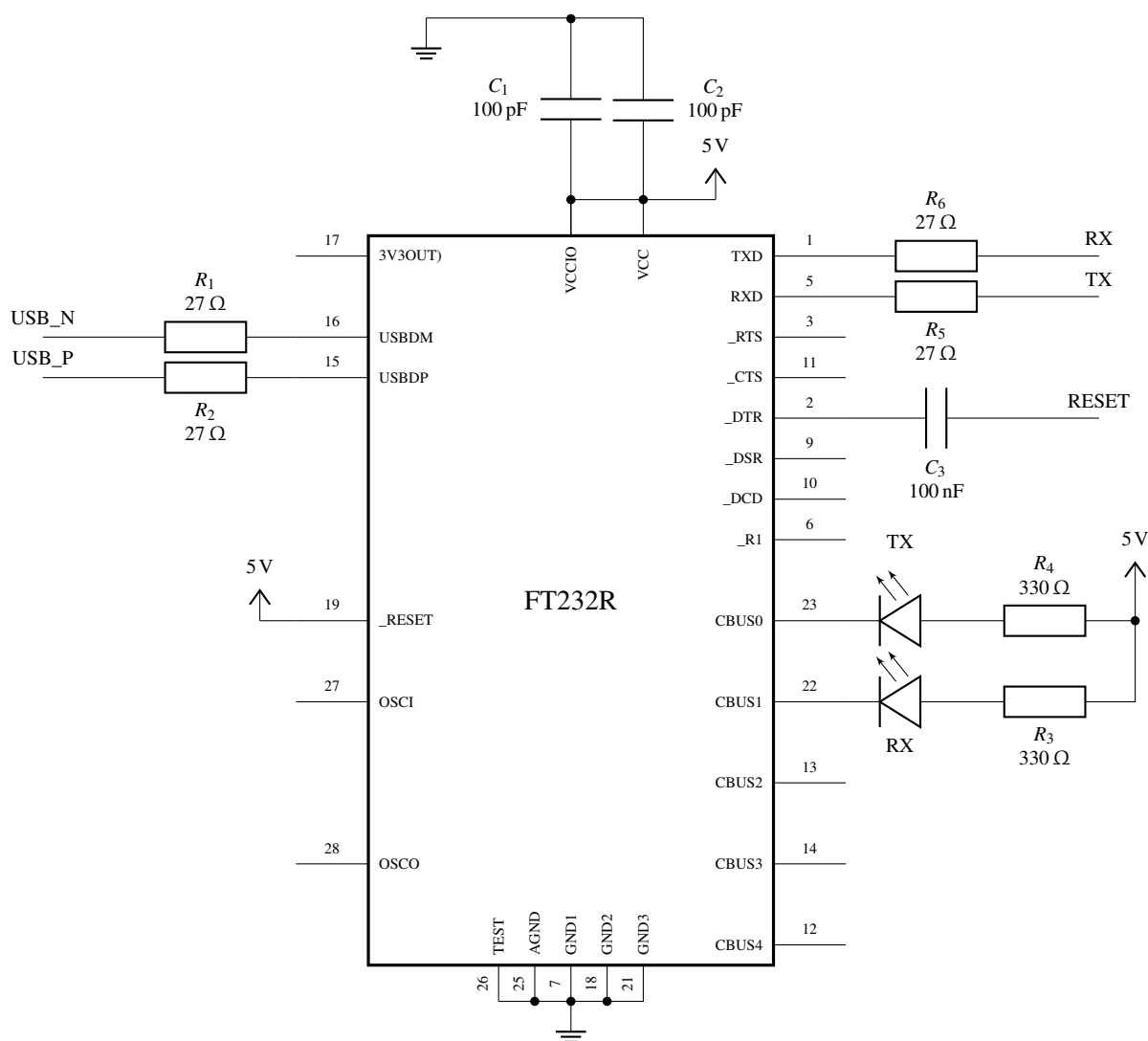


Figure A.6: Schematic diagram of the FT232R USB UART Integrated Circuit [7, 12].

A.3.4 Real-Time Clock

The DS1307 serial real-time clock is a low-power, full binary-coded decimal (bcd) clock plus 56 bytes of nonvolatile static random access memory (NV SRAM). Address and data are transferred serially through an I2C bus [14]. The clock provides seconds, minutes, hours, day, date, month, and year information. The rtc uses a 3 V battery as a power source in the absence of external power. The operating circuit of the DS1307 serial real-time clock is shown in Figure A.7.

- The V_{CC} is the primary power supply pin of the microchip and connected to 3.3 V.
- The V_{BAT} is the back supply input pin and connected to a 3 V battery.
- A decoupling capacitor of 100 nF is attached across the VCC pin and ground to improve the noise immunity.
- A 16 MHz crystal [9] is employed across the pin X1 and X2 to generate a clock signal.
- The SQW is the square wave pin and requires a pullup resistor of 10 k Ω .
- The SDA is the serial data input/output while SCL is serial clock input for the I2C interface.

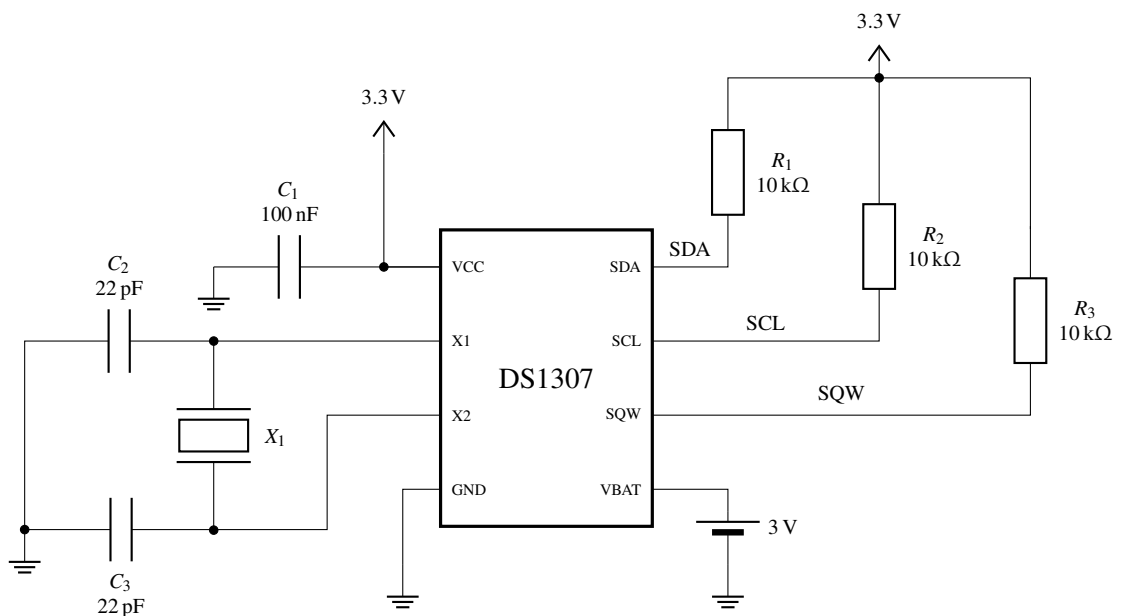


Figure A.7: Operating circuit configuration of the DS1307 serial real time clock.

A.3.5 EEPROM

The schematic overview of the 32-Kb I2C Complementary Metal Oxide Semiconductor (CMOS) serial Electrically Erasable Programmable Read-Only Memory (EEPROM) device [15] is shown in Figure A.8. The ATmega328P microcontroller had a built-in of 1 K bytes EEPROM as mentioned earlier. However, it is a good practice to add an external EEPROM memory into the system board for extra data storage if required.

- The supply voltage range of the microchip is 3.7 V to 5.5 V.
- The A0, A1 and A2 are the device address input pins.
- The VSS is connected to the ground while VCC is the power supply pin and connected to the 5 V.
- The SCL and SDA are connected to the power supply pin via a pull-up resistor of 3.9 k Ω .
- The WP is the write protect input pin of the microchip.

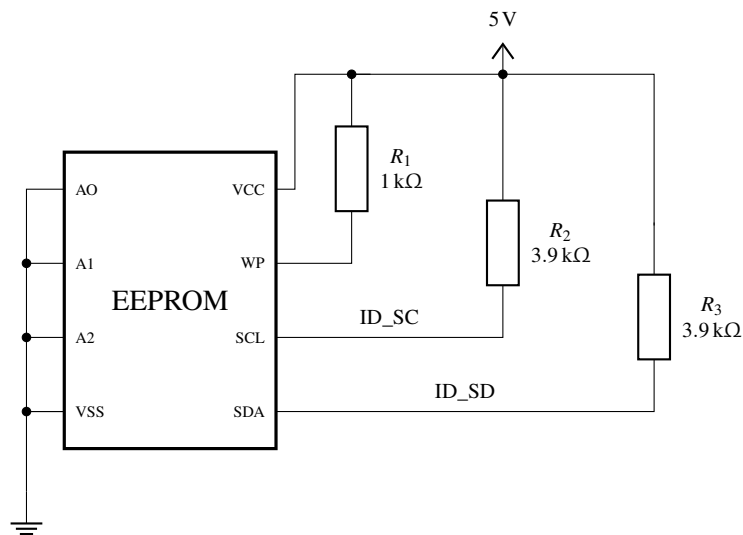


Figure A.8: EEPROM microchip circuit arrangement in the PCB schematic diagram.

A.3.6 3.3 V Voltage Regulator

As described earlier that the operating voltage of the microcontroller is 3.3 V. Therefore, a 3.3 V voltage regulator is used to regulate the 5 V into a fixed voltage of 3.3 V. Figure A.9 shows the operating circuit of the 3.3 V voltage regulator [16].

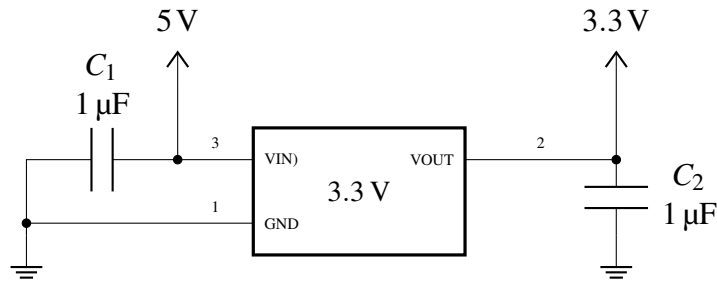


Figure A.9: Schematic diagram of the 3.3 V voltage regulator circuit.

A.3.7 USB Connector

The schematic diagram of the type B mini USB connector [17] is shown in Figure A.10. The connector is used for powering the system board, as well as for programming the microcontroller.

- The VBUS is the output pin of 5 V of the usb connector.
- A fuse with the maximum current rating of 1.5 A is used to protect the circuit from over-current.
- The pin $D+$ is labelled as USB_P respectively which is connected to the pin USBDP of the FT232R USB URT IC.
- The pin $D-$ is labelled as USB_N which is connected to the pin USBDM FT232R USB URT IC.

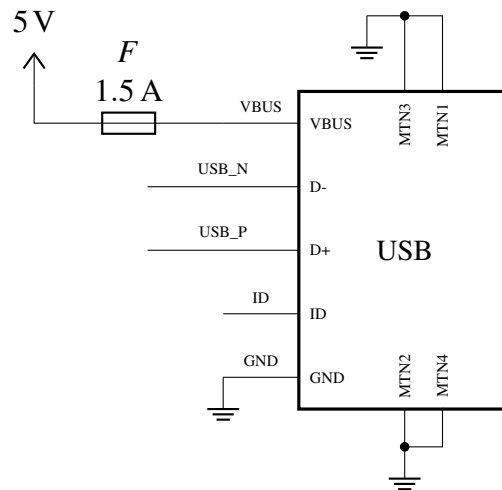


Figure A.10: Schematic diagram of the mini USB connector.

A.3.8 Serial Peripheral Interface

There are six pin connectors in the PCB design for Serial Peripheral Interface (SPI). The pins are 3.3 V, MISO (multiple input slave output), SCK (serial clock), MOSI (multiple output slave input), RESET and GND are connected to the respective pins in the microcontroller.

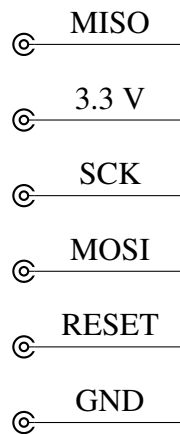


Figure A.11: Pin header for the Serial Peripheral Interface.

A.3.9 Raspberry Pi

The Raspberry Pi 3 Model B [18] is a single board computer with the WiFi and Bluetooth connectivity on board. Figure A.12 illustrates the configuration of the pins for the Pi in the schematic diagram of the central monitoring unit. The proposed system uses a Raspberry Pi for logging, processing and visualising electrical data. The electrical data can be logged locally to the Raspberry Pi microSD card, as well as to a remote Emoncms server [26].

- The operating voltage of the Pi is 5 V.
- The Pi is configured with the ID EEPROM via *ID_SD* and *ID_SC* pins.
- The pin 10 (RXD) and 8 (TXD) are connected to the pin 30 (RXD) and 31 (TXD) of the ATmega328P microcontroller respectively. These pins are used for communication between the microcontroller and the Raspberry Pi.
- The Pi SDA and SCL pins form the I2C interface.
- The pin 11 (GPI017) is connected to the SQW pin of the real time clock microchip.

The Raspberry Pi Model B is embedded with a chip antenna operating in the 2.45 GHz WiFi ISM band. The Pi has a maximum range of 100 m.

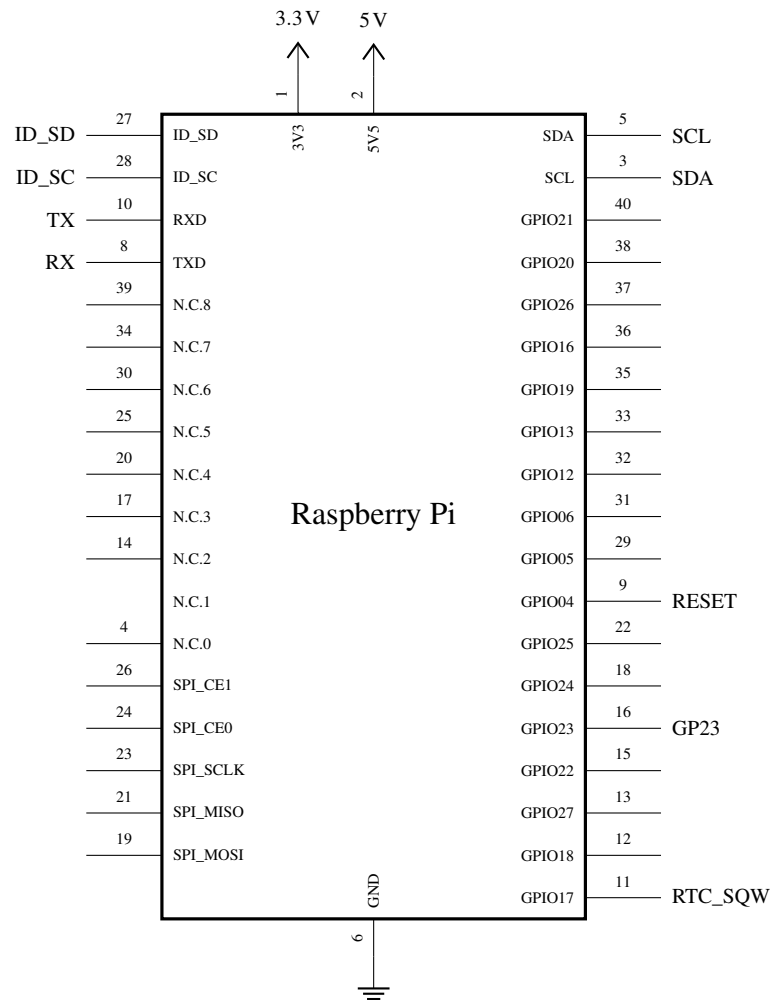


Figure A.12: The pins configuration for the Raspberry Pi module in the PCB schematic diagram.

A.3.10 24-Bit ADC Board

The Pmod AD5 [19] is a 24-bit analogue-to-digital converter embedded with an Analog Devices microchip of AD7193 [20]. The AD7193 is a high precise 24-bit Sigma-Delta analogue-to-digital converter on up to 8 different analogue input channel that can perform the high accurate voltage measurements with an rms noise as low as 11 nV through SPI protocol. The prototype of the Pmod AD5 is shown in Figure A.13. The length and width of the board is 48.26 mm and 20.32 mm respectively.

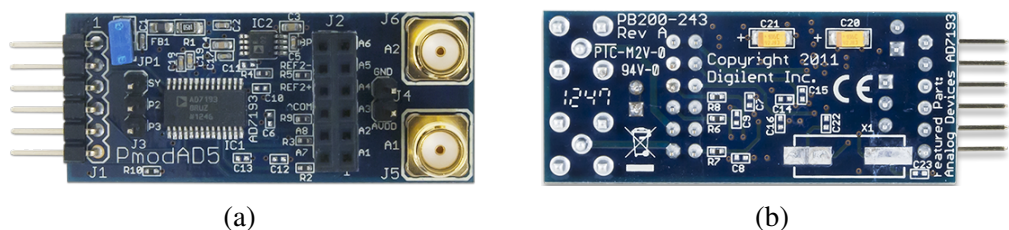


Figure A.13: Pmod AD5: 4-channel, 4.8 kHz, 24-bit analog-to-digital converter. (a) Top view, and (b) bottom view.

The output code for the analog input is:

$$Code = 2^{N-1} \times \left[\left(AIN \times \frac{GAIN}{V_{REF}} \right) \right] + 1 \quad (A.3)$$

where AIN is the analog input voltage, Gain is the PGA setting (1 to 128) and N is equal to 24. The Pmod header J1 contains six output pins [21], Table A.1, which are used to communicate with the system board via SPI protocol. Furthermore, the Pmod header J2 contains twelve input pins as described in Table A.2, which consists of eight analogue input channels of 24-bit resolution. The default reference voltage for adc is 2.5 V. However, external reference voltage for the adc can be applied across the reference input pins REFIN2+ and REFIN2- [21]. There are six pins connectors in the PCB design where the Pmod AD5 will be linked to the central monitoring unit.

Table A.1: Description of the Pmod AD5 header J1 pins

Header J1	Signal
Pin 1	CS
Pin 2	MOSI
Pin 3	MISO
Pin 4	SCLK
Pin 5	GND
Pin 6	VCC

Table A.2: Description of the header J2 pins of the Pmod AD5.

Header J2	Signal	Description
Pin 1–8	AI 1–8	Analogue input 1–8
Pin 9	AINCOM	Common analog input
Pin 10	REFIN2+	Reference input 2 +
Pin 11	REFIN2-	Reference input 2 -
Pin 12	BPDSW	Bridge power down switch

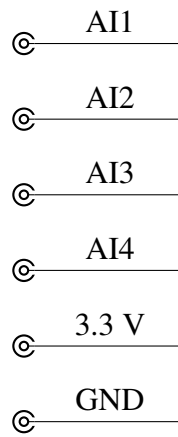


Figure A.14: Pins header for the Pmod AD5 in the PCB layout.

A.4 PCB Layout

The Autodesk Eagle software is used to design the PCB schematic and layout of the power monitor unit. The layout of the PCB design of the monitoring unit is shown in Figure A.15. The total length of the PCB design is 99 mm with a total width of 76 mm. The board has common ground and was fabricated by [22]. The board consists of two layers: (i) a top copper layer; and (ii) a bottom copper layer. The red copper traces lie on the top layer while the blue copper traces lie on the bottom layer. The width of the signal traces is 16 mil and the width of the power traces is 20 mil. The drill size of the vias is 23.6 mil. The passive components of 0603 size are mounted on the board. The IC1, IC2 and U1 represents the real time clock, the USB URT IC and ID EEPROM respectively. Additionally, the X4 represent the header pins for the Raspberry Pi. Furthermore, the SPI1 represent the pin header for the serial peripheral interface. The JP1, JP2, JP3, JP5, JP6 JP7, JP9 and JP8 are the pin headers where the PMOD AD5 board will be connected into the base board. A 2.1 mm dc barrel power jack (J4) is used to feed the dc voltage sample and 3.5 mm 4 pole jack socket is used to connect the output leads of the dc current sensor to the central processing unit. A mini usb connector (U\$7) is used to plug the 5 V dc to the system board, as well as used for programming the microcontroller. Figure A.16 shows the final prototype of the PCB board for the smart power monitoring system. As mentioned earlier that the Pmod AD5 comes with six 90 degree pins (header J1) which are used to communicate with the system board via SPI protocol. The 90 degree pin headers in Pmod AD5 were desoldered and replaced with the straight pin header so the it can be easily connected to the host system board.

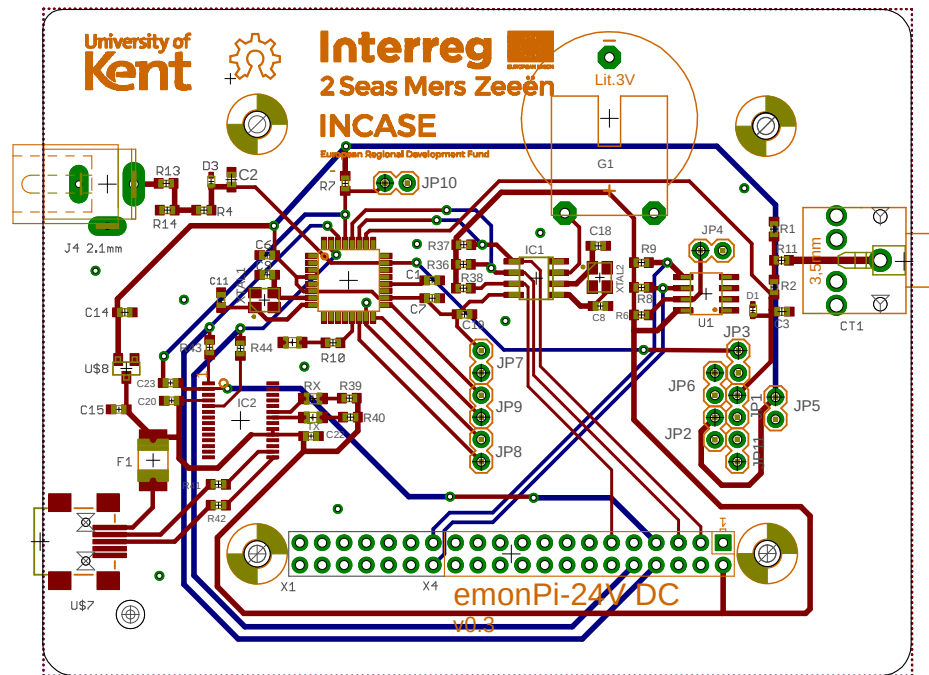


Figure A.15: PCB layout of the 24 V dc power monitoring system.

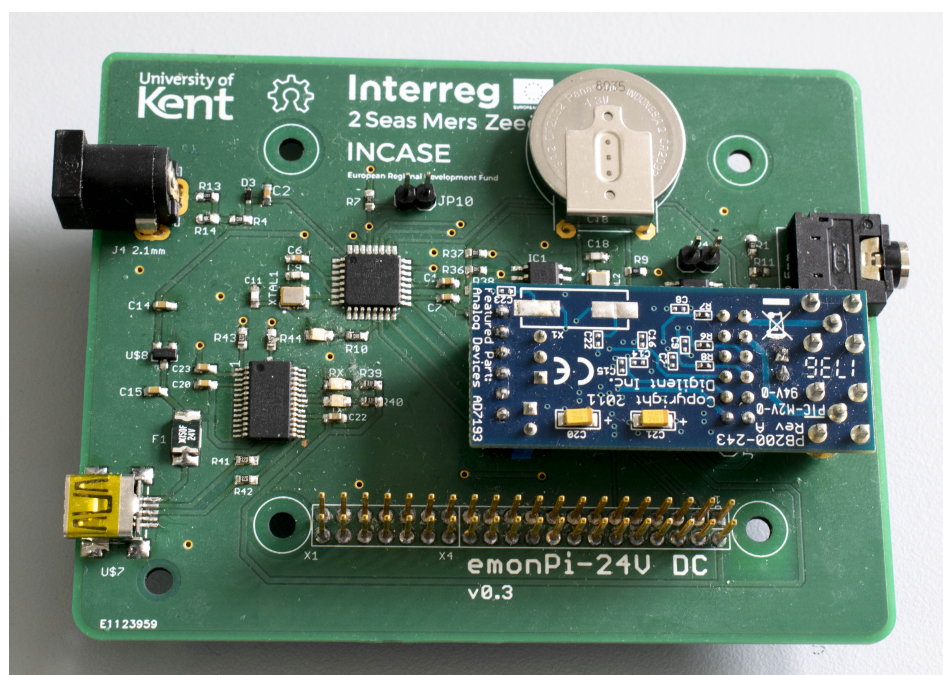


Figure A.16: A prototype of the 24 V dc power monitoring system.

A.5 Software

The Arduino integrated development environment [23] is used to write and upload code to the system board. The code is written in the C and C++ programming language. There are two source codes provided which can be used to evaluate the current, voltage and power

values: (i) a source code 1; and (ii) a source code 2. The source code 1 [24] is used to extract data from the 24-bit adc board. The 24-bit adc board is connected with the host board via SPI protocol. However, as discussed earlier that the microcontroller has 5 adc input channels which can be used to convert analogue signals to digital signals. The source code 2 can be used to extract data for adc input channel of the microcontroller.

A.5.1 Source Code 1

```
// https://www.arduino.cc/en/Reference/SPI
#include <SPI.h>

// Use the built-in AD7193 library
#include <AD7193.h>

//Code for the voltage measurement in the AD7193 library:
//if (mPolarity == 1){
//voltage = (((double)rawData / 16777216 / (1 << PGAGain)) *
    mVref)) * VOLTAGEDIVIDERRATIO_DCVOLTAGE;}
//else if (mPolarity == 0){
//voltage = (((float)rawData/ (float)8388608) - (float)1) *
    (mVref / (float)PGAGain)) * VOLTAGEDIVIDERRATIO_DCVOLTAGE;}

//Code for the current measurement in the AD7193 library:
//if (mPolarity == 1){
//current = (((double)rawData / 16777216 / (1 << PGAGain)) *
    mVref)) * VOLTAGEDIVIDERRATIO_DCCURRENT;}
//else if (mPolarity == 0){
//current = (((float)rawData / (float)8388608) - (float)1) *
    (mVref / (float)PGAGain)) * VOLTAGEDIVIDERRATIO_DCCURRENT ;}

AD7193 AD7193;

void setup() {
    Serial.begin(9600);
```

```
    delay(1000);
    while (!Serial) {
        ;
    }
    AD7193.begin();
    // Device setup
    AD7193.AppendStatusValuetoData();
    // Set the gain of the PGA
    AD7193.SetPGAGain(1);
    // Set the Averaging
    AD7193.SetAveraging(100);
    // Calibrate the PGA settings
    AD7193.Calibrate();
    // Check for the register map values
    AD7193.ReadRegisterMap();

    Serial.println("\nBegin AD7193 conversion - single conversion");
}

void loop() {

    float ch1Voltage;
    unsigned long ch1Data;

    float ch2Current;
    unsigned long ch2Data;

    // Read adc channel 1 and channel 2 measurement data
    ch1Data = (AD7193.ReadADCCchannel(0) >> 8);
    ch2Data = (AD7193.ReadADCCchannel(1) >> 8);
    // Convert into the voltage and current value
    ch1Voltage = AD7193.DataToVoltage(ch1Data);
    ch2Current = AD7193.DataToCurrent(ch2Data);
```

```

// Print the voltage value
Serial.print(" \n\n\t\tCH1 data: ");
Serial.print(ch1Data, HEX);
Serial.print("\n\t\tChannel 1 Voltage Measurement (V): ");
Serial.println(ch1Voltage, 3);
// Print the current value
Serial.print(" \n\t\tCH2 data: ");
Serial.print(ch2Data, HEX);
Serial.print("\n\t\tChannel 2 Current Measurement (A): ");
Serial.println(ch2Current, 3);
// Print the power value
Serial.print("Power (W): ");
Serial.print(ch2Current * ch1Voltage);
Serial.println(" W\n\n");
delay(1000);
}

```

A.5.2 Source Code 2

```

// Take 200 analogue samples and add them up
#define CURRENT_SAMPLES 200
#define VOLTAGE_SAMPLES 200

// Voltage divider factor is determined by Vin / Vout
#define VOLTAGEDIVIDERRATIO_DCVOLTAGE 16
#define VOLTAGEDIVIDERRATIO_DCCURRENT 62.5
#define VOLTAGE_CALIBRATION 0.144
#define CURRENT_CALIBRATION 0.131

float current = 0.0;
double currentSum = 0;
unsigned char currentSampleCount = 0;

```

```
float voltage = 0.0;
double voltageSum = 0;
unsigned char voltageSampleCount = 0;

// the setup code goes here and run once
void setup() {
    Serial.begin(9600);
}

// the main code goes here and run repeatedly
void loop() {
    while (currentSampleCount < CURRENT_SAMPLES) {
        currentSum+ = analogRead(PC3); // Read raw current value
        currentSampleCount++;
    }

    while (voltageSampleCount < VOLTAGE_SAMPLES) {
        voltageSum+ = analogRead(PC0); // Read raw voltage value
        voltageSampleCount++;
    }

    // Print the current value
    float Current = (((float)currentSum / (float)CURRENT_SAMPLES *
        3.3028) / 1023.0) * VOLTAGEDIVIDERRATIO_DCCURRENT;
    Serial.print("Current: ");
    Serial.print(Current + CURRENT_CALIBRATION );
    Serial.println (" A");
    currentSampleCount = 0;
    currentSum = 0;

    // Print the voltage value
```

```
float voltage = (((float)voltageSum / (float)VOLTAGE_SAMPLES *
    3.3028) / 1023.0) * VOLTAGEDIVIDERRATIO_DCVOLTAGE;
Serial.print("Voltage: ");
Serial.print(voltage + VOLTAGE_CALIBRATION);
Serial.println (" V");
voltageSampleCount = 0;
voltageSum = 0;

// Print the power value
Serial.print("Power: ");
Serial.print((voltage + VOLTAGE_CALIBRATION) * (current +
    CURRENT_CALIBRATION ));
Serial.println (" W\n\n");
delay(1000);
}
```

A.6 Measurement Results

A.6.1 Measurement Setup

The measurement setup is shown in Figure A.17. A wire wound power resistor is used as an electrical load. A 15.5 V dc power supply [25] with a maximum current output of 40 A is used to power the electrical load. The output voltage of the power supply can be adjusted between 2.8 V and 15.5 V. The power supply comes with a digital LED displays for voltage and current readings. A dc current sensor is employed between the 15.5 V dc power supply and the electrical load. Several measurements were performed to observe the current, voltage and power readings on both devices, the dc power supply and the dc energy logger.

A.6.2 Current, Voltage and Power Measurement

Figure A.18, Figure A.19 and Figure A.20 shows the measured current, voltage and power readings of the 24 V dc power monitoring system, respectively. The current, voltage and

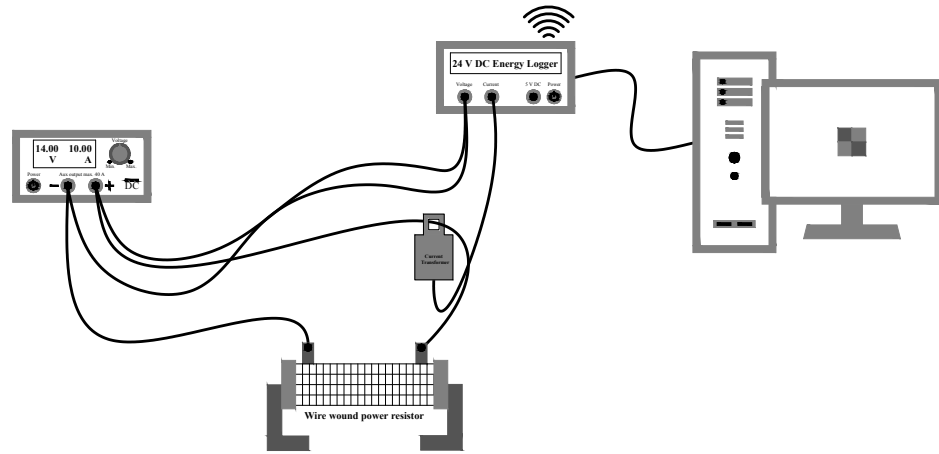


Figure A.17: Testing set up for the 24 V dc monitoring system.

power readings were compared with readings displayed on the power supply. The percentage error of the system is calculated using (A.4). The percentage error is 0.12% for true voltage value of 15.5 V, 1.18% for true current value of 10.1 A, and 1.32% for true power value of 156.55 W. Furthermore, Emoncms, Figure A.21, is a web interface for logging and visualising energy data. The Emoncms can be installed on the Raspberry Pi as described in [26].

$$\text{Percentage error} = \left| \frac{v_A - v_E}{v_E} \right| \times 100\% \quad (\text{A.4})$$

where v_A is the approximate (measured) value and v_E is the exact value.

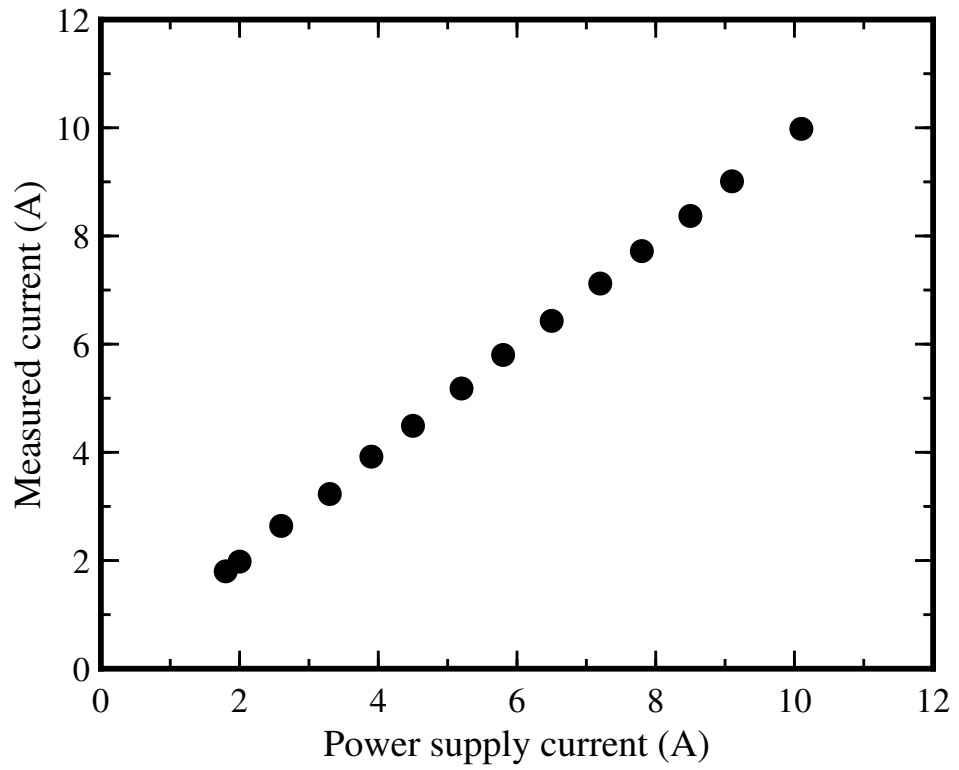


Figure A.18: Current measurements of the proposed system.

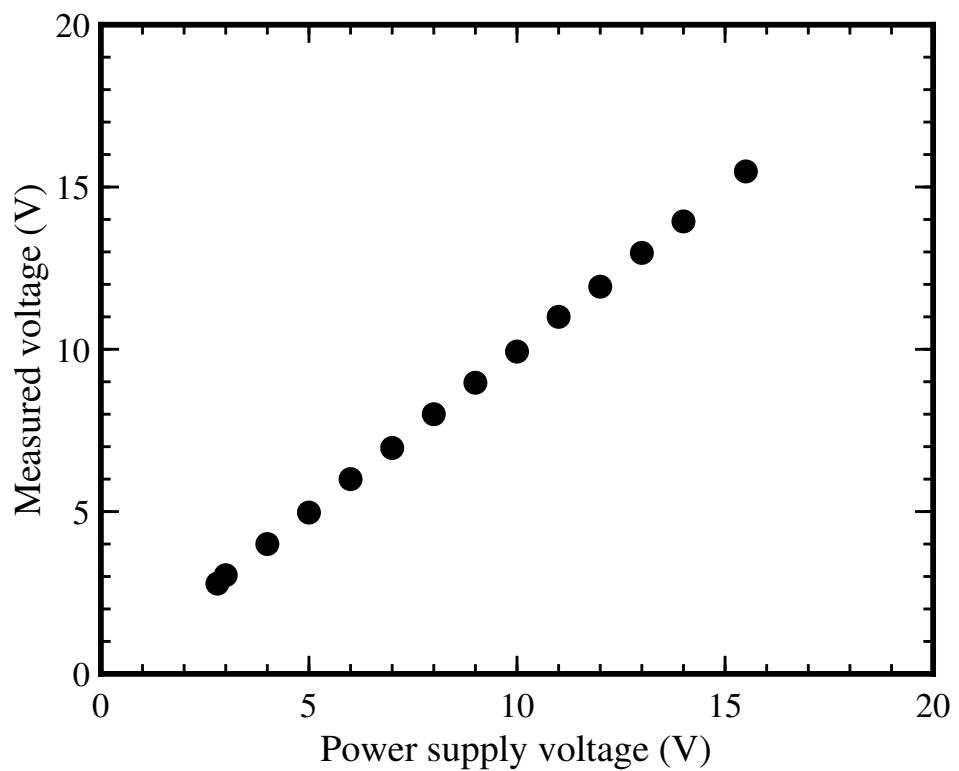


Figure A.19: Voltage measurements of the proposed system

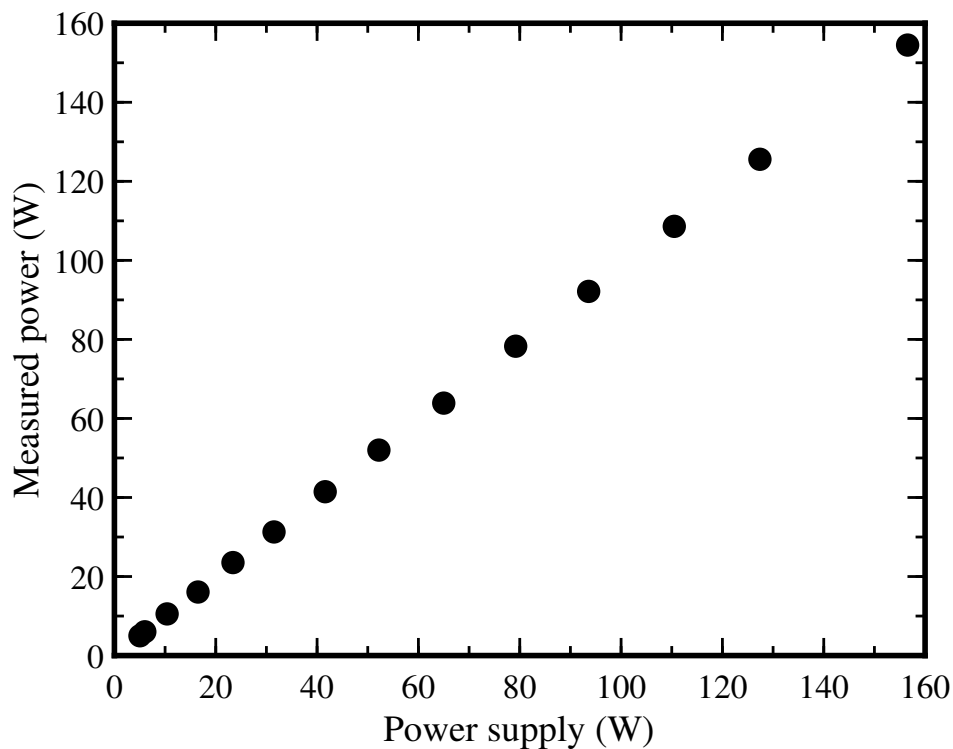


Figure A.20: Power measurements of the proposed system.

A.7 Comparison

Table A.3 shows the comparison of the 24 V dc wireless energy logger with the RFID tag system. The estimated cost of the energy logger is about \$120.00 while the estimated cost of the tag system is about \$50.00. In terms of size, the RFID tag system is much smaller than the 24 V dc wireless energy logger. Moreover, the tag system was designed for small current measurements in range of 0 A to 13 A although the dc power monitoring system can measure from 0 A to 100 A.



Figure A.21: Emoncms.org web interface for visualising energy data [26].

Table A.3: Comparison between the proposed 24 V dc wireless energy logger and the RFID tag system in terms of communication, cost, current range and power type.

Sensors	Communication	Cost (\$)	Current Range (A)	Power Type
RFID tag system	RFID	50.00	0–13	Passive
24 V dc energy logger	WiFi	120.00	0–100	Active

A.8 Conclusion

This chapter demonstrated a 24 V dc smart power system for monitoring three electrical parameters: (i) current; (ii) voltage; and (ii) power consumption of individual electrical appliances in smart homes and industries. A Hall effect current transducer is used for detecting dc current from 0 A to 100 A in a power cable. However, the dc voltage measurements from 0 V to 24 V is performed by directly feeding a dc voltage sample from the power supply to the central monitoring unit. The Atmel ATmega328P microcontroller with five adc input channels of 10-bit resolution on board is used in the system board which can be easily programmed with Arduino integrated development environment. Additionally, the system board incorporate with an optional 24-bit adc for very low current and voltage measurements with high accuracy. Furthermore, the system board is linked with the Raspberry Pi for logging and visualising electrical data on the Emoncms web server. The Pi model B board is embedded with a chip antenna operating in the 2.45 GHz WiFi ISM band. The Pi has a maximum range of 100 m. The data can be transmitted via WiFi network, as well as with an ethernet connection. The proposed system is suitable for tracking energy usage of electrical devices in home solar power systems and industries operating at 24 V dc power system. The overall size of the device is small and can be easily installed in homes and industries. The input current sensor node in the system board can be easily increased when multiple individual electrical appliances monitoring is required.

The main contribution of this chapter has been,

- The development of a 24 V dc smart power monitoring system.

References

- [1] Bayite. (2020, Jun. 2). Bayite dc 6.5–100 V 0–100 A lcd display digital current voltage power energy meter multimeter ammeter voltmeter with 100 A current shunt [Online]. Available: http://www.bayite.com/index.php?route=product/product&path=64_63&product_id=83
- [2] Interreg 2 Seas Mers Zeeën INCASE European Regional Development Fund. (2020, June 18). INCASE towards Industry 4.0 via Networked Control Applications and Sustainable Engineering [Online]. Available: <https://www.incase2seas.eu/>
- [3] Magnelab. (2020, June 7). HCT-0016 Hall effect split-core current transducer [Online]. Available: <https://www.magnelab.com/products/hall-effect-split-core-current-transducer-hct-0016/>
- [4] Xin Ai, Hai Bao and Y. H. Song, “Novel method of error current compensation for Hall-effect-based high-accuracy current transformer,” in *IEEE Transactions on Power Delivery*, vol. 20, no. 1, pp. 11–14, Jan. 2005, doi: 10.1109/TPWRD.2004.837820.
- [5] Ideal power. (2020, Apr. 20). 5 V dc usb power adapter [Online]. Available: <https://www.idealpower.co.uk/>
- [6] Autodesk. (2020, June 7). Autodesk Eagle PCB design made easy [Online]. Available: <https://www.autodesk.co.uk/products/eagle/overview>
- [7] Open energy monitoring. (2020, June 23). Resources: a definitive list of resources for OpenEnergyMonitor hardware, firmware and software [Online]. Available: <https://guide.openenergymonitor.org/technical/resources/>

- [8] Microchip. (2020, June 14). Microchip ATmega328P [Online]. Available: <https://www.microchip.com/wwwproducts/en/ATmega328p>
- [9] TXC corporation. (2020, June 14). 7M-16.000MAAJ-T - Crystal, 16 MHz, smd, 3.2 mm x 2.5 mm, 30 ppm, 18 pF, 30 ppm, 7M series [Online]. Available: <https://www.txccrystal.com/crystal.html>
- [10] Microchip, "Atmel ATmega328P 8-bit AVR microcontroller with 32 K bytes in-system programmable flash," ATmega328P datasheet, Jan. 2015.
- [11] Arduino. (2020, June 23). Arduino uno rev3 smd [Online]. Available: <https://store.arduino.cc/arduino-uno-rev3-smd>
- [12] FTDI chip, "Future technology devices international Ltd. FT232R USB UART IC," FTDI chip FT232R USB UART IC datasheet, Dec. 2009 [Revised May 2020].
- [13] Microchip, "CMOS low dropout (LDO) voltage regulators " MCP1700 low quiescent current LDO, Aug. 2013.
- [14] Maxim integrated, "64 x 8, Serial, I2C Real-Time Clock," DS1307 datasheet, Mar. 2015.
- [15] ON semiconductor, "32-Kb I2C CMOS serial EEPROM," CAT24C32 datasheet, Mar. 2015.
- [16] Microchip, "Low quiescent current low dropout (LDO)," MCP1700 datasheet, Nov. 2005 [Revised Oct. 2013].
- [17] Molex. (2020, June 23). Molex, 67503 right angle, SMT Mount, Version 2.0 type B mini USB connector [Online]. Available: <https://www.molex.com/molex/products/family/usb>
- [18] Raspberry Pi. (2020, June 7). Raspberry Pi Model B [Online]. Available: <https://www.raspberrypi.org/products/raspberry-pi-3-model-b/>
- [19] Digilent a national instruments company (2020, June 10). Pmod AD5: 4-channel 4.8 kHz 24-bit A/D converter [Online]. Available: <https://www.analog.com/media/en/technical-documentation/data-sheets/AD7193.pdf>

-
- [20] Analog Devices (2020, June 20). AD7193: 4-channel, 4.8 kHz, ultralow noise, 24-bit sigma-delta adc with PGA, datasheet, 2017.
- [21] Digilent a national instruments company (2020, June 10). Pmod AD5 reference manual [Online]. Available: <https://reference.digilentinc.com/reference/pmod/pmodad5/reference-manual>
- [22] Euro circuits (2020, June 7). [Online]. Available: <https://www.eurocircuits.com/>
- [23] Arduino. (2020, June 15). Arduino software [Online]. Available: <https://www.arduino.cc/en/main/software>
- [24] Arduino library list. (2020, June 23). AD7193 [Online]. Available: <https://www.arduinolibraries.info/libraries/ad7193>
- [25] Rapid online (2020, June 23). Rapid PS1540S SMPS (Switch Mode Power Supply) 15 V 40 A with digital display [Online]. Available: <https://www.rapidonline.com/rapid-ps1540s-smps-switch-mode-power-supply-15v-40a-with-digital-display-85-1828>
- [26] Emoncms.org. (2020, June 20). Docs, github and install [Online]. Available: <https://emoncms.org/>

Appendix B

Experimental Devices

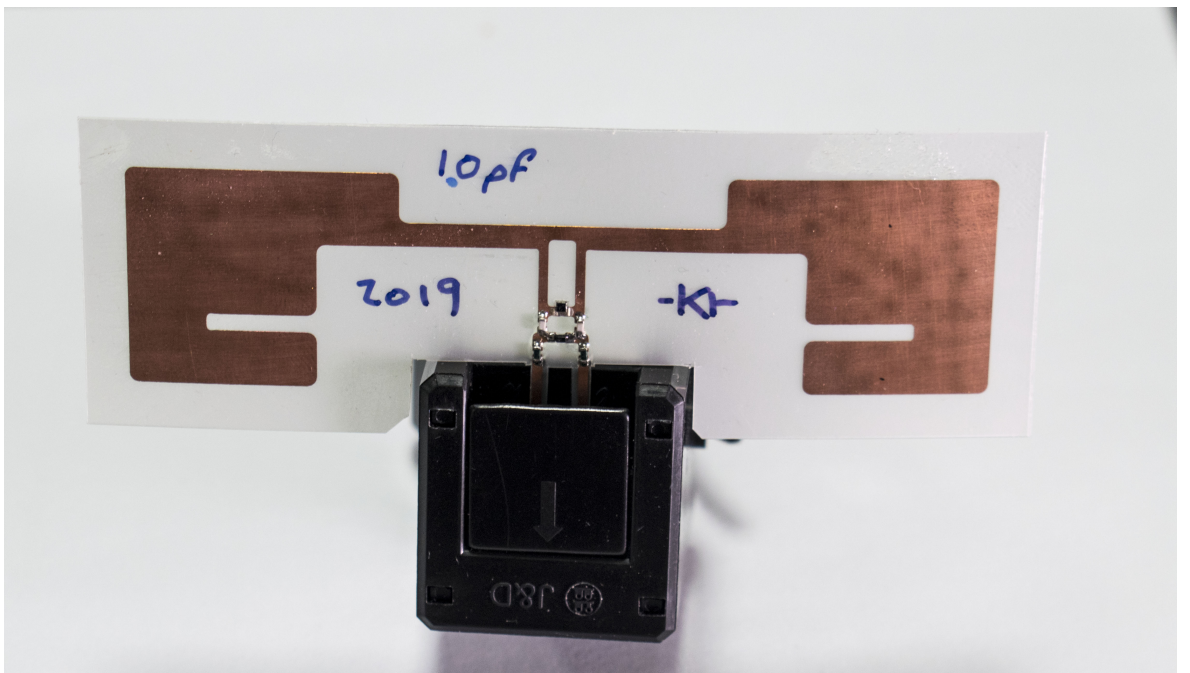


Figure B.1: A prototype of the RFID ac current sensor (bottom view).

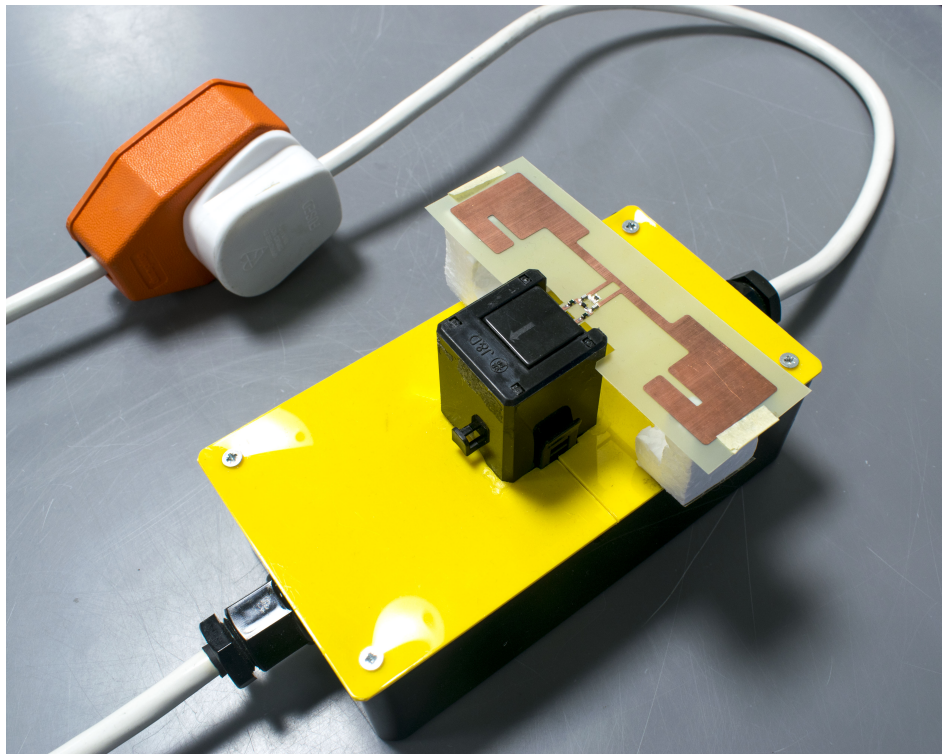


Figure B.2: The RFID ac current sensor enclosed in an insulated box.



Figure B.3: An electrical fan heater used for ac current measurements.

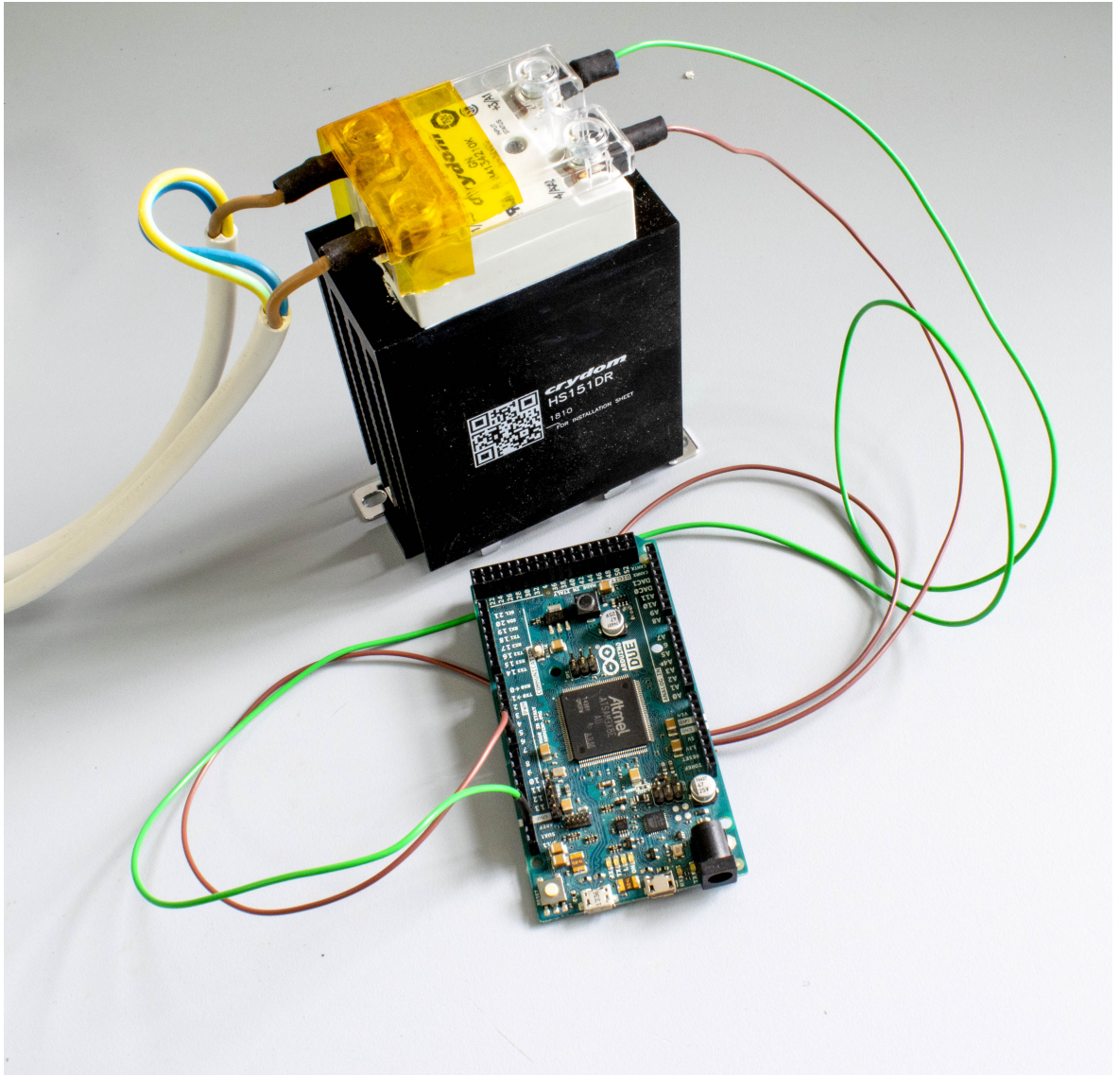


Figure B.4: Solid state relay connected to a microcontroller used in the sensing setup for measuring the rise and fall time of the sensor.

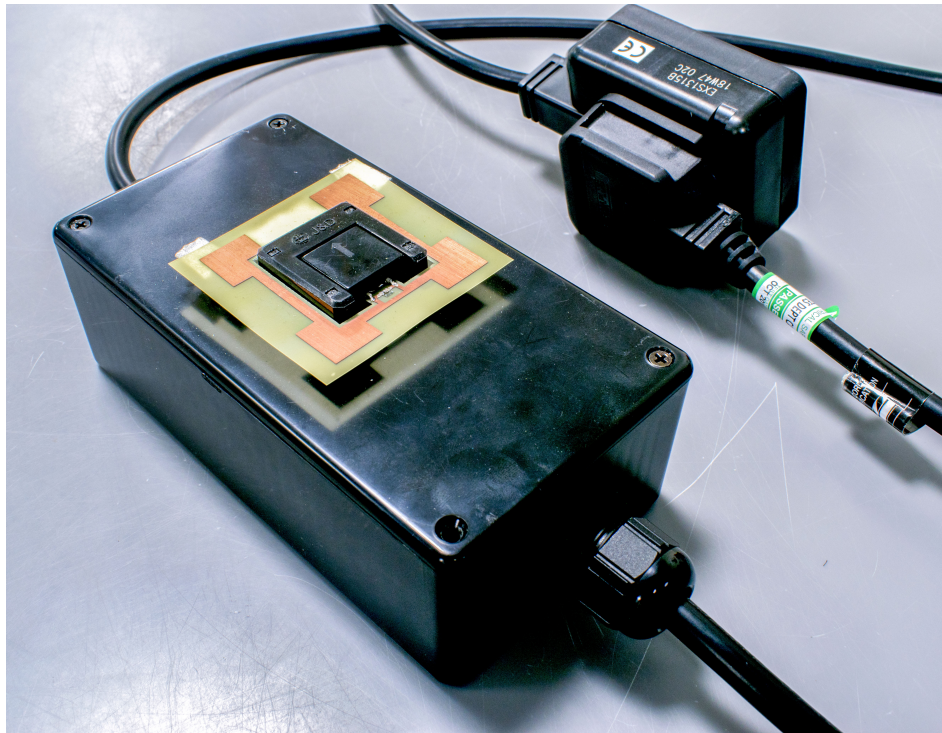


Figure B.5: The magnetic part of the current transformer is enclosed in an insulating box.

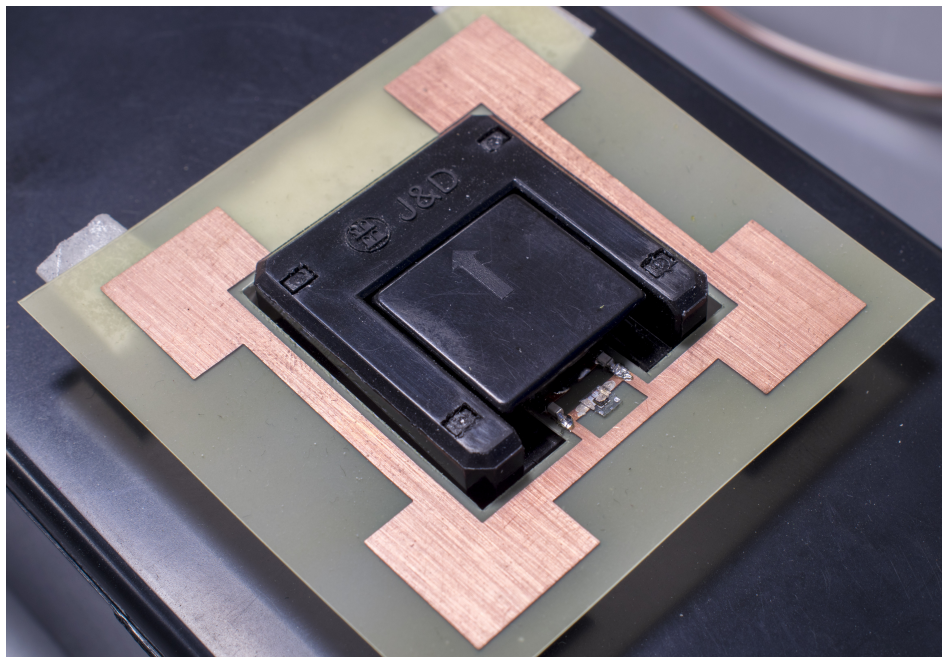


Figure B.6: An optimised tag antenna for the current transformer. The antenna is bent around the transformer housing.



Figure B.7: A Hall effect split-core current transducer for dc current sensing.

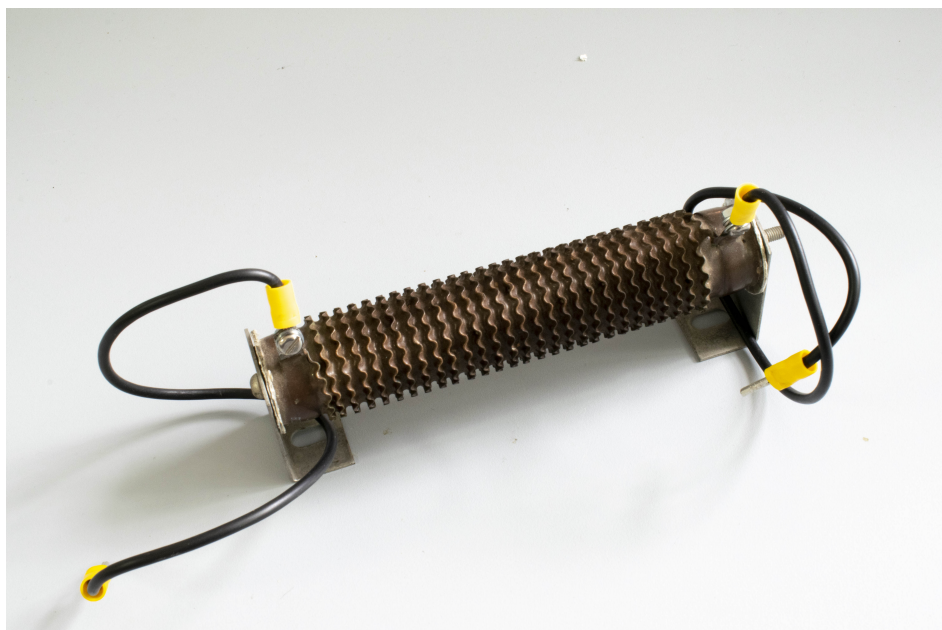


Figure B.8: An electrical load used for dc current measurements.

